Real-Time Sensor Data Acquisition for Borehole Trajectory Tracking and Telemetry over an Underground Wireless Ad hoc Network

DISSERTATION
zur Erlangung des Grades eines Doktors
der Ingenieurwissenschaften

vorgelegt von
M.Sc. Emmanuel Odei-Lartey

eingereicht bei der Naturwissenschaftlich-Technischen Fakultät
der Universität Siegen
Siegen 2018

Stand: April 2018

Betreuer und erster Gutachter

Prof. habil. Dr.-Ing. habil. Otmar Loffeld

Universität Siegen

Zweiter Gutachter

Prof. Dr.-Ing. Claus-Peter Fritzen

Universität Siegen

Tag der mündlichen Prüfung

08.03.2019

Gedruckt auf alterungsbeständigem holz- und säurefreiem Papier

ACKNOWLEDGEMENT

I would like to extend my gratitude to my immediate supervisor Dr.-Ing. Klaus Hartmann, for his understanding, support, advice and guidance during the entire duration of my Ph.D. study. His open-door policy and helpfulness in pointing me in the right direction during the cause of my work is greatly appreciated. He went out of his way to arrange for access to practical equipment and field trips to perform relevant experiments and tests which were beneficial for the completion of this thesis.

A special thank you to the Research School MOSES (Multi Modal Sensor Systems for Environmental Exploration and Safety) program and a special thank you too to the German Research Foundation (DFG) program for the grant which provided the opportunity to concentrate on my thesis work during these past years.

I would like to acknowledge Prof. Dr.-Ing. Otmar Loffeld for taking the time to go through my thesis and providing essential feedback and comments for further improvement of my writing. I also wish to acknowledge my second supervisor Prof. Dr.-Ing. Claus-Peter Fritzen for his patience in going through my thesis and also giving valuable comments for further corrections.

I thank my colleague Dr. rer. nat. Stefan Lammers for taking his time to proof read my thesis and offering insightful suggestions and pointing out issues for proper addressing. Those insightful comments and enlightening debates we had on applied concepts were of great benefit. I also appreciate the various discussions we had on open-source and programming. I thank my fellow research colleagues, both past and present, with a special mention to Mussab Zubair and Aiman Hsino for the memorable times we shared.

My appreciation goes to Mr. Wolf Twelsiek, and Mr. Bodo Ohrndorf, of ZESS for their helpful technical assistance during experimental setups and hardware implementation throughout the cause of my research and project work. Also, not forgetting to mention the secretaries Katharina Haut, Susanne Hoffmann, Caterina Sinner and Silvia Niet-Wunram whose immense commitment in terms of coordinating and helping me with processing administrative documents and making other useful information and notifications available to me.

A special thanks to companies Keller Geräte & Service GmbH and STDS-Jantz GmbH & Co.Kg for making available their facilities where I was able to make real-life tests and measurements.

Finally, I extend my immense gratitude to my dear wife, parents, brothers, and friends for their continuous support and encouragement throughout the entire duration of the thesis. It was this support that kept me going throughout those difficult and trying times. The accomplishment would not have been possible without them. Thank you.

ABSTRACT

This work provides a contribution to the positional tracking of the drill head in directional drilling considering real-time communication along the drill string. Particularly in the context of the development of oil and gas fields where target-oriented positions including the orientation of the drill head at large depths should be achieved. There are relatively large budgets available for such drilling projects to create suitable solutions using the latest technologies. In the construction industry, various deep drilling concepts are used, but with considerably lower depths. At the same time, high demands are also placed on position tracking. However, with these applications, lower technology budgets are available. Appropriate automatic measuring methods that provide online data in the process are not yet available even if the basic measurement technologies exist. An overall concept, which can meet the various requirements, is missing.

Regarding the scope of application, special attention is paid to the vertical drilling process used in Deep Soil Mixing. The Deep Soil Mixing process mixes the in-situ soil with cement or other binders to improve the mechanical and physical properties. This process results in a higher strength, lower permeability and low compressibility of the original soil [1-2]. Based on these systemic constraints, a new model is being developed and validated for the acquisition of sensor data and communication in the soil along the drill string and in real time during the drilling process (MWD). Based on the geometric model of the drill string, the signal model is developed to provide precise navigation data along the entire drill string. With the help of a new communication technology and the signal model, it is investigated which implementation concepts are possible and which performance is generated in each case. To provide a suitable reference, an error model is used, which has been defined by the Industry Steering Committee for Wellbore Accuracy (ISCWA). This model is used as a uniform basis for evaluation to improve the overall accuracy with regard to the tracking of the drilling process. The newly developed communication technology enables a new form of sensor data acquisition, data distribution and data fusing. Precision and stability can be significantly increased without increasing the cost of the technology. An important aspect here is the possibility of transporting sensor data in an ad-hoc sensor network in both directions along the drill string. This concept is also independent of the length of the drill string and thus also of the depth of a drilling operation to be achieved. The consequent use of navigation concepts and their optimized adaptation to the developed system model allows the acquisition of all position parameters of the drill head in a directional drilling. The consistent use of known fault model specifications allows a deep analysis of the developed navigation concept with other known measuring technology components and different sensor platforms. The analysis of the realization platforms with data from field tests gives a further Impression of the practicability of the developed concept.

---

[1] "Deep Soil Mixing (DSM), Improvement of weak soils by the DSM method," Brochure 32-0IE, Keller Group plc, 2016, http://www.kellerholding.com/download-keller-publications.html, Downloaded: 09/08/2016

[2] H. Leung, C. Ghani, W Okada, S. Terzaghi, "Comparison of the effectiveness of Deep Soil Mix columns using 2-D and 3-D plaxis," Plaxis Practice, SKM Sydney

KURZFASSUNG

Diese Arbeit liefert einen Forschungsbeitrag zum Positions-Tracking des Bohrkopfs bei Richtbohrungen unter Berücksichtigung einer Echtzeitkommunikation entlang des Bohrstrangs Besonders im Zusammenhang mit der Erschließung von Erdöl- und Gas-Feldern sind zielgenau Positionen inklusive der Orientierung des Bohrkopfes in großen Tiefen zu erreichen. Für solche Bohrvorhaben stehen relativ große Budgets zur Verfügung, um mit Hilfe neuster Technologien geeignete Lösungen zu schaffen. In der Bauindustrie werden ebenfalls vielfältige Tiefbohrkonzepte, Allerdings bei deutlich geringeren Tiefen, eingesetzt. Gleichwohl werden dabei ebenfalls hohe Anforderungen an ein Positions-Tracking gestellt. Bei diesen Anwendungen stehen allerdings geringere Technik-Budgets zur Verfügung. Geeignete automatisch messende Verfahren, die Online-Daten im Prozess bereitstellen sind bisher nicht verfügbar, auch wenn die prinzipiellen Mess-Technologien existieren. Es fehlt bisher ein Gesamtkonzept, welches die verschiedenen Anforderungen erfüllen kann.

Hinsichtlich des Anwendungsbereichs liegt das besondere Augenmerk auf dem vertikalen Bohrprozess, der beim Deep Soil Mixing angewandt wird. Der Deep Soil Mixing Prozess vermischt das vorgefundene Erdreich mit Zement oder anderen Bindemitteln, um die mechanisch-physikalischen Eigenschaften zu verbessern. Dieser Prozess verhilft zu einer höheren Festigkeit, geringerer Durchlässigkeit und niedriger Komprimierbarkeit des ursprünglichen Bodens[1-2].

Ausgehend von diesen systemischen Randbedingungen wird hier ein neues Modell für die Erfassung von Sensordaten und der Kommunikation im Erdreich entlang des Bohrstrangs und in Echtzeit während des Bohrvorgangs (MWD) entwickelt und validiert.

Auf Basis des geometrischen Modells des Bohrstrangs wird das Signalmodell entwickelt, um präzise Navigationsdaten entlang des gesamten Bohrstrangs bereitzustellen.

Mit Hilfe einer neuen Kommunikations-Technologie und dem Signalmodell wird untersucht, welche Realisierungskonzepte möglich sind und welche Leistungsfähigkeit dabei jeweils entsteht. Um eine geeignete Referenz zu ermöglichen, wird ein Fehlermodell verwendet, welches vom Industry Steering Comittee for Wellbore Accuracy (ISCWA) festgelegt wurde. Dieses Modell wird als einheitliche Basis zur Evaluation eingesetzt, um eine Verbesserung der Gesamtgenauigkeit hinsichtlich des Tracking des Bohrvorgangs zu erreichen.

Die neu entwickelte Kommunikationstechnologie ermöglicht eine neue Form der Sensordatenerfassung, Datenverteilung und der Datenfusion. Präzision und Stabilität können deutlich erhöht werden ohne die Kosten für die Technologie vergleichbar zu erhöhen. Wesentlicher Gesichtspunkt ist hier die Möglichkeit, Sensordaten in einem Ad-hoc Sensornetzwerk in beide Richtungen entlang des Bohrstrangs zu transportieren. Dieses Konzept ist im besonderen Maße auch unabhängig von der Länge des Bohrstrangs und somit auch von der zu erreichenden Tiefe eines Bohrvorgangs.

Die Systematische Verwendung von Navigationskonzepten und deren optimierte Anpassung an das entwickelte Systemmodell ermöglicht die Erfassung von allen Lageparametern des Bohrkopfes bei einer Richtbohrung.

Die systematische Verwendung von bekannten Fehlermodellvorgaben ermöglicht eine tiefgehende Analyse des erarbeiteten Navigationskonzepts mit anderen bekannten Messtechnik-Komponenten und verschiedenen Sensorplattformen.

Die Analyse der Realisierungsplattformen mit Daten von Feldversuchen gibt einen weiteren Eindruck für die Praxistauglichkeit des erarbeiteten Konzeptes.

---

[1] “Deep Soil Mixing (DSM), Improvement of weak soils by the DSM method,” Brochure 32-0IE, Keller Group plc, 2016, http://www.kellerholding.com/download-keller-publications.html, Downloaded: 09/08/2016

[2] H. Leung, C. Ghani, W Okada, S. Terzaghi, “Comparison of the effectiveness of Deep Soil Mix columns using 2-D and 3-D plaxis,” Plaxis Practice, SKM Sydney

CONTENTS

TABLE OF FIGURES

LIST OF TABLES

NOMENCLATURES

Symbols

ΔNx	Change in the north direction of the survey station x
ΔEx	Change in the east direction of the survey station x
ΔMDx	Change in the measured depth at the survey station x
$\Delta TVDx$	Change in the true vertical depth at the survey station x
SSx	Survey station x
A_x	Azimuth angle at survey station x
I_x	Inclination angle at survey station x
ψ	Angle the sensor node face makes with the north direction of the designated frame of reference
f'_x, f'_y, f'_z	x-, y- and z-axis accelerometer output unresolved to the designated reference frame
f_x, f_y, f_z	x-, y- and z-axis accelerometer output resolved to the designated reference frame
α	Tool-face angle
$\Delta N, \Delta E, \Delta TVD$	Change in the north, east and true vertical depth
$\delta N, \delta E, \delta TVD, \delta MD$	Small change in the north, east, true vertical depth and measured depth
δA	Small change in azimuth
Δt	Change in time
G_z	z-axis gyroscope output
G_z^{bias}	z-axis gyroscope output bias
$\vec{r}_p \begin{bmatrix} n_p \\ e_p \\ v_p \end{bmatrix}$	Measured position of the BHA with the north, east and vertical coordinates
$\Delta\vec{r}$	Error position vector
$\lvert\cdot\rvert$	Magnitude of a vector

Numenclatures

$f(n_a, n_p, e_a, e_p, v_a, v_p)$	Error vector magnitude between the measured survey position and the actual survey position traced by the BHA
$\vec{y}_i$	i^{th} observation vector
$\vec{\varepsilon}_i$	i^{th} regression vector
$\vec{\Theta}_{1,i}, \Theta_{2,i}$	Parameters that establish the linear relationship between the observations and the regression vector at i^{th} survey station
Π	Known regression parameter matrix
$\vec{Y}$	A number of observations made
R	Measurement Covariance matrix
$E\{\cdot\}$	Expectation
$f_{\square}(\cdot)$	Probability density function
$\arg\max$	Argument that maximizes
$\ln(.)$	Natural Logarithm
e_i	Error magnitude in the north, east and true vertical depth in the designated reference frame
σ_i	Magnitude of the i^{th} error source
x_k	State at time instant k
f_k	Non-linear state transition matrix at time instant k
u_k	Input at time instant k
w_k	Process noise at time instant k
h_k	Non-linear observation matrix at time instant k
v_k	Measurement noise at time instant k
Q_k	Covariance matrix of the process noise at time instant k
R_k	Covariance matrix of the measurement noise at time instant k
P_k^-	A priori estimate of the state covariance at time instant k
P_k^+	A posteriori estimate of the covariance at time instant k

G_k	Noise gain matrix at the time instant k
K_k	Kalman filter gain matrix at the time instant k
H_k	Measurement matrix at the time instant k
z_k	Measurement at time instant k
$\hat{x}_k^+$	A posteriori state estimate
$\vec{\omega}, \vec{\omega}_t$	Measured and true angular rate
$\vec{n}_b$	Driving process noise
$\vec{n}_v$	Wideband process noise
$\sigma(.)$	Standard deviation
$\delta(.)$	Dirac Function
$\Delta(\cdot)$	A unit change
$f_{\cdot\mid\cdot}(\cdot/\cdot)$	Conditional probability density function
$f_{\cdot}(\cdot)$	Probability density function
$\Lambda(\cdot)$	Likelihood function
$\sum(\cdot)$	Summation
$\overline{\mu}$	Mean
$P_r(dB_{mW}), P_t(dB_{mW})$	Power at the receiver and transmitter
$G_r(dB), G_t(dB)$	Receiver and transmitter gains
$L_o(dB), L_m(dB)$	Path loss in free space and soil medium

Acronyms

I-TUBE	Intelligent Tube
ZESS	Zentrum Fur SensorSysteme
DSM	Deep Soil Mixing
MWD	Measurement While Drilling
BHA	Bottom Hole Assembly

Numenclatures

MEMS	Micro-Electromechanical Systems
IMU	Inertial Measurement Unit
ISCWSA	Industrial Steering Committee for Wellbore Survey Accuracy
IPM	Instrument Performance Model
TVD	True vertical depth
MD	Measured depth
VWC	Volumetric water content
RSS	Received Signal Strength
EM	Electromagnetic
API	American Petroleum Institute
SPE	Society of Petroleum Engineers

CHAPTER 1

1. Introduction

1.1 Motivation

The Intelligent Tube (I-TUBE) Project is an on-going project at the Center for Sensor and Systems (ZESS), University of Siegen and served as the framework within which this thesis work was based. The main goal of the I-TUBE project is to develop a borehole telemetry system with the objective of obtaining the latest information in real-time on all relevant data during a drilling operation. This data is taken into account for faster complex decision-making process, which affect the actual drilling (drilling, completion, intervention and process control). This is motivated by but not limited to the deep soil mixing process, a process whereby the ground soil is mixed in situ with cement or compound binders to form a soil-mix or soil-cement column, where quality and accurate vertical drilling is essential to save cost. In a deep soil mixing process, there are several considerations made at the planning stages, geotechnical design phase and the execution phase [1]. One such consideration of which has been established from field experience is that the effectiveness of the columns is bounded, that is, when columns are too close there is no further gain in overall strength of the column, and too far apart, the columns behave individually with no net benefits [2]. Secondly, there is the tendency of the vertical bore to deviate from its straight-line course thereby also compromising the overall strength of the columns especially with longer columns [5-6]. These are caused by factors such as layered formations through which the drill hole passes, alternating hard and soft layers within rock formation through which the drill hole passes, the type of bit, rate of feed, and bit load and their influence on hole deviation [5]. Such a situation, when detected, requires for counter measures to mitigate the effect on the overall strengthening capacity. The extent of the lateral overlap of the columns are basically due to factors such as difficulty in predicting the properties of the underground soil and difficulty in assurance of a precise straight vertical drilling process as planned or designed. As a result, in defining the spacing of the columns, an acceptable error margin is determined based roughly from past drilling processes within the location or the same type of terrain. This method however results in the over-usage of resources and errors are sometimes unavoidable thus increasing the overall production cost and time. Figure 1.1-3 shows results of deep soil mixing (DSM) processes, the column pattern as well as how the process is undertaken.

Figure 1: Exposed cut-off wall with secant DSM columns: Courtesy: Keller, Deep Soil Mixing [1].

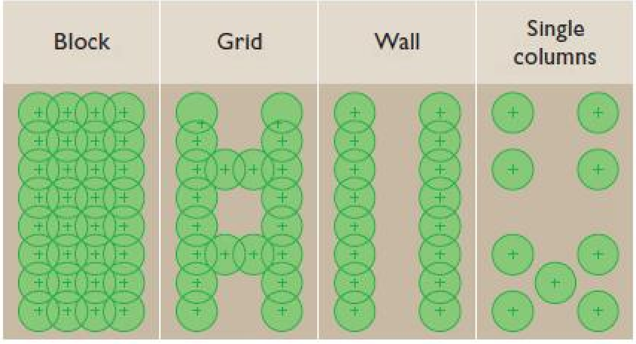

Figure 1.2: DSM column pattern: Courtesy: Keller, Deep Soil Mixing [1].

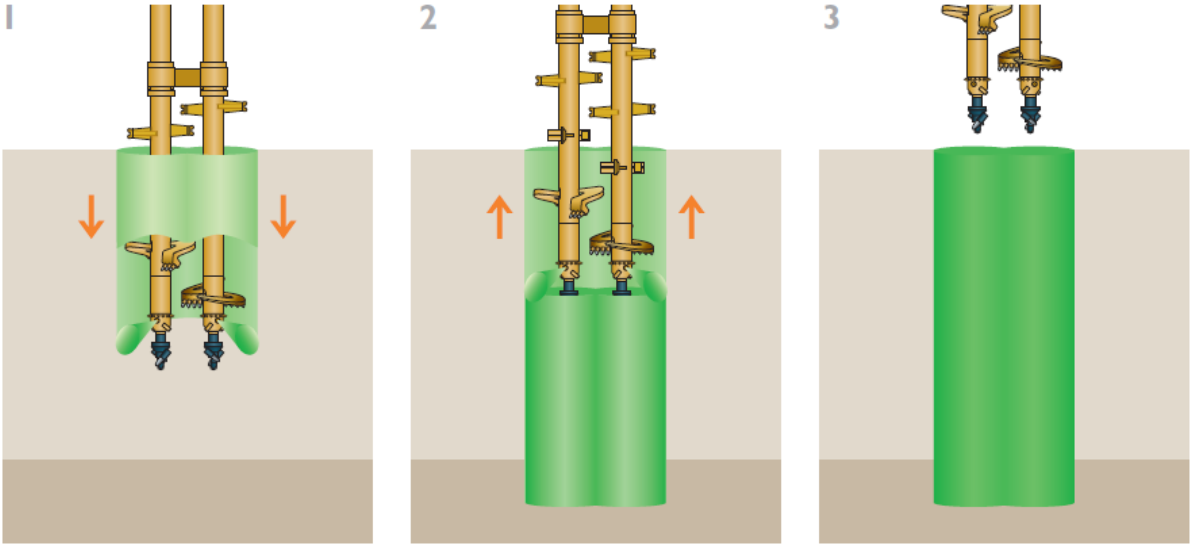

Figure 1.3: Grout is injected during penetration and withdrawal phases with the amount varied depending on soil conditions. Courtesy: Keller, Deep Soil Mixing [1]

In the aforementioned process, after the required drilling depth is reached, the displacement measurements of the wellbore at uniform depth intervals are logged for further analysis. This recording is carried out before the grout jetting process is initiated. Jetting is the spewing of grout; a mixture of water, cement, sand and sometimes fine gravel from the nozzle of the drill head as the drill pipe is slowly retracted from the borehole bottom at a very low rotation speed.

The wellbore survey is done by disconnecting the immediate top drill tube above ground and slowly guiding the measuring instrument, for instance a cabled digital inclinometer probe, through the middle inner tube to the bottom of the borehole [1]. The wellbore survey measurements in the form of x- and y-axis displacements in a defined reference frame, are taken at incremental steps of about 2 meters until the bottom of the wellbore is reached. This information is post-processed at a later time to obtain a high resolution wellbore profile in the designated reference frame. From the preceding description, it can be inferred that the actual trajectory is not known immediately until after the drilling process is complete. This measurement method adds to the production time depending on factors such as the depth and shape of the wellbore, the instrument handling technique and, moreover, there is a risk of loosing pressure in the tube which keeps fluid from seeping into an outer channel. Not so much importance has been associated with measurement while drilling during the vertical drilling processes despite such issues as miss-guided trajectories, which results in re-drilling and in effect raises production costs. Figure 1.4 shows a real-world example of wall damage due to column deviation during the deep soil mixing process.

Figure 1.4: Wall damage due to column deviation during the deep soil mixing process. Courtesy: Deep Foundations Institute, TreviGroup [3].

Figure 1.5 shows a real example of the results of an “as-built drawings” of a jet grouting cut-off formed by the deep mixing process with over 60% of the columns deeper than 30 meters. The number of jet grouting columns was 1100 and the spacing was at 0.75 meters with the required thickness of the wall at 0.80 meters [3, 4].

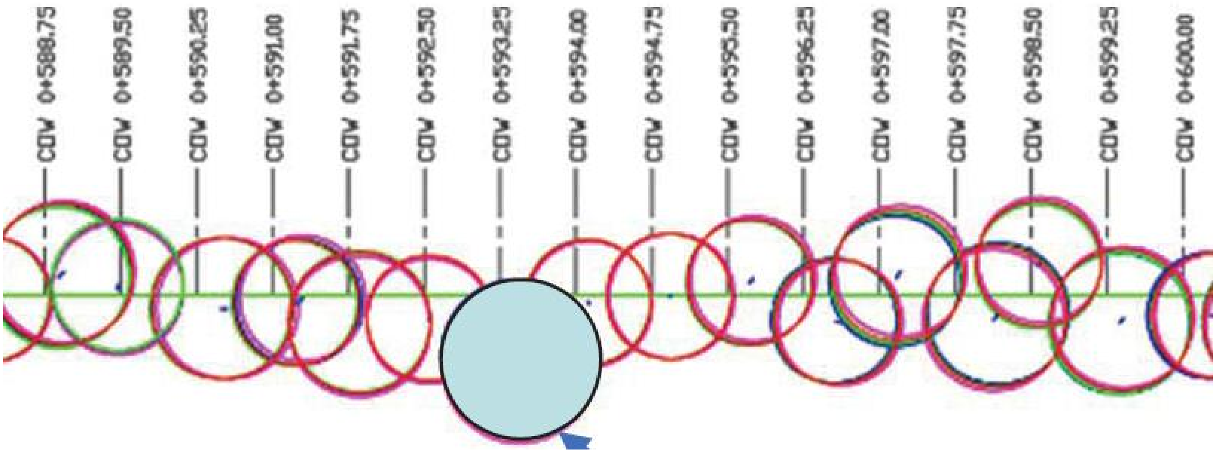

Figure 1.5: Jet grouting cut-off. Courtesy: Diavik A418, Deep Foundations Institute, TreviGroup [3]

The blue circle shows an additional column added because of the notable deviation at point COW 0+593.25. The acceptable margin of error or accuracy of the survey instrument of use can be deduced from the specification depending on the application of interest. In this case, for a thickness of 0.80 m and spacing of 0.75m, the diameters of the column should basically be greater than or equal to 0.55 m assuming perfect symmetry.

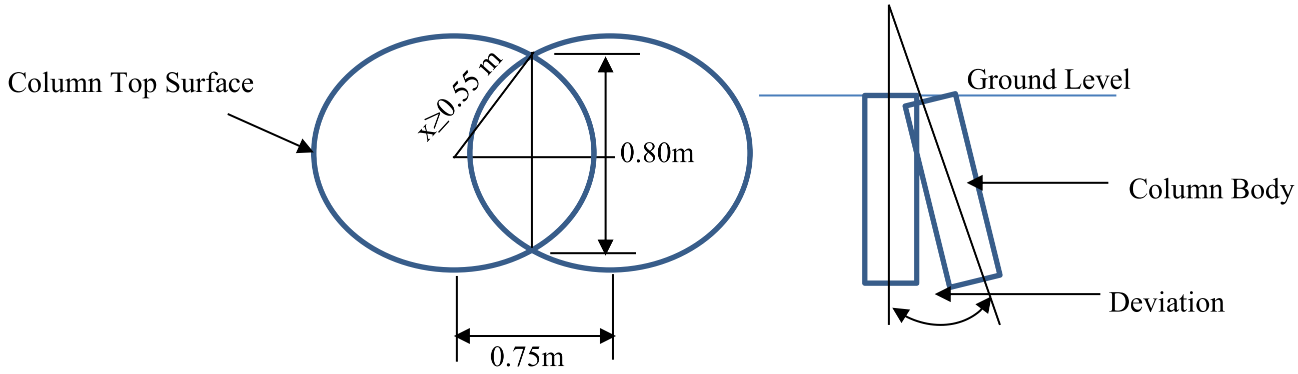

Figure 1.6: Plan and vertical sectional view of two adjacent columns; assuming perfect symmetry.

Figure 1.6 shows the plan and vertical view of two adjacent columns as specified by the Jet Grouting Cut-off described above. Assuming perfect symmetry and a column top surface radius, x of value 0.6 m which implies an extra thickness of approximately 0.14 m, the deviation angle below which the thickness of 0.80 m is maintained for a given length of column can be deduced using simple geometry. The value of the deviation angle is worked out to be approximately 0.27° for a column length of 30m which represents a 0.46% deviation. In reality, such symmetry might not be achievable as shown in figure 1.5 but such deduction could serve as a guide for determining the acceptable error margin for the survey instrument to be used. For instance, an error tolerance of +/- 5 cm could be considered sufficient for such an application. In Chapter 4, analysis of the uncertainty of different IMU sensors utilized for survey measurements is made to acetain their suitability for the drilling application of interest.

1.2 Previous Research

Measurement while drilling (MWD) provides data which is utilized in directional drilling to monitor the position and orientation of the lower part of the drill string also called the bottom hole assembly (BHA) [8]. In the drilling industry, the conventional magnetometer-based MWD surveying system is generally used. This normally consists of three accelerometers and three magnetometers mounted in three mutually orthogonal directions. At a predetermined survey station, the accelerometers measure the earth gravity components to determine the BHA inclination and tool face angles while the magnetometers measure the earth's magnetic field to determine the BHA azimuth [8]. The trajectory between two survey stations is then computed geometrically by a standard method, such as the minimum curvature method [12]. The magnetometer-based MWD surveying system is characterized by high costs and severely degraded performance due to geomagnetic interferences [9]. The option of using the gyro-based MWD technique as an alternative to the magnetometer based downhole surveying has also been researched [9]. This uses compensated data from an inertia measurement unit sensor to calculate its position and orientation. An inertia measurement unit (IMU) is a microelectromechanical system (MEMS) sensor that measures and reports a craft's velocity, orientation and gravitational forces using a combination of accelerometers and gyroscopes, sometimes also magnetometers. Through a machination estimation process, the position and orientation of the IMU sensor can be determined. Furthermore, there has also been research on the use of Adaptive-Filter-Based In-Drilling Alignment techniques which is shown experimentally to successfully limit the error growth associated with both gyro- and magnetometer-based MWD [9-10]. In the aforementioned technique, the induction of precisely controlled and observed motion of the IMU sensor in the horizontal north-east plane is done while the entire BHA is at rest. This enables for the observability of the azimuth error for estimation in an extended Kalman filter implementation. Analysis of the observability of the azimuth error as a result of this horizontal controlled motion is further detailed in another referenced publication. This dynamic observation is then used as a reference measurement to align the IMU if of a smaller variance than the routine IMU measurements. However, for vertical drilling processes, such controlled linear motion in the north-east geographical frame is difficult to attain due to mechanical restrictions of the drilling tubes.

1.3 Thesis Assumptions

Survey measurements are taken at designated points or depths along the wellbore-path called survey stations as shown in figure 1.7 and made available in real-time over a wireless underground ad hoc network borehole telemetry system. These survey measurements are used for the estimation of the wellbore trajectory between any two survey stations. There are several wellbore-survey techniques for estimating the wellbore trajectory between two stations, but due to the nature of the trajectory [12], which is close to a straight line, the approach using the balanced angle method was considered. This is basically an improvement to the average angle method because it takes into consideration survey measurements at both survey stations [7]. The measurements taken at the survey stations are used to compute the north, east and true vertical depth coordinate positions with respect to a designated reference frame. These measurements are recorded at each survey station during the entire drilling process and, finally, a high-resolution trajectory is plotted from the vector additions of the coordinate positions after the borehole survey process is completed. Figure 1.7 shows a three-dimensional view of a wellbore trajectory showing how the various measurement parameters are used to determine its overall trajectory. A_k denotes the azimuth angle at survey station k relative to the designated frame of reference, I_k represents the inclination angle at survey station k, SS_k denotes the survey station k, $\Delta\mathrm{N}_k$ and $\Delta\mathrm{E}_k$ represents the change in the north and east direction of the designated frame of reference respectively at survey station x. ΔMD_k denotes the measured depth which is the length along the drill tube in the ground and ΔTVD_k denotes the true vertical depth of the wellbore. Figure 1.8 shows the inclination and yaw angle orientation of the sensor node within the drill tube. ψ denotes the angle the sensor node face makes with the north direction of the designated frame of reference.

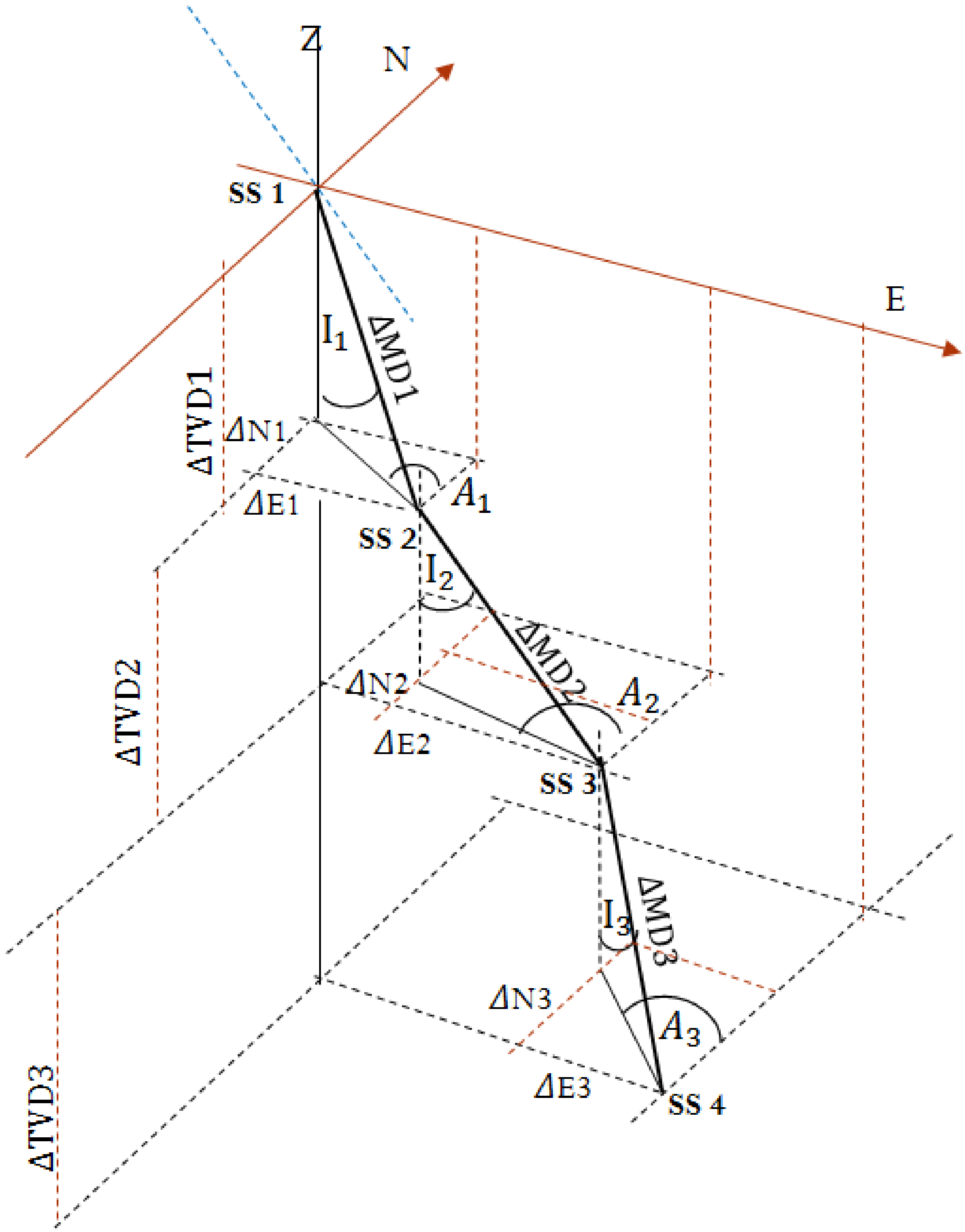

Figure 1.7: A three-dimensional view of the wellbore trajectory.

Basically, the aim is to track the yaw angle position of the sensor ψ, which is body-fixed, aligned with the drill tube and rotates with the tube about its axis of rotation. This angle is required to resolve the 3-axis accelerometer output data relative to the designated frame of reference before the direction of tilt angle I_x is determined.

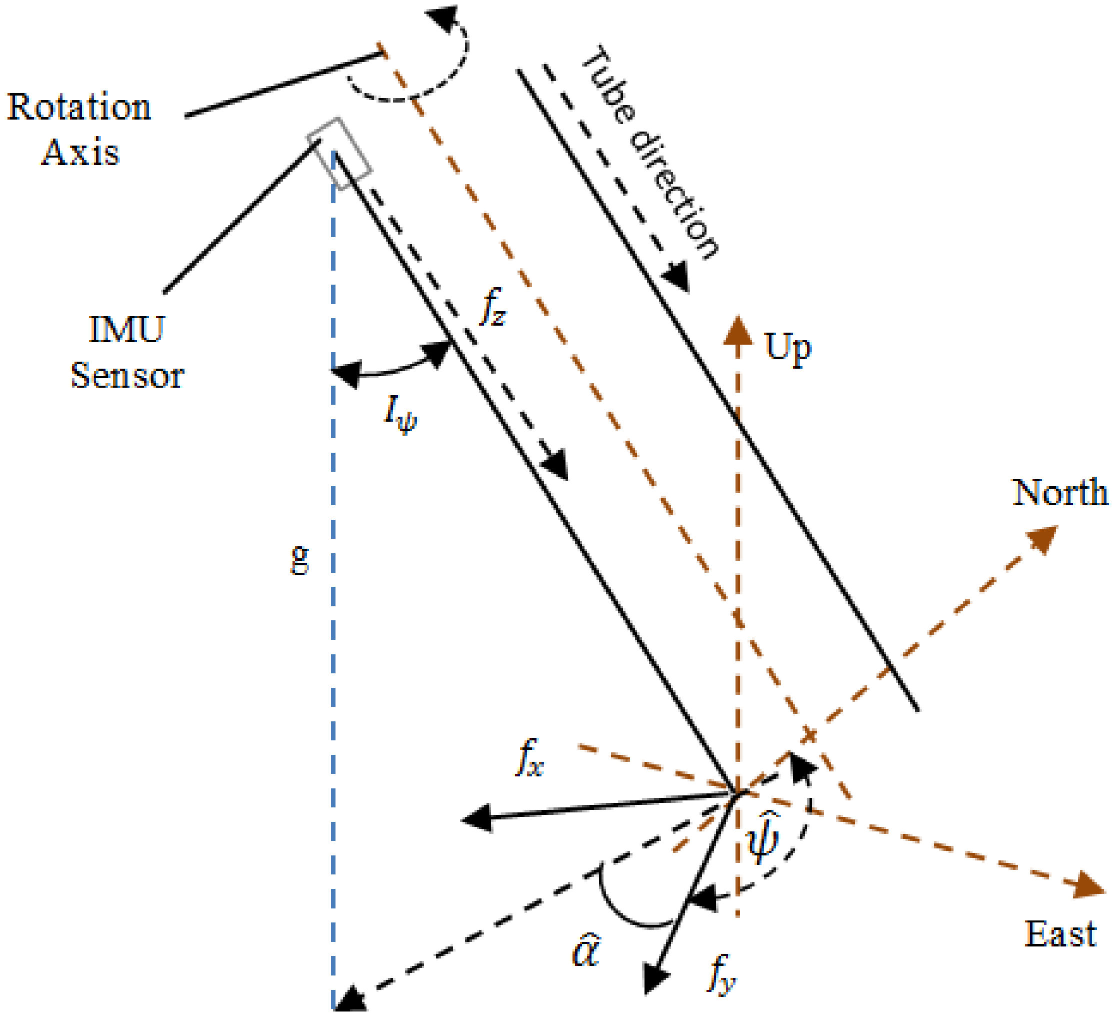

Figure 1.8: Inclination and yaw angle orientation of sensor within the drill tube

The resolution of the accelerometer output data to the designated frame of reference is given in Eq. 1.1

$$\begin{bmatrix} f_x \\ f_y \\ f_z \end{bmatrix} = \begin{bmatrix} \cos\psi & -\sin\psi & 0 \\ \sin\psi & \cos\psi & 0 \\ 0 & 0 & 1 \end{bmatrix} \begin{bmatrix} f'_x \\ f'_y \\ f'_z \end{bmatrix} \tag{1.1}$$

where $f_x^{'}$, $f_y^{'}$ and $f_z^{'}$ denote the x-, y- and z-axis accelerometer output when sensor position is displaced at a yaw position of ψ from the reference north position of the designated reference frame while f_x, f_y and f_z denotes the resolved x-, y- and z-axis accelerometer output

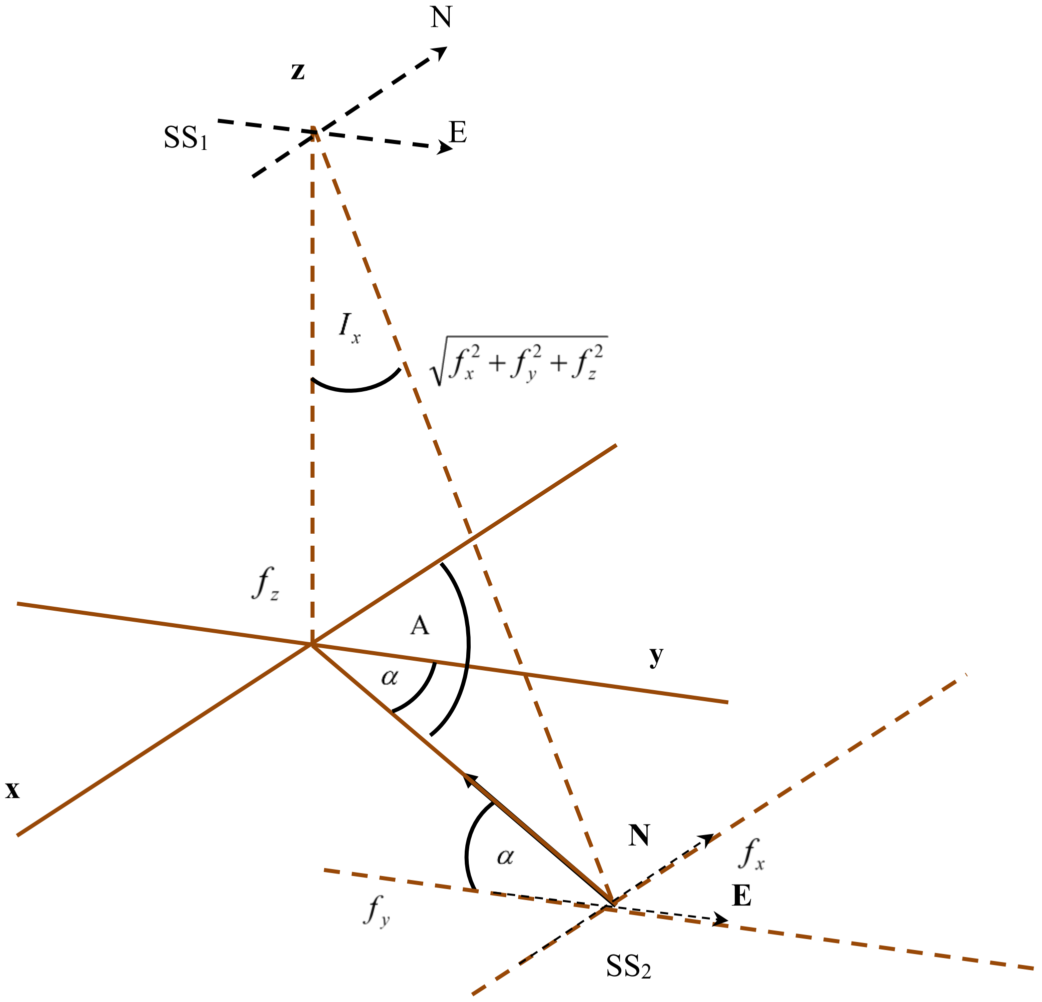

Figure 1.9: The trajectory between two survey stations; station one and two with the indicated inclination and azimuth as well as the accelerometer output

$$I_{\psi} = \cos^{-1}\left[\frac{f_z}{\sqrt{f_x^2+f_y^2+f_z^2}}\right] \tag{1.2}$$

$$\alpha = \tan^{-1}\left[\frac{f_x}{f_y}\right] \tag{1.3}$$

where I_{ψ} denotes the inclination and α denotes the tool-face angle which is the angle between the y-axis and the north reference position of the tube. For a clearer insight into the concept explained in this section, the next section discusses the error model of the wellbore trajectory and further elaborates the error sources, how it effects the survey measurements which consequently effect the north, east and true vertical depth position coordinates in the designated frame of reference at each survey station. Keeping accurate track of the sensor node yaw angle position improves the accuracy of both the inclination and the azimuth measurements which further reduces the uncertainty at the target location. Due to the challenge that arises by the periodic stoppages of the drilling process to insert or remove a drill tube, it is essential to enable the sensor node keep track of its yaw position autonomously. Periodic update of the sensor node yaw angle position relative to a pre-defined reference frame is essential to ensure that the yaw angle position errors are bounded.

1.4 Thesis Objectives and Contributions

1.4.1 Thesis Objectives

The primary objective of this thesis is to reduce the margin of uncertainty (ellipsoid of uncertainty) mostly attributed to the measurement instrument capabilities, in reaching a targeted location under consideration. The main purpose of which is to improve the overall accuracy of the wellbore trajectory by means of the possibility of introducing corrective measures in real-time. To accomplish this, the position of the sensor node within the borehole assembly is required to be accurately tracked in the designated frame of reference so that there is improved accuracy in the computation of the inclination angle and its direction of tilt or azimuth. The design of this scheme is motivated by the known challenges attributed to mechanical and borehole telemetry network architecture constraints of the deployment environment; size constraints of metal drill tube and an unpredictable underground terrain in terms of the physical and chemical properties of the ground soil, lateral and vertical vibrations etc [6].

A second objective is to investigate the feasibility for real-time sensor data acquisition over a wireless ad hoc network underground independent of the depth to be used as a borehole telemetry system. As mentioned earlier, this is to enable for critical intervention or control tools to be deployed.

1.4.2 Thesis Contributions

This thesis introduces a mathematical model representation and implemented of a data processing scheme to enable the fusion of higher accurate data source at low bandwidth from an external aid with a high bandwidth noisy data output from locally embedded inertia sensors for tracking a sensor toolface position within a defined reference frame. Essentially, this shows the feasibility of the use of this scheme for wellpath surveying as used within a vertical drilling process which is further extended to directional drilling. Application of the affornentioned concepts shows the improvement of the trajectory tracking capabilities of the BHA wellpath with the acquisition of sensor data for observation executed by an in-house developed borehole telemetry scheme.

Secondly, the thesis analyzes the feasibility of sustaining a wireless underground ad hoc network for borehole telemetry. Elaboration is made on the propagation of the electromagnetic waves between nodes within the soil medium and within the metal drill tubes with further emphasis on the factors that enable for the sustained connectivity. It further describes an implementation of it and some field results for verification. This telemetry system enables for real-time acquisition of the measurement information for prompt interventions to be made during the drilling process.

1.5 Thesis Structure

This thesis is structured as follows, chapter 2 describes the wellbore positioning error model which is the standard model designed by the Industrial Steering Committee for Wellbore Survey Accuracy (ISCWSA). It describes how the position uncertainty is computed from the survey station observations and how the measuring instrument errors translate into the position errors at each survey station, survey leg and finally the target position. Chapter 3 describes the approach to improve the estimation of the trajectory using the indirect Kalman filter processing scheme in the feedforward configuration, where the optimal estimate of the filter is used as a measurement update for the Kalman filter process in an adjacent node. Chapter 4 gives the performance analysis of the data processing scheme; some simulation results as well as results from laboratory and field tests of the applied mathematical model. Chapter 5 describes the work done with regards to the feasibility of a wireless ad hoc network underground for real-time data acquisition for the borehole telemetry system. Chapter 6 finally gives a conclusion and an outlook of the thesis. Also included are the appendices, which give further elaboration of some used mathematical concepts within the thesis.

Chapter 2

2. Wellbore Navigation

2.1 Error Model Description

The error model defines how various error sources affect the observations in the wellbore and therefore the positional uncertainties along the wellbore. The Industry Steering Committee for Wellbore Survey Accuracy (ISCWSA) which is a recognized body of industry wellbore surveying experts has developed a model for error representation to be used as an industrial standard [7]. The ISCWSA defines the Instrument Performance Model (IPM) which describes the error sources, their magnitudes and how they propagate. Basically, the error sources are multiple and varied in which each error source affects the positional accuracy of the given survey station. The ISCWSA error model defines the effect of the error sources on the measured depth, the inclination and the azimuth observations at the respective survey station and how this in turn affects the respective north, east and true vertical depth (TVD) position in the designated frame of reference. These definitions are represented by what is referred to as the weighting functions [7]. The weighting function is obtained by the partial derivative of the function relating the survey measurement of interest; measured depth, inclination or azimuth, with respect to the sensor output of interest. The error model basically refers to the inaccuracies of instruments and measurement systems.

The planned trajectory is represented in 3-dimensional space by vector coordinates that link the various survey stations which therefore imply that the total trajectory from the start point to the target is calculated geometrically. A survey station coordinate position in the given 3-dimensional space is associated with the measured depth, the inclination and the azimuth and is represented by the north, east and true vertical depth Position with respect to the designated frame of reference. There are several methods of estimating the trajectory between two survey stations which include the average angle method, minimum curvature method, balanced angle method and the tangential angle method. The balanced tangential method gives a near accurate approximation of the true trajectory between the two survey stations for less curvy trajectories. The computation method for the balanced tangential method is illustrated in Figure 2.1 and Eqns. 2.1-3. Figure 2.1 shows the wellbore path between two survey stations and the various parameters used in defining the wellbore position.

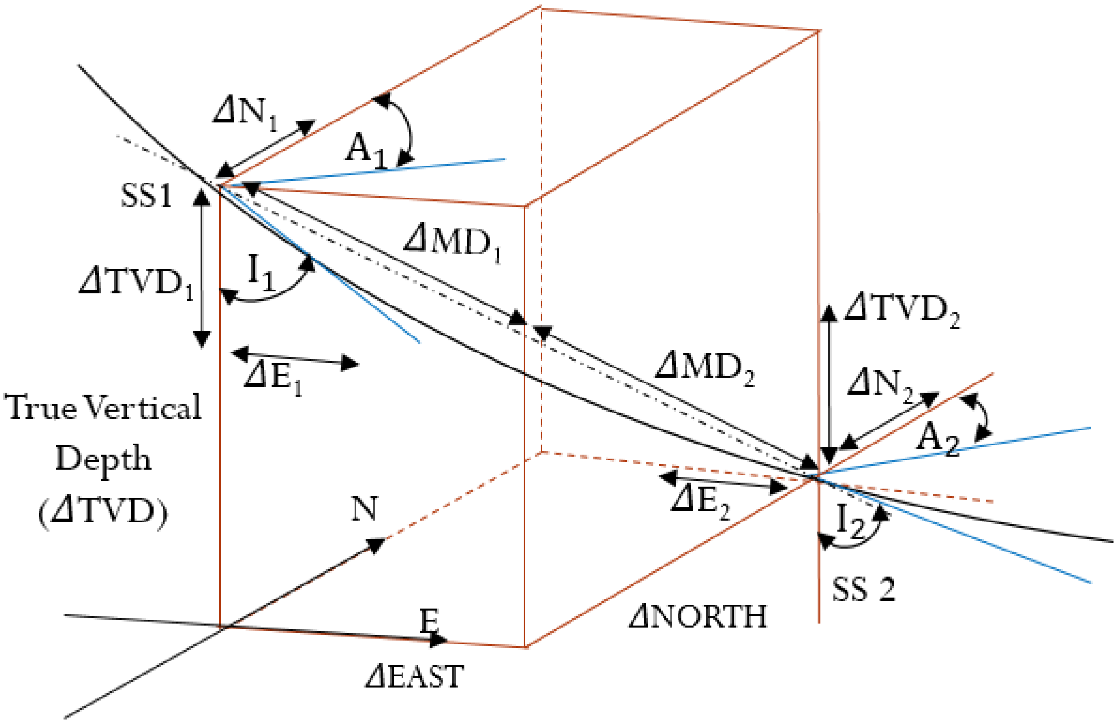

Figure 2.1: Wellbore path or trajectory between two survey stations.

The formulation for finding the coordinates for the position at the respective survey stations using the balanced tangential method is shown in Eq. 2.1-3 with further background on the derivation of the equations given in Appendix IV

$$\Delta \mathrm{N}_{k,k+1} = \frac{MD_{k+1} - MD_k}{2} \cdot \left[\sin \mathrm{I}_k \cdot \cos \mathrm{A}_k + \sin \mathrm{I}_{k+1} \cdot \cos \mathrm{A}_{k+1} \right] \tag{2.1}$$

$$\Delta \mathrm{E}_{k,k+1} = \frac{MD_{k+1} - MD_k}{2} \cdot \left[\sin \mathrm{I}_k \cdot \sin \mathrm{A}_k + \sin \mathrm{I}_{k+1} \cdot \sin \mathrm{A}_{k+1} \right] \tag{2.2}$$

$$\Delta TVD_{k,k+1} = \frac{MD_{k+1} - MD_k}{2} \cdot \left[\cos \mathrm{I}_k + \cos \mathrm{I}_{k+1} \right] \tag{2.3}$$

where $\Delta N_{k,k+1}$, $\Delta E_{k,k+1}$ and $\Delta TVD_{k,k+1}$ denotes the change in the north, east and true vertical depth respectively from survey station k to survey station $k+1$ in the designated reference frame. I_k, I_{k+1}, A_k, A_{k+1} are the inclination angles and azimuths measured at stations one and two respectively. MD_k and MD_{k+2} are the measured depths at survey stations k and $k+1$ respectively and are associated with the north, east, true vertical depth of the designated reference frame. However, the accumulation of errors from sources such as sensor residual errors cause a deviation from the planned wellbore trajectory as shown in figures 2.2a-b. It is important to know how each error source affects the survey measurements at each survey station and how these errors subsequently effect the position measurement errors. An illustration of how the various error sources affect the observations at the survey stations is given in figures 2.2a-b.

It is important to know how each error source affects the observations at each survey station and how the observation errors affect the well path in the North N , East E and True Vertical Depth TVD directions. A description of how the various error sources affect the observations at the survey stations is given in figures 2.2a-b.

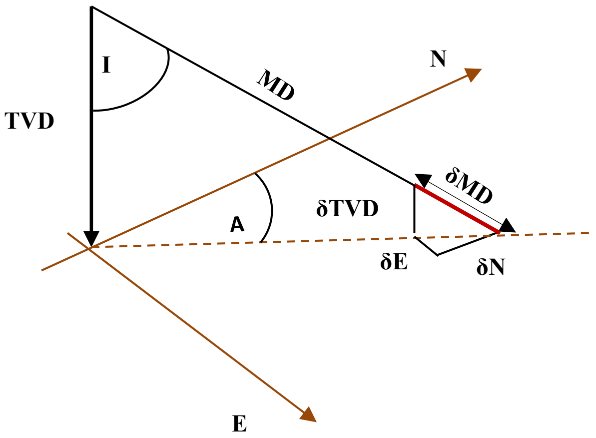

$$\delta TVD = \delta MD \cdot \cos \mathrm{I}$$

$$\delta N = \delta MD \cdot \sin \mathrm{I} \cdot \cos \mathrm{A}$$

$$\delta E = \delta MD \cdot \sin \mathrm{I} \cdot \sin \mathrm{A}$$

Figure 2.2a: Effect of measured depth MD error on the North (N), East (E) and the True Vertical Depth (TVD) observations at the survey stations with fixed inclination and azimuth.

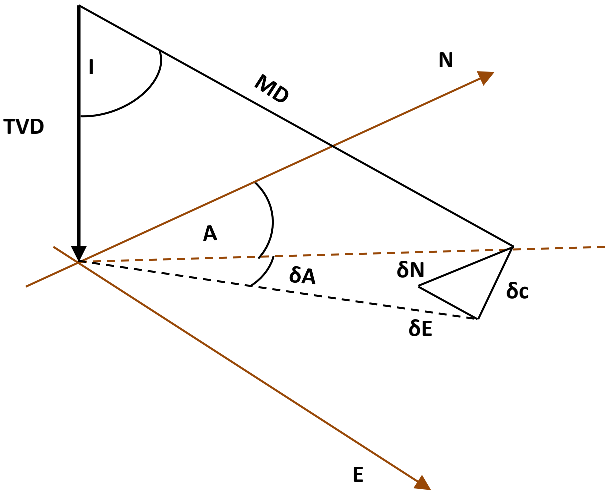

$$\delta c = MD \cdot \sin \mathrm{I} \cdot \sin \delta \mathrm{A}$$

$$\delta N = MD \cdot \sin \mathrm{I} \cdot \sin \delta \mathrm{A} \cdot \sin \mathrm{A}$$

$$\delta E = MD \cdot \sin \mathrm{I} \cdot \sin \delta \mathrm{A} \cdot \cos \mathrm{A}$$

Figure 2.2b: Effect of azimuth error on the north and east observations at the survey station with fixed inclination and measured depth.

$\delta \mathrm{A}$, $\delta \mathrm{N}$, $\delta \mathrm{E}$, δTVD and δMD denote the error in the azimuth, north, east, true vertical depth respectively and the measured depth, I and A denote the inclination and the azimuth respectively. Figure 2.2a illustrates how the measured depth error affects the north, east and true vertical depth observations at the survey stations while Figure 2.2b shows the effect of azimuth error on the north and east observations in the designated reference frame. There is no effect of the azimuth error on the true vertical depth as observed. A weighting function is used to determine the effect any error source will have on the measured depth, inclination and azimuth respectively. The weighting function is determined by finding the partial derivative of the equation relating the survey measurement and the sensor output source with respect to the latter. For instance, from chapter 1, combining Eq. 1.1 and 1.3, and writing the yaw angular position as a function of the z-axis gyroscope output and change in time given as

$$\psi = \Delta t \cdot G_z \tag{2.4}$$

results in the equation relating the azimuth to the gyroscope output which is written as

$$A = \arctan\left[\frac{f_x}{f_y}\right] = \arctan\left[\frac{f'_x \cos[\Delta t \cdot G_z] - f'_y \sin[\Delta t \cdot G_z]}{f'_y \cos[\Delta t \cdot G_z] + f'_x \sin[\Delta t \cdot G_z]}\right] \tag{2.5}$$

where G_z denotes the z-axis gyroscope output and Δt denotes the time duration over which the integration is done. The weighting function of the z-axis gyroscope bias is given as the partial derivative of Eq. (2.5) as shown in Eq. (2.6) below

$$\frac{\partial A}{\partial G_z} = \Delta t \ . \tag{2.6}$$

The azimuth error in the designated frame of reference due to the z-axis gyroscope bias is therefore given as

$$\frac{\partial A}{\partial G_z} \cdot G_z^{bias} = \Delta t \cdot G_z^{bias} . \tag{2.7}$$

Since the z-axis gyroscope bias error source affects just the azimuth, the weighting function is given as the vector [0, 0, Δt] implicit that there is no effect of the error source on the measured depth (MD) and the inclination as indicated by the zeros in the first two components of the vector representation.

Figure 2.3 shows the measured position at SS2 denoted by the vector $\vec{r}_p$ and the actual or true position of the borehole assembly or drill-head denoted by the vector $\vec{r}_a$. n_p, e_p, v_p denotes the north, east and vertical depth components of the postion vector $\vec{r}_p$ while n_a, e_a, v_a denotes the north, east and vertical depth components of the position vector $\vec{r}_a$. These two vector positions represent the measured and the true coordinate positions of the drill head in the designated frame of reference. n_i, e_i, v_i, denote the coordinates in the north, east and true vertical directions in the designated reference frame.

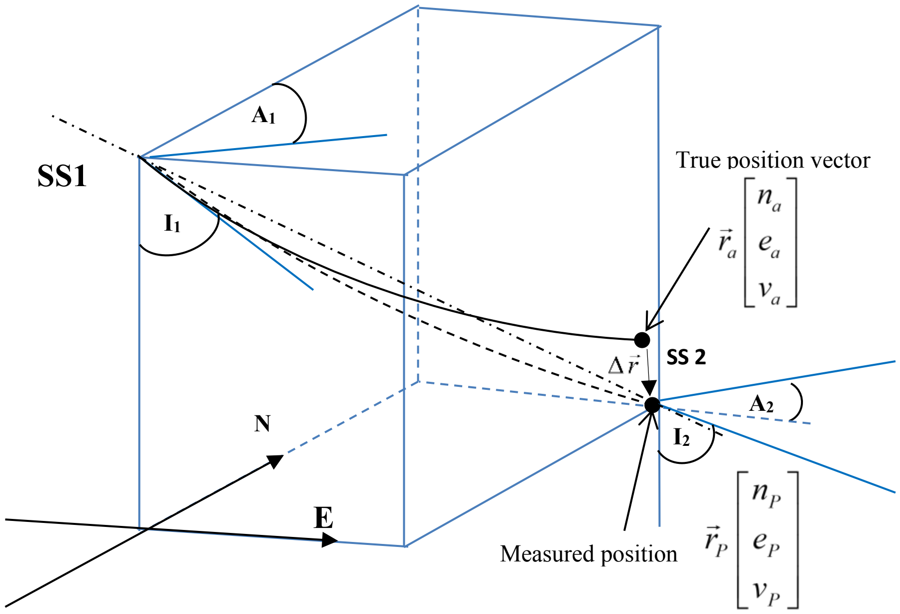

Figure 2.3: The measured wellbore trajectory and the actual wellbore trajectory

The difference between the measured and the actual/true position is represented as the vector difference between the two position vectors $\vec{r}_p$ and $\vec{r}_a$. This is denoted by the error position vector $\Delta\vec{r}$. $\Delta\vec{r}$ is a function of the survey measurements; measured depth, inclination and azimuth, along the planned path and its magnitude is given as

$$|\Delta\vec{r}| = |\vec{r}_p - \vec{r}_a| \tag{2.8}$$

A representation of Eqn. 2.8 is expressed as

$$f(n_a, n_p, e_a, e_p, v_a, v_p; \Lambda) = |\Delta\vec{r}| \tag{2.9}$$

$$f(n_a,n_p,e_a,e_p,v_a,v_p;\Lambda)=\sqrt{\left(n_p-n_a\right)^2+\left(e_p-e_a\right)^2+\left(v_p-v_a\right)^2} \qquad (2.10)$$

where $f(n_a,n_p,e_a,e_p,v_a,v_p;\Lambda)$ denotes the distance or error vector magnitude between the measured survey position and the actual survey position traced by the borehole assemble/drill-head. The aim is to determine the most likely estimate of the error function by finding the values of n_p, e_p, and v_p for which the measured survey position is closest to the actual survey position of the borehole assembly (accurately reflects the error). Λ denotes the particular survey measurement of interest (N, E, TVD). To obtain this, the derivative of the function $f(n_a,n_p,e_a,e_p,v_a,v_p;\Lambda)$ with respect to the components n_a, e_a, v_a is found and the result is assigned to zero. This is given as

$$\frac{df(n_a,n_p,e_a,e_p,v_a,v_p;\Lambda)}{d(n_a,e_a,v_a)}=\frac{df(n_a,n_p,e_a,e_p,v_a,v_p;\Lambda)}{dn_a}+\frac{df(n_a,n_p,e_a,e_p,v_a,v_p;\Lambda)}{de_a}+\frac{df(n_a,n_p,e_a,e_p,v_a,v_p;\Lambda)}{dv_a} \qquad (2.11)$$

Differentiating Eqn. 2.11 results in

$$\frac{df(n_a,n_p,e_a,e_p,v_a,v_p;\Lambda)}{d(n_a,e_a,v_a)}=\frac{\left(n_p-n_a\right)\frac{d(n_p-n_a)}{d\Lambda}+\left(e_p-e_a\right)\frac{d(e_p-e_a)}{d\Lambda}+\left(v_p-v_a\right)\frac{d(v_p-v_a)}{d\Lambda}}{\sqrt{\left(n_p-n_a\right)^2+\left(e_p-e_a\right)^2+\left(v_p-v_a\right)^2}}=0 \qquad (2.12)$$

which is further expressed as

$$\left(n_p-n_a\right)\frac{dn_p}{d\Lambda}+\left(e_p-e_a\right)\frac{de_p}{d\Lambda}+\left(v_p-v_a\right)\frac{dv_p}{d\Lambda}=0 \qquad (2.13)$$

2.2 Borehole Assembly Position Uncertainty

The borehole assembly position error at a survey station is represented as a 3-dimensional ellipse of uncertainty which indicates the uncertainty in the inclination, azimuth and measured depth or projected as uncertainties in the north, east and true vertical depth planes in the designated reference frame. The uncertainty is generally modelled as a 3-dimensional Gaussian probability density function. The phenomenon described in the preceding section can be modelled as a linear regression problem to enable the estimation of the parameters that relate the independent true values of the survey station position to the observed or measured values. The expression for the linear regression analysis is given as

$$\vec{y}_i=\vec{\Theta}_{1,i}+\Theta_{2,i}\vec{r}_i+\delta\vec{r}_i \qquad (2.14)$$

where $\vec{y}_i$ depict the i^{th} observation vector; the measured position of the borehole assembly at the i^{th} survey station, $\vec{r}_i$ represents the i^{th} regression vector parameters and is the true/actual position at the same survey station. $\vec{\Theta}_{1,i}$ and $\Theta_{2,i}$ denote the parameters that establish the linear relationship between the observations and the regression vector at i^{th} survey station and $\delta\vec{r}_i$ denotes the zero-mean white Gaussian noise of the measurement. Another form of this equation is written as

$$\vec{Y} = \Pi\vec{\Theta} + \delta\vec{r} \tag{2.15}$$

where $\vec{Y}$ denotes with m observations and is an $m \times 1$ vector where $m \geq 2n$ such that the number of observations made is equal or greater than the number of unknowns , Π denotes the known regression parameter matrix of size $n \times 2n$ which is also a matrix of the regression vector parameters $\vec{r}_i$ as shown in Eq. 2.16, $\vec{\Theta}$ denotes the parameters that is to be found which is a vector of size $2n \times 1$ and $\delta\vec{r}$ denotes the zero-mean Gaussian noise vector of size $n \times 1$.

$$\vec{Y} = \begin{bmatrix} y_1 \\ y_2 \\ \vdots \\ y_m \end{bmatrix}; \Pi = \begin{bmatrix} 1 & 0 & \cdots & r_{1,n+1} & 0 & \cdots \\ 0 & 1 & 0 & \cdots & r_{2,n+2} & 0 \\ \vdots & \ddots & \ddots & \ddots & \ddots & \ddots \\ 0 & \cdots & \cdots & 1 & \cdots & r_{n,2n} \end{bmatrix}; \vec{\Theta} = \begin{bmatrix} \Theta_{1,1} \\ \vdots \\ \Theta_{1,n} \\ \Theta_{2,1} \\ \vdots \\ \Theta_{2,n} \end{bmatrix}; \delta\vec{r} = \begin{bmatrix} \delta r_1 \\ \delta r_2 \\ \vdots \\ \delta r_n \end{bmatrix} \tag{2.16}$$

The covariance of the error vector $\delta\vec{r}$ is expressed as shown in Eqn. 2.17

$$E\{\delta\vec{r} \cdot \delta\vec{r}^T\} = R = \begin{bmatrix} E\{\delta r_1 \delta r_1\} & \cdots & \cdots & E\{\delta r_1 \delta r_n\} \\ \vdots & \ddots & & \vdots \\ \vdots & & \ddots & \vdots \\ E\{\delta r_n \delta r_1\} & \cdots & \cdots & E\{\delta r_n \delta r_n\} \end{bmatrix} \tag{2.17}$$

where $\delta\vec{r}$ which denotes the zero-mean white Gaussian noise vector is expressed as

$$\delta\vec{r} = \vec{Y} - \Pi\vec{\Theta} \tag{2.18}$$

This is further represented as a probability density function given as

$$f_{\delta\vec{r}}(\delta\vec{r}_i) = \frac{1}{(2\pi)^{3/2}\sqrt{\det[R_i]}} e^{-\frac{1}{2}(\vec{y}_i - \Pi\vec{\Theta}_i)^T \cdot R_i^{-1} \cdot (\vec{y}_i - \Pi\vec{\Theta}_i)} \tag{2.19}$$

The aim is to find the maximum likelihood estimate of the parameter $\vec{\Theta}$ conditioned on n observations of $\vec{y}_i$ that maximizes the probability density function $f_{\delta\vec{r}}(\delta\vec{r}_i)$. This is written further in terms of natural log to enable easier differentiation. This is given as

$$\hat{\vec{\Theta}}_{i,ML}(\hat{y}_i) = \arg\max_{\delta\vec{r}} f(\vec{y}_i \mid \vec{\Theta}_i) \tag{2.20}$$

$$\ln\left(f_{\delta\vec{r}}(\delta\vec{r}_i)\right) = \ln\left(\frac{1}{(2\pi)^{3/2}\sqrt{\det[R_i]}}\right) + \ln\left(e^{-\frac{1}{2}(\vec{y}_i - \Pi\vec{\Theta}_i)^T \cdot R_i^{-1} \cdot (\vec{y}_i - \Pi\vec{\Theta}_i)}\right) \tag{2.21}$$

Differentiating (2.21) with respect to $\vec{\Theta}_i$, we have

$$\left.\frac{\partial \ln\left(f_{\delta\vec{r}}(\delta\vec{r}_i)\right)}{\partial\vec{\Theta}_i}\right|_{\vec{\Theta}_i \to \hat{\vec{\Theta}}_i} = 0 \tag{2.22}$$

$$\frac{\partial}{\partial\hat{\vec{\Theta}}_i}\left(\frac{1}{2}(\vec{y}_i - \Pi\hat{\vec{\Theta}}_i)^T \cdot R^{-1} \cdot (\vec{y}_i - \Pi\hat{\vec{\Theta}}_i)\right) = 0 \tag{2.23}$$

$$\hat{\vec{\Theta}}_i = \left(\Pi^T \cdot R_i \cdot \Pi\right)^{-1} \Pi^T \vec{y}_i \tag{2.24}$$

$$\hat{\vec{\Theta}} = \left(\Pi^T \cdot R \cdot \Pi\right)^{-1} \Pi^T \vec{Y} \tag{2.25}$$

where Π^T denotes the transpose of Π. $\hat{\vec{\Theta}}$ is a $n \times 1$ vector. The calculated survey position can be obtained using Eqn. 2.22

In the special case where the covariance matrix R is diagonal, the probability density function can be further written as

$$f_{\delta\vec{r}}(\delta\vec{r}_i) = \frac{1}{(2\pi)^{3/2}\sqrt{\det[R_i]}} e^{-\frac{1}{2}\left(\frac{\left[n_i - (\hat{\Theta}_{1,i} + \hat{\Theta}_{2,i} n_{t,i})\right]}{R_{n_i}} + \frac{\left[e_i - (\hat{\Theta}_{1,i} + \hat{\Theta}_{2,i} e_{t,i})\right]}{R_{e_i}} + \frac{\left[v_i - (\hat{\Theta}_{1,i} + \hat{\Theta}_{2,i} v_{t,i})\right]}{R_{e_i}}\right)} \tag{2.31}$$

where $[n_i]$, $[e_i]$ and $[v_i]$ represents the position error covariance in the north, east and true vertical depth coordinates at i^{th} survey station in the designated reference frame. A representation of the 3-dimensional ellipse of uncertainty is therefore obtained such that each ellipse has the length of the north, east and true vertical depth semi-major axes given as $s \cdot \sqrt{R_n}$, $s \cdot \sqrt{R_e}$ and $s \cdot \sqrt{R_v}$ where s is the normalized length of the semi major principal axes of the confidence region ellipsoid.

2.3 Error Model Equation

The error model equation for the propagation of errors from the error source; the noise characteristic of the sensor element, through to the survey position error is defined as [7]

$$e_i = \sigma_i \cdot \frac{\partial r(p)}{\partial p} \cdot \frac{\partial p(\varepsilon)}{\partial \varepsilon_i} \tag{2.32}$$

where e_i denotes the error size in the north, east and true vertical depth in the designated reference frame and due to the error source i at the current survey station; a 3×1 vector. σ_i denotes the magnitude of the i^{th} error source (a scalar), $\frac{\partial p(\varepsilon)}{\partial \varepsilon_i}$ denotes the weighting functions (3×1 vector) which is the effect of the i^{th} error source on the survey measurements, i.e. the measured depth, inclination and azimuth. This is a partial derivative of survey measurement as a function of the sensor element outputs with respect to the sensor element output of interest. $\frac{\partial r(p)}{\partial p}$ is the effect of the survey errors in measured depth, inclination and azimuth on the wellbore position in the north, east and the true vertical depth in the designated reference frame (3×3 matrix). This represents the partial derivatives of the survey position as a function of the survey measurements with respect to the survey measurements. This is further written as a Jacobian given as

$$\frac{\partial r(n,e,v)}{\partial p(MD,I,A)} = \begin{bmatrix} \frac{\partial n(MD,I,A)}{\partial MD} & \frac{\partial n(MD,I,A)}{\partial I} & \frac{\partial n(MD,I,A)}{\partial A} \\ \frac{\partial e(MD,I,A)}{\partial MD} & \frac{\partial e(MD,I,A)}{\partial I} & \frac{\partial e(MD,I,A)}{\partial A} \\ \frac{\partial v(MD,I,A)}{\partial MD} & \frac{\partial v(MD,I,A)}{\partial I} & \frac{\partial v(MD,I,A)}{\partial A} \end{bmatrix} \tag{2.33}$$

The matrix depends on the surveys at either end of the interval. Further details of the mathematical derivation of the error model can be found in Appendix I.

CHAPTER 3

3. Data Fusion Approach for Wellbore Trajectory Tracking

3.1 Approach using Data Fusion

Data fusion is the aggregation of observations made by a distributed group of sensors observing a common physical phenomenon to form a robust and true representation of what pertains in the real world based on which decisions are made. Data fusion approach is basically sub-divided into a four-level hierarchy of processing [57]. Process levels 1 and 2 on the hierarchy are composed mainly of track formation, identity, information estimation and the fusion of information from several sources to arrive at an estimate of the location and identity of objects in an environment while levels 3 and 4 are concerned with knowledge or intelligence extraction and decision making [57]. The focus of this work is within the scope of process levels 1 and 2 which entails numerical information and numerical fusion methods. This basically includes the direct fusion of sensor data or information and the indirect fusion of estimates obtained from the local fusion centers.

3.2 Data Fusion Approach used in the I-Tube Drill-head Position Tracking

The data fusion architectures considered in this thesis are both the centralized data fusion architecture and the distributed or decentralized data fusion architecture. With the centralized data fusion architecture, unprocessed or raw sensor data is transferred to a central processing station called the ground station where the data or information is fused to obtain a true representation of the survey parameters being observed. In this scenario, virtually little or no processing is done at the sensor nodes whereas in the distributed data fusion system some level of data processing and fusion is done on each node having its own local processor from which extraction of useful information from the sensor data prior to communication is possible. This obviously reduces the computational load on the central processor but in turn reduces the level of control of the individual nodes from the central fusion station. In this thesis, a combination of the centralized and the distributed data fusion architecture in creating a true representation of the wellbore trajectory is considered. Estimation of the inclination and azimuth of the well path at each station is done using the probabilistic data fusion technique where a recursive update of these states is made at a central fusion station (ground station). The distributed data fusion approach is used for the local tracking of the sensor position within the drill tube using a suitable tracking algorithm. Tracking information is computed or estimated locally in each node using the Kalman filter after which the information is communicated to an adjoining sensor node and made available at a central processing unit known as the ground station. The ground station fuses the information to give a true representation of the trajectory of the well path in this context. Figure 3.1 shows an illustration of a single level hierarchical multiple sensor tracking system where $Y(k)$ represents the observations made by the sensors, and $\hat{x}(k)$ denotes the estimates of the observed phenomenon computed by the tracking system which is transferred to a central fusion center where the track fusion algorithms are used to fuse the information from the sensor to generate the combined track.

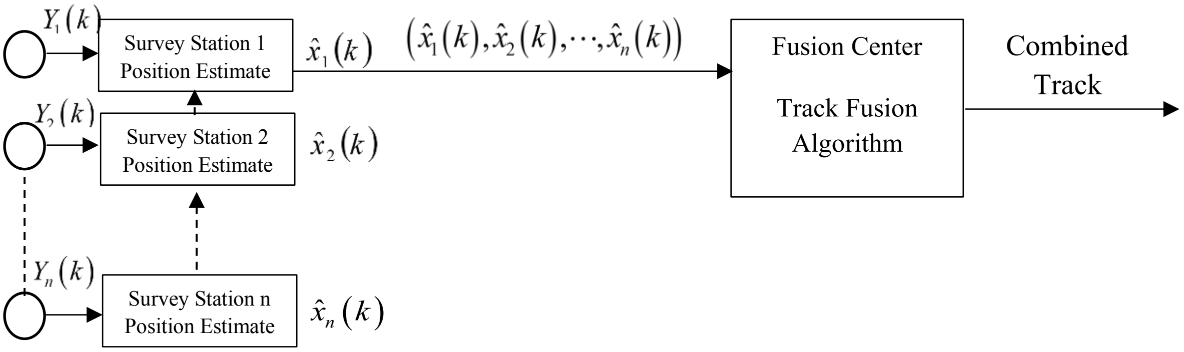

Figure 3.1: A single level hierarchical multiple sensor tracking system approach for the Wellbore trajectory tracking.

3.3 Data Fusion Approach using the Kalman filter

To track the sensor position within the drill tube, a data fusion method using the Kalman filter in the indirect feedforward configuration is utilized. This is whereby the error state space or indirect Kalman filter estimates the error in the yaw position using the difference between the noise-corrupted output of the internal mathematical model and an external data source. The output of the mathematical model for tracking the sensor location is fused with measurement data from an external rotatory encoder for the estimation of the yaw angle position in a designated reference frame. In this data fusion approach, the reference measurement update information provided by the rotary encoder is propagated sequentially over the successive nodes until the main sensor node embedded within the BHA located at the bottome end of the drillstring is updated

3.4 The Basis of the Development of the System Model Description for the Wellbore Trajectory Tracking Approach

The z-axis of the sensor module is body aligned with the z-axis of the body frame of the BHA and at a fixed radial distance from its central axis and rotates with it during drilling. Figures 3.2-3 show the internal placement and alignment of the sensor module axis with that of the drill tube. At periodic intervals, reference measurement information from the external aiding system; the rotary encoder, is made available to update the yaw angle position at each node. This is done sequentially until the final measurement update is made at the main sensor node in the borehole assembly. Each node has an embedded IMU sensor within which there is an implementation of the internal mathematical model for tracking the sensor position. The output of the internal model is fused with the measurement data from the encoder using the indirect Kalman filter to provide an optimal estimate of the yaw angle position. Due to processor resource constraints of the nodes in terms of execution speed and memory storage, the Euler method was the numerical method of choice for integrating the rate output of the gyroscope. The top node obtains its reference yaw angle measurement update information directly from the aiding system. It then makes an optimal prediction of its yaw angle position at each time step during the data outage period until the next measurement update is available. At regular intervals, it transmits its current optimal yaw angle position estimate with its error covariance to the next node as measurement update information. This process repeats sequentially over all connected nodes until the final update is made at the main sensor node. At each survey station or position, the drilling process is stopped, and the optimally estimated yaw angle position is used to resolve the accelerometer output into the designated frame of reference to compute the inclination and azimuth.

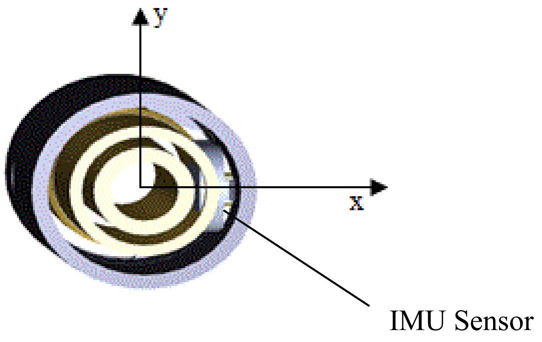

Figure 3.2: A cross-section of the drill string showing the position of the embedded sensor node

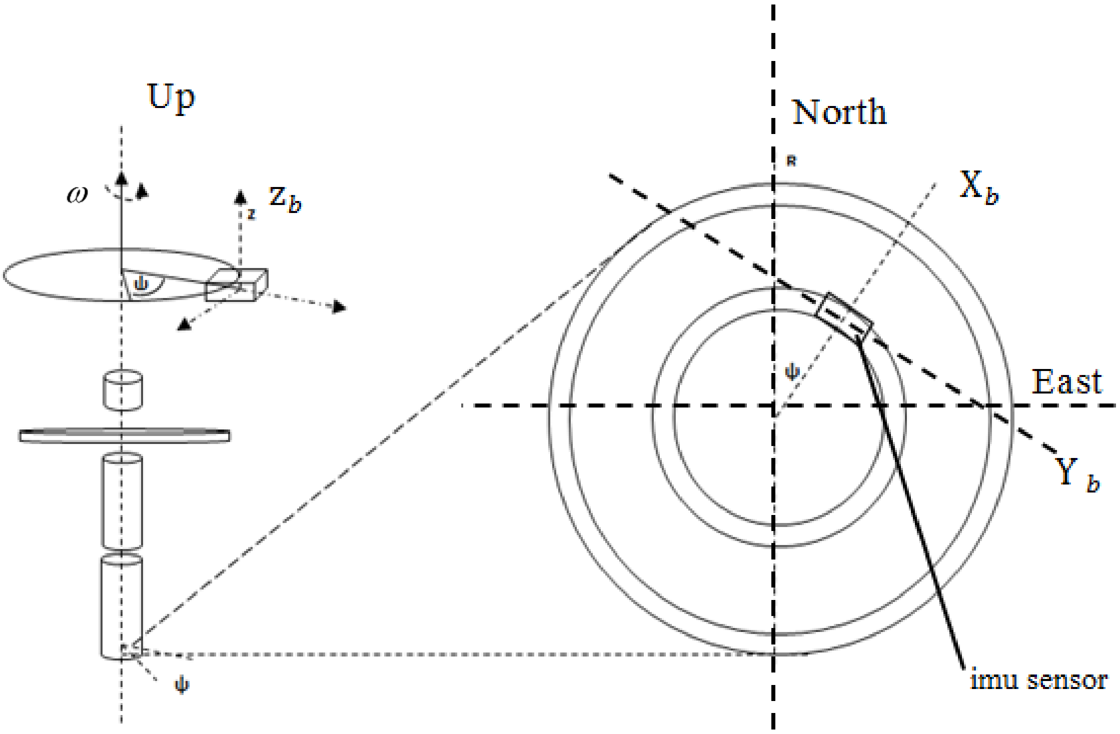

Figure 3.3: A top view of the borehole assembly with embedded sensor module aligned with the body frame of reference. X_b, Y_b, and Z_b represents the axis of body frame of reference

The yaw angle position ψ is saved during this transition and then continued from the saved state upon resumption of the drilling process. A newly inserted tube is given an attitude measurement update from the encoder, which then propagates and provides measurement information updates on the adjoining lower nodes sequentially until the main sensor node in the borehole assembly receives its yaw angle position measurement update.

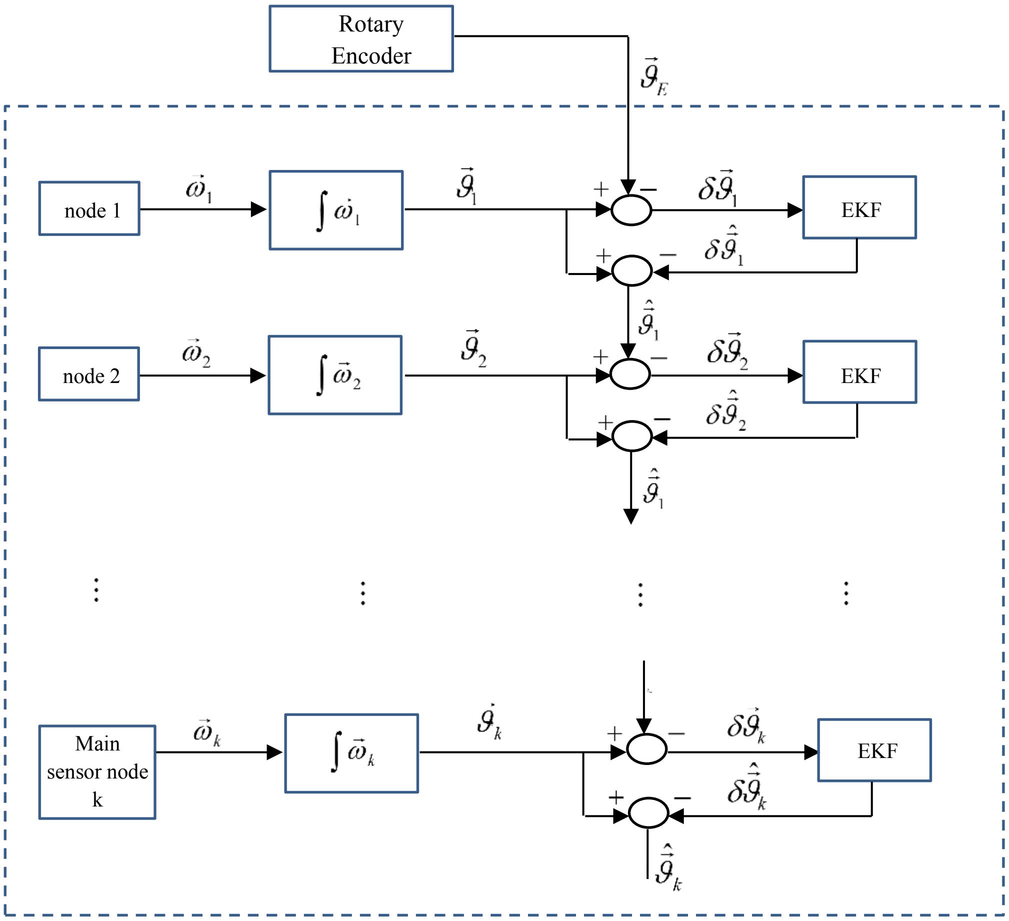

Figure 3.4: A block diagram of the processing scheme with the indirect Kalman filter in the feed-forward configuration for the estimation of the yaw angle position.

where EKF denotes the extended Kalman filter. Figure 3.4 shows the block diagram of the processing scheme with the indirect Kalman filter in the feed-forward configuration for the estimation of the yaw angle position where $\vec{\omega}_n$ denotes the angular rate plus noise as output from node n; a 3×1 vector, $\vec{\vartheta}_n$ denotes the calculated attitude; roll, pitch and yaw from node n, $\hat{\vec{\vartheta}}_n$ denotes the estimated attitude update from node n, $\delta\vec{\vartheta}_n$ denotes the attitude difference between node n and the incoming update from node $n-1$ and $\int\vec{\omega}_n$ denotes the estimated attitude difference between node n and the incoming update from node $n-1$. Figure 3.5 shows the measurement update formulations at each node during each transmit-receive cycle where Δt_n denotes the time difference from the point of reading the optimal estimate of the yaw angle position at node $n-1$, to the instant at which it is used as measurement update in node n. This update procedure is repeated sequentially over the connected nodes at each transmission-reception window until the main sensor node in the borehole assembly is updated.

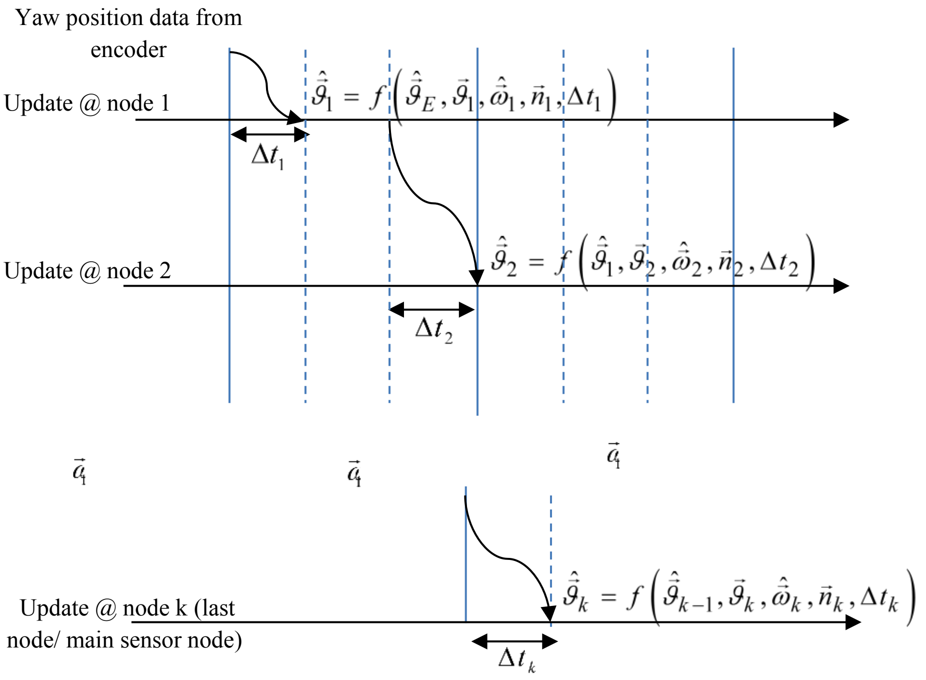

Figure 3.5: Measurement update of each node during the transmit-receive cycle of each node until the sensor node is reached.

3.5 Mathematical Model Description

3.5.1 The Extended Kalman filter

The Kalman filter is a recursive optimal estimator which is used to make an optimal estimation of the states of a discrete-time controlled process described by a linear model. In applications where the state transition and the mapping of the states into the observation space are nonlinear, the extended Kalman filter could be used. It basically combines the stochastic characteristics of the internal model of the system and that of the external aiding system to give a better estimation of the states of interest. Since the target system for its implementation is a digital computer system, its formulation using discrete-time dynamics and discrete-time measurements is given as follows; given the angle state vector $\vec{x} \in R^n$ and the measured angle vector also given as $\vec{z} \in R^m$; the non-linear state space model is given as:

$$\vec{x}_k = f_{k-1}\left[\vec{x}_{k-1}, \vec{u}_{k-1}, \vec{w}_{k-1}\right] \tag{3.1}$$

$$\vec{z}_k = h_k\left[\vec{x}_k, \vec{v}_k\right] \tag{3.2}$$

f_{k-1} is a non-linear state transition map at time $k-1$, $\vec{x}_{k-1}, \vec{u}_{k-1}$ and $\vec{w}_{k-1}$ denote the state vector, the input vector and the process noise vector at time instant $k-1$ respectively. h_k denotes the non-linear observation map at time instant k, and $\vec{v}_k$ denotes the measurement noise. $\vec{w}_{k-1}$ and $\vec{v}_k$ are assumed to be non-correlated zero-mean white Gaussian noise and their covariance are given as shown in Eq. (3.3-4).

$$\mathrm{E}\{\vec{w}_k\}=0,\ \ \mathrm{E}\{\vec{w}_k\cdot\vec{w}_j^T\}=\begin{cases}Q_k & k=j\\ 0 & k\neq j\end{cases} \tag{3.3}$$

$$\mathrm{E}\{\vec{v}_k\}=0,\ \ \mathrm{E}\{\vec{v}_k\cdot\vec{v}_j^T\}=\begin{cases}R_k & k=j\\ 0 & k\neq j\end{cases}. \tag{3.4}$$

where Q_k represents the covariance matrix of the process noise and R_k denotes the covariance matrix of the measurement noise [24]. The prediction step or time update of the extended Kalman filter is computed by first finding the Jacobian matrices given as

$$F_{k-1}=\left.\frac{\partial f_{k-1}}{\partial \vec{x}}\right|_{\hat{\vec{x}}_{k-1}^{+}} \tag{3.5}$$

$$G_{k-1}=\left.\frac{\partial f_{k-1}}{\partial \vec{w}}\right|_{\hat{\vec{x}}_{k-1}^{+}} \tag{3.6}$$

And consequently, the time update of the state estimate and estimation-error co-variance is given as

$$\hat{\vec{x}}_k^{-}=f_{k-1}\left(\hat{\vec{x}}_{k-1}^{+},\vec{u}_{k-1},0\right) \tag{3.7}$$

$$P_k^{-}=F_{k-1}P_{k-1}^{+}F_{k-1}^{T}+G_{k-1}Q_{k-1}G_{k-1}^{T} \tag{3.8}$$

where P_k^- denotes the a priori estimate of the state covariance at time instant k, P_k^+ denotes the a posteriori estimate of the covariance at time instant $k-1$, G_{k-1} denotes the noise gain matrix at the time instant $k-1$. The correction or measurement update of the EKF is computed by first finding the Jacobian matrices given as

$$H_k=\left.\frac{\partial h_k}{\partial \vec{x}}\right|_{\hat{\vec{x}}_k^{-}} \tag{3.9}$$

$$M_k=\left.\frac{\partial h_k}{\partial \vec{v}}\right|_{\hat{\vec{x}}_k^{-}} \tag{3.10}$$

and consequently, results in the measurement update of the state estimate and estimation-error covariance given as

$$K_k = P_k^- H_k^T [H_k P_k^- H_k^T + M_m R_k M_k^T]^{-1} \tag{3.11}$$

$$\vec{r}_k = \vec{z}_k - h\left[\hat{\vec{x}}_k^-, 0\right] \tag{3.12}$$

$$\hat{\vec{x}}_k^+ = \hat{\vec{x}}_k^- + K_k \vec{r}_k \tag{3.13}$$

$$P_k^+ = P_k^- - K_k H_k P_k^- \tag{3.14}$$

where K_k , H_k , $\vec{z}_k$ and $\vec{r}_k$ represent the gain matrix, the measurement matrix, the measurement vector and the residual vector at time instant k respectively. $\hat{\vec{x}}_k^+$ and P_k^+ denote the a posteriori state estimate and a posteriori state covariance matrices respectively. The initial value of the state estimate and covariance is given as

$$\hat{\vec{x}}_0^+ = \mathrm{E}\{\hat{\vec{x}}_0\} \tag{3.15}$$

$$P_0^+ = \mathrm{E}\{(\vec{x}_0 - \hat{\vec{x}}_0)(\vec{x}_0 - \hat{\vec{x}}_0)^T\} \tag{3.16}$$

3.5.2 The Design Model

The mathematical model for the gyroscope sensor output is given in Eqn. 3.17-18

$$\vec{\omega} = \vec{\omega}_t + \vec{b} + \vec{n}_v \tag{3.17}$$

$$\dot{\vec{b}} = -\frac{1}{\tau}\vec{b} + \vec{n}_b \tag{3.18}$$

where $\vec{\omega}$ represents the measured angular rate, $\vec{\omega}_t$ denotes the true angular rate, $\vec{b}$ represents the bias modelled as an exponential time-correlated Gaussian random process with a correlation time of τ seconds, $\vec{n}_b$ denotes the driving process noise and $\vec{n}_v$ is the wideband process noise represented as a zero-mean Gaussian white noise. The variance of the wideband process noise is given in the continuous form as

$$\mathrm{E}\left\{\vec{n}_v(t) \cdot \vec{n}_v^{\mathrm{T}}(t')\right\} = \sigma(t)_v^2 \cdot \delta(t - t') \cdot I_{3\times3} \tag{3.19}$$

where $\sigma(t)_v$ denotes the standard deviation of the zero-mean Gaussian process noise. $\delta(t - t')$ and $I_{3\times3}$ represents the Delta function and a three-by-three-unit matrix respectively. The power spectral density of the driving process noise for the bias $Q_{\vec{n}_b}$ is described by the standard deviation of the bias $\sigma_{\vec{b}}$ and the time constant τ . This is given as

$$Q_{\vec{n}_b} = \frac{2 \cdot \vec{\sigma}_b^2}{\tau} \tag{3.20}$$

Eqs. 3.1-3.20 are used in developing the 6-state EKF for the estimation of the attitude information. The dynamic equation for the propagation of the Euler angles which describes the attitude is given in (3.21)

$$\begin{bmatrix} \dot{\alpha} \\ \dot{\beta} \\ \dot{\gamma} \end{bmatrix} = \begin{bmatrix} 1 & \sin\alpha\tan\beta & \cos\alpha\tan\beta \\ 0 & \cos\alpha & -\sin\alpha \\ 0 & \sin\alpha\sec\beta & \cos\alpha\sec\beta \end{bmatrix} \begin{bmatrix} \omega_x \\ \omega_y \\ \omega_z \end{bmatrix} \tag{3.21}$$

where the variables α , β and γ represent the roll, pitch and yaw angles respectively and the variables, ω_x , ω_y and ω_z represent the angular rate measurements obtained from the three orthogonal rate gyroscope. Further details of the derivation of Eqn. 3.21 are given in Appendix II. The scale factor and misalignment errors are assumed to be constant and therefore are estimated and removed using the mean square estimate as described in Appendix III. Inclusion of the scale factor and the inclination errors modeled as Gaussian white noise results in nine extra states which presents a challenge considering the limitation of the processor on which implementation is to be done.

3.5.3 Error State Dynamic Model

For the indirect Kalman filter, the error state dynamic model is used. The error state dynamic model with bias estimation is written as a linear model in the form

$$\Delta\dot{\vec{x}} = F \cdot \Delta\vec{x} + G \cdot \vec{w} \tag{3.22}$$

The error state vector $\Delta\vec{x}$ is given as

$$\Delta\vec{x} = \begin{bmatrix} \Delta\alpha & \Delta\beta & \Delta\gamma & \Delta b_{\omega_x} & \Delta b_{\omega_y} & \Delta b_{\omega_z} \end{bmatrix} \tag{3.23}$$

where F denotes the error state dynamic matrix as defined in Eq. 3.5, G denotes the noise gain matrix as defined in Eq. 3.6, and $\Delta\vec{x}$ denotes the error state vector and $\vec{w}$ represents the process noise vector. The state space representation of the error state dynamic Jacobian matrix, the noise gain matrix and the process noise covariance matrix is therefore given as in Eqs. 3.24-26.

$$F = \begin{bmatrix} \frac{s_\beta}{c_\beta}[c_\alpha \omega_y - s_\alpha \omega_z] & \frac{1}{c_\beta^2}[s_\alpha \omega_y + c_\alpha \omega_z] & 0 & 1 & \frac{s_\alpha s_\beta}{c_\beta} & \frac{c_\alpha s_\beta}{c_\beta} \\ -\omega_y s_\alpha - \omega_z c_\alpha & 0 & 0 & 0 & c_\alpha & -s_\alpha \\ \frac{1}{c_\beta}[c_\alpha \omega_y - s_\alpha \omega_z] & \frac{s_\beta}{c_\beta^\alpha}[\omega_y s_\alpha + \omega_z c_\alpha] & 0 & 0 & \frac{s_\alpha}{c_\beta} & \frac{c_\alpha}{c_\beta} \\ 0 & 0 & 0 & -\frac{1}{\tau_x} & 0 & 0 \\ 0 & 0 & 0 & 0 & -\frac{1}{\tau_y} & 0 \\ 0 & 0 & 0 & 0 & 0 & -\frac{1}{\tau_z} \end{bmatrix} \tag{3.24}$$

$$G = \begin{bmatrix} 1 & \frac{s_\alpha s_\beta}{c_\beta} & \frac{c_\alpha s_\beta}{c_\beta} & 0 & 0 & 0 \\ 0 & c_\alpha & -s_\alpha & 0 & 0 & 0 \\ 0 & \frac{s_\alpha}{c_\beta} & \frac{c_\alpha}{c_\beta} & 0 & 0 & 0 \\ 0 & 0 & 0 & 1 & 0 & 0 \\ 0 & 0 & 0 & 0 & 1 & 0 \\ 0 & 0 & 0 & 0 & 0 & 1 \end{bmatrix} \tag{3.25}$$

$$Q = \begin{bmatrix} \sigma_\alpha^2 & 0 & 0 & 0 & 0 & 0 \\ 0 & \sigma_\beta^2 & 0 & 0 & 0 & 0 \\ 0 & 0 & \sigma_\gamma^2 & 0 & 0 & 0 \\ 0 & 0 & 0 & \frac{2\sigma_{\omega_x}^2}{\tau_{\omega_x}} & 0 & 0 \\ 0 & 0 & 0 & 0 & \frac{2\sigma_{\omega y}^2}{\tau_{\omega_y}} & 0 \\ 0 & 0 & 0 & 0 & 0 & \frac{2\sigma_{\omega_z}^2}{\tau_{\omega_z}} \end{bmatrix} \tag{3.26}$$

where σ_α, σ_β and σ_γ denote the standard deviation of the wideband measurement errors on the ω_x, ω_y and ω_z gyroscope outputs and σ_{ω_x}, σ_{ω_y} and σ_{ω_z} denote the standard deviation of the driving noise terms and τ_{ω_x}, τ_{ω_y} and τ_{ω_z} denote their correlation times respectively, s_α, s_β c_α

and c_β denote the compact notations for the trigonometric functions $\sin\alpha$, $\cos\alpha$, $\sin\beta$, and $\cos\beta$, respectively.

3.5.4 Compensation and Measurement Model

The attitude measurement update information received from the previous node's optimal prediction estimate is adjusted to consider transmission delays. This is given as the angular state estimate plus the attitude angle difference due to the time difference from the point of reading the optimal estimate of the yaw angle position at node $n-1$, to the instant at which it is used as measurement update in node n . The measurement model at each node is given as

$$\vec{z}_k = h\left[\vec{x}_k\right] + \vec{v}_k \tag{3.27}$$

$$h[\vec{x}_k] = \begin{bmatrix} \alpha_{k,n} \\ \beta_{k,n} \\ \gamma_{k,(n-1)} + \hat{\omega}_{k,n} \cdot \Delta t_n \end{bmatrix} \tag{3.28}$$

which is further written as,

$$\gamma_{k,(n-1)} + \hat{\omega}_{k,n} \cdot \Delta t_n = \gamma_{k,n} \tag{3.29}$$

$$h[\vec{x}_k] = \begin{bmatrix} \alpha_{k,n} \\ \beta_{k,n} \\ \gamma_{k,n} \end{bmatrix} \tag{3.30}$$

$$\left.\frac{\partial h[\vec{x}_k]}{\partial \vec{x}_k}\right|_{\hat{\vec{x}}_k^-} = H = \left[I_{3x3} \quad 0_{3x3}\right] \tag{3.31}$$

$\alpha_{k,n}$, $\beta_{k,n}$, $\gamma_{k,n}$ represent the roll, pitch and yaw update at node n from node $n-1$, $\hat{\omega}_{k,n}$ and Δt_n represent the yaw angular rate and the time interval (as defined earlier) at node n . The measurement noise covariance in the discrete form is given as

$$\mathrm{E}\{\vec{v}_k \cdot \vec{v}_l^T\} = \begin{cases} R_k & k=l \\ 0 & k \neq l \end{cases} \tag{3.32}$$

3.6 Innovative Approach to Wellbore Trajectory Tracking Improvement

During the buildup of the wellbore path or drill trajectory, multiple survey measurements at a single survey station of interest are made whereby drilling is stopped temporarily. These survey measurements at the survey station of interest is identified as an independent, identical distribution of measurements. The survey measurements at this single survey station are therefore fused to obtain a single estimate of the survey measurement at that survey station of interest which is used later in the overall estimation of the wellbore path or trajectory. Two main considerations in view of obtaining the observations or measurements at the single survey station of interest are made. These are

a) a cluster of sensors (IMU sensors) mounted on the same tube and making observations simultaneously at the same survey station of interest. This involves the fusion of data from two or more independent sources with the capability of inclination and azimuth measurements based on the previously derived processing scheme.
b) the survey measurements made by different sensor clusters mounted on separate tubes, at the survey station of interest whereby the measurements are displaced in both space and time. This is where each tube sensor cluster makes a measurement upon arriving at the given survey station of interest.

Furthermore, two scenarios are considered as the survey measurements are processed. These are:

a) The ideal situation where survey measurements at each survey station can be described as non-biased in the sense that they are considered identical and independent since the quantity of interest being measured; inclination and azimuth, does not change – no dynamics involved.
b) The second situation can be described as when the quantity of interest; inclination and azimuth, undergo some degree of dynamics such that the measurements at the survey station of interest are not identical.

3.6.1 Background Theory using Probabilistic Data Fusion Approach with Recursive Bayes Updating

Survey measurements made at each survey station i.e. the inclination and the azimuth are the observations made by the inertial sensors and are estimated using probabilistic models based on the concept of recursive Bayes updating. This concept of probabilistic data fusion is associated with the incremental or recursive addition of new information in the determination of revised posterior distribution on the state defined as the inclination and the azimuth in this context. The Bayes Theorem can be stated as a conditional probability density function, given given that it exists for the corresponding probability distribution function, of the variable of interest conditioned on the available measurement at that time and is given as

$$f_{x|y}(\xi / y=\rho)=\frac{f_{x,y}(\xi,\rho)}{f_y(\rho)}=\frac{f_{y|x}(\rho \mid \xi)\cdot f_x(\xi)}{f_y(\rho)} \tag{3.33}$$

where x denotes the phenomenon of interest; a Gaussian random variable which could either be the inclination, the azimuth or the measured depth. ξ denotes the realized or actual value of x in Euclidean 1-dimensional space, y denotes the measurement variable; also a Gaussian random variable, and ρ denotes the realized (observed) measurement also in Euclidean 1-dimensional space. $f_x(\xi)$ denotes the prior probability density function of the variable of interest, $f_y(\rho)$ denotes the survey measurement also a probability density function. The posterior likelihood density distribution $f_{x|y}(\xi \mid y=\rho)$ is a function of the true state of nature by variable x; that is the true inclination, azimuth or measured depth. This is computed from the prior distribution of x and the information gained by observation as in the distribution represented by $f_{y|x}(\rho \mid \xi)$ as given in Eqn. 3.33. Therefore, using the concept of recursive Bayes updating, and given all measurements at a survey station of interest up to the present measurement as $Y^k \equiv \{y_k, Y^{k-1}\}$ where y^k denotes the single observation at k, the following can be expressed:

$$f_{x|y}(\xi \mid Y^k)=\frac{f_{y|x}(y_k \mid \xi) f_{x|y}(\xi \mid Y^{k-1})}{f_y(y_k \mid Y^{k-1})} \tag{3.34}$$

which represents the recursive Bayes updating formulation. The posterior likelihood, $f_{x|y}(\xi \mid Y^{k-1})$ is the only term computed and stored. The sensor model, represented as a likelihood function, is a probability distribution about a specific observation y_k with known variance σ_y^2 and is expressed as

$$f_{y|x}(y_k \mid \xi)=\frac{1}{\sqrt{2\pi}\sigma_y} e^{-\frac{1}{2}\frac{(\mathrm{x}-y_k)^2}{\sigma_y^2}} \tag{3.35}$$

Given that the a priori distribution of x after taking the first $k-1$ observations is also Gaussian with variance σ_{k-1}^2 and expressed as

$$f_{x|y}(\xi \mid Y^{k-1})=\frac{1}{\sqrt{2\pi}\sigma_{k-1}} e^{-\frac{1}{2}\frac{(x-\xi)^2}{\sigma_{k-1}^2}}, \tag{3.36}$$

the posterior distribution of x after the first k observations is therefore expressed as

$$f_{x|y}(\xi \mid Y^k) = C \cdot \frac{1}{\sqrt{2\pi}\sigma_y} e^{-\frac{1}{2}\frac{(\mathrm{x}-y_k)^2}{\sigma_y^2}} \cdot \frac{1}{\sqrt{2\pi}\sigma_{k-1}} e^{-\frac{1}{2}\frac{(x-\xi)^2}{\sigma_{k-1}^2}}, \tag{3.37}$$

$$f_{x|y}(\xi \mid Y^k) = \frac{1}{\sqrt{2\pi}\sigma_k} e^{-\frac{1}{2}\frac{(x_k-x)^2}{\sigma_k^2}} \tag{3.38}$$

where C is a constant independent of x chosen to ensure that the posterior is approximately normalized. The resultant or new mean is written as

$$x_k = \frac{\sigma_{k-1}^2}{\sigma_{k-1}^2+\sigma_y^2} \cdot y_x + \frac{\sigma_y^2}{\sigma_y^2+\sigma_{k-1}^2} \cdot x_{k-1} \tag{3.39}$$

and the variance is given as

$$\sigma_k^2 = \frac{\sigma_y^2 \cdot \sigma_{k-1}^2}{\sigma_{k-1}^2+\sigma_y^2} \tag{3.40}$$

3.6.2 Weighted Position Estimate from Survey Station Measurements in View of Trajectory Dynamics

The scenarios in the introductory of section 3.6 is used to subsequently describe or define the context by which the data fusion technique is approached in this analysis. At each survey station, independent, identical measurements also known as random measures are made, figure 3.7. In this regard, multiple independent identical measurements of inclination and azimuth at any the survey station of interest is made. The approach using probability distributions as a set of weighted samples of the underlying state space values by using probabilistic inference through the Baye’s rule can be used. The state space values in this context are the observed inclinations and azimuths.

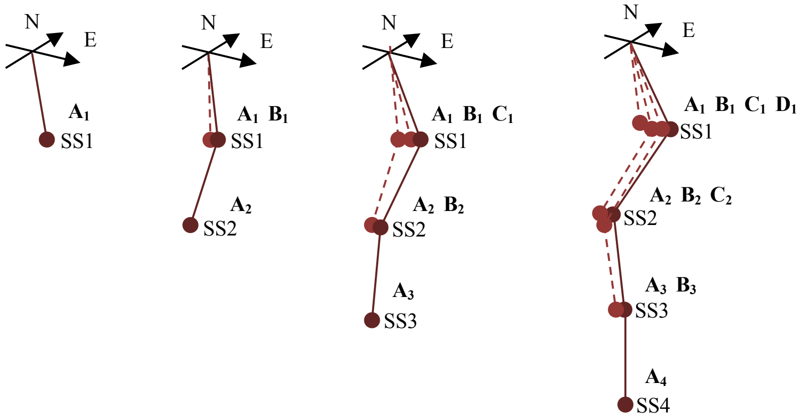

Figure 3.7. Trajectory movement dynamics as drilling progresses: Measurements at each survey station are subject to movement dynamics as each node is inserted.

Figure 3.7 shows how each survey station is measured by a cluster of sensors embedded within each tube. The measurement from the first sensor cluster, A, at survey station 1(SS1) is denoted as A_1. Upon insertion of the second tube associated with sensor cluster B, a second measurement B_1 is made again at SS1. This approach is used for all subsequent measurements at SS1 as well as the other adjoining survey stations with each insertion of a drill tube as illustrated in figure 3.7. All measurements at SS1; A_1, B_1, C_1 and D_1 as noted in this case are statistically combined to obtain an estimate of the survey measurement at SS1. This is done as explained in section 3.6 with further explanation given later. Each cluster has N sensors such that the state of interest; inclination or azimuth, measured by each of the sensors within a sensor cluster is given as $x_t^i;\ i = 1\cdots N$ where t denotes the time at which the survey measurement at a given survey station of interest is taken and i denotes the i^{th} sensor within the sensor cluster of N sensors and with a corresponding set of normalized weights $w_t^i; i = 1\cdots N$ which is deduced from the noise variance of each of the sensors within the cluster. The weights are taken as the reciprocal of the error variance of each sensor and normalized such that $\sum w_t^i = 1$. Therefore, for a given sensor cluster within a tube, ρ, at a given survey station, m the posterior probability distribution function $F_{p,m}(x_t)$ at m at a given time ρ is given as

$$F_{p,m}(x_t) = \frac{1}{N}\sum_{i=1}^{N} w_t^i \cdot F_p(x_t^i), \tag{3.42}$$

Considering the measurements made by the different sensor clusters mounted on separate tubes at a survey station of interest as described earlier and illustrated in figure 3.7, the posterior probability distribution at survey station m then becomes

$$F_{\bar{m}}(x_t) = \frac{1}{M}\sum_{k=1}^{M}\rho_t^k \cdot F_{k,m}(x_t), \tag{3.43}$$

where ρ represents the weighting assigned to the measurement made at survey station m by the sensor cluster of interest, and M denotes the total number of measurements made by the different sensor clusters at survey station m. Where again $\sum_{i=1}^{N}\rho_t^i$. As drilling proceeds, the number of survey stations increases and the distribution of the importance weights for each cluster measurement at a given survey station becomes difficult to gauge or assign as measurements from past sensor clusters at a survey station of interest might due to changed dynamics become of less or no significance. This is to the extent that after a couple of tubes are inserted, some past survey measurements may not be necessary to consider in the survey measurement estimation at the survey station of interest. To address this issue, an empirical determination of the significance of the various survey measurements on the estimate of the survey measurement at the station of interest is observed using simulation to capture the effects of changing dynamics on the survey measurement. This is to enable adequate representation of the posterior distribution of the survey measurements at the survey station of interest. Also, of interest and to be deduced is how current measurements in the adjoining stations affects the survey measurement at the survey station of interest. In a situation where accuracy is not a stringend requirement, a threshold system could be used. In this case, a threshold defined as the two times the standard deviation of $F_{p,m}(x_t)$ is set such that a measurement within this deviation implies not much dynamics has taken place and thus equal weight ρ are placed on all measurements made at that survey station. In the event of a measurement falling out of twice the standard deviation, a check is made to sense if there is a corresponding change in the two adjacent observations of survey station m i.e., $m-1$ and $m+1$. If the nature of change correlates with the new measurement, then full weight is given to the new measurement while weights from previous measurements are assigned 0 to nullify the influence of the previous measurements.

3.7 Conclusion

This chapter presented the mathematical model scheme developed for processing data from the inertia measurement unit output data with measurements from the external encoder for the overall tracking of the wellbore path. It also discussed a probabilistic approach to improving survey station measurements using data from multiple sensor clusters. These input data are available because of different sensor clusters taking measurements at the same survey station of interest sequentially in the time domain as the wellbore depth increases. Furthermore, as described in chapter 2, the region of uncertainty is generally modelled as a 3-dimensional Gaussian probability density function whereby the phenomenon is modelled as a linear regression problem to enable the estimation of the parameters that relate the independent true values of the survey station position to the observed or measured values.

CHAPTER 4

4. Design, Analysis and Verification of the Proposed Model

In this chapter, an application of the concepts described in chapter 3 is used with actual field data as well as simulated data to investigate the overall effectiveness of the outlined methods therein. However, to develop a basis by which to appreciate the use of the outlined concept, the ISCWSA error model is first used for the analysis of the region of uncertainty in error using sensors with different performance specifications. This approach not only highlights the main error sources which are of more significance to the region of uncertainty in error of the survey measurements, it also serves as a prelude to help compare to the results of the implementation of the mathematical model and processing scheme and to show the improvement achieved in the survey position measurements thereof. It begins by showing how the performance specification on the datasheet is converted to the required error source magnitude used in the error model to compute the region of uncertainty in error at each of the survey stations. Finally, the probabilistic scheme is applied to investigate how the effect of multiple measurements at a single survey station which are statistically combined are affected by a shift in the measurement at a survey station under investigation and how the weights can be distributed to the respective measurements to improve the overall accuracy of the survey station of interest.

This chapter is categorized into two main sections with regards to experiments conducted and analysis done. The first part analyses actual field data and investigates the error of uncertainty of the measurements made using sensors of different performance specifications based on the ISCWSA error model. It shows how the sensor performance specifications or intrinsic noise characteristics of the sensor element effect the region of uncertainty in error in the survey position measurement of the wellpath at each survey station. It further makes a comparison using two times the standard deviation error uncertainties, assuming conservativeness, to highlight the direct effect of the noise characteristics on the accuracy of the wellbore trajectory. The second part shows the results of the direct implementation of the outlined mathematical model in chapter 3 on the wireless sensor node modules. It shows its effect on the limitation of the azimuth errors and thereby improving the overall wellbore trajectory accuracy. It makes a comparison of the results to acceptable error uncertainty limits in survey measurements defined by the ISCWSA. Finally, the probabilistic scheme is applied to investigate how the effect of multiple measurements at a single survey station which are statistically combined are affected by a shift in the measurement at a survey station under investigation and how the weights can be distributed to the respective measurements to improve the overall accuracy of the survey station of interest.

4.1 Field Data Analysis using the ISCWSA Error Model for IMU Sensors with Differing Performance Specifications

In this section, an analysis was made from actual recorded data of two field drilling. As mentioned in chapter one, these measurements were made after the completion of the drilling process. This involved two approximately 20-meter deep vertical wellbores for the purposes of deep soil mixing at a location in Potsdam, Berlin. The data recorded showed the displacement of the wellbore at intervals of 2 meters on an A-, B- axis orthogonal to each other and which defined the frame of reference for the wellbore trajectory. This reference frame is synonymous to the North-East plane on the geographical reference frame. A comparison based on the standard ISCWSA error model with regards to the measuring instrument used to take the actual measurements to when such same measurements are done using three alternative IMU sensors of different performance specification was made. In other words, the comparison was based on the error in uncertainty in position attributed to each IMU sensor considered as compared to an acceptable error tolerance limit which is dependent on the application at hand and deemed acceptable by the ISCWSA standards committee. This is further compared to when such measurements are made using the processing scheme as described in Chapter 3 in the next section. The recorded field data provided by the company was used to calculate the azimuth at each survey station up until the target or last survey station. This is shown in Tables 4.1-2. The calculated inclination and azimuth were then used to compute the error of uncertainty in position at each survey station using the parameter specifications of the digital inclinometer probe within a confidence region of double the standard deviation error. This was compared to the error of uncertainty for the same trajectory but using IMU sensors with different performance specifications. Figures 4.1-2 shows the 2-dimensional trajectory of the wellbore path in the A- vertical depth plane, A-B horizontal plane and B-vertical depth plane of each wellbore path. The gyroscope survey method used was the continuous measurement mode since orientation of tool is known at the start with continuous integration of gyroscope measurement done as survey tool transverses the well path [30].

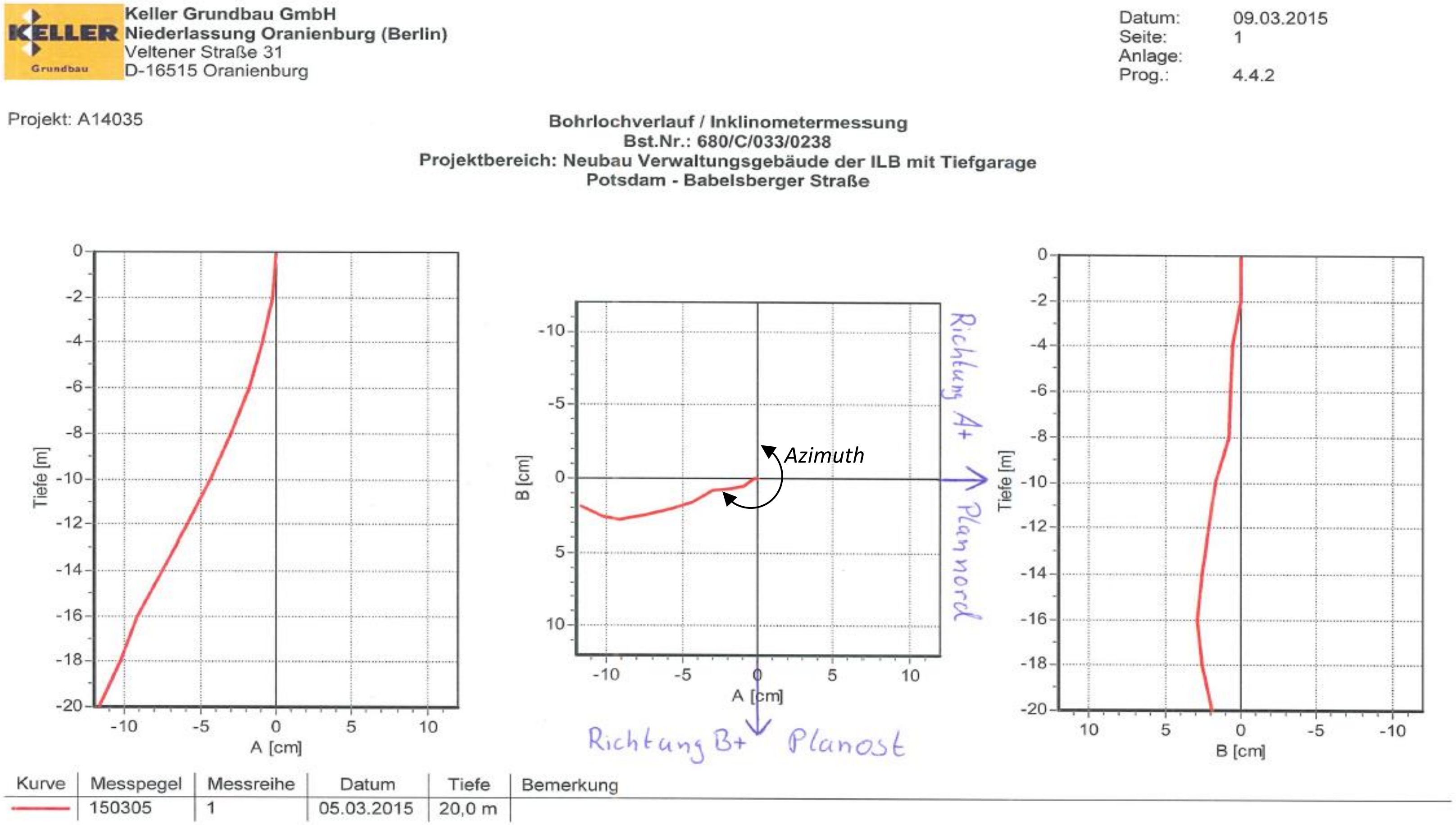

Keller Grundbau GmbH
Niederlassung Oranienburg (Berlin)
Veltener Straße 31
D-16515 Oranienburg

Datum: 09.03.2015
Seite: 1
Anlage:
Prog.: 4.4.2

Projekt: A14035

Bohrlochverlauf / Inklinometermessung
Bst.Nr.: 680/C/033/0238
Projektbereich: Neubau Verwaltungsgebäude der ILB mit Tiefgarage
Potsdam - Babelsberger Straße

Kurve	Messpegel	Messreihe	Datum	Tiefe	Bemerkung
🟥	150305	1	05.03.2015	20,0 m	

Figure 4.1: A 2-dimensional trajectory of first wellbore path in the A-depth plane, A-B horizontal plane and B-depth plane, WELLBORE 1

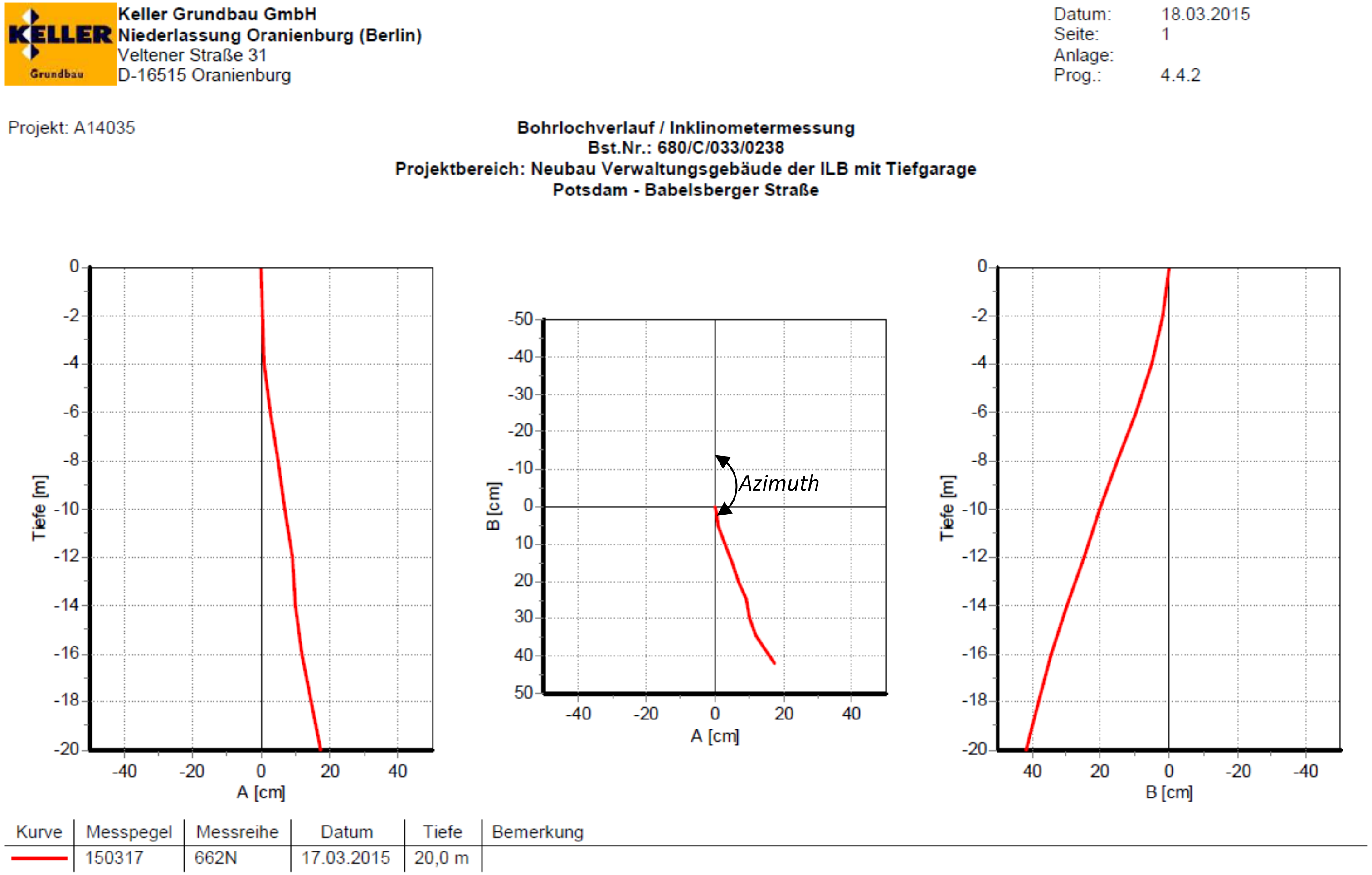

Keller Grundbau GmbH
Niederlassung Oranienburg (Berlin)
Veltener Straße 31
D-16515 Oranienburg

Datum:	18.03.2015
Seite:	1
Anlage:	
Prog.:	4.4.2

Projekt: A14035

Bohrlochverlauf / Inklinometermessung
Bst.Nr.: 680/C/033/0238
Projektbereich: Neubau Verwaltungsgebäude der ILB mit Tiefgarage
Potsdam - Babelsberger Straße

Kurve	Messpegel	Messreihe	Datum	Tiefe	Bemerkung
▬	150317	662N	17.03.2015	20,0 m	

Figure 4.2: A 2-dimensional trajectory of second wellbore path in the A-depth plane, A-B horizontal plane and B-depth plane, WELLBORE 2

Table 4.1: WELLBORE 1: A summary of the calculated inclination and azimuth data from the measurement record in Figure 4.1

Survey Station No.	B-axis (cm)	A-axis (cm)	I_B (deg)	I_A (deg)	**Inclination (deg)**	**Azimuth (deg)**
Wellbore Top:	0	0	0.00	0	0	0.00
Survey Station 1:	0.1	-0.25	0.03	-0.07	0.08	248.20
Survey Station 2:	0.5	-1	0.14	-0.29	0.32	243.43
Survey Station 3:	0.75	-2	0.21	-0.57	0.61	249.44
Survey Station 4:	0.75	-3	0.21	-0.86	0.89	255.96
Survey Station 5:	1	-4.5	0.29	-1.29	1.32	257.47
Survey Station 6:	1.75	-5.75	0.50	-1.65	1.72	253.07
Survey Station 7:	2.75	-7.75	0.79	-2.22	2.35	250.46
Survey Station 8:	3	-9.25	0.86	-2.65	2.78	252.03
Survey Station 9:	2.25	-10.25	0.64	-2.93	3.00	257.62
Survey Station 10:	2	-11.75	0.57	-3.36	3.41	260.34

Table 4.2: WELLBORE 2: A summary of the calculated inclination and azimuth data from the measurement record in Figure 4.2

Survey Station No.	B-axis (cm)	A-axis (cm)	I_B (deg)	I_A (deg)	**Inclination (deg)**	**Azimuth (deg)**
Wellbore Top:	0	0	0.00	0	0.00	0.00
Survey Station 1:	2	0.1	0.57	0.03	0.57	177.14
Survey Station 2:	5	1	1.43	0.29	1.46	168.69
Survey Station 3:	9	2	2.58	0.57	2.64	167.47
Survey Station 4:	16	5	4.57	1.43	4.79	162.65
Survey Station 5:	20	8	5.71	2.29	6.15	158.20
Survey Station 6:	24	10	6.84	2.86	7.42	157.38
Survey Station 7:	30	12	8.53	3.43	9.20	158.20
Survey Station 8:	34	13	9.65	3.72	10.34	159.08
Survey Station 9:	38	14	10.76	4.00	11.48	159.78
Survey Station 10:	42	18	11.86	5.14	12.93	156.80

The inclination $I_{A,B}$ was calculated as

$$I_{A,B} = \arcsin\left[\frac{d_{A,B}}{L}\right] \tag{4.1}$$

where L denotes the length between the two survey stations of interest. In this case, the survey interval was 2 m as deduced from the measurement data sheets in Figures 4.1-2. and d_x denotes the displacement from the A or B axis. The resultant inclination l is therefore given as

$$I = \sqrt{I_A^2 + I_B^2} \tag{4.2}$$

4.1.1 Accelerometer Error Influence on Survey Measurements

In the real world, there is a duration between the time the sensor cluster is switched on to the time the survey measurements are made at the respective survey station. As mentioned earlier, the inclination measurement is derived from the accelerometer measurements as explained in chapter 2. An important consideration therefore, is the effect of this time duration on the accelerometer or inclinometer bias which consequently affects the accuracy of the measured inclination. Firstly, an investigation into the significance of the accelerometer or inclinometer bias on the inclination is highlighted in the decription given below after which the effect of the time duration is investigated in view of the intrinsic noise characteristics of the accelerometer. For a given angle of inclination, I, and the known gravity constant g, the x-axis, y-axis and z-axis components of the accelerometer output is deduced and subsequently an expression for the the corresponding inclination error δI because of the bias errors is obtained.

$$f_z = g \cdot \cos I \tag{4.3}$$

$$f_z^{'} = g \cdot \cos\left(I + \delta I\right) \tag{4.4}$$

$$\delta f_z = f_z - f_z^{'} = g \cdot \left(\cos I - \cos\left(I + \delta I\right)\right) \tag{4.5}$$

$$\delta f_z\big|_{I=0} = f_z^{bias} = g \cdot \left(1 - \cos \delta I\right) \tag{4.6}$$

Therefore, given the z-accelerometer bias f_z^{bias}, the resulting inclination error δI is given as

$$\delta I = \arccos\left(1 - \frac{f_z^{bias}}{g}\right) \tag{4.7}$$

The resulting inclination error given the x, y accelerometer bias is derived as shown below

$$f_x = f_y = g \cdot \sin I \tag{4.8}$$

$$f_x^{'} = g \cdot \sin\left(I + \delta I\right) \tag{4.9}$$

$$\delta f_x = f_x - f_x^{'} = g \cdot \left(\sin\left(I + \delta I\right) - \sin I\right) \tag{4.10}$$

$$\delta f_x\big|_{I=0} = f_x^{bias} = g \cdot \sin \delta I \tag{4.11}$$

This also results in an inclination error given as

$$\delta I = \arcsin\left(\frac{f_{x,y}^{bias}}{g}\right) \tag{4.12}$$

where f_x, f_y, f_z denotes the x, y, z components of the accelerometer output given an inclination, I , and $f_x^{'}$, $f_y^{'}$, $f_z^{'}$ denotes the three axis components of the accelerometer output given an inclination of $I + \delta I$. From Eqn. 4.7 and 4.12 it is easy to see the effect the accelerometer or inclinometer bias on the inclination error.

Secondly, the time duration effect on the sensor bias is best captured by looking at the analysis of both the short and long-term stability; in view of their stochastic errors, of the accelerometer/inclination IMU sensors bias. The Allan variance (defined by IEEE std. 952-1997) used as the method for this analysis (analysis is in the time domain for easy interpretation and it has a lower computational complexity as compared to the power spectral density method). It shows the intrinsic noise characteristic of the sensor as a function of the integration time in the time domain. A further derivation and explanation of the Allan variance method is given in Appendix I and further elaborated in Appendix V. From the Allan variance plot, the velocity random walk, bias instability, rate random walk and rate ramp can be observed. If the noise sources are statistically independent, the computed Allan variance is the sum of the squares of each error type. The significance of Allan variance results in view of the related measurements and the subsequent effect on the inclination measurement is highlighted by the following example sample whereby a given IMU accelerometer, the STIM300 accelerometer is considered with its Allan variance plot shown in figure 4.3 (from datasheet). The STIM300 accelerometer, a typical example with the 10g accelerometer is observed to have a velocity random walk of 0.06 m/s/ $\sqrt{h}$.

The Allan variance plot in figure 4.3, enables important processes such as the velocity random walk and bias instability of the accelerometer output data from all 3 axes to be determined. Table 3.1 gives a summary of the random walk and bias instability values of the STIM300 accelerometer as determined by the Allan variance plot given in figure 4.3. The value of acceleration due to gravity was taken as 9.81m/s^2.

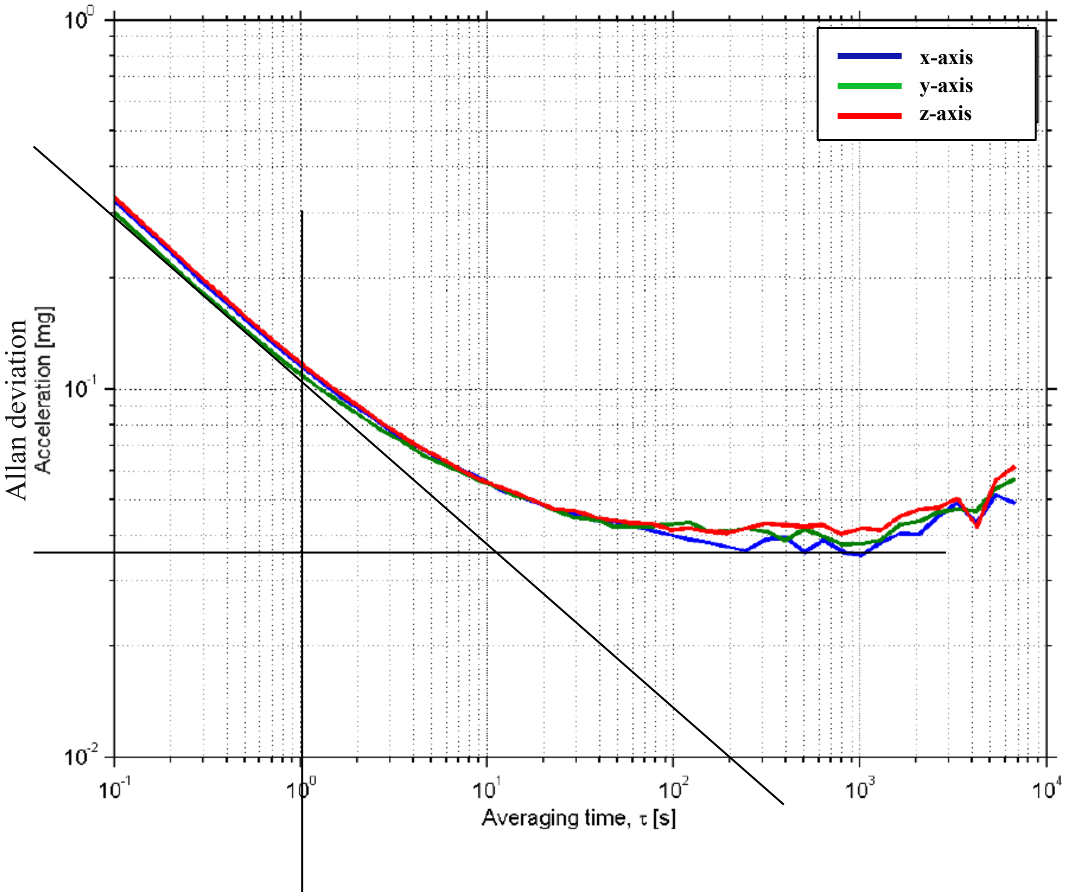

Figure 4.3: Allan variance of STIM300 accelerometer (10g) showing the instantaneous outputs of the x-axis, y-axis and z-axis of the accelerometer in g respectively

Table 4.3: A summary of the random walk and bias instability noise measurements of all three axes of the STIM300 accelerometer

	Bias Instability	**Velocity Random Walk**
x-axis	0.035mg=1.236m/s/h	0.00128m/s/sqrt(s) =0.077m/s/ $\sqrt{h}$
y-axis	0.038mg=1.342m/s/h	0.00108m/s/sqrt(s) = 0.065m/s/ $\sqrt{h}$
z-axis	0.04mg=1.413m/s/h	0.00108m/s/sqrt(s) = 0.065m/s/ $\sqrt{h}$

Further details of the Allan variance plot are given in Appendix V. The white noise component appears in the Allan deviation plot the gradient portion of -0.5. Fitting a straight line through the slope and reading its value at t=1 results in the velocity random walk. The bias instability appears on the plot as a flat region around the minimum section of the plot. Its numerical value is the minimum value on the Allan deviation plot where by the correlation time is the time the minimum value occurs on the integration time axis. The standard deviation of the velocity random walk grows proportionally to the square root of time. This is obtained by the integration of the white noise of the accelerometer over time. The effect of the accelerometer white noise on the position measurement is also obtained by the double integration of the accelerometer white noise. A detailed description is given in [58]. The quoted value of 0.06m/s/$\sqrt{h}$ for the y-axis for example is sometimes given in units given as ~0.001m/s^2/$\sqrt{Hz}$ obtained by dividing by 60 as illustrated below.

Explanation hereby is given as:

$$1\cdot\frac{m}{s}\cdot\frac{1}{\sqrt{h}}=1\cdot\frac{m}{s}\cdot\frac{1}{\sqrt{3600s}}=\frac{1}{60}\cdot\frac{m}{s}\cdot\frac{1}{\sqrt{s}} \tag{3.59}$$

$$=\frac{1}{60}\cdot\frac{m}{s}\cdot\frac{1}{\sqrt{s}}\cdot\frac{\sqrt{s}}{\sqrt{s}}=\frac{1}{60}\cdot\frac{m}{s^2}\cdot\frac{1}{\sqrt{Hz}} \tag{3.60}$$

The significance of which is that the standard deviation of the velocity random walk because of the accelerometer white noise after for instance 10 minutes unaided and under stable conditions e.g. temperature is given as:

$$\frac{\sqrt{10\cdot 60s}}{\sqrt{3600s}}\cdot 0.06m/s=0.0245m/s \tag{3.61}$$

The bias instability, with definition given in Appendix I, of the STIM300 is also observed to be ~0.04mg which is equivalent to 3.924 x 10^{-4} m/s^2. The summation of the biases, after conversion to white noise first standard deviation values, therefore gives an approximation of the accelerometer bias and its effect on the inclination measurement is obtained using the formulation in Eqn. 4.3-4.12. This bias is factored into the determination of the error of uncertainty contributing to the inclination error at each respective survey station. Another consideration of importance is the temperature effect on the accelerometer or inclinometer bias. The datasheet provides the temperature effect on bias per degree celsius rise in temperature. Adjustments for varying temperature can therefore be obtained with respect to a given reference which is normally given at 25°C. In the case of the STIM300, a degree-celsius change in temperature per minute results in a bias of +/-2mg root mean square error which therefore leads to a measurement adjustment given as:

$$\Delta T/^{\circ}\cdot\left(T_m-T_{ref}(25^{\circ})\right)\cdot f_o \tag{3.62}$$

where $\Delta T/^{\circ}$ denotes the change in degree rise, T_m denotes the measured temperature, $T_{ref}(25^{\circ})$ denotes the reference temperature taken at 25° and f_o denotes the accelerometer output.

4.1.2 Description of Calculation Method for the Region of Uncertainty in Error

The error of uncertainty model enables one to determine how far one could be when estimating a position. As mentioned in chapter 2, the error in uncertainty in position is derived from the effect of the physical errors of the sensor element on the survey measurements; inclination, azimuth and measured depth, which subsequently translate to survey position errors; north, east and true vertical depth, in the designated reference frame. To further highlight this explanation, a simple calculation using a fundamental approach for finding the error of uncertainty is given below.

To determine the error of uncertainty in the survey position measurements at survey station two given the wellbore path scenario shown in Figure 4.4. which uses the balanced angle method wellbore trajectory computation (see Appendix III) is given as follows

Station 1 (Top)	Station 2
Measured depth (MD_1) = 0m	Measured depth (MD_2) = 3m
Inclination (I_1) = 0°	Inclination (I_2) = 5.0°
Azimuth (A_1) = 0°	Azimuth (A_2) =30.0°

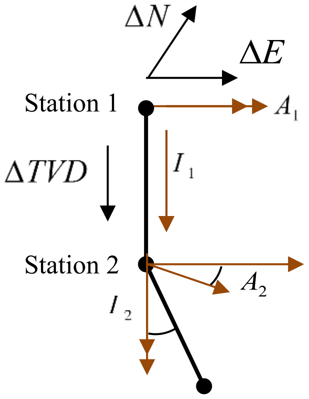

Figure 4.4: Wellbore trajectory showing the inclination and azimuth measured at station 2

Survey Position Error due to IMU sensor accelerometer biases:

This calculation is based on the derivation given in Eqs. 4.3-4.12. Assuming an inclination error of +/- 0.01° implies that for the 3-axis IMU accelerometer, the error magnitudes are given as;

x-axis, y-axis accelerometer bias f_{xy}^{bias} = 1.712168 * 10^{-3} m/s^2

z-axis accelerometer bias f_z^{bias} = 1.494 * 10^{-7} m/s^2

To obtain the corresponding survey position errors; 1st standard deviation, in the north, east and true vertical depth, in the designated frame of reference, the given equations in Eqs. 2.1-2.6 are used which results in:

error in the northern direction ΔN =2.259 * 10^{-4} m

error in the eastern direction ΔE =1.304 * 10^{-4} m

error in the vertical direction ΔTVD =2.284 * 10^{-5} m

The alternative to the calculation above of the region of uncertainty in error is using the error model as given by Eqs. 2.32 with the derivation given in Appendix I. The given error model equation is used with the weighting functions which have already been pre-computed as given in the appendix of [7]. The error model equation is repeated here as given in the equation below

$$\frac{\partial \Delta r_2}{\partial p_2} = \frac{1}{2}\begin{pmatrix} \sin I_1 \cos A_1 + \sin I_2 \cos A_2 & (MD_2 - MD_1)\cos I_2 \cos A_2 & -(MD_2 - MD_1)\sin I_2 \sin A_2 \\ \sin I_1 \sin A_1 + \sin I_2 \sin A_2 & (MD_2 - MD_1)\cos I_2 \sin A_2 & (MD_2 - MD_1)\sin I_2 \cos A_2 \\ \cos I_1 + \cos I_2 & -(MD_2 - MD_1)\sin I_2 & 0 \end{pmatrix} \tag{4.3}$$

$$\vec{e}_t = \sigma_t \cdot \left(\frac{\partial \Delta r_2}{\partial p_2} \right) \cdot \frac{\partial p_2}{\partial \varepsilon} \tag{4.4}$$

$$E_{total} = \left(\sum \vec{e}_t \cdot \vec{e}_t^{\mathrm{T}} \right) \tag{4.5}$$

where $\vec{e}_t$ denotes the total errors due to the error source t which in this case represents the accelerometer biases; x-,y-,z-axis, as the different error sources, σ_t denotes the error magnitude due to each source t, $\frac{\partial \Delta r_2}{\partial p_2}$ denotes the partial derivative of the position coordinates in the north, east and true vertical depth with respect to the survey measurements; measured depth, inclination and azimuth at the survey station two, $\frac{\partial p_2}{\partial \varepsilon}$ denotes the partial change in the survey measurements with respect to the error sources. It is assumed that there are no errors at station one.

Applying this computation scheme to our simple example, we obtain

$$\begin{pmatrix} \Delta N \\ \Delta E \\ \Delta TVD \end{pmatrix} = \begin{pmatrix} 0.000225 \\ 0.0001299 \\ 0.00002273 \end{pmatrix} m$$

which agrees with the previous computation of the error in the north, east and true vertical depth survey position at survey station two. A similar computation for that of the IMU gyroscope is given as shown below

Survey Position Error due to IMU gyroscope biases:

Given the z-axis gyroscope bias $G_z^{bias} = 0.01°/s$ with elapsed time being 100 seconds, the corresponding survey position errors using Eq. 2.7 are computed to give:

error in the northern direction $\Delta N = 1.141 * 10^{-3}$ m

error in the eastern direction $\Delta E = 1.976 * 10^{-3}$ m

error in the vertical direction $\Delta TVD = 0$ m.

Computation using Eqs. 4.3-5 gives the error in survey position as

$$\begin{pmatrix} \Delta N \\ \Delta E \\ \Delta TVD \end{pmatrix} = \begin{pmatrix} 0.00114081 \\ 0.0019759 \\ 0 \end{pmatrix} m$$

So basically, taking the parameter specification of the IMU sensor of interest, one can determine, using the error model with the appropriate weighting functions, the error of uncertainty at every given survey station. The list of weighting functions is given in the appendix of [5].

4.1.3 Determination of the Region of Uncertainty in Error of Survey Position Measurements for Sensors with Different Performance Specification

The error sources used were as per-given in the performance specifications listed in the respective data sheet of the sensor elements. The main sensors used as listed below:

The Digital Inclinometer Probe:	- RST Digital Inclinometer Probe
IMU:	- Vectornav-100T IMU Sensor
	- STIM300 IMU Sensor
	- IPST-RQH Sensor

The RST digital inclinometer probe which is embedded with a 2-axis accelerometer is used in the following section to show how the listed performance specifications map to the error sources defined by the ISCWSA standard board.

The RST digital inclinometer probe:

The digital inclinometer probe consists of a 2-axis MEMS accelerometer sensor which fits in the model error profile defined by the ISCWSA with the weighting function of the respective error sources for a 2-axis accelerometer also defined.

Error source 1: System accuracy maps to the accelerometer bias defined in the ISCWSA error model. This is given as +/- 2mm per 25 m in the RST digital inclinometer probe datasheet.

Representation in degrees: $\sin^{-1}(2/25000) = +/-0.004584°$

Representation in ms^{-2}: $g * \sin(0.004584°) = \sim 7.85 * 10^{-4}\, ms^{-2}$

Error source 2: Axis alignment maps to accelerometer misalignment. RST system is digitally nulled due to 2-way measurement.

Error source 3: Cable stretch maps to depth stretch type defined in the ISCWSA error model. This is given as 7.0mm per 50m and considered in the generation of the uncertainty envelope during the analysis. See table 4.3.

Error source 4: Data resolution defined as; the ratio between the maximum signal measured to the smallest part that can be resolved or the degree to which a change can be theoretically detected, also as known as the sensitivity. It maps to the scale factor error of the accelerometer in the ISCWSA error model. This is given in the datasheet as 0.005mm deviation per 500mm distance.

Represented in degrees = $\sin^{-1}(0.005/500) = 5.73 * 10^{-4}\, °$ per 500mm

Represented in (x-, y- acceleration axes) $ms^{-2} = g * \sin(5.73*10^{-4}\, °) = 9.81 * 10^{-5} ms^{-2}$ per 500mm.

Finally, table 4.4 subsequently gives a summary of the performance specification of the digital inclinometer probe while tables 4.5-6 shows the results of the computed two times the standard deviation errors obtained from applying the error model to the performance specifications of the digital inclinometer probe.

Table 4.4: Summary of the digital inclinometer probe performance specification.

Inclinometer Parameter	Metric System	Notes
Full-scale range	+/- 30°	
Data resolution	0.005mm per 500mm	SF: 5.73 * 10^{-4} ° or x/y- SF=9.81 * 10^{-5}ms^{-2}
Repeatability	+/- 0.002°	
System Accuracy	+/- 2mm per 25 m	+/-0.004584°or x/y- accel: ~7.85 * 10^{-4} ms^{-2}
Axis alignment	Digitally nulled	2-way measurement
Temperature rating	-40° to +70°	
Sensor Type	MEMS Accelerometer, Biaxial	
Cable Stretch	7.0mm	Per 50 meters… => 0.00014m Per meter

Table 4.5: WELLBORE 1: Summary of the region of uncertainty in error (2 x standard deviation) in the A-, B- and TVD axis for the digital inclinometer probe

Survey Station	B uncertainty (+/- cm)	A uncertainty (+/- cm)	TVD uncertainty (+/- cm)
	$2\cdot\sigma$	$2\cdot\sigma$	$2\cdot\sigma$
Wellbore Top:	0	0	0
Survey Station 1:	0.028	0.064	2.1
Survey Station 2:	0.042	0.096	2.96
Survey Station 3:	0.026	0.128	3.64
Survey Station 4:	0.056	0.16	4.2
Survey Station 5:	0.062	0.194	4.7
Survey Station 6:	0.074	0.23	5.14
Survey Station 7:	0.088	0.27	5.54
Survey Station 8:	0.1	0.314	5.94
Survey Station 9:	0.106	0.358	6.3
Survey Station 10:	0.108	0.37	6.38

Table 4.6: WELLBORE 2: Summary of the region of uncertainty in error (2 x standard deviation) in the A-, B- and TVD axis for the digital inclinometer probe.

Survey Station	B uncertainty (+/- cm)	A uncertainty (+/- cm)	TVD uncertainty (+/- cm)
	$2\cdot\sigma$	$2\cdot\sigma$	$2\cdot\sigma$
Wellbore Top:	0	0	0
Survey Station 1:	0.092	0.012	2.04
Survey Station 2:	0.152	0.028	2.9
Survey Station 3:	0.226	0.052	3.54
Survey Station 4:	0.316	0.09	4.08
Survey Station 5:	0.414	0.138	4.56
Survey Station 6:	0.52	0.188	5
Survey Station 7:	0.634	0.238	5.38
Survey Station 8:	0.754	0.284	5.74
Survey Station 9:	0.876	0.332	6.08
Survey Station 10:	0.906	0.346	6.16

The scale factor and misalignment are calibrated for and removed at the beginning using the least square estimate method (see Appendix III). To reflect this, misalignment is divided by a factor of 100. The time duration between two adjacent survey stations, in view of the gyro drift, is assumed to be 1 minute (60 s) for each case. Furthermore, no external updates or correction was used.

The Vectornav-100T IMU Sensor:

Table 4.7: A summary of the Vectornav-100T performance specification.

Vectornav-100T	**Parameter**	**Value**
Bias Instability (0.04mg) => 0.0023° deviation	f_{xy}^{bias}	$4.99611 * 10^{-4}$ m/s^2
”	f_{z}^{bias}	$1.2722 * 10^{-8}$ m/s^2
Linearity <0.5% Full Scale	$f^{S.F.error}$	$8.0 * 10^{-3}$
Misalignment (calibrated out normally)	$f^{Misalignment}$	0.05° /100
Bias Instability	G^{Drift}	$2.78 * 10^{-3}$ °/s
Gyro Angle Random walk	G^{ARW}	$3.5 * 10^{-3}$ °/s/$\sqrt{Hz}$

Table 4.8: WELLBORE 1: A summary of the region of uncertainty in error (2 * standard deviation) for the A-, B- and TVD axis – Vectornav-100T

Survey Station	**B uncertainty (+/- cm)**	**A uncertainty (+/- cm)**	**TVD uncertainty (+/- cm)**
	$2\cdot\sigma$	$2\cdot\sigma$	$2\cdot\sigma$
Wellbore Top:	0	0	0
Survey Station 1:	1.28	0.84	$7.2*10^{-4}$
Survey Station 2:	3.4	1.76	0.002
Survey Station 3:	6.34	2.52	0.004
Survey Station 4:	10.26	3.28	0.002
Survey Station 5:	15.06	4.56	0.008
Survey Station 6:	20.9	6.8	0.01
Survey Station 7:	27.76	9.34	0.014
Survey Station 8:	34.78	11.02	0.018
Survey Station 9:	42.1	11.98	0.02
Survey Station 10:	43.96	12.18	0.022

Table 4.9: WELLBORE 2: A summary of the region of uncertainty in error (2 * standard deviation) in the A-, B- and TVD axis – Vectornav-100T

Survey Station	**B uncertainty (+/- cm)**	**A uncertainty (+/- cm)**	**TVD uncertainty (+/- cm)**
	$2\cdot\sigma$	$2\cdot\sigma$	$2\cdot\sigma$
Wellbore Top:	0	0	0
Survey Station 1:	1.4	7.54	0.004
Survey Station 2:	3.72	16.88	0.008
Survey Station 3:	8.6	31.78	0.016
Survey Station 4:	16.6	50.1	0.024
Survey Station 5:	25.64	68.86	0.036
Survey Station 6:	35	89.94	0.046
Survey Station 7:	44.14	112.98	0.038
Survey Station 8:	52.78	136.52	0.07
Survey Station 9:	62.88	160.76	0.082
Survey Station 10:	65.74	166.8	0.086

The STIM300 IMU Sensor:

Table 4.10: A Summary of the performance specification of the STIM300 IMU sensor from Sensornor ButterflyGyro

STIM300	**Parameter**	**Value**
Bias instability (0.05mg) => 0.002865° deviation	f_{xy}^{bias}	$4.905 * 10^{-4}$ m/s^2
“	f_{z}^{bias}	$1.222 * 10^{-8}$ m/s^2
Scale factor accuracy => +/- 200ppm	$f^{S.F.error}$.	$2 * 10^{-4}$
Misalignment (calibrated out normally) => 1mrad	$f^{Misalignment}$	0.057° /100
Bias instability (0.5°/h)	G^{Drift}	$1.39 * 10^{-4}$ °/s
Gyro Angle Random Walk (0.15°/sqrt(hr))	G^{ARW}	$2.5 * 10^{-4}$ °/s/$\sqrt{Hz}$

Table 4.11: WELLBORE 1: A summary of the region of uncertainty in error (2 * standard deviation) in A-, B- and TVD axis – STIM300

Survey Station	**B uncertainty (+/- cm)**	**A uncertainty (+/- cm)**	**TVD uncertainty (+/- cm)**
	$2\cdot\sigma$	$2\cdot\sigma$	$2\cdot\sigma$
Wellbore Top:	0	0	0
Survey Station 1:	0.006	0.26	$8.12*10^{-4}$
Survey Station 2:	0.14	0.4	0.002
Survey Station 3:	0.36	0.54	0.004
Survey Station 4:	0.66	0.64	0.006
Survey Station 5:	1	0.78	0.008
Survey Station 6:	1.42	0.98	0.012
Survey Station 7:	1.92	1.18	0.016
Survey Station 8:	2.42	1.36	0.01

Survey Station 9:	2.98	1.46	0.022
Survey Station 10:	3.12	1.48	0.024

Table 4.12: WELLBORE 2: A summary of the region of uncertainty in error (2 * standard deviation) in A-, B- and TVD axis – STIM300

Survey Station	**B uncertainty (+/- cm)**	**A uncertainty (+/- cm)**	**TVD uncertainty (+/- cm)**
	$2 \cdot \sigma$	$2 \cdot \sigma$	$2 \cdot \sigma$
Wellbore Top:	0	0	0
Survey Station 1:	0.32	0.54	0.004
Survey Station 2:	0.56	1.2	0.01
Survey Station 3:	0.96	2.28	0.018
Survey Station 4:	1.58	3.62	0.028
Survey Station 5:	2.28	4.98	0.014
Survey Station 6:	3.02	6.52	0.052
Survey Station 7:	3.74	8.22	0.066
Survey Station 8:	4.4	9.94	0.078
Survey Station 9:	5.18	11.74	0.092
Survey Station 10:	5.4	12.18	0.096

The IPST-RQH Sensor:

Table 4.13: A summary of the performance specifications of IPST-RQH

	Parameter	Value
Accuracy (pitch & Roll) = 0.25°	f_{xy}^{bias}	4.9653 * 10^{-3} m/s^2
	f_{z}^{bias}	1.25658 * 10^{-6} m/s^2
Resolution (100ug)	$f^{S.F.error}$	9.81 * 10^{-4}
Alignment Error (calibrated Out)	$f^{Misalignment}$	0.00
Bias stability (0.003°/h)	G^{Drift}	8.33 * 10^{-7} °/s
Gyro random walk (0.003°/sqrt(hr))	G^{ARW}	5.0 * 10^{-5} °/s/$\sqrt{Hz}$

Table 4.14: WELLBORE 1: A summary of the region of uncertainty in error (2 * standard deviation) in the A-, B- and TVD axis – IPST-RQH

Survey Station	**B uncertainty (+/- cm)**	**A uncertainty (+/- cm)**	**TVD uncertainty (+/- cm)**
	$2 \cdot \sigma$	$2 \cdot \sigma$	$2 \cdot \sigma$
Wellbore Top:	0	0	0
Survey Station 1:	0.074	0.174	6.52×10^{-4}
Survey Station 2:	0.1	0.248	0.0017
Survey Station 3:	0.11	0.31	0.002
Survey Station 4:	0.112	0.362	0.004
Survey Station 5:	0.114	0.41	0.006
Survey Station 6:	0.118	0.452	0.006

Survey Station 7:	0.118	0.492	0.012
Survey Station 8:	0.118	0.53	0.016
Survey Station 9:	0.12	0.566	0.018
Survey Station 10:	0.12	0.574	0.02

Table 4.15: WELLBORE 2: A summary of the region of uncertainty in error (2 * standard deviation) in the A-, B- and TVD axis – IPST-RQH

Survey Station	**B uncertainty (+/- cm)**	**A uncertainty (+/- cm)**	**TVD uncertainty (+/- cm)**
	$2\cdot\sigma$	$2\cdot\sigma$	$2\cdot\sigma$
Wellbore Top:	0	0	0
Survey Station 1:	0.186	0.004	0.004
Survey Station 2:	0.264	0.004	0.008
Survey Station 3:	0.332	0.022	0.014
Survey Station 4:	0.392	0.042	0.022
Survey Station 5:	0.45	0.066	0.032
Survey Station 6:	0.504	0.102	0.042
Survey Station 7:	0.558	0.148	0.052
Survey Station 8:	0.608	0.198	0.062
Survey Station 9:	0.66	0.248	0.074
Survey Station 10:	0.672	0.26	0.076

Tables 4.4-15 shows the $2\cdot\sigma$ region of uncertainty in error results of 5 different survey measuring sensors using the measurement data obtained from two wellbores shown in Tables 4.1-2. Measurements using the digital inclinometer probe, with specifications shown in Table 4.4, for the first wellbore; WELLBORE 1, shows its maximum error uncertainty of +/-0.108cm for the B-axis of the reference frame while that for the A-axis were approximately +/-0.37cm at the final target depth. That for the second well showed a maximum error uncertainty of approximately +/-0.906 cm on the B-axis of the defined reference frame while that of the A-axis were approximately +/-0.346 cm respectively. Due to the cable stretch factor of the digital inclinometer probe as shown in Table 4.3, approximately +/-6.2 cm region of uncertainty error was observed in both wellbore measurements. Depending on the application at hand, these uncertainties can be considered as an acceptable tolerance limit of the measurement. However, the disadvantage with this survey method is that it is done after the drilling process has been completed such that there is hardly a possibility of corrective actions or a control measure to be carried out in real time. Secondly, due to handling, human influenced errors, which can not be specifically quantified and eliminated are prone to occur.

The second sensor considered is the Vectornav-100T IMU Sensor with its specifications shown in Table 4.7 basically considering its on-board processing scheme. The first wellbore analysis showed a maximum error uncertainty of about +/-44cm in deviation on the B-axis of the designated reference frame while that of the A-axis was approximately +/-12.2cm. For the second wellbore, the maximum error uncertainty was approximately +/-65.7cm in deviation on the B-axis while that for the A-axis was approximately +/-167cm. The region uncertainty in the true vertical depth was approximately +/-0.09 cm without the effects of stretching as observed with the digital inclinometer probe. Although it is of moderate cost and the data can be obtained in real-time with a suitable borehole telemetry system, the obvious disadvantage here is the large values for the region of uncertainty in error in determining the displacements of the survey stations in the designated reference frame.

The STIM300 IMU sensor with specifications shown in Table 4.10, for the first wellbore analysis, showed a maximum error uncertainty of approximately +/-3.12cm in deviation on the B-axis of the designated reference frame while that of the A-axis were approximately +/-1.48cm. For the second wellbore, the maximum error uncertainty was approximately +/-5.4cm in deviation on the B-axis while that for the A-axis was about +/-12.2cm respectively. The region of uncertainty in error in the true vertical depth was approximately +/-0.07cm without the effects of stretching as was observed with the case of the digital inclinometer probe. In addition to the fact that the high-end STIM300 IMU has high cost implications, the moderate values of the error uncertainty may not satisfy the acceptable error limit of measuring instruments in certain applications

The third sensor under consideration was the iPST-RQH, a high-performance navigation grade IMU sensor from iMAR Navigation and Control GmbH. This is originally a pipeline surveying tool normally used for pipeline inspection and its performance specifications are given in Table 4.13. The first wellbore analysis shows a maximum error uncertainty of approximately +/-0.12cm in deviation on the B-axis of the designated reference frame while that of the A-axis was approximately +/-0.57cm respectively. For the second wellbore, the maximum error of uncertainty was +/-0.67cm for the deviations on the B-axis while that for the A-axis was approximately +/-0.26cm respectively. The uncertainty in the true vertical depth was approximately +/-0.076cm and also without the effects of stretching as observed with the digital inclinometer probe. The results for this IMU sensor obviously shows very desirable or low values for error uncertainty, but the main challenge is its high cost as well as the difficulty in adapting it for use in such borehole assembly system.

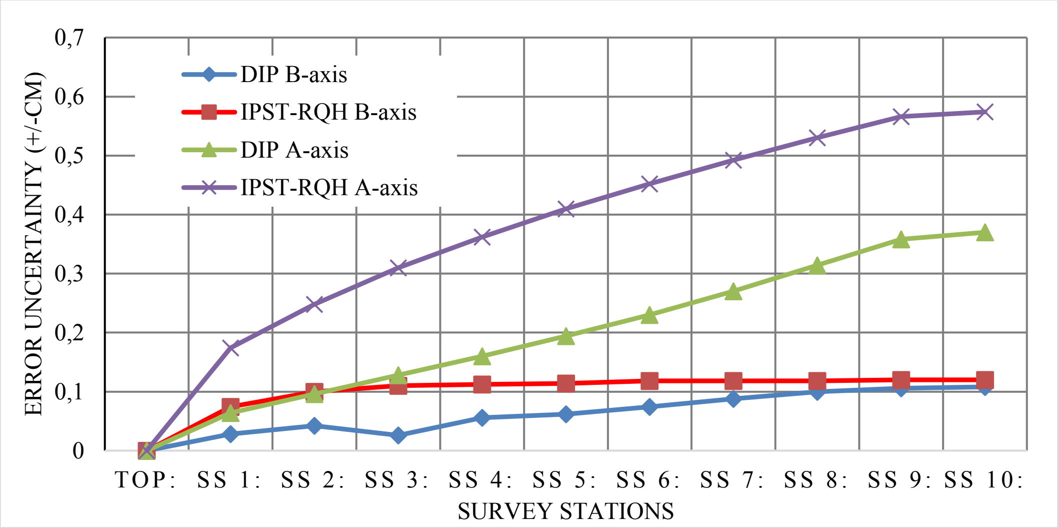

Figure 4.5: Comparison of the two times the standard deviation region of uncertainty in error for the B- and A- axis displacement for the Digital Inclinometer Probe (DIP) and the IPST-RQH IMU sensor; tables 4.3-5 and tables 4.12-14: WELLBORE 1.

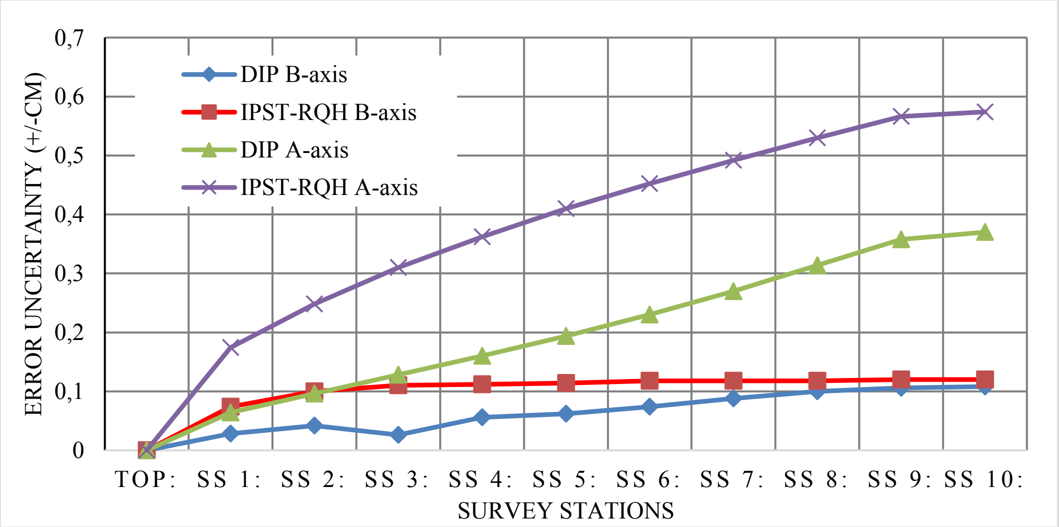

Figure 4.6: Comparison of the two times the standard deviation region of uncertainty in error for the B- and A- axis displacement for the Vectornav-100T IMU sensor and the STIM300 IMU sensor derived from tables 4.6-11: WELLBORE 1.

Figure 4.5 shows a graph of the comparison of the two high-performance measurement sensors taking into consideration the second standard deviation region of uncertainty in error for both axis while Figure 4.6 shows the comparison of the two MEMS IMU sensors of lesser performance specification in the same regard. It is clear from Eqn 2.33 that the region of uncertainty depends also on the survey measurements at a given survey station such that the survey instrument or IMU sensor would have a lower error uncertainty for smaller values of inclination and azimuth. This explains why generally, from both graphs, for a given IMU sensor, the uncertainty on the B-axis is higher than that of the A-axis. In the case of the STIM300, its uncertainty falls within the acceptable error margin for the first trajectory but falls short of the acceptable range in the second trajectory scheme if to be used in the real-world example (+/-5cm – either axis) discussed in Chapter 1. The digital inclinometer probe and the IPST-RQH both fall within the acceptable error margin in both trajectories while the Vectornav-100T, without measurement updates do not meet the preset accuracy requirement. Taking into consideration the jet grouting cut-off example given in Chapter 1, for a tolerance of +/-3 cm deviation uncertainty, the IPST-RQH sensor form iMAR best meets this criterion. This is followed by the digital inclinometer probe when considering the displacement uncertainty in the B- and A-axis. However, as mentioned earlier, the former is of a high cost while the latter can basically only be used after the completion of the drilling process and is also prone to human influenced errors.

4.2 Experiment to Investigate the Improvement in Accuracy using the Described Processing Scheme

This experiment was done to investigate the improvement in accuracy attained after the implemented mathematical model. The low-cost consumer grade MPU6500 IMU sensor was used as the sensor of choice due to its low power consumption, as well as ease of integration into the sensor node module for usage. To give a perspective of the performance of the MPU6500 IMU sensor, the standard deviation region of uncertainty in error was first determined using the ISCWSA error model as shown in tables 4.16-18 with its performance specifications given as per data sheet in table 4.16.

Table 4.16: A summary of the performance specification of the MPU6500 IMU Sensor.

MPU6500	**Parameter**	**Value**
Accuracy (pitch & Roll) ~0.02°	f_{xy}^{bias}	$5.886*10^{-1}$ m/s^2
	f_{z}^{bias}	$5.378*10^{-6}$ m/s^2
Scale Factor Error	$f^{S.F.error}$	$1.0*10^{-3}$
Alignment Error	$f^{Misalignment}$	$1.0*10^{-3}$
Bias stability	G^{Drift}	$<1.0*10^{-2}$ °/s
Gyro random walk	G^{ARW}	$<1.0*10^{-2}$ °/s/$\sqrt{Hz}$

Table 4.17: WELLBORE 1: A summary of the region of uncertainty in error (standard deviation) in the A-, B- and TVD axis – MPU6500.

Survey Station	**B uncertainty (+/- cm)**	**A uncertainty (+/- cm)**	**TVD uncertainty (+/- cm)**
	σ	σ	σ
Wellbore Top:	0.000	0.000	0.000
Survey Station 1:	4.980	12.173	0.060
Survey Station 2:	6.034	17.663	0.153
Survey Station 3:	6.068	22.472	0.273
Survey Station 4:	8.529	26.959	0.431
Survey Station 5:	14.658	31.762	0.629
Survey Station 6:	24.687	37.784	0.879
Survey Station 7:	39.512	44.922	1.170
Survey Station 8:	57.963	51.409	1.459
Survey Station 9:	80.347	56.673	1.750
Survey Station 10:	87.007	57.940	1.824

Table 4.18: WELLBORE 2: A summary of the region of uncertainty in error (standard deviation) for A-, B- and TVD axis – MPU6500.

Survey Station	B uncertainty (+/- cm)	A uncertainty (+/- cm)	TVD uncertainty (+/-
	σ	σ	σ
Wellbore Top:	0.000	0.000	0.000
Survey Station 1:	14.152	0.507	0.373
Survey Station 2:	20.976	5.746	0.840
Survey Station 3:	28.827	19.908	1.601
Survey Station 4:	40.602	43.202	2.566
Survey Station 5:	56.632	73.877	3.573
Survey Station 6:	76.603	116.466	4.692
Survey Station 7:	99.738	171.397	5.896
Survey Station 8:	125.062	235.999	7.115
Survey Station 9:	157.457	310.979	8.391
Survey Station 10:	167.779	332.589	8.715

Figure 4.7 shows the graphical representation of the region of uncertainty in error for the B- and A- axis displacement for WELLBORE 1 using the MPU6500 IMU sensor. The error uncertainty at the final survey positions is approximately +/-87cm and +/-131cm for the A- and B- axis displacement respectively without any form of processing. To achieve better accuracy and as well as real-time data acquisition in view of moderately cost IMU sensors, the experimental setup in the next section was conducted to show a proof of the concept. The results of the experiment in the next section gives an insight in terms of the improvement of the gyroscope drift and angular random walk and how this in turn improves the overall error of uncertainty of the survey measurements based on the field data given in Tables 4.1-2.

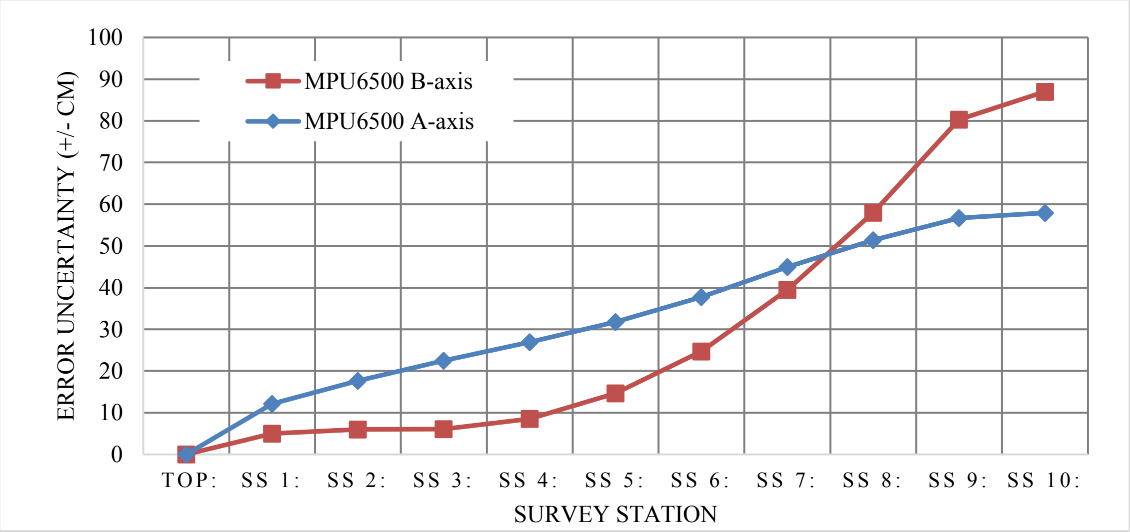

Figure 4.7 The region of uncertainty for the B- and A- axis displacement for the low-cost MPU6500 IMU Sensor: WELLBORE 1.

4.2.1 Determination of Accuracy and Precision of Sensor

The error characteristics or performance specifications of the IMU sensor was verified against the provision made in the datasheet using the results from Allan variance curve (see Appendix V). The accuracy of the MPU6500 IMU sensor was determined by taking the inclination measurement values of the sensors at pre-defined deviation settings on the Acutronic AC1120S turn table. The accuracy is given as the difference between the preset value on the turn-table and the reading given by the sensor which is then converted to a percentage. The mean of the determined accuracies and precision was then obtained to determine the accuracy and precision of the MPU6500; and that of the Vectornav-100T for comparison.

Several measurements were made at each of the preset values after which the mean value and the standard deviations are calculated. The accuracy at each of the preset inclinations were then computed by finding the difference between the preset value (true value) and the calculated mean value and expressed as a percentage. This difference represented the observed sensor accuracy at each preset position of which a probability distribution for the sensor accuracy is deduced. Preceding the experiment, a calibration of the sensor was made. This was a six-point calibration process using known gravity with the vertically placed turn-table at room temperature. The bias and misalignment vector and matrix were determined respectively using the least square estimate method with the corresponding adjustment for the temperature effect. See more details in Appendix III for more details on the background theory and the determined vector and matrix values. The determination of the accuracy and precision for both Vectornav-

100T and MPU6500 was done. The turn-table placement of sensor module for near perfect pitch and roll measurements for deducing the sensor accuracy as decribed earlier and the precision of the inclination measurements were made. This was used to establish the probability density distribution for each of the sensors in terms of their respective accuracies and the precision where the accuracy denotes the mean error and the precision denotes the first standard deviation from the mean value. Table 4.19 below shows the values obtained after the measurements were taken

Table 4.19: Summary of the relative accuracy and standard deviations from a series of measurements taken at preset inclinations on a turn-table.

Preset Inclination (x_k) (degrees)	0.5°	1°	1.5°	2.5°	3.5°	5°	10°
Mean ($\hat{x}_k$) (degrees)	0.488	1.006	1.480	2.478	3.429	4.982	9.966
Standard Deviation (σ) (degrees)	0.027	0.022	0.038	0.025	0.141	0.014	0.029
Relative Accuracy $y_k = \frac{x_k - \hat{x}_k}{x_k} \cdot 100\%$	2.388	0.571	1.313	0.867	2.041	0.368	0.336

where the percentage accuracy is given as the preset inclination minus the mean with the result expressed as a percentage of the preset value. Considered, is the conditional probability distribution $F_{y|x}\left(y_k \mid x_k\right)$, which represents the sensor's probability distribution model with k representing the different angular measurements taken. This is interpreted as the probability distribution of the relative accuracy y_k conditioned on the preset inclination x_k. Assuming $F_{y|x}\left(y_k \mid x_k\right)$ is differentiable, the expressed probability density function is given as

$$f_{y|x}(y_k \mid x_k) = \frac{1}{\sqrt{2\pi\sigma_y^2}} e^{-\frac{1}{2}\frac{(y_k-\mu)^2}{\sigma_y^2}} \tag{4.6}$$

Since y_k represents the accuracy with zero-mean and therefore $\mu = 0$. The distribution is represented by the mean of $y_k - \mu$ written as μ_{y_k} , and the standard deviation denoted as σ_y . This is represented as $F\left(\mu_{y_k}, \sigma_y\right)$ in this context. The prior distribution $F\left(x\right)$ also represented in this context as $F\left(\mu_x, \sigma_x\right)$ is given as the turn-table model described with a zero-mean accuracy and a standard deviation which is given as ~1/3600° from the datasheet. The posterior distribution hence considering the observed inclination difference and the known a priori distribution (from turn-table model) and expressed as a probability density function is given as

$$f_{x|y}(x_k \mid y_k) = \frac{f_{x|y}(y_k \mid x_k) \cdot f_x(x_k)}{f_y(y_k)}, \tag{4.7}$$

$$F(\bar{\mu}_k, \sigma) = F(\mu_{y_k}, \sigma_y) \cdot F(\mu_x, \sigma_x), \tag{4.8}$$

where $f_y\left(y_k\right)$ is considered a normalizing factor. The resultant means, and standard deviation as deduced from the formulation in Eq. 4.7 is given as

$$\bar{\mu}_k = \frac{\sigma_x^2}{\sigma_x^2 + \sigma_{y_k}^2} \cdot \mu_{y_k} + \frac{\sigma_{y_k}^2}{\sigma_{y_k}^2 + \sigma_x^2} \cdot \mu_x \tag{4.9}$$

and the variance is given as

$$\sigma^2 = \frac{\sigma_{y_k}^2 \cdot \sigma_x^2}{\sigma_x^2 + \sigma_{y_k}^2} \tag{4.10}$$

The mean relative accuracy and σ for the MPU6500 IMU sensor from the results of the experiment is shown in Table 4.20 and illustrated graphically in Figure 4.8.

Table 4.20: Mean relative accuracy and standard deviation for MPU6500 sensor

Relative Accuracy $\bar{\mu}$	1.126
σ	0.0422

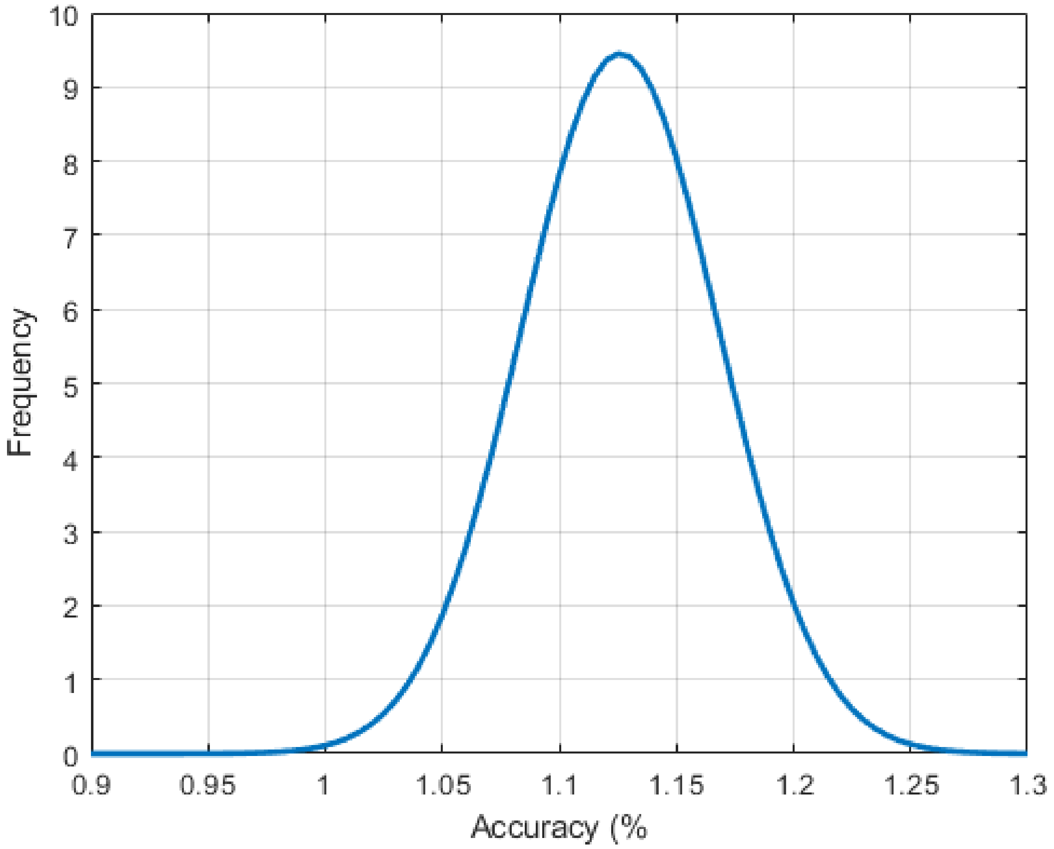

Figure 4.8: A representative distribution showing the mean accuracy ($\bar{\mu}$) of 1.126% and the standard deviation (σ) of 0.0422 for the MPU6500 sensor

This implies that any time a measurement is taken, the accuracy of the measurement would be +/-1.126% of the measured value with a distribution of 0.0422°.

The mean relative accuracy; and the standard deviation for the Vectornav-100T with preset inclinations of 0°, 1°, 2°, 3°, 4°, 5° and 10° are shown in table 4.21

Table 4.21: Mean accuracy and 1st standard deviation for the Vectornav-100T IMU sensor

Vectornav Angle (deg)	**Inclination**	**Inclination accuracy**	**Inclination % accuracy**	**Inclination 1st st. Dev. (deg)**
0	0.000	0		0.005
1	1.002	0.002	0.2	0.005
2	2.005	0.005	0.25	0.005
3	3.005	0.005	0.167	0.006
4	4.006	0.006	0.15	0.005
5	5.006	0.006	0.12	0.005
10	10.012	0.012	0.12	0.005
			0.168	**0.0052**

Table 4.22: Mean relative accuracy and σ for Vectornav-100T IMU Sensor

Relative Accuracy $\bar{\mu}$	0.168
σ	0.0052°

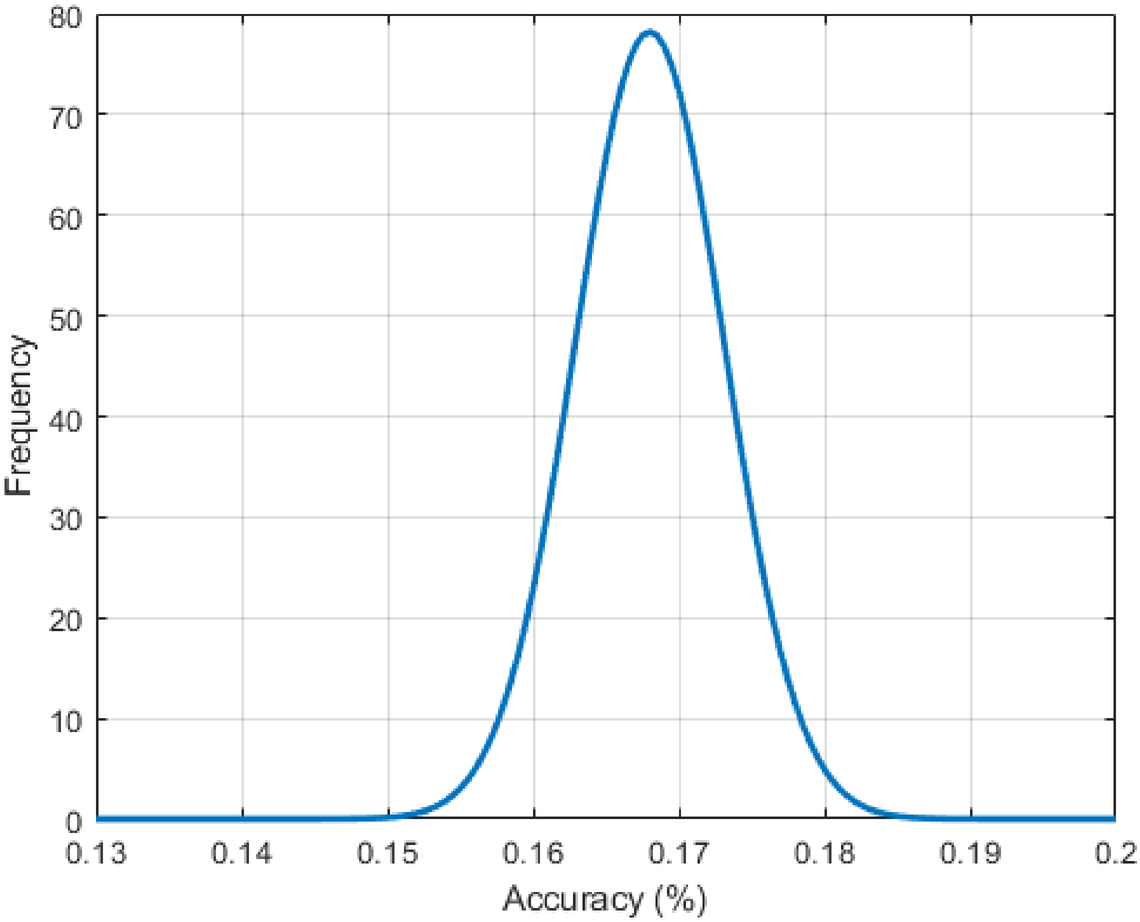

Figure 4.9: Representative distribution showing the mean accuracy of 0.168% and the first standard deviation of 0.0052° for the Vectornav-100T sensor

This implies that any time a measurement is made, the accuracy of the measurement would be +/-0.168% of the measured value with a distribution of 0.0052.

Table 4.23: Resultant mean accuracy and precision: MPU6500 and Vectornav-100T combined

	$\bar{\mu}$ %	σ
MPU6500	1.126	0.0422
Vectornav-100T	0.168	0.0051
Combined_1	0,182	5.06E-3

The accuracy of the combined reading of both MPU6500 and Vectornav-100T is 0.182% with a slightly improved standard deviation of 5.06E-3°. Increase in the number of different measurement sensors with better accuracy characteristics results in higher accuracy and standard deviation. Consequently, if a more accurate inclinometer is added to the sensor fray at the given position of measurement, an improvement in the measurement accuracy is achieved with a smaller variance spread. For example, addition of a hypothetical sensor, Sensor C with accuracy 0,1% and standard deviation 0.0005

Table 4.24: Resultant mean accuracy and precision: MPU6500 and Vectornav-100T

	$\bar{\mu}$ %	σ
mpu6500	1.126	0.0422
vn-100T	0.168	0.0051
Combined 1	0.182	0.00506
Sensor C	0.1	0.0001
Combined_2	0.100032	9.998E-5

Addition of Sensor C improves the accuracy to 0.100032% with a standard deviation of 9.998E-5.

4.2.2 Filter Tuning

The initial phase of the experiment involved the tuning of the Kalman filter. As mentioned before, the noise characteristics of the gyroscope includes the deterministic errors i.e. the constant bias which is estimated and removed from subsequent gyroscopic data measurements and the stochastic bias which includes the bias modeled as a time correlated Gaussian random process described by the variance and a correlation time. In addition to the stochastic error is the zero-mean white Gaussian noise process (Eq. 3.17-18). The gyroscope noise characteristics was determined from over 2 hours of data collected with the IMU sensor at stand still using the Allan variance curve (see description and results in Appendix V). However, during operation, due to noise noise effects caused by engine activity and vibrations during the drilling process, the noise characteristics change during operation making it difficult to determine the level of noise to attribute to the process noise within the filter for optimal tuning. Tuning the Kalman filter is done by re-location of the Kalman filter estimator poles, which is described shortly. The Kalman filter gain is mapped to the error state covariance as given in Eq. 4.11 and the error state covariance is consequently mapped to the noise gain matrix as shown in Eq. 4.12. The noise gain matrix is written as a function of the tuning factors A and B as shown in Eq. 4.14-15.

$$K_k = P_k^- H_k^T [H_k P_k^- H_k^T + R_k]^{-1} \tag{4.11}$$

$$P_k^- = F_{k-1} P_{k-1}^+ F_{k-1}^T + G_{k-1} Q_{k-1} G_{k-1}^T \tag{4.12}$$

where F_{k-1} denotes the error state dynamic matrix, K_k and H_k denotes the gain matrix and the measurement matrix at time instant k respectively. P_k^- denotes the a priori estimate of the state covariance at time instant k, P_{k-1}^+ denotes the a posteriori estimate of the covariance at time instant $k-1$, G_{k-1} denotes the noise gain matrix at the time instant $k-1$. Formulation for the closed loop characteristics of the extended Kalman filter of the error model is given as

$$\Delta\hat{x}_k^+ = (I - K_k H)\Delta\hat{x}_k^- + K_k z_k \tag{4.13}$$

where $\Delta\hat{x}_k^+$, z_k and P_k^+ denote the a posteriori error state estimate, the measurement vector and a posteriori state covariance matrices respectively with the eigenvalues of the matrix $I - K_k H$ being the poles of the estimator. The noise gain matrix Eq. 3.25 is re-written with the tuning factors as shown in Eq. 4.15.

$$\bar{G} = \begin{bmatrix} 1 & \frac{s_\alpha s_\beta}{c_\beta} & \frac{c_\alpha s_\beta}{c_\beta} & 0 & 0 & 0 \\ 0 & c_\alpha & -s_\alpha & 0 & 0 & 0 \\ 0 & \frac{s_\alpha}{c_\beta} & \frac{c_\alpha}{c_\beta} & 0 & 0 & 0 \\ 0 & 0 & 0 & 1 & 0 & 0 \\ 0 & 0 & 0 & 0 & 1 & 0 \\ 0 & 0 & 0 & 0 & 0 & 1 \end{bmatrix} \tag{4.14}$$

where the variables α, β, γ represent the roll, pitch and yaw angles respectively and s_α, s_β c_α and c_β denote the compact notations for the trigonometric functions $\sin\alpha$, $\cos\alpha$, $\sin\beta$, and $\cos\beta$, respectively.

The noise gain matrix written further as

$$G = \begin{bmatrix} \mathrm{A}\bar{G}_C & 0_{3x3} \\ 0_{3x3} & \mathrm{B}\bar{G}_D \end{bmatrix} \tag{4.15}$$

$\bar{G}_C = \bar{G}_{i,j+3}$ and $\bar{G}_D = \bar{G}_{i+3,j+3}$, where $1 \le i \le 3$ and $1 \le j \le 3$ where A and B are the tuning parameters for the Kalman filter estimator and affect the pole locations of the estimator. Large values of A and B results in faster poles thereby resulting in a faster response time but at the cost of a noisier signal. In the filter tuning process, a suitable value of B is selected that enables a faster estimation of the bias. The results of the comparison of the tuned filter with B = 5 compared with B = 1 is shown in the graphs of Figure 4.11b. The rate bias is estimated during the measurement update period. The filter is tuned such that the gyro bias convergence speeds up without significantly magnifying the noise in the Euler angle estimate.

Procedure:

1. A miniature drill string on which a sensor node is attached is set to an inclination of 2° as shown in figure 4.12.
2. The bias estimation and alignment offset correction is executed from the 1^{st} to 300^{th} second
   - String is kept stationary for the first 100 seconds at a pre-defined position.
   - 3.6°/sec rotation rate for 2 revolutions to estimate and remove the alignment offset. This is described further in section 4.2.2.
3. This is followed by 20 rotations at 71°/sec beginning at the 300^{th} second
4. Observation of the estimated yaw angle position error and gyroscope bias were made. Also recorded were the encoder position measurement, raw gyroscope position measurement; estimated yaw position, computed inclination and toolface/azimuth, and the gyroscope integration time.
5. The data rate is set at 1.9Hz whereby the sensor data is read, measurement data received, data processed by the indirect Kalman filter and the result transmitted. The execution cycle with the timing for each event is shown in figure 4.10

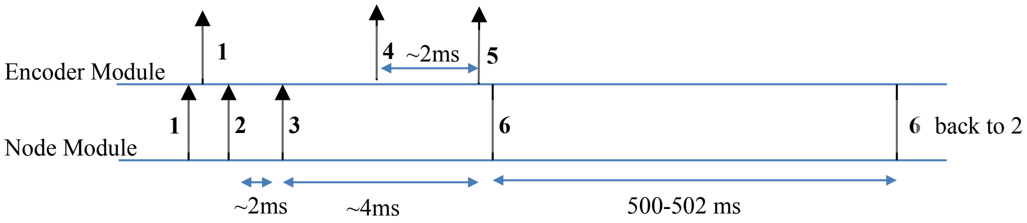

Figure 4.10: The execution cycle showing the acquisition and processing times of the sensor data and incoming measurement data as implemented on the micro-processor.

Table 4.21: Summary of the Explanations of the Events Shown in Execution Cycle Diagram in figure 4.10.

Event	Details
1	Synchronization of encoder and node module timers or clocks
2	Execution begins
3	Request for encoder information by the node module
4	Read encoder data by encoder module
5	Send encoder data by encoder module and receive encoder data by node module
6	Processing (Extended Kalman filter)

Figure 4.11a shows the velocity profile of the drill string used in the experiment with a total operation time of approximately 620s. The velocity profile shows the first stationary phase where the bias estimation is done and then followed by the slow rotation phase to enable for the correction of inclination alignment offset. This is followed by the second stationary phase where by the system transients' decays before the first set of initial readings is taken after which the rotation phase, which simulates the actual drilling, occurs. Finally, the last stationary phase; again, the system transients are made to decay before readings are taken. Figure 4.11b shows the estimated bias in all phases and shows the effect of the tuning parameters used as explained in section 4.2.1. Figures 4.11c-d show the computed inclination and azimuth for the various phases from the accelerometer output data and the processed gyroscope data output after the yaw position angle has been estimated using the indirect Kalman filter with measurement update data from the encoder; the aiding system.

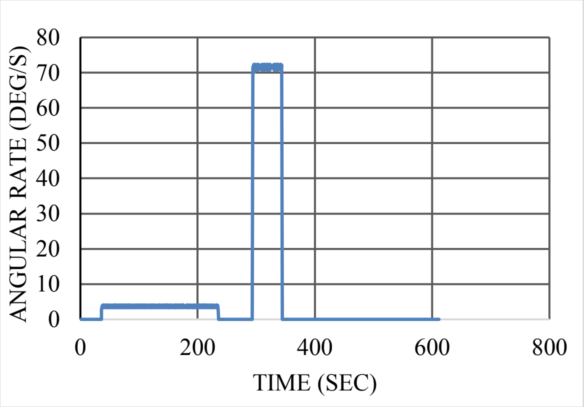

Figure. 4.11a: Velocity profile used: ~45sec for online bias estimation, alignment offset determination and removal with slow rotation of 3.6°/s from 36th to 235th second and then rotation at 71°/s from ~278s to 343s.

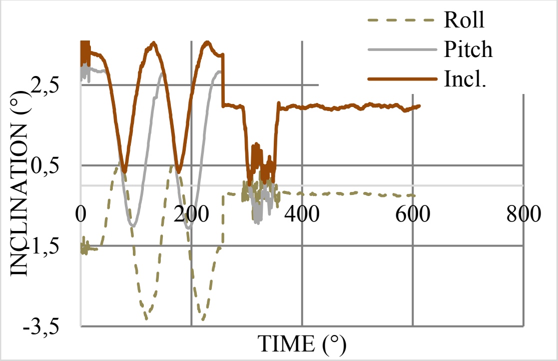

Figure. 4.11c: Computed inclination data from accelerometer output data. Inclination measurements are read at stationary phases after applying a moving average filter to smoothing the signal.

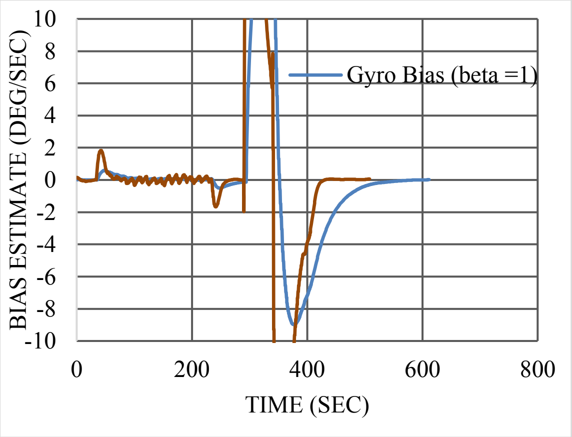

Figure 4.11b: The tuned filter (with $B = 5$) shows a faster convergence at approximately 0.2°/s after rotation stops i.e. ~82.8sec compared to ~177.98sec in the case where B = 1.

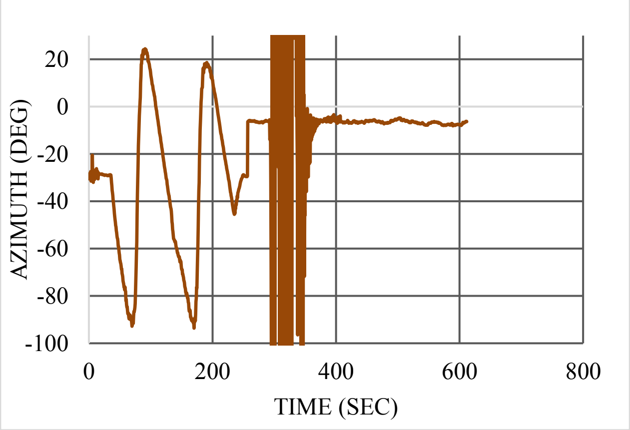

Figure. 4.11d: Computed azimuth data from accelerometer output data and the estimated yaw position. Azimuth measurements are read at stationary phases after applying a moving average filter for signal smoothing.

4.2.3 Description of Experimental Setup

Two categories of tests were made to investigate the ability of the sensor node module with the implemented filter algorithm as described in Chapter 3 to accurately track the position of the sensor node with respect to defined measurement update modes and consequently, the effect it has on the azimuth errors. The two main test conditions include

a. Continuous measurement updates interspersed with data timeout periods where data timeout refers to periods of unavailability of measurement updates.
b. Single measurement updates with decreasing frequency.

And finally, multiple nodes sequential measurement update for the above two scenarios. The first condition consists of continuous measurement updates at 1.9Hz; the same bandwidth as gyroscope sampling rate, with periodic data timeouts by which the filter coasts through relying on gyroscope data alone for estimation of the yaw position. This is further categorized into

i. Update at 1.9Hz continuously (no measurement data timeout periods)
ii. Continuous 20s measurement updates at 1.9Hz with 5s, 10s, 15s, 20s, 25s, 30s, 35s, 40s, 45s, 50s, and 1-minute data timeout periods over a given time duration.

The miniature drill string setup as shown in figure 4.10 has a 1024 count incremental encoder interfaced to the C1101 868Hz transceiver and serves as the aiding system attached to it. It reads the angular position relative to the pre-defined reference position and sends it alongside the angular velocity information to the sensor node. The sensor node consists of the MPU6500 IMU sensor also interfaced with the 868Hz, C1101 wireless transceiver. The encoder, as an aiding system, provides the measurement update to the sensor node. The sampling rate at which the MEMS MPU6500 triple-axis gyroscopic sensor is read is at 1.9Hz, which includes reading sensor data, application of the moving average filter, and execution of the indirect Kalman filter; see figure 4.8, while ensuring that dynamics of the rotating drill string or rotation rate does not exceed 0.95Hz (57rev/min) to satisfy the Nyquist rate. At each iteration of the filter, the node receives measurement data from the aiding system as measurement update when available. This implies that the measurement update would be at the same frequency of 1.9Hz in the event of its continuous availability. The test begins with an initial 50s for the estimation and removal of the fixed bias of the gyroscope output data using simple averaging followed by the calibration phase which involves a very slow rotation at ~7°/s for 2 revolutions for the removal of the alignment offset error. This occurs from the 50th to the 250th second. During this phase, the maximum and minimum pitch and roll measurements are determined, added and divided by two for subtraction from each subsequent pitch and roll reading to correct for any alignment offset. The inclination data is then generated from the pitch, roll measurement as the square root of the square sum of the pitch, and roll measurements. This removes the alignment errors in the inclination measurement.

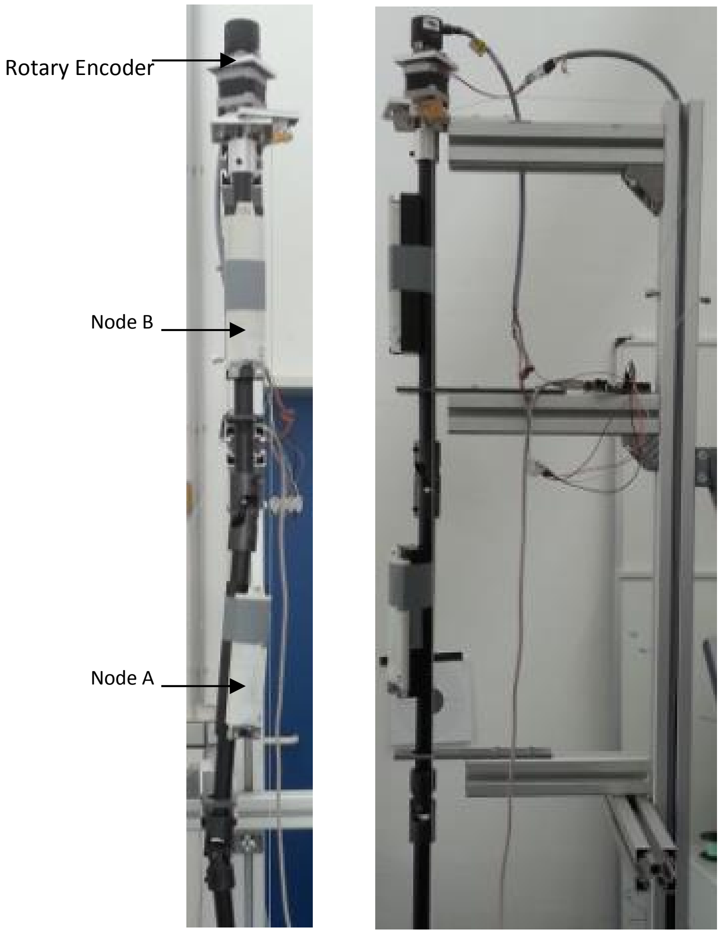

Figure 4.12: Miniature drill string as setup in the laboratory for the experiment; first picture is the frontal view and the next picture is the side view.

The tuned indirect Kalman filter is applied, in the estimation of the yaw position and the bias of the system both during and after the rotation dynamics and the observations are herein noted. The consequent effect on the survey measurements; the inclination and azimuth, and then subsequently, the resulting effect on the error uncertainty in the position measurements with respect to the designated frame of reference is investigated. As mentioned before, the survey measurements are taken at stationary positions after the drill string rotation comes to a stop. To reduce the noise on the sensor measurement, a 32-point moving average filter is applied and therefore a period of approximately 20 seconds is required for the measurements to stabilize before the survey measurements are taken. Preceeding each test run, the true inclination and azimuth is determined after the initial calibration. The miniature drill string is then rotated at 71°/s for 20 revolutions and then brought to a halt. The survey measurements were logged during the entire process together with the encoder position data, estimated yaw position, raw gyroscope position data, gyroscope angular rate data, encoder velocity and the gyroscope bias.

After the removal of the constant bias and the alignment offset error, the bias estimate is observed to converge to its true value of approximately -0.02°/s. Observation is made of the time duration for the bias estimation after rotation (at 71°/s) comes to a stop. The thin dashed vertical lines in the graphs in figures 4.14 shows the periods of available measurement updates and the measurement data timeout periods where the update sequence value 0 denotes the data timeout periods for the respective measurement update modes.

4.2.4 Continuous Measurement Update Interspersed with Measurement Update Timeout Periods

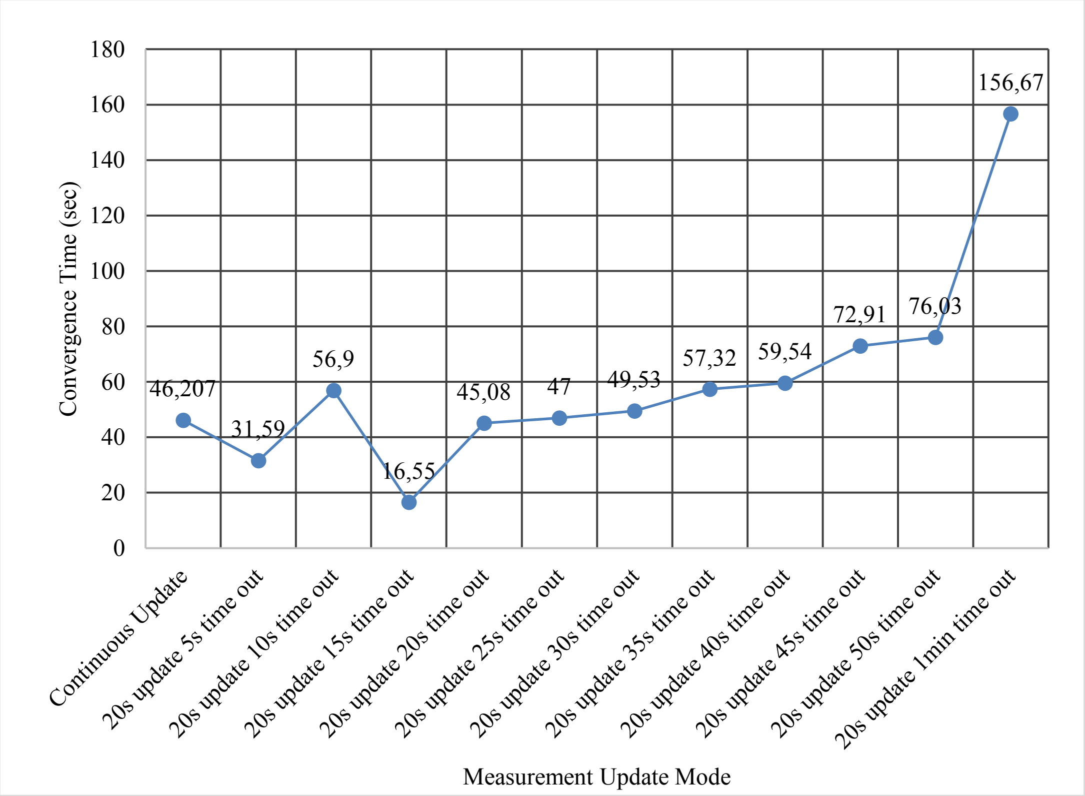

Figure 4.13: Convergence time of the bias estimation of the different measurement modes defined for continuous measurement update scheme interspersed with data timeout periods.

Figure 4.13 shows the convergence time for the estimated bias to be averaging at 50s for the measurement update mode with data timeout periods less than 45 seconds with a gradual increase in the convergence time as the timeout approaches one minute. Convergence time is defined here as the time the estimated bias reaches approximately -0.02°/s. Considering selected measurement modes; in the first measurement update mode with continuous measurement updates, the time duration for convergence of the bias to its true value after stoppage is approximately 46s (320th – 366th second). In the measurement update mode with 10s timeout periods, after rotation, convergence of the estimated bias is after approximately 57s (314th – 371st second) with the delay attributed to a data timeout period occurring at the time of rotation stoppage as shown in figure 4.14b. For that of the 30s-timeout period, after rotation, the convergence time for the estimated bias is approximately 49s (347th to 396th second). In the final measurement update mode with one-minute timeout periods, there is a delay in the bias estimation because of the long data timeout period that occurs just before rotation comes to an end, figure 4.14d. The convergence time is approximately 156s (320th – 476th second). Convergence of the bias estimate is faster when the measurement update period coincides with the period during rotation stoppage. Figure 4.14a shows the estimated yaw position error for the continuous measurement update case. Since the measurement update rate or frequency is the same as the time update rate due to the fact that measurements are only recorded after the system transients have decayed after rotation comes to a stop, the measurement data with a much lower measurement noise covariance acts as a reset thereby assigning a high weight to the Kalman gain which makes the data from the encoder of more significance. Figures 4.14b, d, f, and h show the estimation of the bias during the entire duration of the test for selected measurement update modes. Generally, the bias is estimated during the period of availability of measurement updates. Appropriate tuning of the indirect Kalman filter provides fast convergence of the bias during the measurement update periods as observed in each case after the rotation comes to a stop. Figure 4.14e shows the estimated position errors where growth of the error occurs during the instances of absence of measurement update information or data timeout periods. However, a higher yaw position error; about 1.3° is observed during the first data time out period (370th to 396th second) when the estimated bias hadn't converged yet to its true value. It is observed that during the subsequent time out periods; within the 423rd to the 446th second period and within the 467th to the 496th second, the estimated yaw position error is much reduced to within +/-0.4°. A similar such observation is seen in Figure 4.14f with the estimation of the yaw positon error. A larger error (~+/-0.7°) is observed during the first data timeout period (417th to 476th second) after which the subsequent data timeout period shows a much-reduced estimated yaw position error during the period 502nd to 550th second within +/-~0.4°.

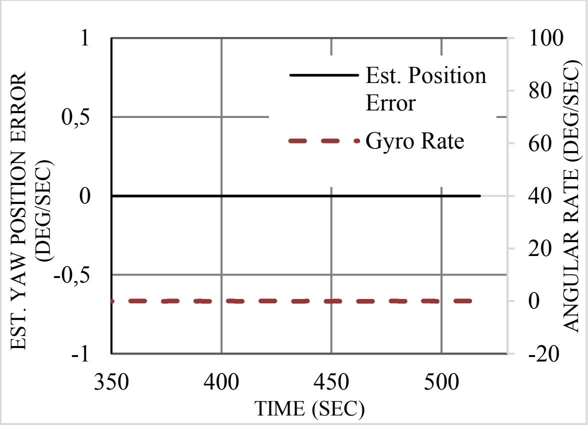

Figure 4.14a: Estimated yaw position error with continuous measurement update at ~1.9Hz.

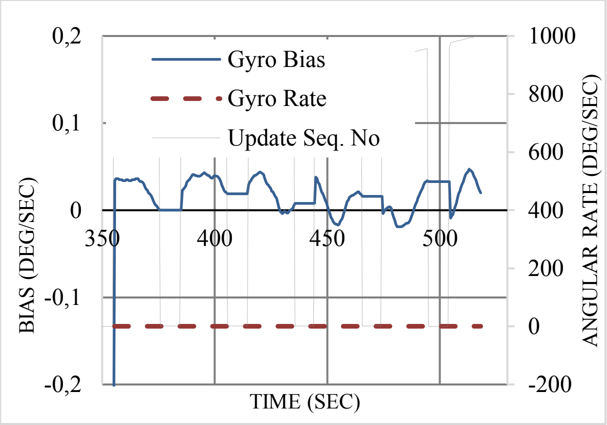

Figure 4.14d: Estimated gyro bias with 20s continuous measurement update periods interspersed with 10 seconds' data timeout periods.

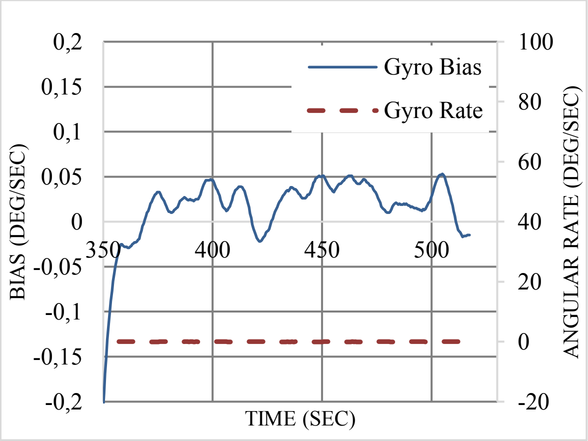

Figure 4.14b: Estimated gyro bias with continuous measurement update at ~1.9Hz

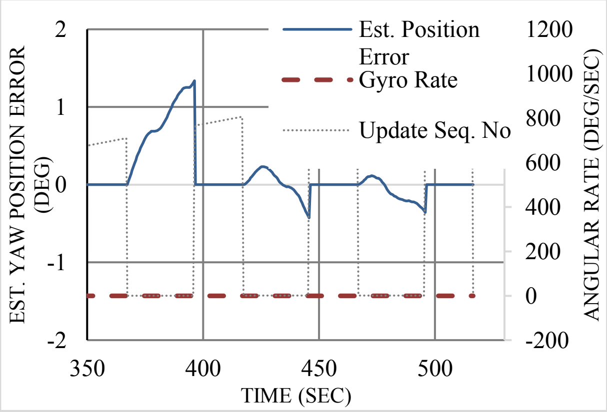

Figure 4.14e: Estimated yaw position error with 20s continuous measurement update periods interspersed with 30s data timeout periods.

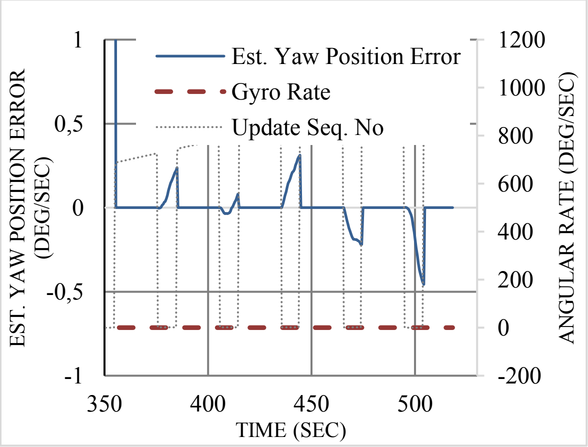

Figure 4.14c: Estimated yaw position error with 20s continuous measurement update periods interspersed with 10 seconds' data timeout periods.

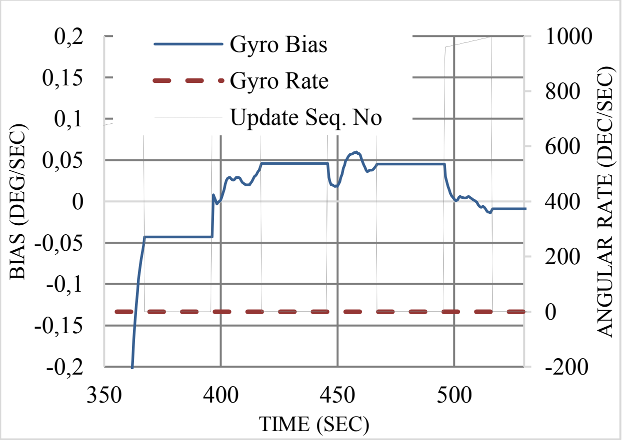

Figure 4.14f: Estimated gyro bias with 20s continuous measurement update periods interspersed with 30 seconds' data timeout periods.

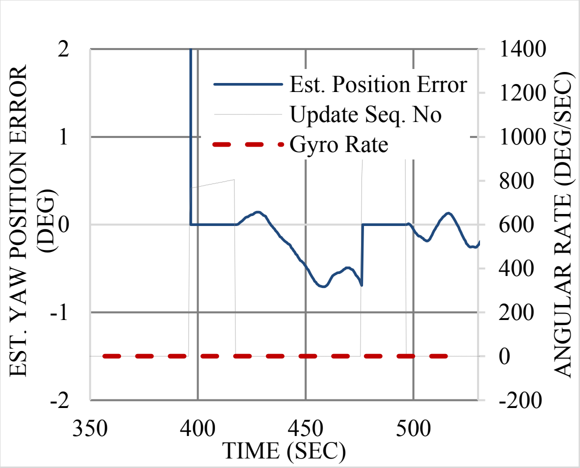

Figure 4.14g: Estimated yaw position error with 20s continuous measurement update periods interspersed with 1-minute data timeout periods. Data timeout when update seq. no = 0.

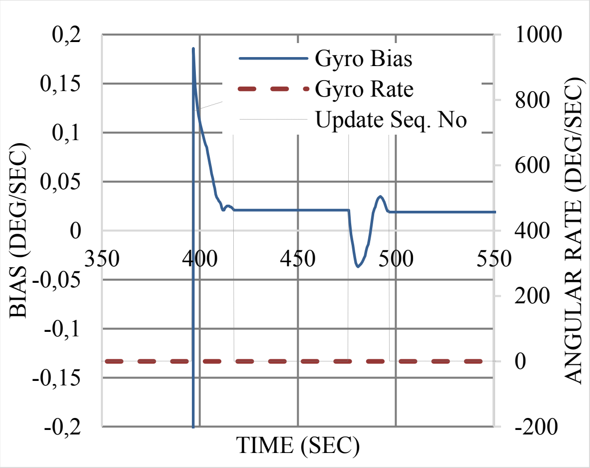

Figure 4.14h: Estimated gyro bias with 20s continuous measurement update periods interspersed with 1-minute data timeout periods. Data timeout when update seq. no = 0.

Effect on Azimuth measurements (continuous)

As mentioned in Chapter 1, what is of importance is how the yaw position errors translates to azimuth errors since it is directly related to the toolface angle as given in Eq. 1.3. Therefore, alongside the bias estimation, the effect of differing measurement update modes on the inclination errors and azimuth errors were observed. Figure 4.15 shows the graphical representation of the computed inclination and azimuth errors from the yaw position estimate results from the indirect Kalman filter.

The graph in figure 4.15 gives a representation of the inclination errors and azimuth errors corresponding to the different measurement update modes mentioned earlier. The root mean squared azimuth error is estimated at approximately 0.4° with measurement update timeout periods between 10 seconds through 35 seconds with better performance observed with continuous measurement update with no timeout; ~0.03°, as well as with 5 seconds timeout periods; ~0.25°, both recording under 0.3° azimuth errors. There is a general increase in the azimuth error with increasing measurement update timeout periods while the inclination errors are unaffected by yaw position errors. The high azimuth error shown with a timeout period of 50 seconds shows the potential irregularity of the azimuth errors as the timeout periods increases. Further analysis for comparison purposes is given in section 4.2.5. From the graphs in Figures 4.16, MAF refers to the 100-point moving average filter applied to the computed inclination and azimuth output data to remove the high frequency noises to enable for a clean signal to be recorded.

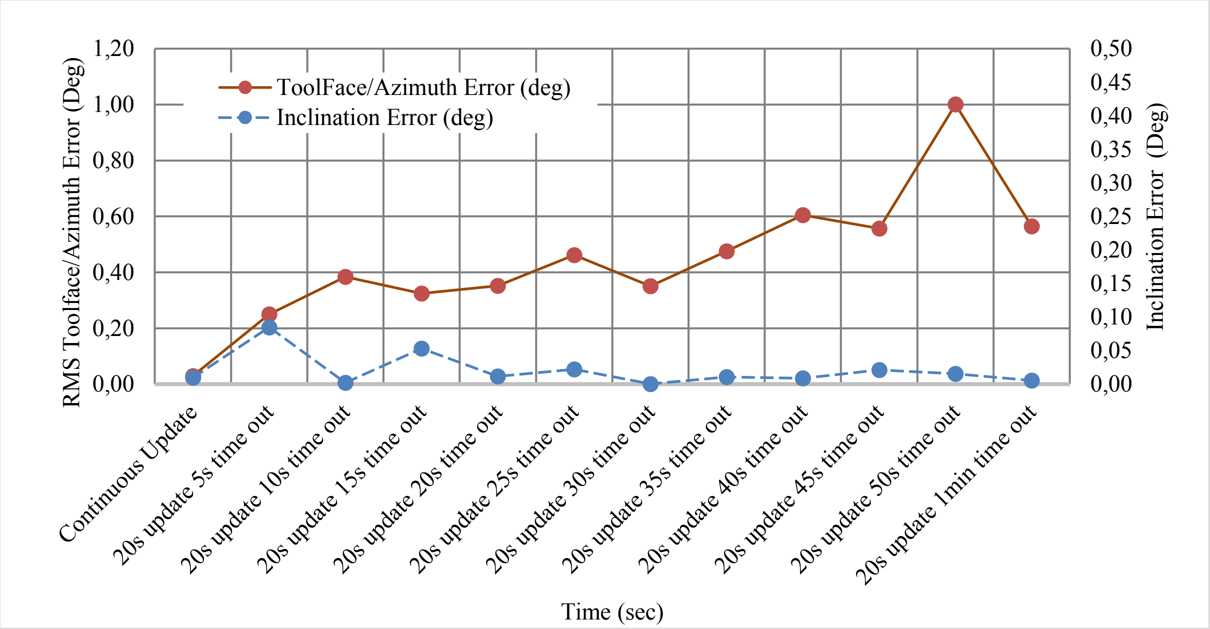

Figure 4.15. Graphical Representation of the Summary of Inclination and Azimuth Errors with Increasing Measurement Data Timeout Periods

Table 4.22 A Summary of Inclination and Azimuth Errors with Increasing Measurement Data Timeout Periods

Measurement Mode	RMS Inclination Error (deg)	RMS Azimuth Error (deg)
Continuous Measurement Update	0.01	0.029
20s update with 5s time out period	0.085	0.250
20s update with 10s-time out period	0.002	0.384
20s update with 30s-time out period	0,000	0.351
20s update with 50s-time out period	0.015	1.0
20s update with 1 min time out period	0.005	0.565

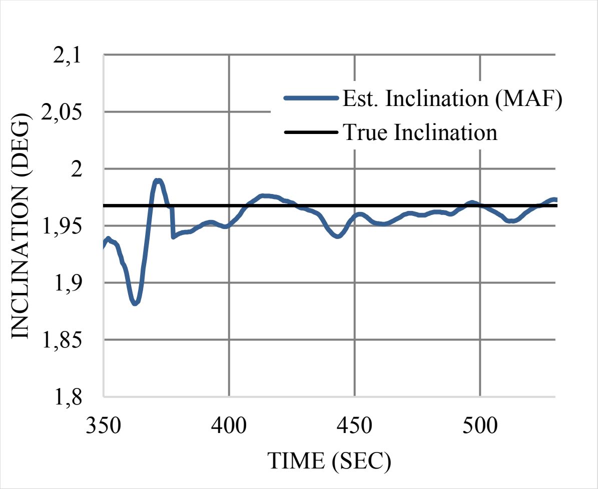

Figure 4.16a: Estimated and True Inclination in continuous measurement update mode

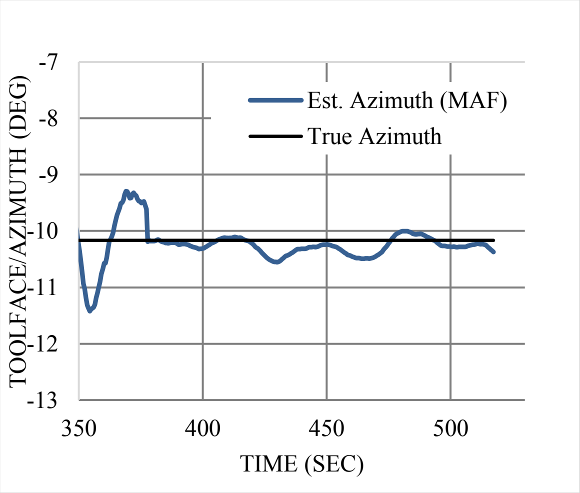

Figure 4.16b. Estimated and True Azimuth in continuous measurement update mode

Figure 4.16a-b shows the estimated inclination and azimuth measurements alongside their true values with continuous availability of measurement update for the observation period between 350th to 550th second within which the sensor was at rest (no rotation was taking place) and the system transients had decayed. The root mean square inclination and azimuth errors are observed for the different measurement modes as shown in Table 4.22. A 32-point moving average filter, implemented in the micro-processor, was applied to the output data to reduce the noise effect. This was used in computation of the azimuth after translation from the body frame of reference to the designated reference frame with the estimated yaw position as given by the equation in Eq. 1.3

4.2.1 Single Measurement Updates with Increasing Frequency

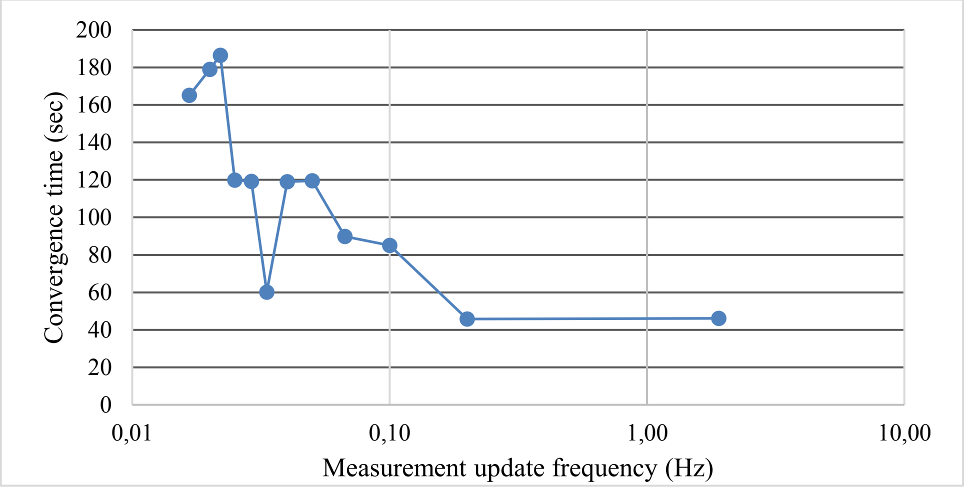

Figure 4.17: Logarithmic plot of the convergence time of estimated bias with increasing measurement update frequency

Figure 4.17 shows a logarithmic plot of the convergence time for the estimated bias with increasing measurement update frequency for selected frequencies. There is a general decrease in convergence time with increasing measurement update frequencies. Measurement update frequencies above 0.1Hz show a convergence time in the region towards 50s. Figure 4.16 shows the estimated positions and their corresponding estimated bias with selected varying measurement update frequencies. The dashed lines show the measurement updates. For selected measurement update rates; at update rate of 0.0167Hz convergence time is after approximately 165s (310th – 476th second), 0.05Hz update rate shows convergence after approximately 120s (317th – 437th second), 0.01Hz update rate shows convergence after approximately 85s (321st – 406th second) and 0.2Hz update rate with convergence time at approximately 46s (336th – 382nd second). Figure 4.16a shows the estimated yaw position error after stoppage with an update frequency of 0.2Hz. The yaw position error is observed to be within +/-0.2°. Figure 4.16c shows much higher yaw position errors within +/-0.4° with the estimated bias clearly showing some noisiness. Figure 4.16e shows much higher estimated positon errors up to the 437th second after which it reduces to within +/-0.4° as the estimated bias gradually becomes steadier. Figure 4.16g shows the same trend with the estimated yaw postion errors during the measurement timeout period with the estimated position error growing to ~-3°. As the bias estimate converges to its true value, the position error is observed to reduce to +/-0.4°. Depending on the required accuracy, the duration of time after stoppage to take measurement is important with respect to the frequency of update. For very low measurement update rate, more time is required to enable for more accurate measurement to be made.

Figure 4.18a: Estimated yaw position error with measurement update frequency of 0.2Hz

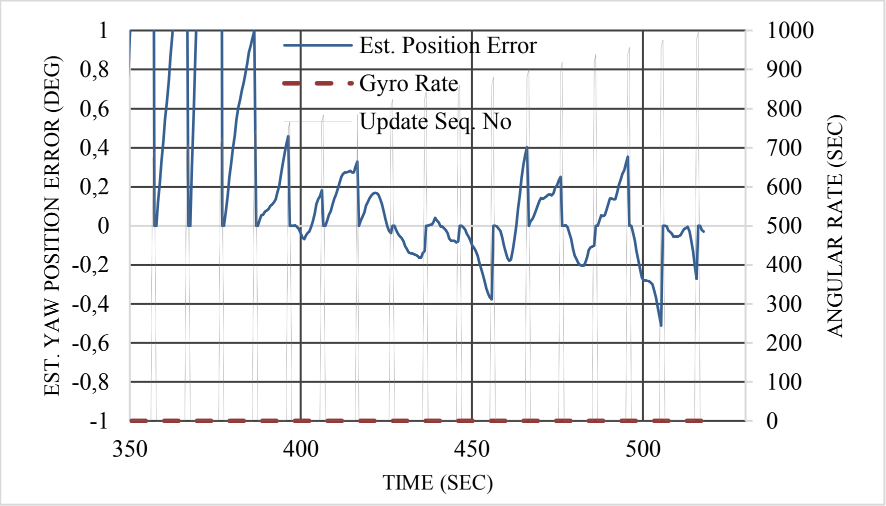

Figure 4.18c: Estimated yaw position error with measurement update frequency of 0.1Hz.

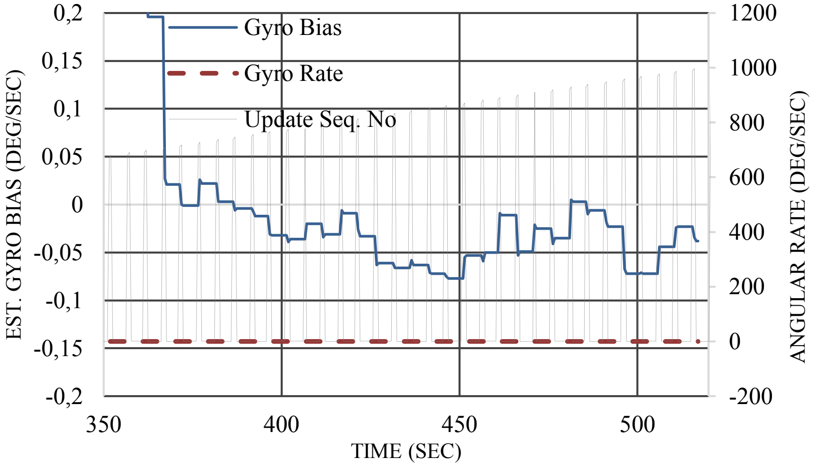

Figure 4.18b: Estimated bias with measurement update frequency of 0.2Hz.

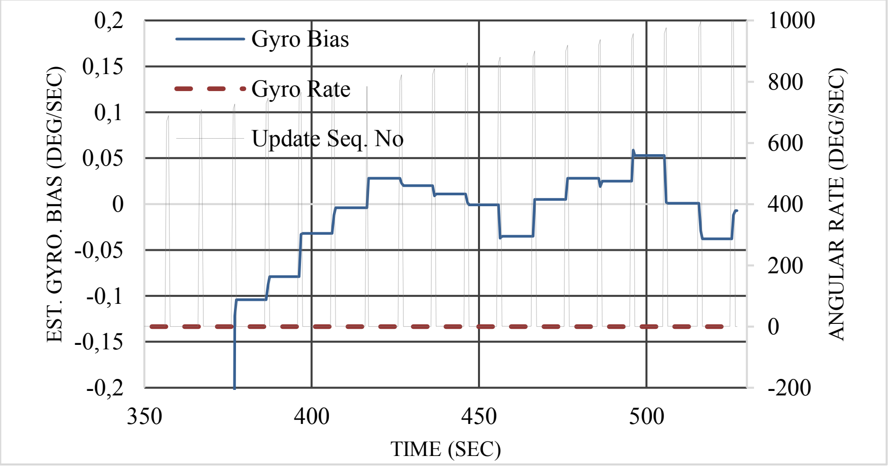

Figure 4.18d: Estimated bBias with measurement update frequency of 0.1Hz.

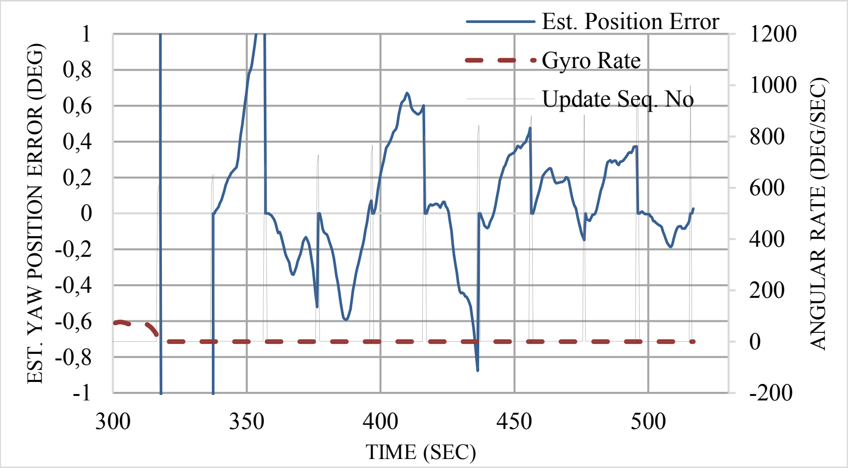

Figure 4.18e: Estimated yaw position error with measurement update frequency of 0.05Hz

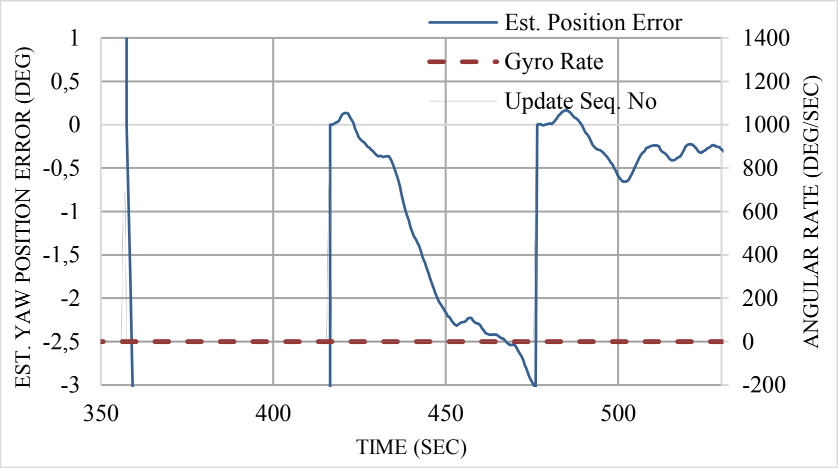

Figure 4.18g: Estimated yaw position error with measurement update frequency of 0.0167Hz

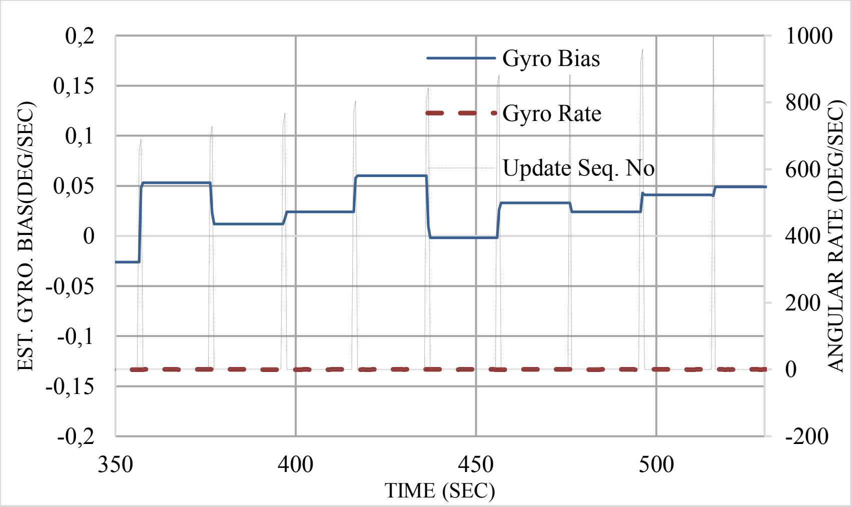

Figure 4.18f: Estimated gyro bias with measurement update frequency of 0.05Hz

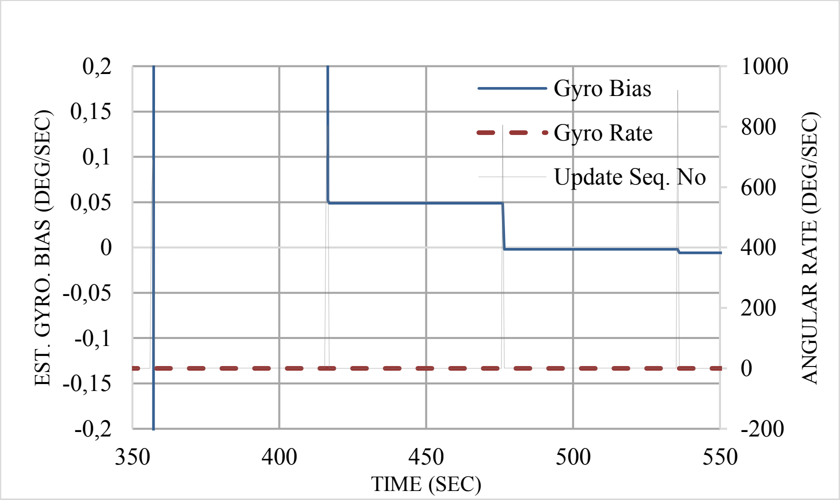

Figure 4.18h: Estimated gyro bias with measurement update frequency of 0.0167Hz

Effect on Azimuth Errors

Figure 4.19 shows the corresponding logarithmic plot of the inclination errors and azimuth errors with increasing measurement update frequency. The azimuth errors are generally higher (averaged at 0.5°) as compared to the measurement mode of continuous updating with interspersed data timeout periods of corresponding data timeout period length and again with the inclination errors independent of the estimated bias observed. Frequencies below 0.03Hz show irregular azimuth errors in addition to the general increase in azimuth error observed. Further analysis for comparison purposes is given in section 4.2.5.

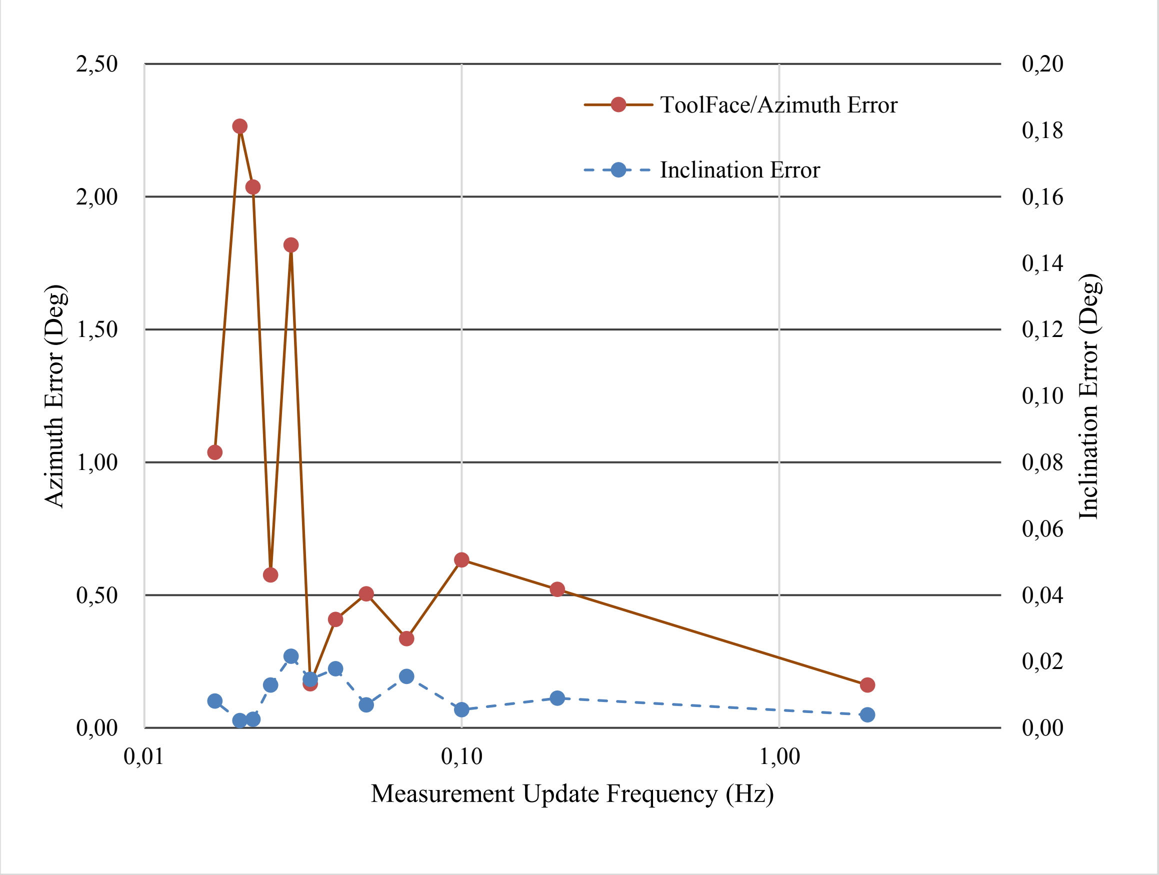

Figure 4.19. Logarithmic plot of the inclination errors and azimuth errors with increasing measurement update frequency

From the graphs in Figures 4.20, MAF refers to the 100-point moving average filter applied to the computed inclination and azimuth output data to remove the high frequency noises to enable for a clean signal to be observed.

Table 4.22 A Summary of Inclination and Azimuth Errors with Increasing Measurement Data Timeout Periods

Measurement Mode	RMS Inclination Error (deg)	RMS Azimuth Error (deg)
Update frequency of 0.2Hz	0.0089	0.5213
Update frequency of 0.1Hz	0.005	0.632
Update frequency of 0.05Hz	0.007	0.504
Update frequency of 0.022Hz	0.003	2.036
Update frequency of 0.02Hz	0.002	2.265
Update frequency of 0.016Hz	0.008	1.037

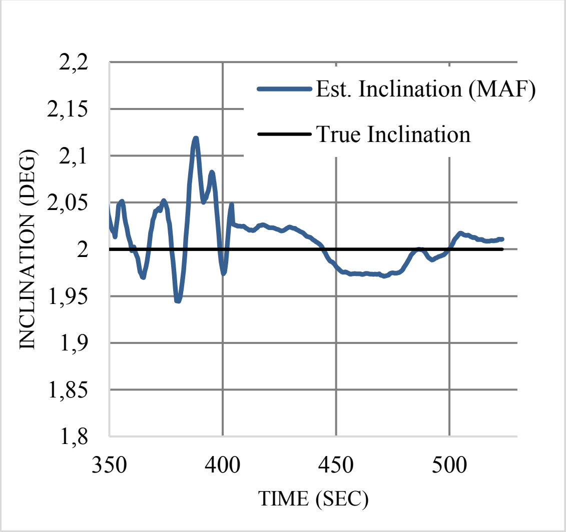

Figure 4.20a: Estimated and true inclination with measurement update frequency of 0.2Hz.

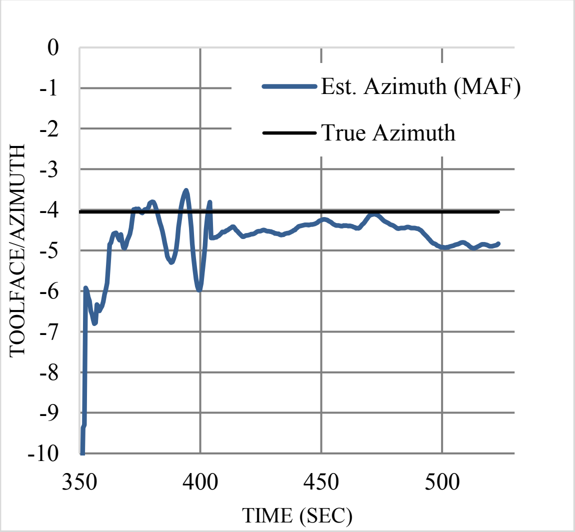

Figure 4.20b: Estimated and true azimuth with measurement update frequency of 0.2Hz.

Figure 4.20a-b shows the estimated inclination and azimuth measurements alongside their true values measurement with update frequency of 0.2Hz for the observation period between 350th to 550th second within which the sensor was at rest (no rotation was taking place) and the system transients had decayed. The root mean square (rms) inclination and azimuth errors are observed to be approximately 0.0089° and 0.5213° respectively.

4.2.2 Multiple Node Measurement Update

The experiment was repeated this time using two nodes for the case of multiple node measurement update. As described in chapter 3, the optimal estimate after the time update period in the top node (node A) was used as the incoming measurement update for node B with the measurement noise covariance equal to the optimal estimate of the error state covariance. This was repeated and showed a azimuth error averaging at 0.4°. The results of the effect on the inclination and azimuth are shown in figures 4.21-22 and Tables 4.24-25. The measurement noise covariance was of negligible change from node A to node B as compared to that of the encoder to node A as the updates from the encoder are highly accurate. This therefore can be approximated to single node updates as in the results of the encoder-single node update.

Measurement Mode	RMS Inclination Error (deg)	RMS Azimuth Error (deg)
measurement update of node A	0.002	0.442
measurement update of node B	0.027	0.761

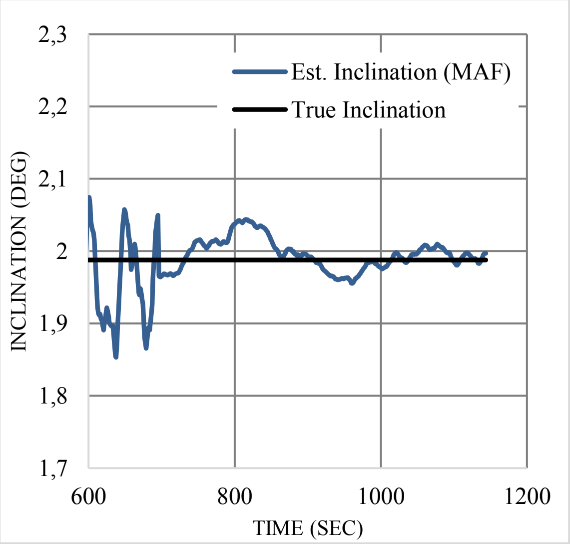

Figure 4.21: Estimated and true inclination with measurement update of node A with update frequency of 0.8Hz.

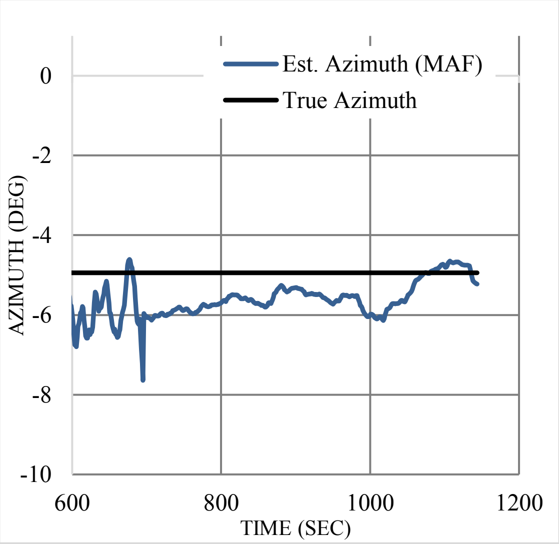

Figure 4.22: Estimated and true azimuth with measurement update of node A with update frequency of 0.8Hz.

Figure 4.21-4.22 shows the Estimated and True Inclination and Azimuth errors with measurement update frequency of 0.8Hz for the observation period between the 600th to 1150th seconds within which the sensor was at rest (no rotation was taking place). The root mean square (rms) inclination and azimuth errors are observed to be approximately 0.002° and 0,442° respectively.

4.2.3 Results Analysis

This section provides a prelude for the basis of comparison of the azimuth results to that of the one defined by the ISCWA. In the case of the magnetic based survey measurement systems used in wellbore surveying, the metallic drill string together with its rotation action causes the drill string to be magnetized in the direction along the drill string axis and consequently, locally influences the earth's magnetic field thereby corrupting the horizontal component of the earth's magnetic field [30]. This makes it difficult to accurately measure the magnetic azimuth. Therefore, further measures such as the insertion of non-magnetic drill collars (NMDC) into the drill string are usually taken to reduce this magnetic effect for better magnetic azimuth measurement. The magnetic interference azimuth error as described by the ISCWSA, is of the order of 0.25° + 0.6 x sin I x sin A which implies that higher azimuth errors are obtained with navigation at higher inclination towards the eastern or western directions, see graph in figure 4.23. The ISCWSA determines an acceptable azimuth accuracy to be 0.25°, when employing the use of a non-magnetic drill collars for reducing the magnetic interference of the drill string in the determination of the azimuth. For standard MWD, the azimuth error uncertainty is prefered to be 0.36° [30]. However, to achieve such acceptable or a defined azimuth error limit, the use of NMDC length selection charts are required for various wellbore inclinations and azimuths for a maximum acceptable azimuth error [30]. Figure 4.23 shows the corresponding azimuth error with increasing inclination angle when drilling is done towards the eastern direction using the magnetic north navigation frame system. In this situation, the azimuth error is observed to increase linearly with increase in the inclination, which therefore requires extra effort of the use of the NMDC to reduce the magnetic influence. The results of the experiments conducted shows an improved azimuth accuracy, better than 0.25°, with a measurement update rate of 1Hz or greater as shown in figure 4.17. However, having continuous measurement updates as in the case with 20s of 1.9Hz continuous measurement update frequency interspersed with 10s through 30s data timeout periods generally showed a better azimuth performance with root mean square azimuth errors averaging at approximately 0.35° as compared to single measurement updates with decreasing update frequencies as in the case of frequencies at 0.05Hz, 0.1Hz and 0.2Hz which have azimuth errors averaging at approximately 0.5°. The azimuth error here is consistent and independent of the direction of drilling with respect to the geographical east or west. An advantage with this scheme is that there is no need for the use of NMDC as the azimuth errors are independent of the inclination or azimuth measurements.

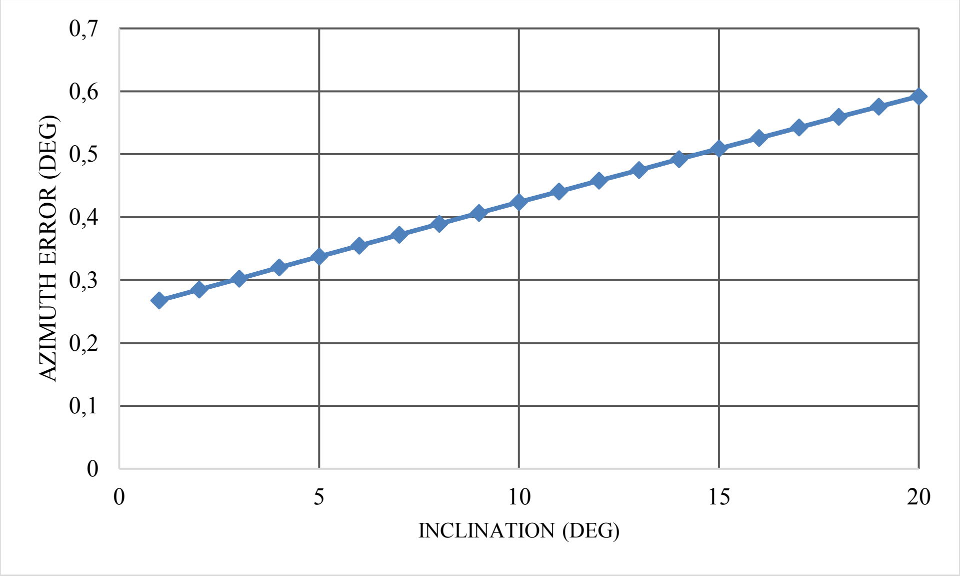

Figure 4.23: The azimuth error assuming drilling in the eastern direction (azimuth =090°) with increasing inclination (ISCWSA).

4.2.4 Effect on the Region of Uncertainties in Error at the Various Survey Stations Along the Wellbore Path.

A further observation is made on how the improved azimuth error affects the region of uncertainty in error at the various survey stations given in tables 4.1-2. Considering the MPU6500 and utilizing the error model defined by ISCWSA; the standard deviation error of the region of uncertainty and an azimuth error of 0.25° is used to plot the graphs in Figures 4.24-27 showing the improvement in the region of uncertainty error in the position survey measurement using the filtered output using the described indirect Kalman filter scheme in comparison to the unfiltered output. In effect, at each survey station, the contribution of the azimuth error is 0.25° and is used in the computation of the region of uncertainty in error of the B- and A-axis displacements at each survey station as a replacement of the product of the weighting function and the error magnitude relating to the gyroscope angle random walk and bias instability. From the standard deviation error in the region of uncertainty plot of WELLBORE 1 shown in figure 4.24, it is observed that after the third survey station (SS3) the region of uncertainty in error of the filtered outputs shows an improvement as compared to the unfiltered output case. It shows to converge to a constant value as the number of survey station increases. On the B-axis the region of uncertainty in error shows improvement after the fifth station and approaches a fixed value of about 9 cm. At the final station there is ~9.5-fold improvement; ~9.2cm for the filtered output as compared to 87cm for unfiltered output, for the B-axis displacement error while for the A-axis displacement error, there is a 1.5-fold improvement; ~39.2cm for the filtered output as compared to ~58cm for the unfiltered output.

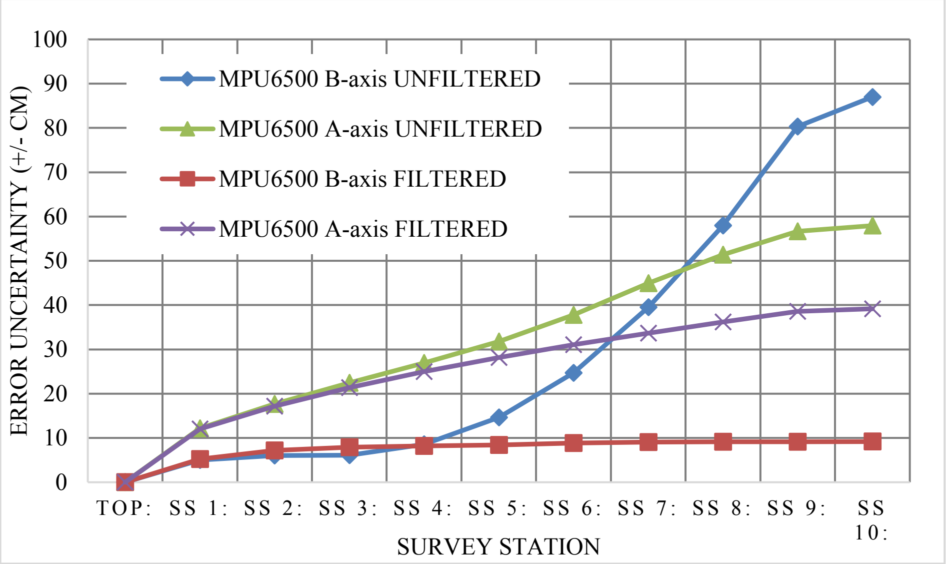

Figure 4.24: WELLBORE 1: The comparison of the filtered and unfiltered estimated standard deviation error uncertainty for B- and A- axis displacements for the low-cost MPU6500 IMU Sensor.

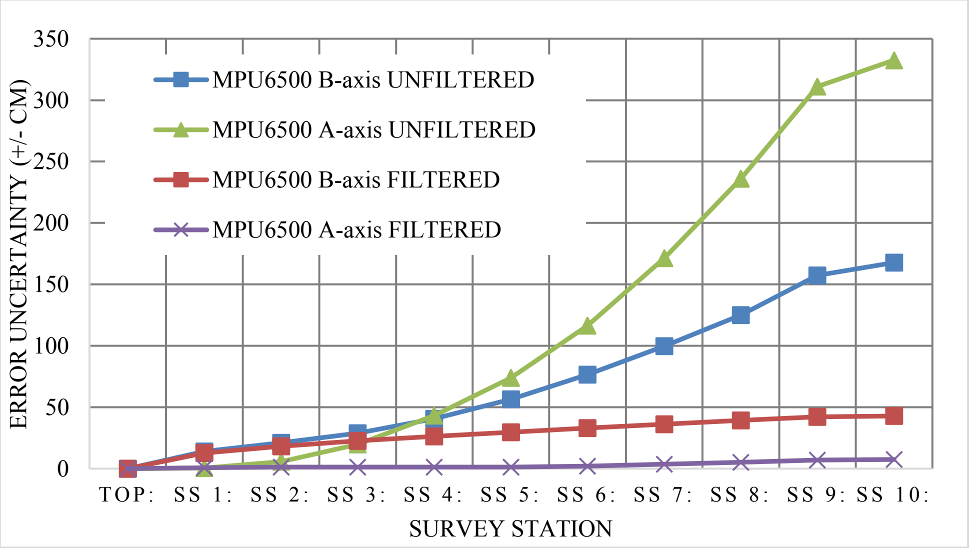

Figure 4.25: WELLBORE 2: The comparison of the filtered and unfiltered estimated standard deviation error uncertainty for B- and A- axis displacements for the low-cost MPU6500 IMU Sensor.

Figure 4.25 shows the improvement of the standard deviation error of uncertainty for the B- and A- axes displacement for the case of WELLBORE 2 trajectory using the MPU6500 IMU sensor. Again, a convergence to a constant value as the number of survey station increases is observed. A 3.9-fold improvement is observed in the B-axis standard deviation error in displacement; ~43 cm for filtered data as compared to ~168cm for unfiltered data, while an ~44.5-fold reduction is observed for the A-axis deviation; ~7.5cm for filtered data as compared to ~333cm for unfiltered data.

An extension of the azimuth error results from the MPU6500 sensors, an application of the improved azimuth error is used in the re-computation of the Vectornav-100T error uncertainties. The Vectornav-100T, regarding its performance specifications, theoretically has a lower azimuth error than that of the MPU6500 IMU sensor. The first standard deviation error uncertainty at each survey station is computed with an azimuth error of 0.25° replacing the product of the weighting function and the error source. In this case, an improvement in the uncertainty for both the B- and A-axis is observed from the second survey station (SS") onwards. An ~4.7-fold improvement in the B-axis displacement error of uncertainty is observed in the B-axis; 7.11cm for filtered data as compared to 33.2cm for unfiltered data, while an ~3.8-fold increase is observed for the A-axis deviation;2.4cm for filtered data as compared to 9.18cm for unfiltered data as shown on the graph of figure 4.26.

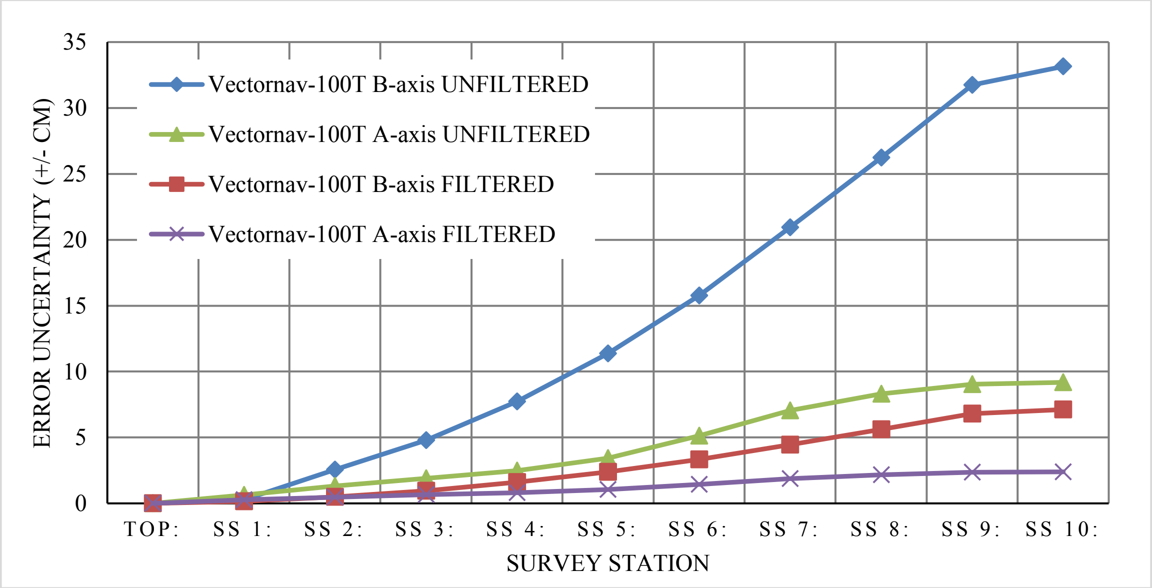

Figure 4.26: WELLBORE 1: The comparison of the filtered and unfiltered estimated first standard deviation error of uncertainty for B- and A- axis displacements for the low-cost MPU6500 IMU Sensor.

Figure 4.27 shows the improvement for the standard deviation region of uncertainty in error for the B- and A- axes displacement for the case of WELLBORE 2 trajectory using the Vectornav-100T IMU sensor. As before, a convergence to a constant value as the number of survey stations increases is observed. A ~4.4-fold reduction is observed in the B-axis second standard deviation error; ~11cm for filtered output data as compared to ~50cm for unfiltered output data, while an approximately 4.6-fold reduction is observed for the A-axis uncertainty; ~27.4cm for filtered output data as compared to ~126cm for unfiltered output data. The asymtotical approach towards a constant value is due to the constant azimuth errors because of using the filter.

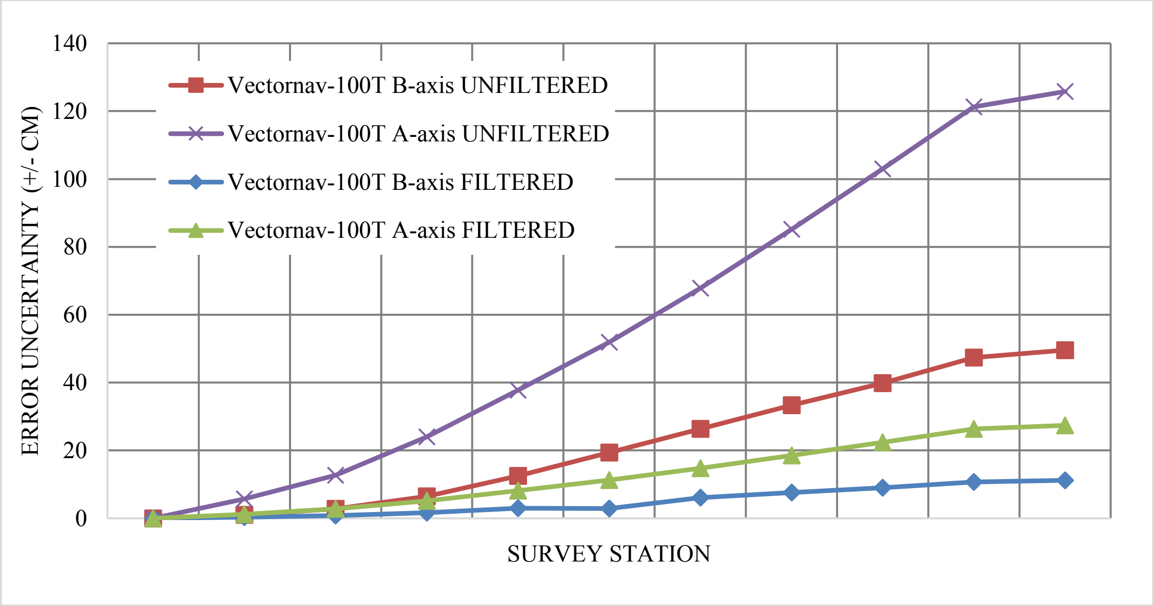

Figure 4.27: WELLBORE 2: The comparison of the filtered and unfiltered estimated second standard deviation error of uncertainty for B- and A- axis displacements for the low-cost MPU6500 IMU Sensor.

In summary, this chapter basically looked at the application of the ISCWSA error model in the determination of the region of uncertainty in error when using key survey instrument measurement tools to establish the accuracy of recorded wellbore trajectory. It looked at actual data recorded in the field to determine the ellipsoid of uncertainty given as the two times the standard deviation of the survey position errors (north, east and true vertical depth) in a designated frame of reference at each survey station. It is based on the performance specification of the sensors used in the measuring tools and given by the manufacturer of the respective sensors used within these tools. It shows how the error sources attributed to the physical sensor translates to the survey measurement errors in terms of the azimuth, inclination and measured depth errors which subsequently effect the survey position errors (north, east and true vertical depth) with the assumption that there is no human influenced errors involved.

On applying the error model computation to some named sensors, it was generally observed that there is a strong correlation between the sensor performance specifications and the region of uncertainty in error of which of significance is the error source due to gyroscope drift. This is manifested by its higher contribution to the region of uncertainty in error in the northern and eastern directions. This is obvious in the analysis with the Vectornav-100T and the STIM300 sensors when no processing is used. The IPST-RQH, which is a fiber-optic gyroscope with very good angle random walk and bias instability specifications shows a better region of uncertainty in error as compared to the MEMS based Vectornav-100T and STIM300 sensors as well as the digital inclinometer probe which consists of a 2-axis MEMs accelerometer. The drawback of which is the extremely high costs and difficulty in its adaptation to the application at hand (implementation within the drill tube). The digital inclinometer probe has no gyroscope and measurements are made in a fixed fame of reference by way of a fixed orthogonal A and B axis frame and therefore shows a better region of uncertainty in error as compared to the other two MEMS sensors. However, due to errors attributed to cable stretch, it is shown to have the worst error uncertainty in the true vertical depth direction in the designated frame of reference.

Secondly, an experiment was conducted to investigate the effect of running the indirect Kalman filter in the feed-forward configuration on a low-cost MEMS IMU gyroscopic sensor with worse performance specifications when compared with the aforementioned IMU sensors. To highlight the resulting improvement, the ISCWSA error model was applied to investigate the region of uncertainty in error associated with using this sensor in the absence of any processing. A description of the experiemental setup was given to show the determination of the noise characteristic of the sensor; its accuracy and precision, which was subsequently used in the model equation used for the Kalman filter to estimate the yaw position of the sensor within the drill tube. The results from the outcome of the experiment shows the improvement in the estimation of the sensor yaw position which translates into improved azimuth accuracy by way of reduced azimuth errors and consequently, improved survey position estimate. it discussed two different measurement update modes considered which includes the continuous measurement update mode interspersed with data timeout periods and single measurement update modes at varying frequencies. The results from the former are observed to be more favourable for a given range of interspersed data timeout periods and generally of better performance in terms of lower azimuth errors as compared to the single measurement updates at varying frequencies within the context of the borehole telemetry system. A further comparison of the results was made with that considered acceptable by the ISCWSA standardization committee. It shows an improvement in general in the sense of the listed below:

1. Reduced survey position error uncertainty especially when drilling is performed towards the eastern or western directions.
2. Position errors, because of using the indirect Kalman filter, in the northern and eastern directions show a convergence asymptotically towards a constant value as the number of survey stations increase since the gyro drift is removed.
3. There is no need for the implementation of the non-magnetic drill colars (NMDC) to mitigate the effects of earth magnetic field components induced along the drilling string which influences the accuracy of magnetic based survey sensors.

4. Due to the need to record measurements at stationary positions and coupled with relatively low dynamics due to relatively slow rotations during drilling, the measurement update rate and time update rate can be decreased effectively thereby reducing network overhead and improving battery life. Furthermore, it enables making a continuous measurement update system feasible which is shown in the experiment to be of better performance wih regards to improvement of the resulting survey position uncertainty errors.

4.3 Probabilistc Approach using Weighting Functions

A trajectory is designed to have four survey stations as shown in figure 3.7. Each of the tubes is fitted with a cluster of four identical sensors and the output of these four sensors statistically combined as explained in sections 3.6 and 3.7 to obtain the estimated survey measurements; inclination and azimuth. The survey measurements are made sequentially as each tube is inserted after the previous has completely entered the ground. Measurements are combined using the weighted average means as elaborated in section 3.7. The measurements are recorded at the following times; t_1, t_2 , t_3 and t_4 as illustrated in the table 4.26.

Table 4.26: A summary of the sequential measurement scheme of the various survey stations showing the measurement times; the previous or old measurements, the new measurement in the ideal case that represents the ground truth, and the actual measurement recorded after combination with previous measurements.

	SS1	**SS2**	**SS3**	**SS4**
Survey Measurement Times	t_1 t_2 t_3 t_4	t_2 t_3 t_4	t_3 t_4	t_4
Combined previous measurements with equal weights used in the weighted average	A_1^o B_1^o C_1^o D_1^o	A_2^o B_2^o C_2^o	A_3^o B_3^o	A_4^o
New Measurement: Ideal Case Equal weight given to all measurement (New trajectory assuming all measurements picked new changeds: Ground Truth)	A_1^N B_1^N C_1^N D_1^N	A_2^N B_2^N C_2^N	A_3^N B_3^N	A_4^N
Actual Measurement Recorded: Change detected only by clusters with measurements at t_4	A_1^o B_1^o C_1^o D_1^N	A_2^o B_2^o C_2^N	A_3^o B_3^N	A_4^N

In table 4.26, A_1^o denotes the sensor cluster A where the subscript represents the survey station number, the superscript denotes measurement category; that is either the previous combined measurement depicted as “o” at observation times t_1, t_2 and t_3 or depicted as “N” which represents the new measurement at t_4. This representation follows for the clusters B, C and D.

Let $\vec{M}_x$ be the new position measurement vector; north, east and true vertical depth, in the ideal case assuming all the clusters always picked up the new change; and represents the ground truth. Then we let $\hat{\vec{M}}_x$ be the actual measurements recorded because of the combined previous measurements and the current measurement at t_4 where the change in trajectory was picked up. The change in trajectory is because of a change in the survey measurement at survey station 2 (SS2). The basis for investigation is centered around the error matrix (covariance matrix) R which is given as

$$R = (\vec{M}_x - \hat{\vec{M}}_x) \cdot (\vec{M}_x - \hat{\vec{M}}_x)^{\mathrm{T}} \qquad (4.16)$$

The square root of the diagonal components which represents the first standard deviation of the error in the north, east and true vertical depth is used. The error trend is investigated by keeping all measurements constant while slowly varying the inclination in steps of 0.5° to observe the effect of the error in the resultant combined measurement; using equal weights for previous and current sensor measurements, on the error in the position measurement with increasing inclination. A similar investigation is done for the azimuth which is also varied in steps of 5° to observe the effect of the error in measurement, also using equal weights for previous and current sensor measurements, on the error in the position measurement with increasing azimuth. The results of which is used to advise on the appropriate weighting ratio to assign to previous and current survey measurements for a good estimate of the survey position measurement at the survey station of interest. It should be noted that this is more of using heurestics and not using the least square estimate method as mentioned in chapter 2. Table 4.27 shows the performance specifications of the 4 identical sensors used in a single sensor cluster.

Table 4.27: A summary of the performance specification of the IMU sensor

	Parameter	**Value**
Bias Instability (0.04mg) => 0.0023° deviation	f_{xy}^{bias}	4.99611 x 10^{-4} m/s^2
”	f_{z}^{bias}	1.2722 x 10^{-8} m/s^2
Linearity <0.5% Full Scale	$f^{S.F.error}$	8.0 x 10^{-3}
Misalignment (calibrated out normally)	$f^{Misalignment}$	0.05 x 10^{-4} °
Azimuth Error Contribution		0.25°

An arbitrary trajectory is then chosen as shown in Table 4.28 below with the respective measured depth, inclination and azimuth given respectively.

Table 4.28: A summary of the survey measurements from the welltop through to survey station 4

Survey Station	Measured Depth (m)	Inclination (°)	Azimuth (°)
Well Top	0	0	0
SS1	2	1	120
SS2	4	1	120
SS3	6	1	120
SS4	8	1	120

The balanced tangential method (see Appendix IV) for wellbore path determination is used to generate the respective changes in the north east and vertical depth position at each survey station. This is shown in the table 4.29.

Table 4.29: A summary of the conversion of the change in the north, east and TVD using the balanced tangential method.

Survey Station	Change North ΔN (cm)	Change East ΔE (cm)	Change in Depth ΔTVD (cm)
Well Top	0	0	0
SS1	-0.87	1.511	2
SS2	-1.75	0.64	2
SS3	-1.75	0.64	2
SS4	-1.75	0.64	2

As mentioned earlier, the inclination in SS2 is increased in steps of 0.5 to simulate a change in inclination at the measurement time t_4 which is only picked up by the clusters at all stations at that measurement time but however incorporated in the resultant estimated survey measurements made by combining previous measurements at each survey station recorded to obtain the actual measurement.

The graphs in figures 4.28a-c show how the error of uncertainty is reduced using increasing number of sensors in a single cluster after statistically combination explained in section 3.6.

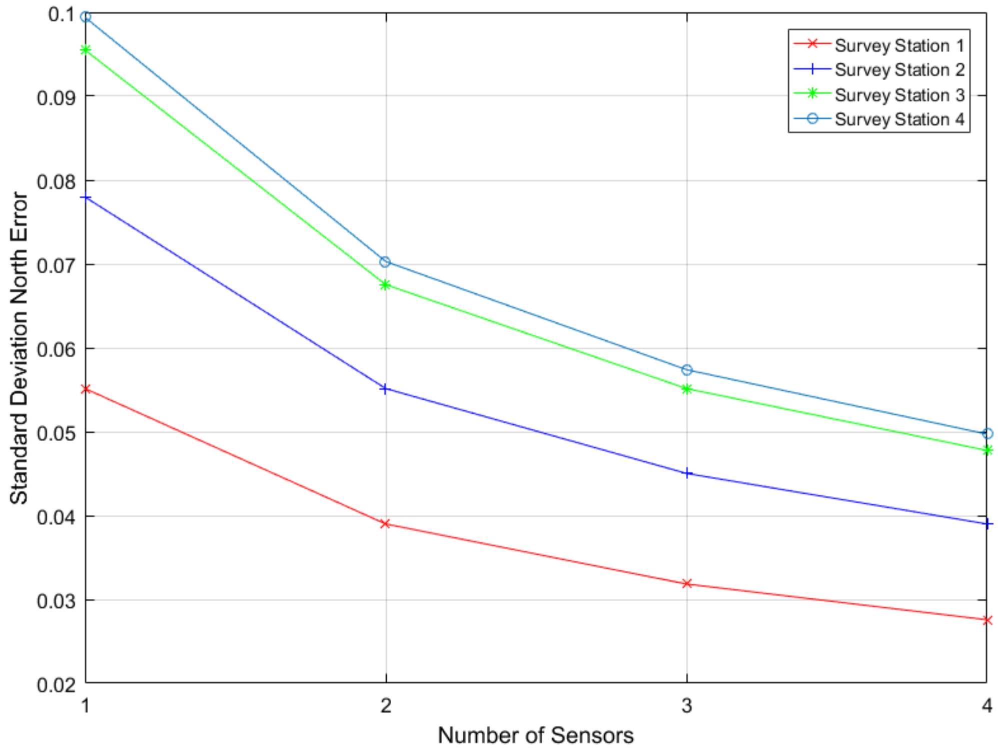

Figure 4.28a: The standard deviation north error for increasing combination of sensor within a cluster at each survey station

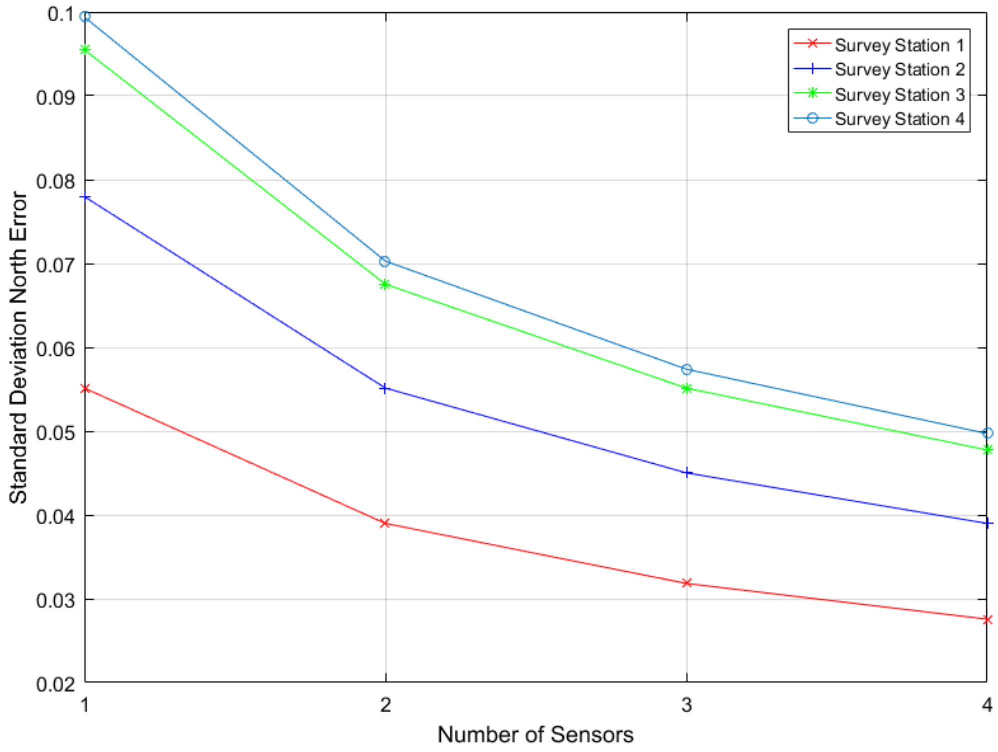

Figure 4.28b: The standard deviation east error for increasing combination of sensor within a cluster at each survey station

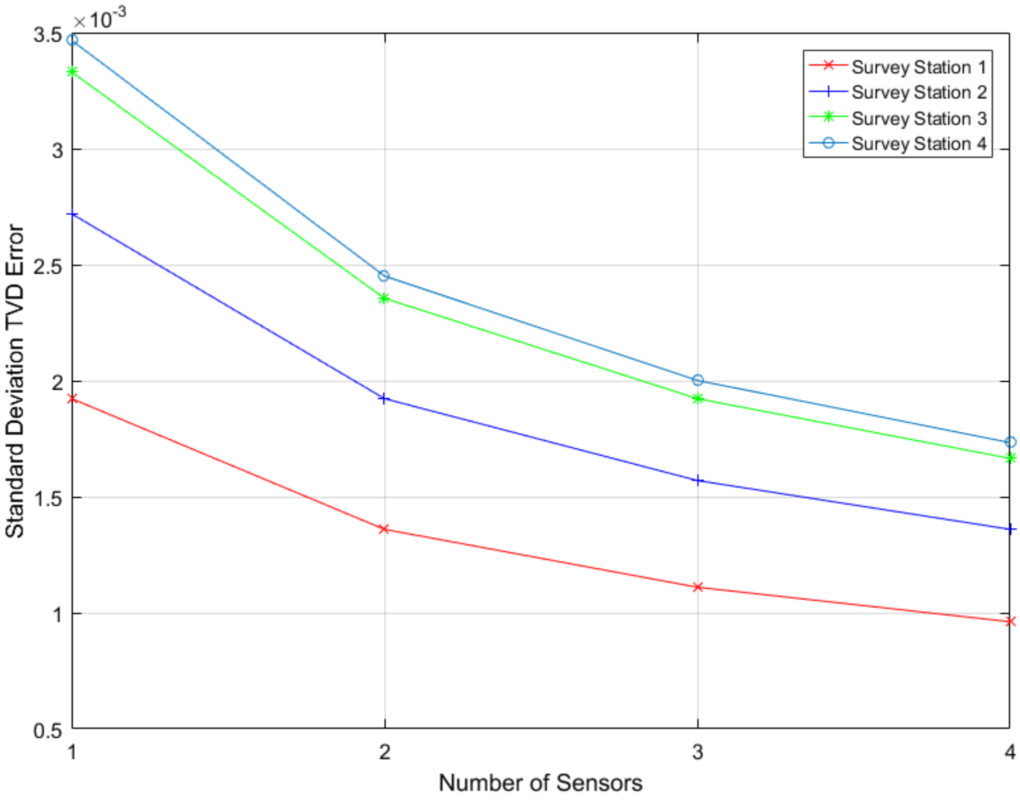

Figure 4.28c: The standard deviation in TVD error for increasing combination of sensor within a cluster at each survey station.

The survey measurements at survey stations 1, 3 and 4 are held constant while the measured inclination for survey station 2 is varied stepwise of 0.5° from 1° to 10° to observe the effect of the error because of combining the previous measurements and the current measurement using equal weights. The next is the variation of the azimuth also at survey station 2 by increments of 5° from 120° to 200° so as the observe the variation of the errors whiles the survey measurements at other stations are also kept constant.

The graphs in figures 4.29a-f show the results of the measurements as described in Table 4.29. The north position change shows the previous measurement trajectory for survey stations 1 through to 4. The ground truth which is the true measurement as explained earlier, is represented by the blue graph in figures 4.28a-c which is the "best" estimate of the true trajectory after the change in the inclination angle at SS2. The green graph, also in figures 4.29a-c, shows the actual measurement recorded after the combination with the previous measurements using equal weighted averaging. The graph, also in figures 4.29a-c, shows the recording of the sensors before the change in survey measurements in SS2 occurred. So basically, figure 4.29d shows errors in the north position of ~1.18cm and ~0.85cm in survey stations 2 and 3 respectively for an inclination increase of 2° at survey station 2. The corresponding errors in the east position, shown in figure 4.29e, is ~ 2cm and ~0.8cm in the survey stations 2 and 3 respectively with the same inclination angle. Finally, the TVD position; figure 4.28f, shows errors of 0.08cm and 0.06cm in the same respective survey positions for the same inclination displacement. These same measurement scenario is done for the mentioned inclination increments as well as similar such recordings for the azimuth measurement increments at the same survey station 2. A plot of the error trend ploted graphically in figures 4.29-33.

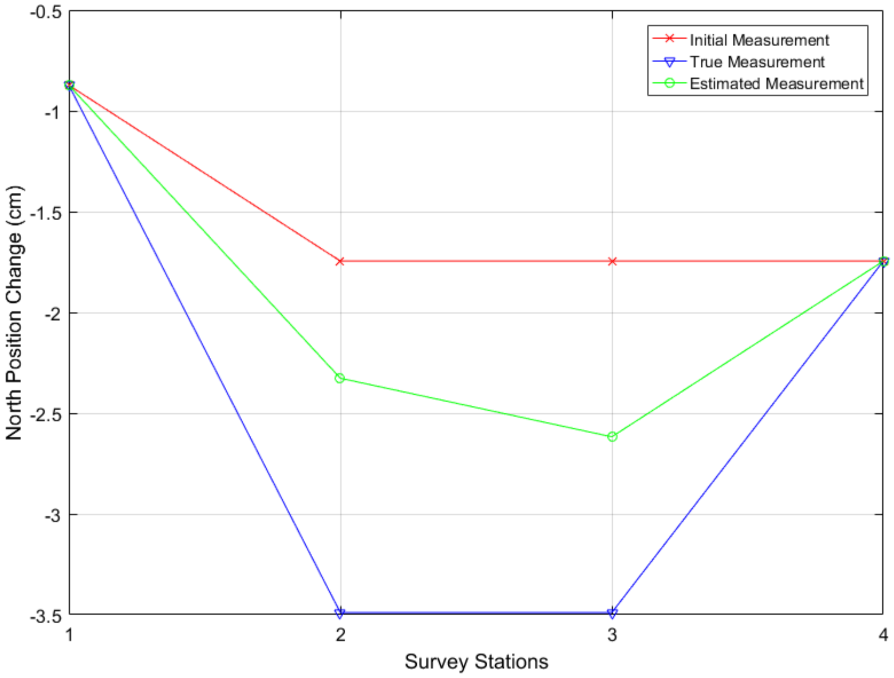

Figure 4.29a: The north position change for the old trajectory, new trajectory and the estimated trajectory measured

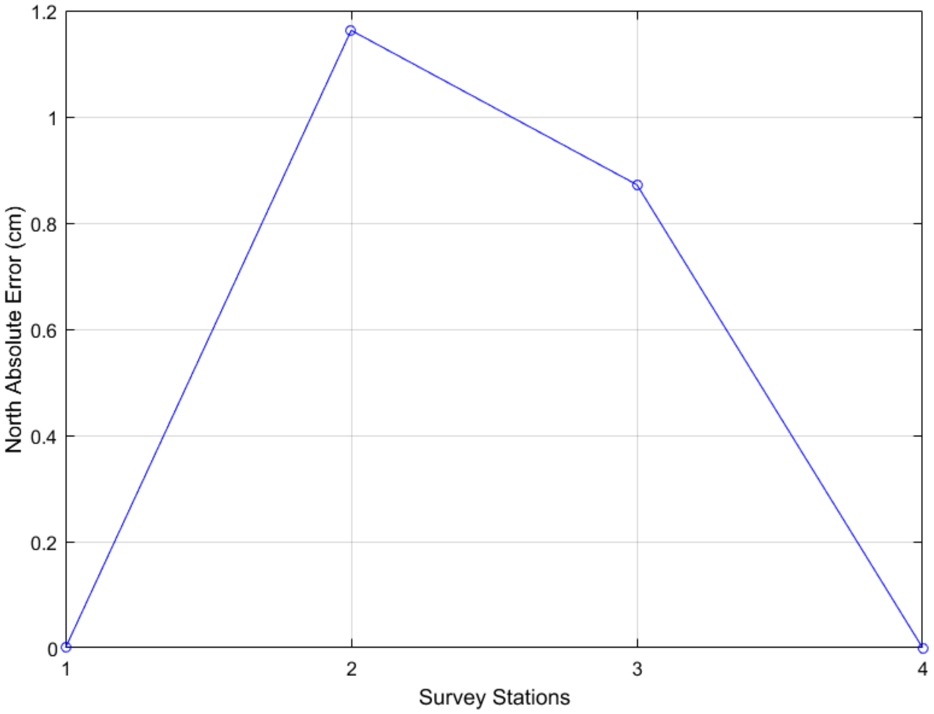

Figure 4.29d: The north absolute error due to the difference between the true trajectory and the estimated trajectory measure

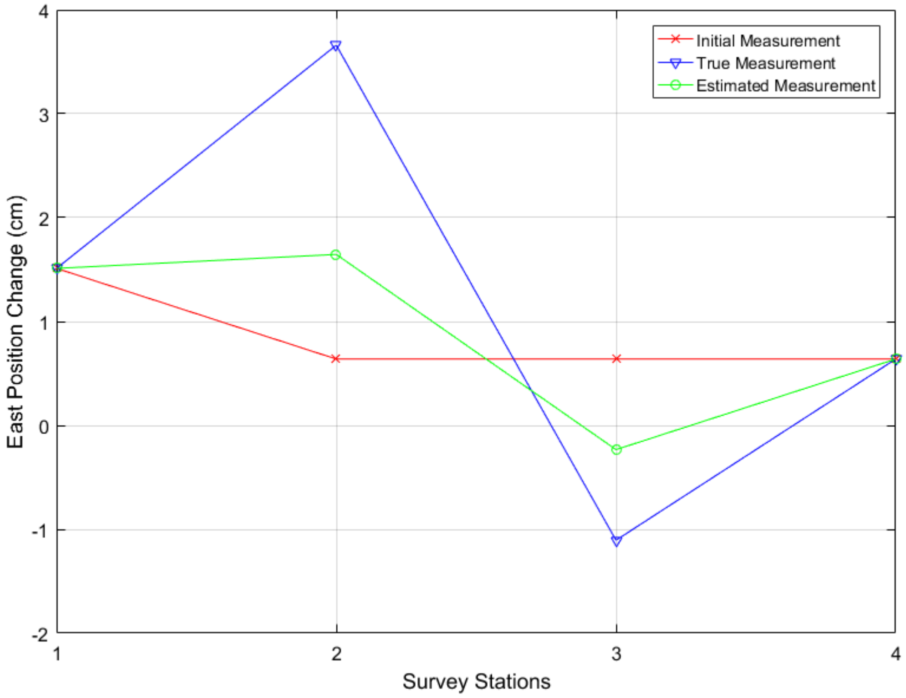

Figure 4.29b: The east position change for the old trajectory, new trajectory and the estimated trajectory measured

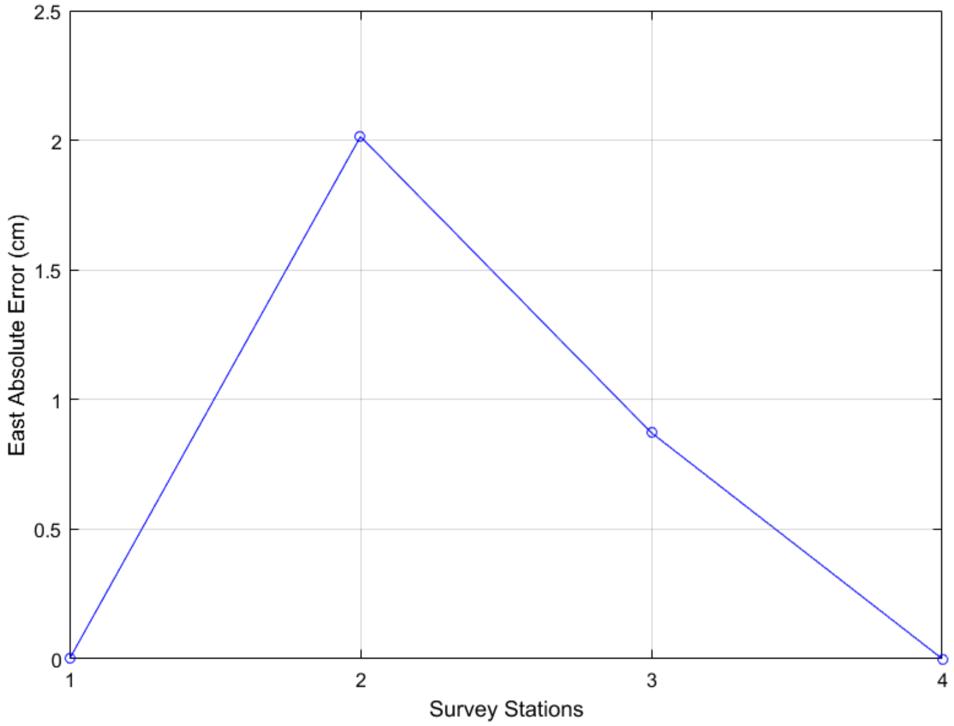

Figure 4.29e: The east absolute error due to the difference between the true trajectory and the estimated trajectory measure

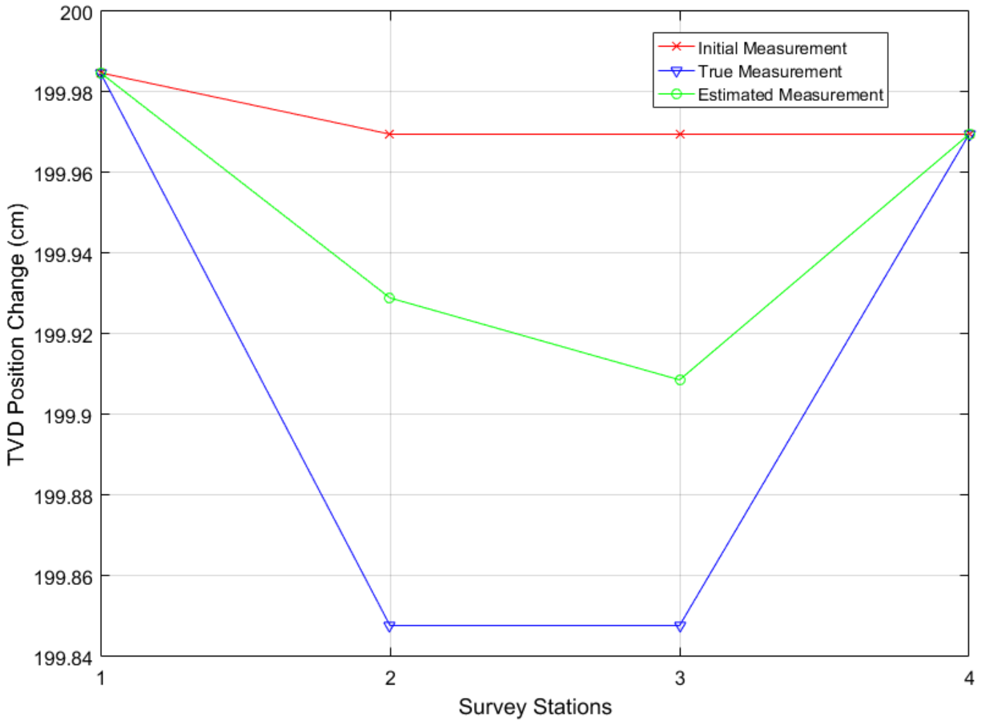

Figure 4.29c: The TVD position change for the old trajectory, new trajectory and the estimated trajectory measured

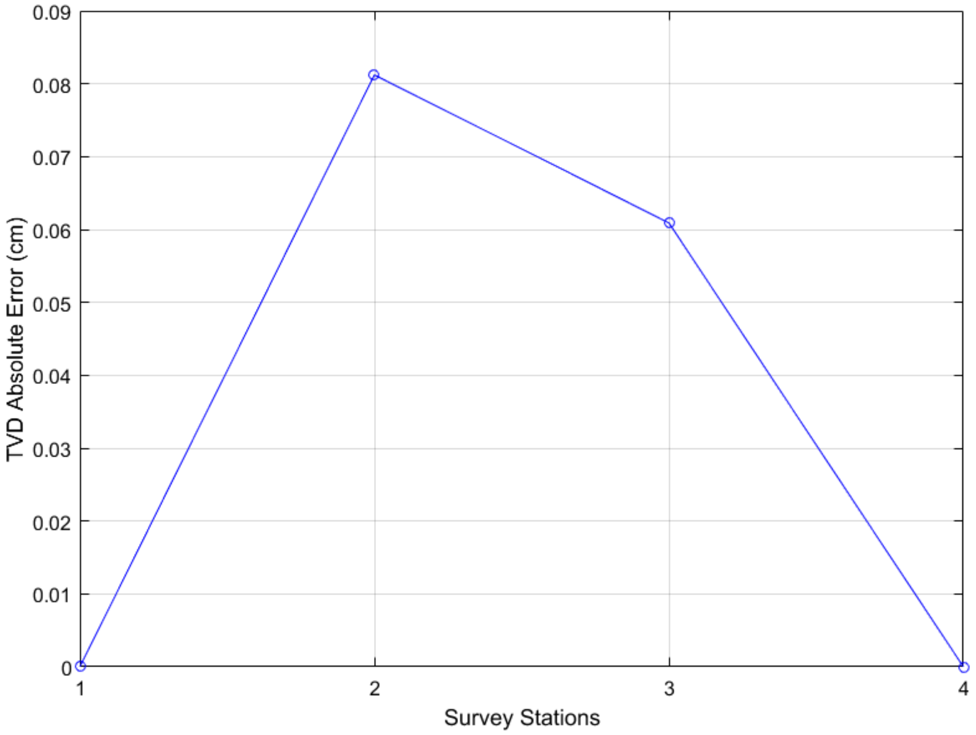

Figure 4.29f: The TVD absolute error due to the difference between the true trajectory and the estimated trajectory measure

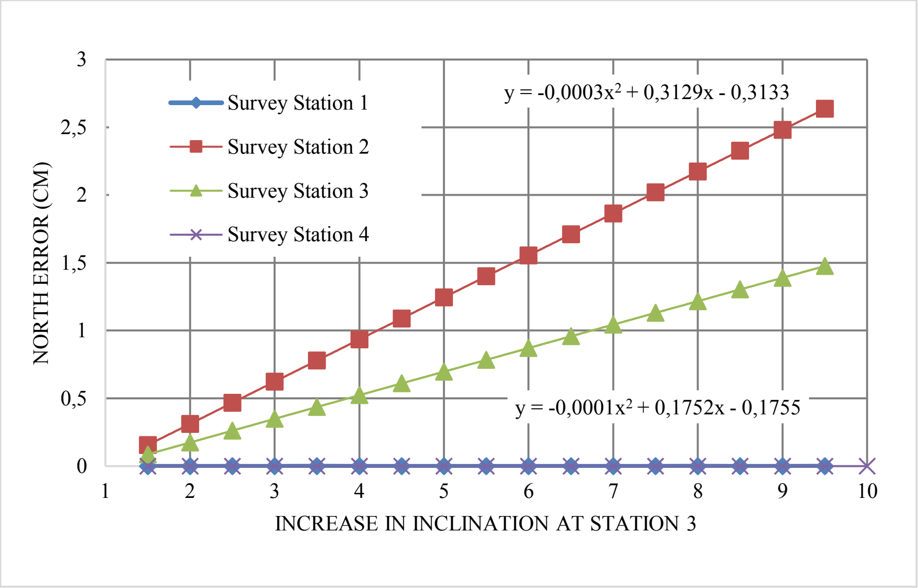

Figure 4.30: The error in north position due to increasing inclination at survey station 3

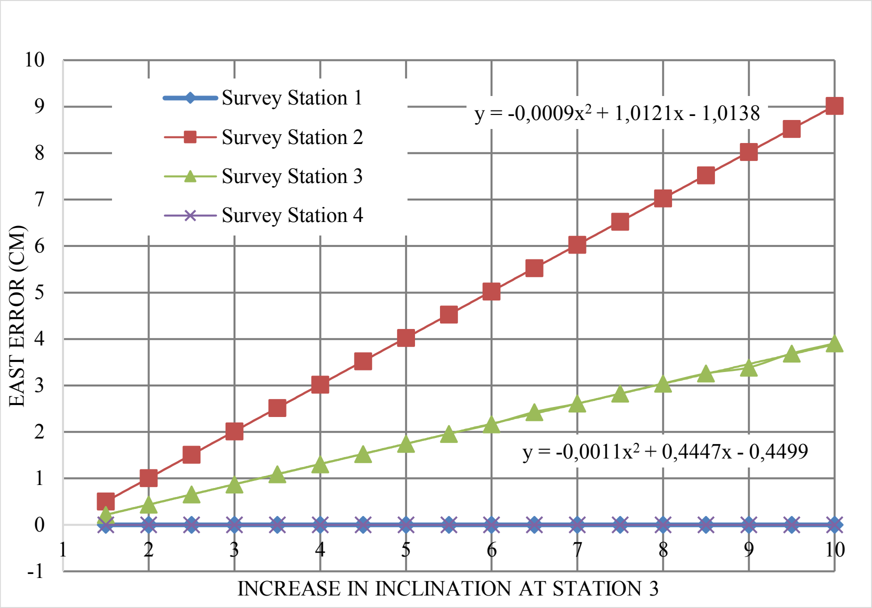

Figure 4.31: The error in east position due to increasing inclination at survey station 3

So basically, figures 4.30-31 show a scaled quadratic increase in the errors observed with the best fit quadratic equation also given for the absolute errors recorded for all stations as a function of increasing inclination angle in the north and east position respectively. It is further observed that negligible errors occur in the first station, SS1 and the 4th stations SS4, for both the northern and eastern positions. The errors basically show a significant effect on survey station 3 although lower in magnitiude for the corresponding absolute error in survey station 2. overall, for a given increase in inclination, the north position error is less than the east position error.

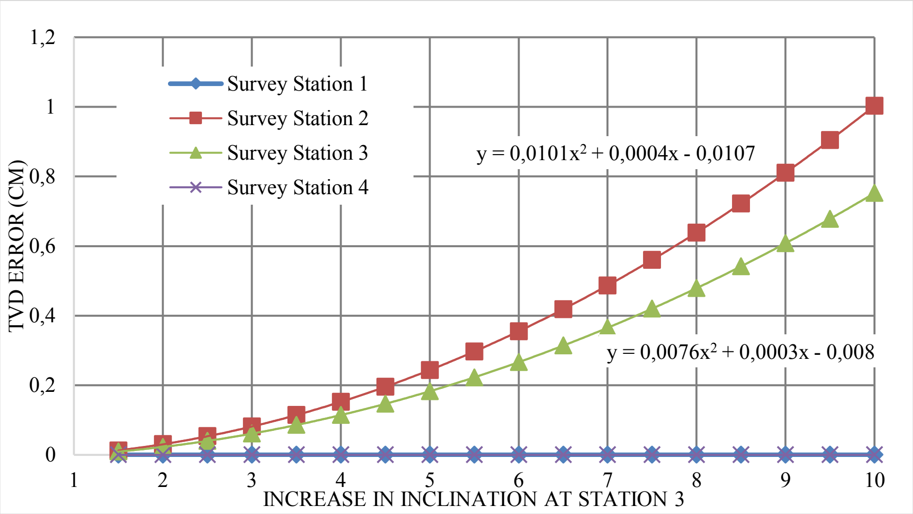

Figure 4.32: The error in TVD position due to increasing inclination at survey station 3

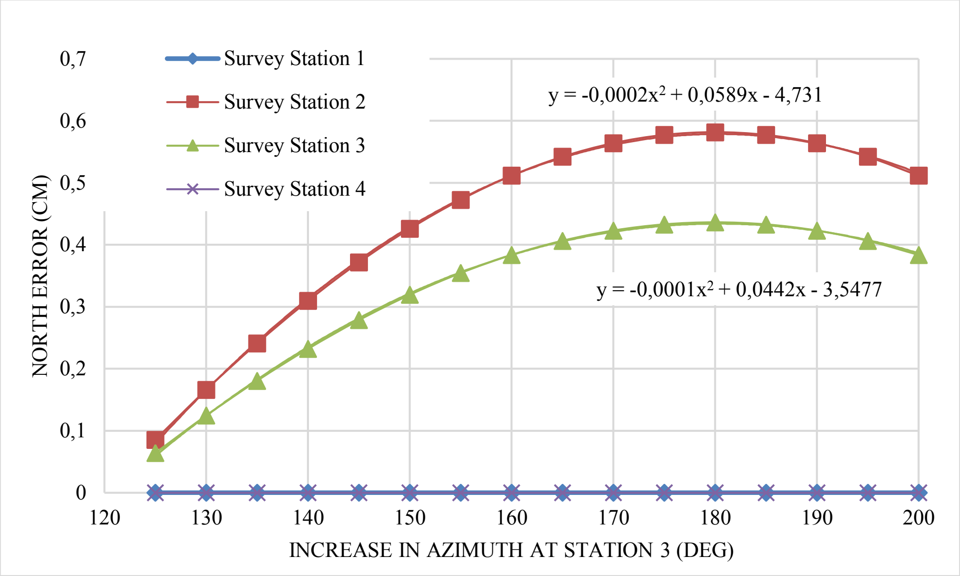

Figure 4.33: The error in north position due to increasing inclination at survey station 3

Figure 4.32-33 show the scaled quadratic increase in the errors in the TVD also with the best fit quadratic equation as in the case of the north and east position errors but with a much lower overall error value as compared to those for the north and east positions. Figure 1 below shows negative scaled quadratic increase in errors at survey stations 2 and 3 with increasing azimuth at survey station 3. Again, errors in survey stations 1 and 4 are observed to be negligible.

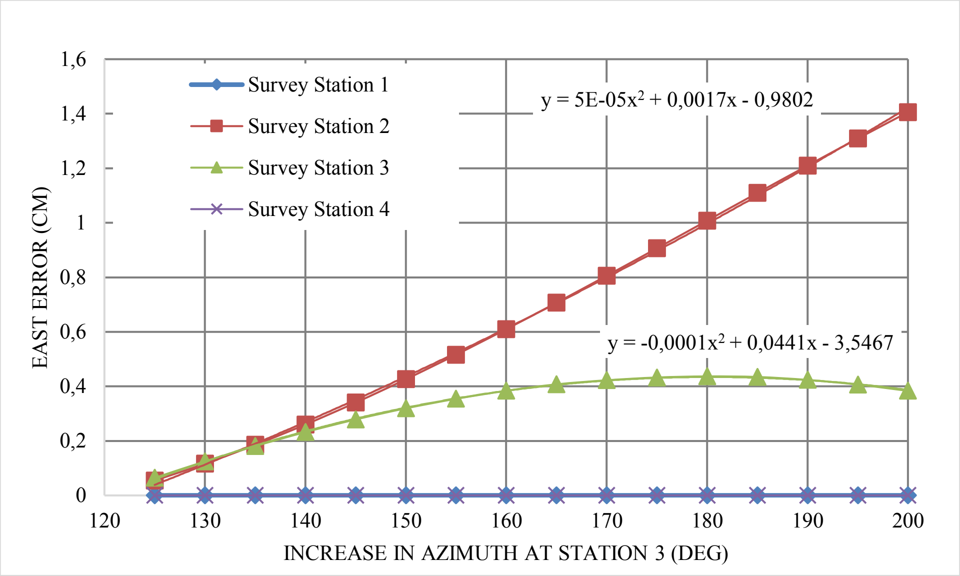

Figure 4.33: The error in east position due to increasing inclination at survey station 3

Figure 4.34 above again shows the error in the east position with again the scaled quadratic increase in position error at survey stations 2 and 3 respectively with increasing azimuth error

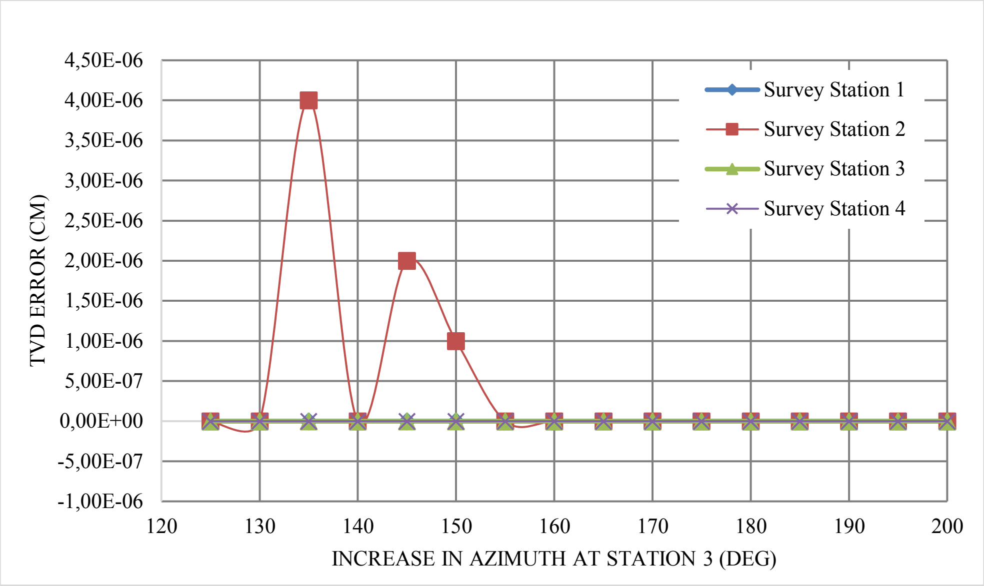

Figure 4.34: The error in TVD position due to increasing inclination at survey station 3

Basically, the increase in the azimuth measurement shows negligible increase in the TVD error measurement in all stations. The weighting scheme considered were; equal weighting, linear weighting 1,2,3,4, quadratic increasing, and cubic increasing. Table 4.30 shows a summary of the weighting rations with the correspoing weights used in the combination of the previous and current measurements.

Table 4.30: A summary of the weighting ratios with the corresponding weights used in the combination of the previous and current measurements

Weighting Ratio				
Sensor Cluster	A	B	C	D
Measurement Time	t_1	t_2	t_3	t_4
Constant (EQUAL)	1/4	1/4	1/4	1/4
	1/3	1/3	1/3	
	1/2	1/2		
	1			
Linear (L_1234)	1/10	2/10	3/10	4/10
	1/6	2/6	3/6	
	1/3	2/3		
	1			
Quadratic (P_O_2)	1/30	4/30	9/30	16/30
	1/14	4/14	9/14	
	1/5	4/5		
	1			
Cubic (P_O_3)	1/154	8/154	81/154	64/154
	1/90	8/90	81/90	
	1/9	8/9		
	1			

In table 4.30 and likewise figure 4.35, EQUAL denotes the use of equal weights for both previous and current measurements, L_1234 denotes a simple linear increase in the weight functions, P_O_2 represents a quadratic increase and P_O_3 denotes the cubic increase as shown table 4.30.

Figure 4.35 shows how the error ratio decreases with the different weighting schemes from which an appropriate weighting function scheme is selected for combination of the errors from the different clusters. As expected, a noticeable error decrease is observed for survey stations 2 and 3, while those of survey stations 1 and 4 are negligible.

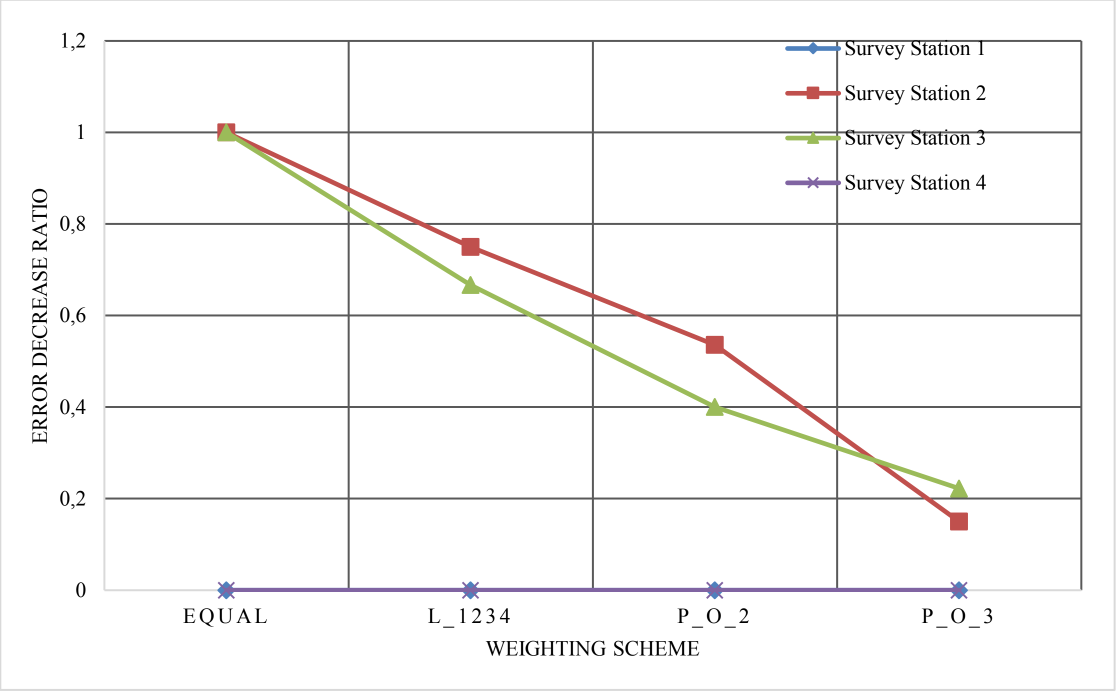

Figure 4.35: Error decrease ratio with the different weighting scheme when used at the different survey stations because of change in the Inclination or azimuth at survey station 2.

The linear weighting scheme used shows a decrease in error by a factor of ~0.75 at survey station 2 and ~0.67 at survey station 3 while that for the quadratic weighting scheme shows a decrease by a factor of ~0.53 at station 2 and a factor of 0.4 at survey station 3. Cubic weighting scheme as observed enables more weight to be assigned to the current measurement while very little weight is assigned to previous measurements. Figures 4.36a-f show the decrease in the absolute position error in the northern and eastern directions over increasing inclination angle stepwisely from 1.5° through to 10° occurring at survey station station 2. As expected, the error decrease factor is observed for each of the measurements made using the mentioned weighting factors. A similar approach is done in figure 4.37a-f which shows the decrease in the absolute position error in the northern and eastern directions over stepwise increase in azimuth from 5° through to 200° occurring at survey station 2. Also, as expected, the error decrease factor is observed for each of the measurements made using the mentioned weighting factors.

A selection should be based on the difference between the current measurement and the statistically combined past measurements and an appropriate weighting scheme selected based on this difference. For instance, for lower differences, a simple linear scheme for the weighting functions could be used. For larger differences, a quadratic weighing scheme or cubic weighting scheme could be adopted to minimize the effect of the error growth given that the cluster sensor can be trusted.

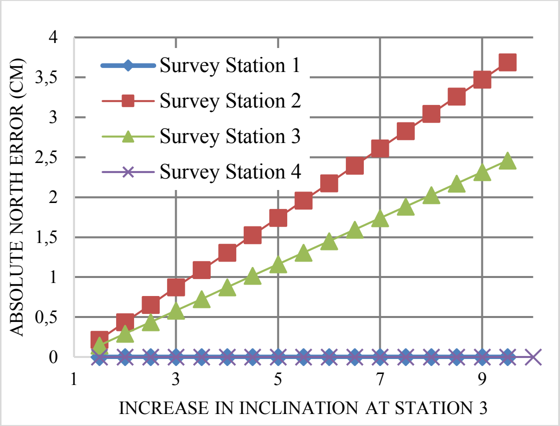

Figure 4.36a: Absolute error in north position for increase in inclination at survey station 3 using a linear weighting ratio

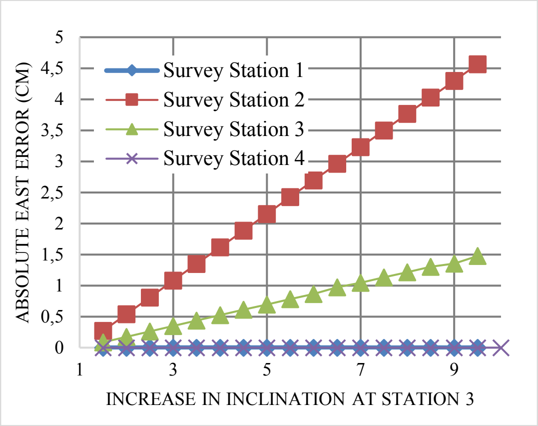

Figure 4.36e: Absolute error in east position for increase in inclination at survey station 3 using a quadratic weighting ratio

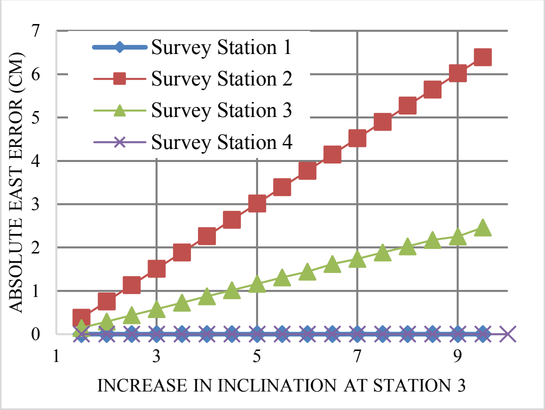

Figure 4.36d: Absolute error in east position for increase in inclination at survey station 3 using a linear weighting ratio

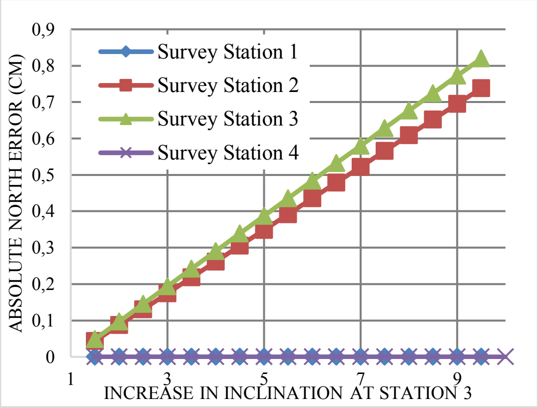

Figure 4.36c: Absolute error in north position for increase in inclination at survey station 3 using a cubic weighting ratio

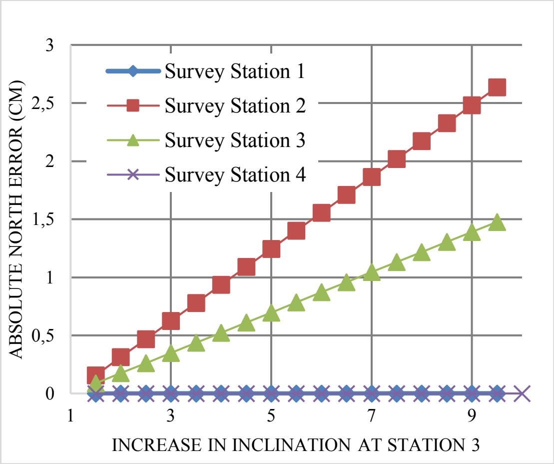

Figure 4.36b: Absolute error in north position for increase in inclination at survey station 3 using a quadratic weighting ratio

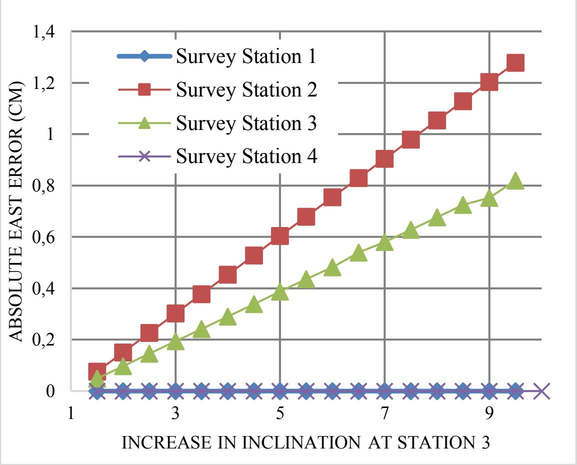

Figure 4.36f: Absolute error in east position for increase in inclination at survey station 3 using a cubic weighting ratio

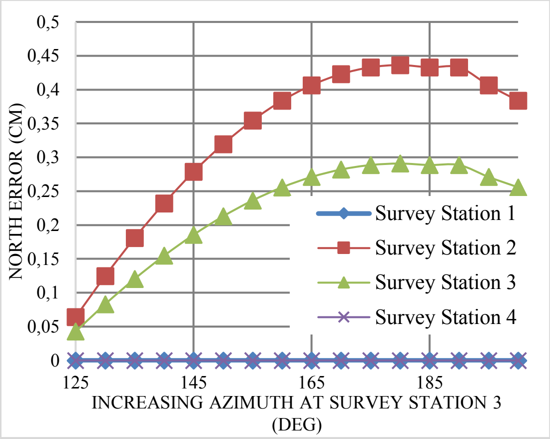

Figure 4.37a: Absolute error in north position for increase in azimuth at survey station 3 using a linear weighting ratio

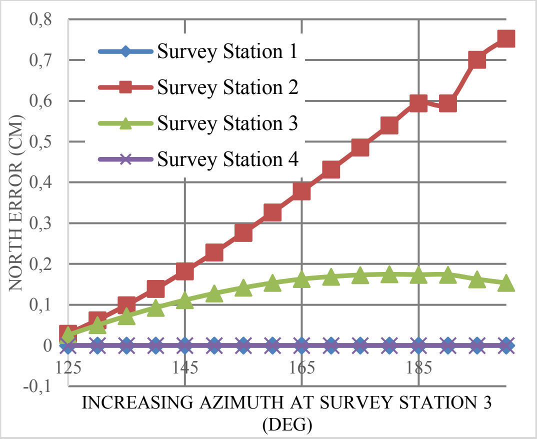

Figure 4.37e: Absolute error in east position for increase in azimuth at survey station 3 using a quadratic weighting ratio

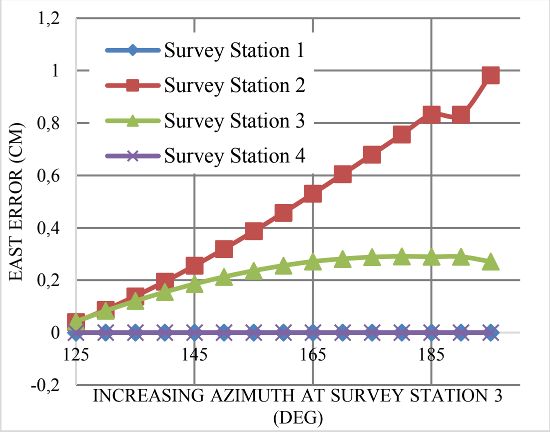

Figure 4.37d: Absolute error in east position for increase in azimuth at survey station 3 using a linear weighting ratio

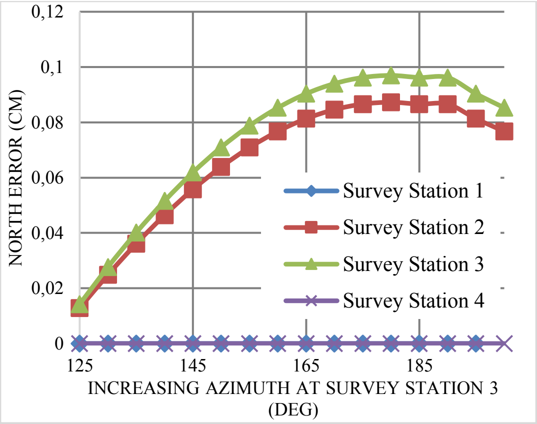

Figure 4.37c: Absolute error in north position for increase in azimuth at survey station 3 using a cubic weighting ratio

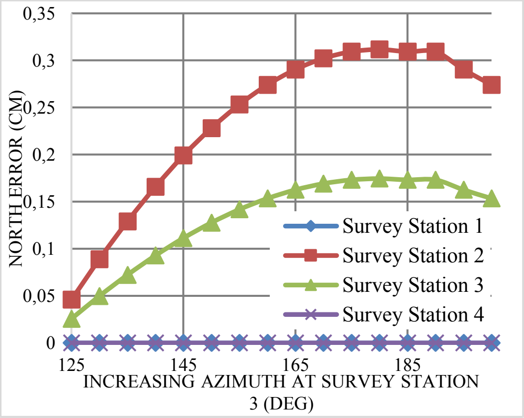

Figure 4.37b: Absolute error in north position for increase in azimuth at survey station 3 using a quadratic weighting ratio

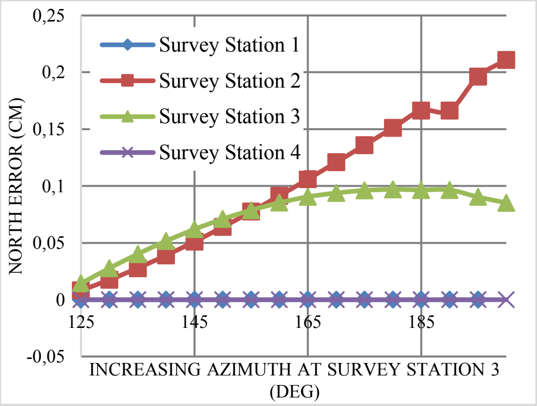

Figure 4.37f: Absolute error in east position for increase in azimuth at survey station 3 using a cubic weighting ratio

CHAPTER 5

5. Wireless Ad hoc Network Underground for Borehole Telemetry

This section describes an innovative approach using a wireless ad hoc and sensor network solution in a borehole telemetry system as developed and implemented within the framework of the I-Tube project. The description of two network structure configurations are given, as embedded in the drill tubes, to enable for telemetry. It further validates the feasibility of achieving a reliable wireless communication network underground with real-time data acquisition with respect to the described borehole telemetry system drawing from the theoretical concepts and the related work of [1-2]. Finally, the results of simulations with further analysis using the model equations to verify the feasibility of a reliable communication framework underground is made.

5.1 Underground Wireless Ad hoc Network Structure

5.1.1 Wireless Telemetry Outside of Drill-Pipes

The borehole telemetry system requires reliable communication between transceiver nodes within the underground environment where the radio transmission packets are received without significant losses irrespective of the prevailing soil medium conditions. To achieve this, the nodes are designed such that the radio transceivers are placed at the ends of each drill tube. This arrangement enables for a proximity of the communicating transceiver modules; ~100mm to ~300mm apart within the underground environment seen in figure 5.1. Within each tube, the end to end transceivers are connected to each other via a microcontroller and a power supply by cable to form a node as again shown in Figure 5.1. The nodes are programmed to enable for routing of data within the wireless ad hoc network setup with the individual wireless nodes forming an ad hoc network strand irrespective of the order of the tubes. Sensor data from the borehole assembly is wirelessly transmitted to the adjacent nodes respectively located in the mechanically flanged pipe of the drill string. On the surface, the last node used in the drill string pipe connects with the base station communication interface outside of the drill string. The base station also known as the ground station forms the interface to various system controls. The next section introduces the model equations used in the verification of the feasibility of a reliable underground wireless communication framework.

5.1.2 Related Work

A modification of the Frii's transmission equation of the received signal strength, as described in [31], expressed in the logarithmic form is given as

$$P_r(dB_{mW}) = P_t(dB_{mW}) + G_r(dB) + G_t(dB) - L_o(dB) - L_m(dB) \tag{5.1}$$

where $P_r(dB_{mW})$ and $P_t(dB_{mW})$ denote the power at the receiver and the transmitter respectively, $G_r(dB)$ and $G_t(dB)$ denotes the receiver and transmitter gains respectively, $L_o(dB)$ and $L_m(dB)$ denotes path loss in free space and soil medium respectively. It is apparent that this modified equation considers the path loss of the signal in the soil medium. The path loss is the reduction in power density or the attenuation of the radio signal as it propagates through a medium. Further deductions [31] show that the direct path loss considering both free space and the soil medium is given as

$$L_p = 6.4 + 20\log d + 20\log\beta + 8.69\alpha d \tag{5.2}$$

$$L_p = L_o + L_m \tag{5.3}$$

where α and β represent the attenuation constant (1/m) and the phase shift constant (radians/m) respectively. These quantities depend on the dielectric permittivity of the medium through which the signal passes as described also in [32, 33]. A further detail of the mathematical model is given in [31]. d denotes the distance between the transmitter and the receiver. Figure 5.1 shows the schematic of the interconnecting drilling tubes with the integrated wireless ad hoc network.

5.1.1 Antenna Selection

As the signals propagate through the soil medium there is a decrease in wavelength as compared to transmission through air [36]. This is taken into consideration in the antenna selection process in view of a higher frequency compared to the specified sub-gigahertz frequency of the transceiver modules. The resulting frequencies during transmission within the ground soil could be deduced using the relation given in [31]. An integrated chip or ceramic antenna designed for such high frequencies is considered for such underground wireless communication purpose.

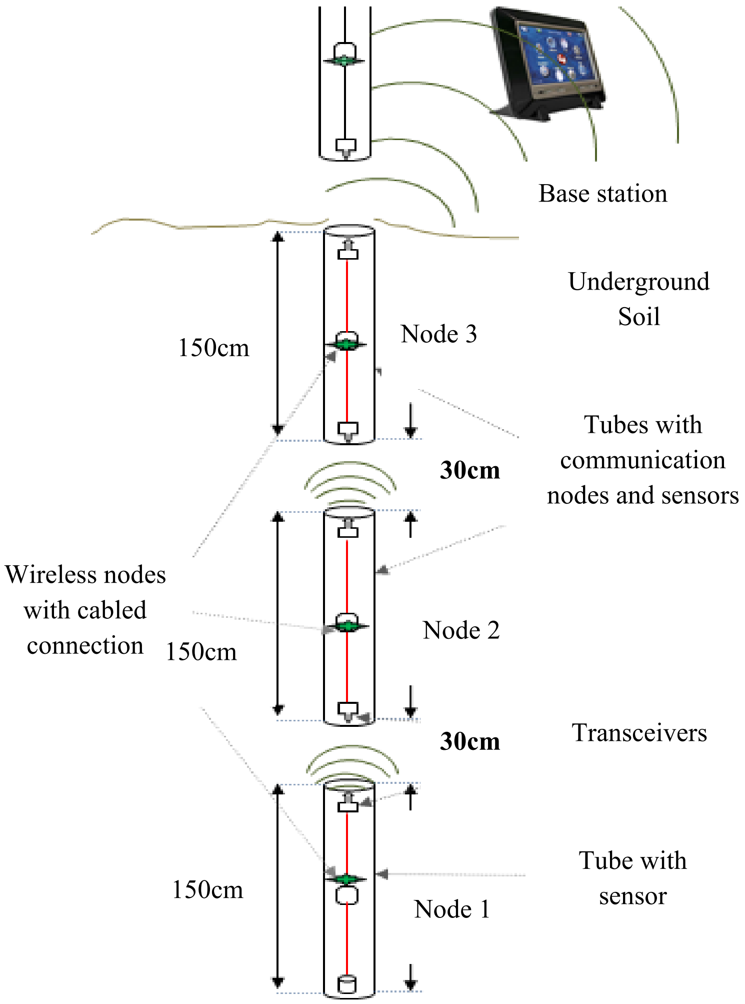

Figure 5.1: The schematic of the interconnecting drilling tubes with the integrated wireless ad hoc network.

5.1.2 Investigation of the Effect of Soil Properties on Signal Strength

Signal path loss depends on the transmission frequency, distance between the transceiver nodes, soil clay content, soil sand content and the volumetric water content of the soil [33]. The I-TUBE project makes use of the sub-gigahertz unlicensed frequency spectrum, which in this test case was a frequency of 868MHz, for wireless transmission between two adjoining transceiver nodes at a distance range of approximately 300mm for wireless communication. Eqn. 5.1-3 model equations were used in a simulation with varying values of clay content, sand content and water content, to determine the feasibility of the underground communication network under different soil conditions with regards to the range for the direct path loss as well as the power received at the receiver node or the received signal strength (RSS). The near ideal case with soil volumetric water content (VWC) of 1% is observed and compared to increasing VWC of 25% and 80% respectively. The volumetric water content here is defined as the ratio of water contained in the soil to the total volume of the soil. The effect of the different proportions of clay to sand content in the soil on the path loss and consequently the received signal strength (RSS) is observed. The RSS is the measurement of the power present in the received radio signal. Figures 5.2-4 show the received signal strength at the receiver at constant volumetric water content with varying ratios of clay to sand in each soil medium for volumetric water content values of 1%, 25% and 80%.

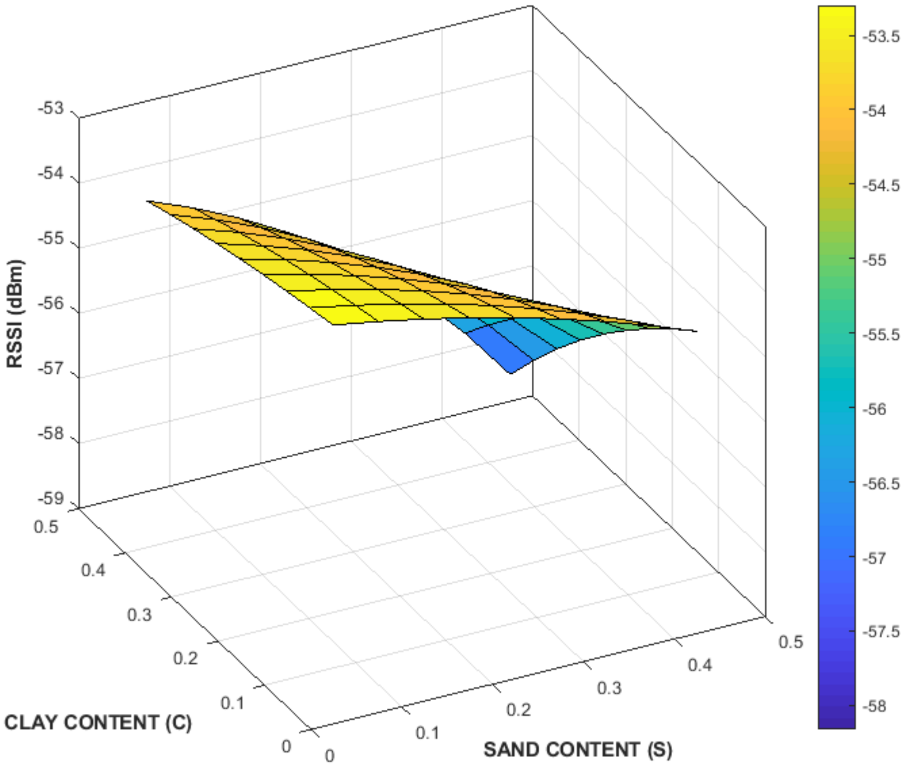

Figure 5.2: The received signal strength of varying ratios of sand and clay with a constant volumetric water content of 1% by volume.

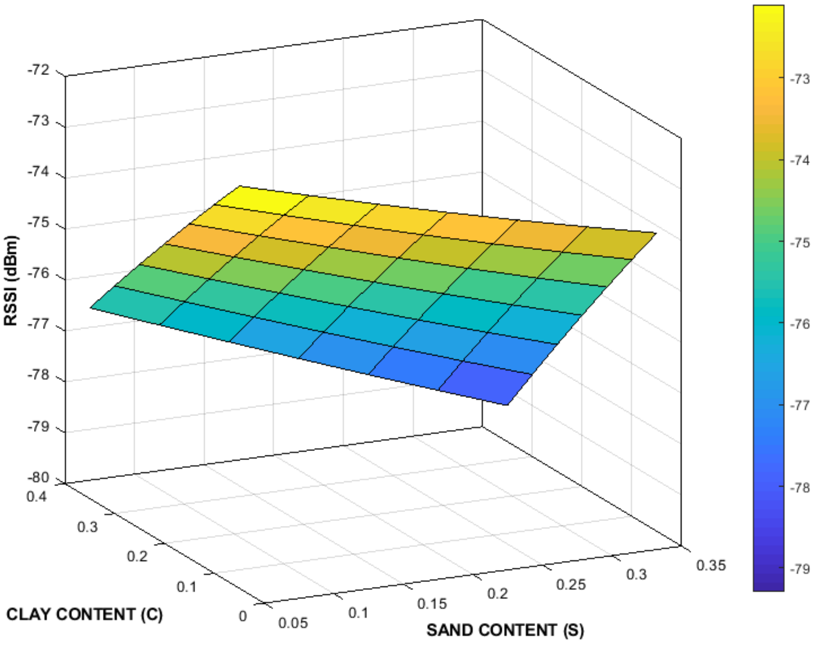

Figure 5.3: The received signal strength of varying ratios of sand and clay with a constant volumetric water content of 25% by volume.

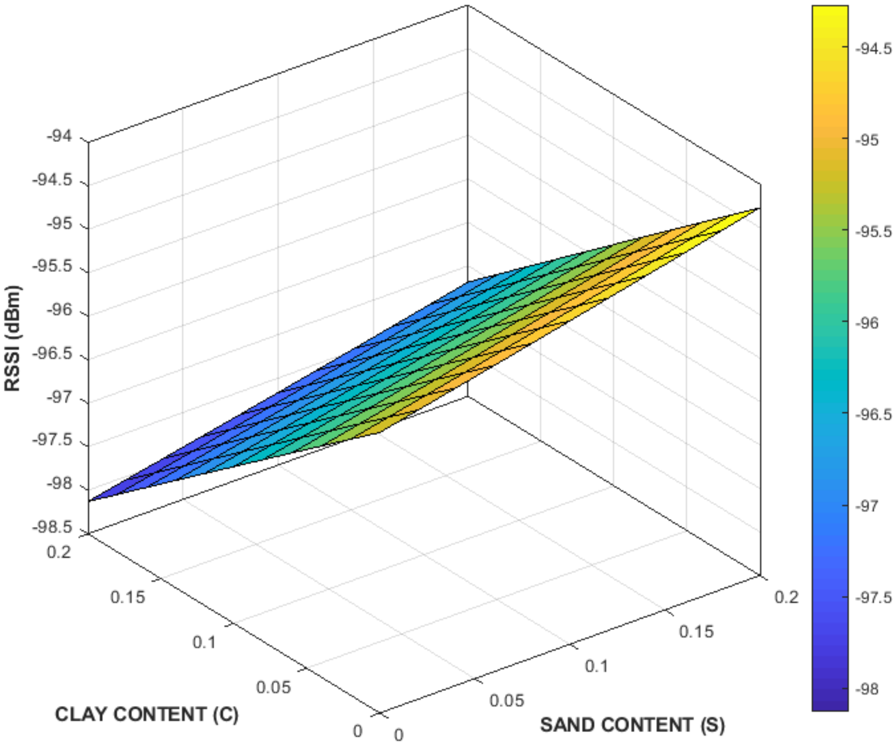

Figure 5.4: The received signal strength of varying ratios of sand to clay with a constant volumetric water content of 80% by volume.

From the datasheet of a practical example of a wireless transceiver module, AMB8420 with an embedded CC1101 transceiver [35], the minimum sensitivity is given as -110dBm for a 50 Ω antenna and the output power of the transmitter is typically 2dBm but also determined by the region of operation. From the results, as indicated in Figures 5.2-4 above, the RSS value in all cases falls within the radio frequency sensitivity limit, which indicates the feasibility of wireless communication for the given condition of the soil medium as indicated by the graphs. Furthermore, it can also be inferred from the graph that the RSS value at the receiver tends to decrease with increase in sand and clay content of the soil. This is more significant with higher volumetric water content of the soil. An increase in the VWC from 1%, through to 80%, also as shown in figures 5.2-4 results in a consequent reduction of the RSS from about -54.5dBm with 1% VWC to about -95.1dBm with 80% VWC which lies within the threshold limits of -103dbm; the transceiver sensitivity limit. This observation therefore suggests that for a transmission frequency of 868MHz and proximity of 300mm between transceiver modules, reliable communication underground is feasible under a wide range of possible soil conditions. However, on the work field, certain properties of the ground soil such as the chemical or salt content also have a significant effect on the dielectric characteristics of the soil [34]. Salty ground soil conditions tend to increase the path losses; therefore, decreasing the power at the receiver node or RSS largely [34].

5.2 Wireless Telemetry within Standard Drill-Pipes

This section investigates the feasibility of a wireless telemetry system within the standard drill-tubes for borehole sensor data acquisition. It looks at the propagation of electromagnetic waves in the well-known industrial, scientific and medical radio bands used for connecting electronic devices wirelessly. Research work has been done in the efficient ways for data acquisition during borehole drilling processes to enable for informed drilling of which includes mud-pulse telemetry, wired-line telemetry, electromagnetic (EM) telemetry and acoustic telemetry [43]. However, these telemetry systems present their own unique limitations. This section identifies some physical properties of the drill-tube that enable for the feasibility of wireless telemetry within the drill-pipe as well as the limitations thereof. The physical attributes of the standard drill tube that enables it act as a metallic cylindrical waveguide for EM wave propagation is given. The attenuation sources of the EM waves within the tube and to which extent it affects it is discussed and with the relevant simulations for verification given.

5.2.1 The Drill-Tube as a Metallic Cylindrical Waveguide

The drill-tube structure is comparable to that of a hollow metallic cylindrical waveguide with an outer conductive metal tube having a fixed radius and a hollow interior; see figure 5.5, which is an air-filled space (insulation medium) through which sometimes fluids are channeled to aid the drilling process [44]. The concept of a waveguide, which allows propagation of electromagnetic waves in the transverse electric or transverse magnetic operating mode based on the frequency of transmission, can therefore be applied to it [39]. The hollow metallic cylindrical waveguide is characterized by a cut-off frequency based on the radius of the waveguide cross-section, the relative electric permittivity of the transmission medium as well as the relative magnetic permeability of the transmission medium [39]. The cylindrical waveguide hence behaves as a high pass filter, which allows signals with frequencies above the cut-off frequency to propagate within the tube while attenuating signals at frequencies below the cut-off frequency. Further description of the mathematical model for the electromagnetic wave propagation and the derivation for the cut-off frequencies for the metallic cylindrical waveguide is provided in [39]. The equations for the cut-off frequency for the metallic cylindrical waveguide transmitting in the transverse electric (T.E.) mode is given as [39]

$$f_{C_{mn}}^{TE} = \frac{X'_{mn}}{2\pi a\sqrt{\mu\varepsilon}} \tag{5.4}$$

and that for transverse magnetic (T.M.) mode is given as

$$f_{C_{mn}}^{TM} = \frac{X_{mn}}{2\pi a\sqrt{\mu\varepsilon}} \tag{5.5}$$

where X'_{mn} and X_{mn} define the n^{th} zero of the m^{th} order Bessel function and Bessel function derivative evaluated at integer orders 0,1, 2…6 respectively [39]. α, μ and ε denote the radius of the metal cylindrical tube, the magnetic permeability and the electric permittivity respectively. The above equations were the basis for the analysis of the different cut-off frequencies of the EM waves within the drill-tubes of different radii.

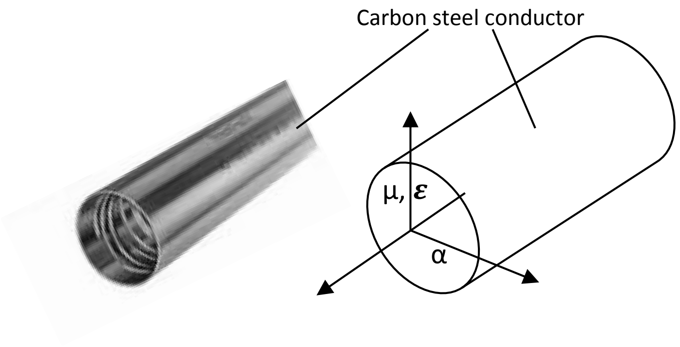

Figure 5.5: The drill-tube structure as compared to a metallic cylindrical wave guide of radius, r.

5.2.2 Attenuation within the Drill-Tube

The drill tube as a metallic cylindrical waveguide is subject to two main loss mechanisms. These are conductor losses due to the carbon steel cylinder and dielectric loss due to the fluid (air) within the hollow space of the tube [39]. Fields associated with the propagating waveguide modes produce currents that flow in the walls of the waveguide [39]. The walls act like resistors and dissipate energy in the form of heat given that the waveguide walls are constructed from an imperfect conductor. The dielectric within the waveguide is not ideal. It also dissipates energy in the form of heat [39, 40]. The general equations for the metallic cylindrical waveguide in both the transverse electric (T.E.) and transverse magnetic (T.M.) mode attenuation constants due to the conductor losses are given by; In the transverse, electric mode:

$$\alpha_{C_{mn}}^{TE} = \frac{R_s}{a\eta'\sqrt{1-\left(\frac{f_{C_{mn}}}{f}\right)^2}}\left[\left(\frac{f_{C_{mn}}}{f}\right)^2 + \frac{m^2}{X'^{\,2}_{mn} - m^2}\right] \tag{5.6}$$

and in the transverse magnetic mode:

$$\alpha_{C_{mn}}^{TM} = \frac{R_s}{a\eta'\sqrt{1-\left(\frac{f_{C_{mn}}}{f}\right)^2}} \tag{5.7}$$

$$\eta' = \sqrt{\frac{\mu}{\varepsilon}} \tag{5.8}$$

where R_s denotes the surface resistance of the waveguide walls, $\alpha_{C_{mn}}^{TE|TM}$ denotes the radius of the cylindrical tube, f denotes the frequency of the electromagnetic wave, $f_{C_{mn}}$ denotes the cut-off frequency. More details about the derivation is given in [39, 40]. These equations are used to perform the simulations as described in the next section. Eqn. 5.6-8 show that the attenuation is dependent on the surface resistivity of the waveguide walls. This observation therefore prompted a further look into the composition and characteristic of the drill tube material which directly affects its electrical resistivity property. The American Petroleum Institute (API) provides the specification: API 5L & API 5LX for carbon steel seamless pipes & tubes used in the drilling industry [9]. The specification gives an indication of the mechanical and chemical properties of the carbon steel grade that makes it suitable for use in conveying gas, water, and oil in both the oil and natural gas industries [41, 47]. What is of interest in this study is the surface resistivity/conductivity of the carbon steel under varying conditions of temperature. It is shown that this effect is also dependent on the carbon content of the steel grades that fall under the API 5L & API 5LX specification [42]. The study of this effect is important because during the normal drilling process, the borehole assembly (BHA) can attain high temperatures beyond 200°C [49]. The main point of this investigation is to know to what extent this temperature increase would affect the attenuation of the EM waves within the tube and subsequently degrade the wireless telemetry performance. In this specification [41], two basic product specifications levels (PSL) are recognized and categorized into PSL 1 and PSL 2. PSL 1 is a standard quality for line pipe while PSL 2 contains additional chemical, mechanical properties, and testing requirement. The grades covered by this specification are A25, A, B, X42, X46, X52, X56, X60, X65, X65 X70, X80. What is of interest here is the carbon content existing for each of the grades enumerated. According to specification described in [41], the percentage by weight of the carbon content in the grades enlisted is specified in Table 5.1.

SMLS refers to seamless steel line pipes and ERW refers to electrical resistance welded steel line pipes. An investigation into the electrical resistivity of carbon steel, considering the effects of the nonlinearities of the temperature and carbon content is investigated in [42]. Figure 5.9 shows the variation of the electrical resistivity for carbon steel with different carbon steel content with increasing temperature. Results from the investigation showed a strong dependence of the electrical resistivity on the carbon content of carbon steel within the range of 0.06-1.22C wt. %. This range covers well the range within which the carbon content of the carbon steel specified in the API 5L & API 5LX specification falls [41] as shown in table 5.1.

Table 5.1: Carbon Content of Carbon Steel Grades for API 5L & API 5LX

Grade	Carbon content %wt
A25	0.21
A (SMLS)	0.22
B (“)	0.27
A (ERW)	0.21
B (“)	0.26
X-42 (SMLS)	0.29
X-46 (“)	0.31
X-52 (“)	0.31
X-60 (“)	0.26
X-42 (ERW)	0.28
X-46 (“)	0.30
X-52 (“)	0.30
X-60 (“)	0.26

More details on the mathematical formulation and regression analysis of this dependency can be obtained from [42].

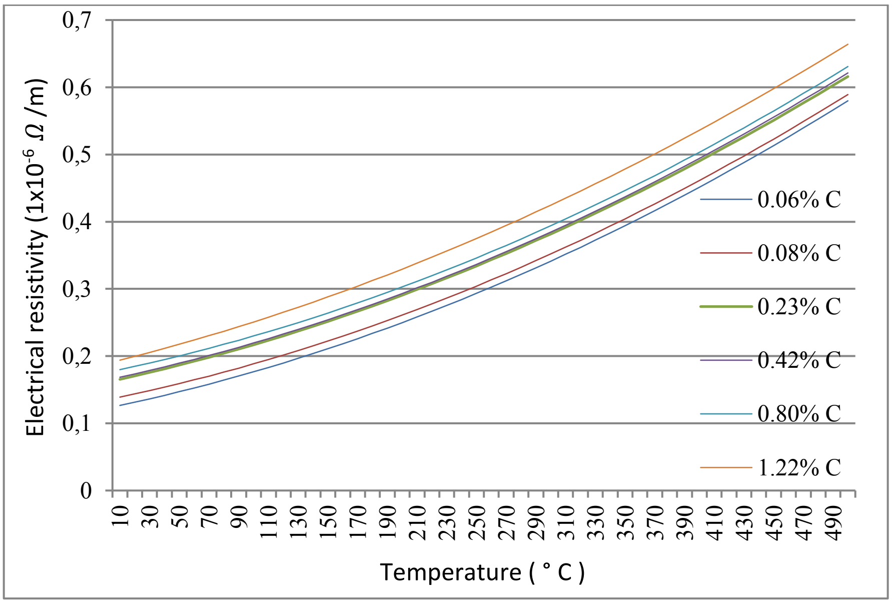

Figure 5.9: Temperature dependence of electrical resistivity for different carbon content (by weight %) of carbon steel.

5.2.3 Simulations and Results

Simulations were done in Matlab to investigate the cut-off frequencies for varying drill tube diameters. The fixed frequencies considered for usage were 2.4GHz and 5GHz band. This is because these frequencies are the available industrial, scientific and medical (ism) frequency band popularly used for wireless connectivity in electronic devices and can be obtained conveniently off the shelf.

5.2.4 Cut-off Frequency Investigation

It has been shown in [39] that X'_{mn} and X_{mn} define the n^{th} zero of the m^{th} - order Bessel function and Bessel function derivative respectively are given as shown in tables 5.2-3 below and their corresponding values are used in the simulations

Table 5.2: Transverse Magnetic Mode

X_{mn}	m=0	m=1	m=2	m=3	m=4	m=5	m=6
n=1	2.4049	3.8318	5.1357	6.3802	7.5884	8.7715	9.9361
n=2	5.520	7.105	8.417	9.761	11.064	12.338	13.589
n=3	8.653	10.17	11.61	13.015	14.372	15.700	17.003

Table 5.3: Transverse Electric Mode

X'_{mn}	m=0	m=1	m=2	m=3	m=4	m=5	m=6
n=1	3.831	1.841	3.054	4.2012	5.317	6.415	7.501
n=2	7.015	5.331	6.706	8.0153	9.2824	10.519	11,734
n=3	10.173	8.536	9.969	11.345	12.681	13.987	15.268

It is observed that the dominant mode in a circular waveguide is the TE_{11} mode, followed in order by the TM_{01} mode and the TE_{21} and TE_{01} modes respectively. The graph in figure 5.10 shows the cutoff frequency curve for the 3 different modes at tube diameters up to 10 cm. From the graph, it is observed that the cut-off frequency decreases with increase in drill tube diameter.

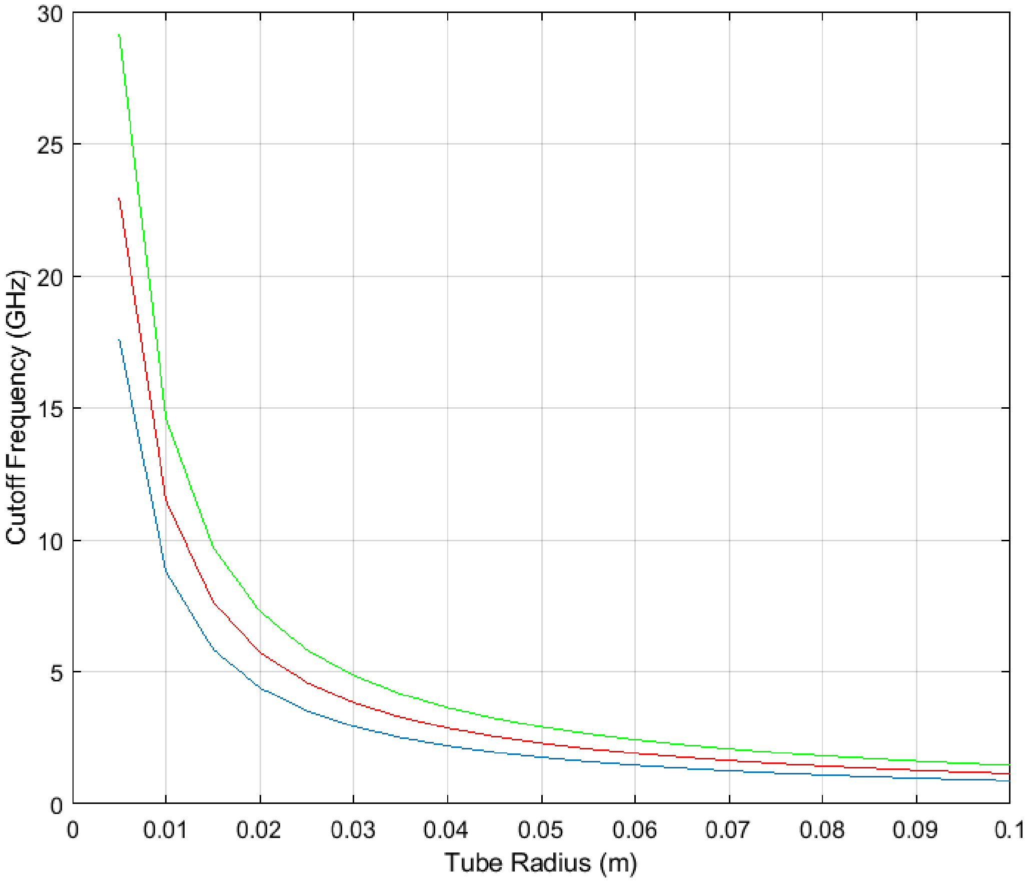

Figure 5.10. The cut-off frequency curves for the TE_{11}, TM_{01} and TE_{21}.

The table shows the cut-off frequencies of the three propagation modes for a selected drill-tube radius of 3cm. The minimum cutoff as shown in table 5.4 is approximately 2.928 GHz. This is above the 2.4GHz ultra high frequency band used for Wi-Fi connectivity, which includes Bluetooth. Transmission at 5.0 GHz, also used in Wi-Fi connectivity, falls within the range for connectivity.

Table 5.4: Cut-off Frequencies at Radius of 3cm

Propagation Mode	Cut-off Frequency
TE_{11}	2.928 GHz
TM_{01}	3.828 GHz
TE_{21}	4.858 GHz

5.2.5 Attenuation Investigation

Figure 5.11 shows the attenuation of the electromagnetic waves in Nepers per unit meter, which can be expressed also in dB, within the drill tube as a metallic cylindrical waveguide at a fixed frequency of 5GHz at varying radii. In the simulation, the dielectric was assumed air and a typical value for carbon content in carbon steel is chosen at room temperature. It is observed that in consistency with non-ideal waveguides, the attenuation per unit length decreases sharply as the radius of the drill tube increases.

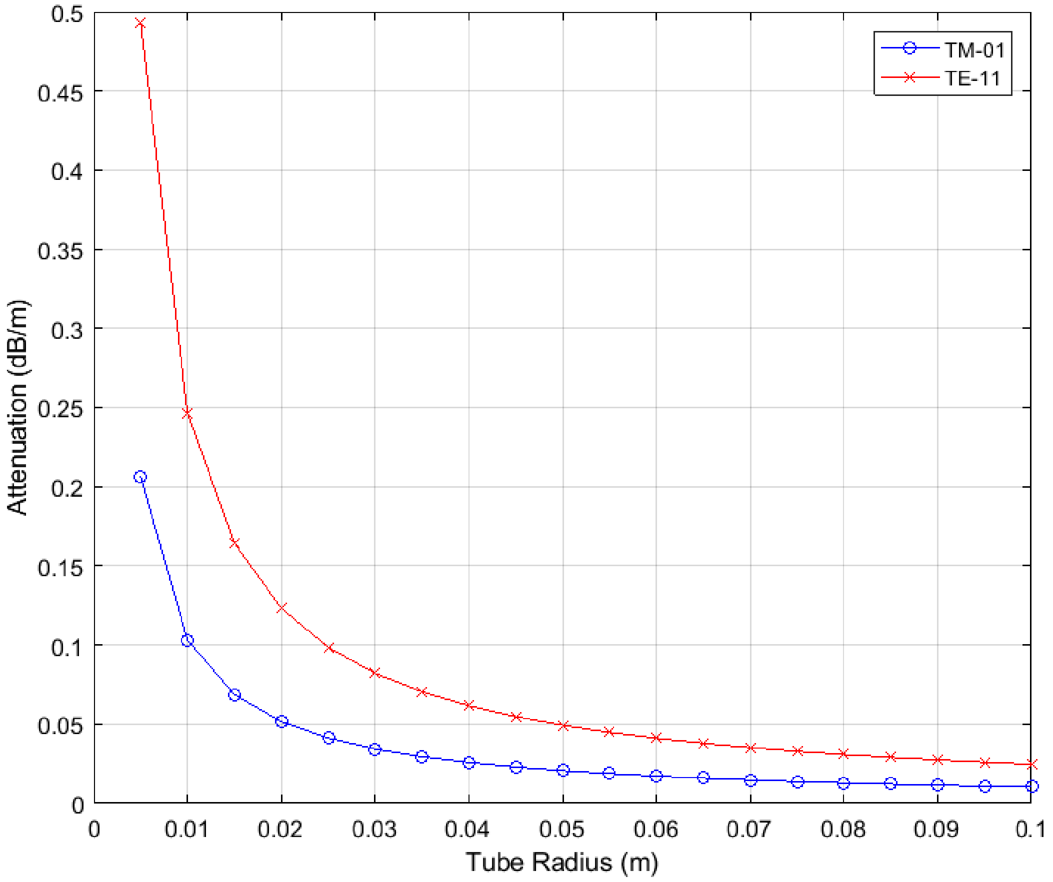

Figure 5.11. Attenuation in dB per meter versus varying drill tube radius for, TE_{11} and TM_{01} modes.

For this analysis, the standard drill tube radius under investigation has a radius of 3cm. The dB loss per meter is observed from the simulation results to be to be ~0.034dB for the case of transmission in the TE_{11} mode while it is ~0.082dB per meter in the TM_{01} mode as observed on the graph in figure 5.11. A further simulation was done to determine the losses in dB with increasing length of tube. The corresponding analysis of the losses in dB of the signal strength within the tube as a relation to its length is shown in the graph of figure 5.12. Considering the sensitivity of the of a typical wireless module at approximately -100dBm and an input power of about 10dBm which corresponds to a loss of 110dB from the graph, the corresponding length of tube is about 3666m. This value is regarded as approximate, given that it is assumed a long uniform tube with uniform material properties μ, within.

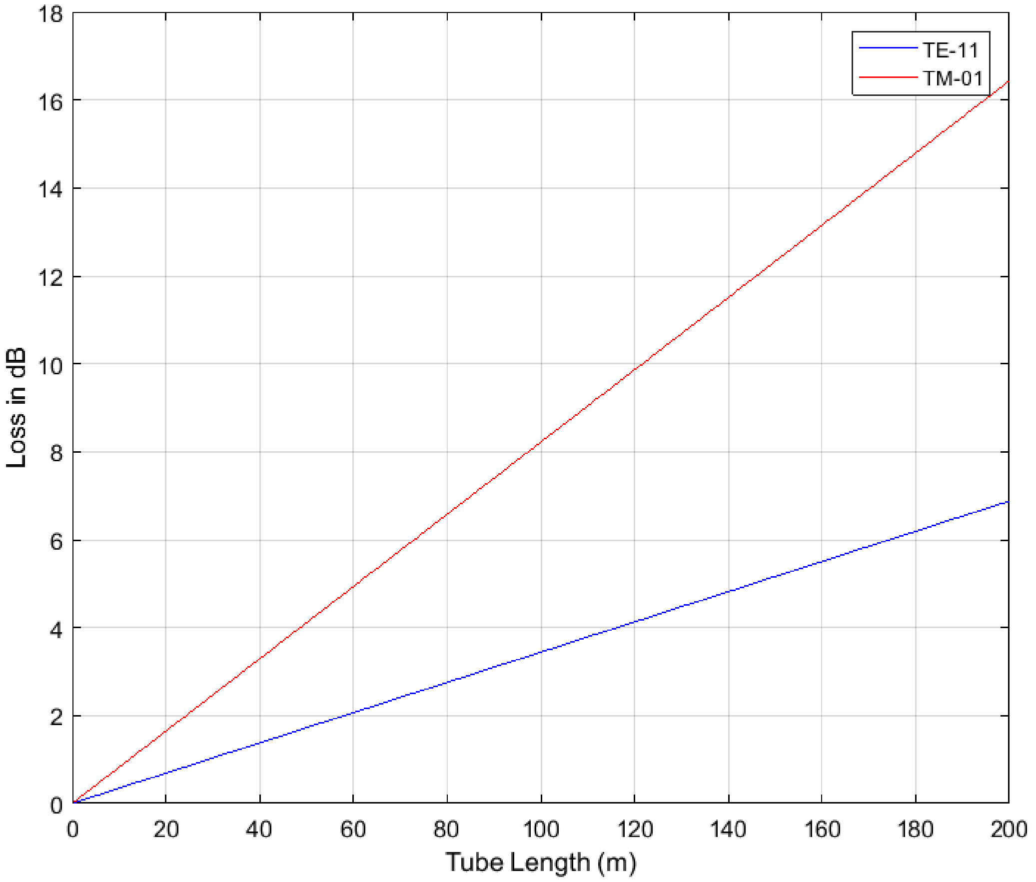

Figure 5.12: Losses in dBm of electromagnetic waves in relation to the length of the metallic cylindrical drill tube.

The implication is that the nodes (wireless modules) could be placed any distance apart within this distance range inside the tube to enable for data communication. However, it must be taken into consideration the fact that there are other factors such as inconsistency of inner material property which might contribute to higher losses (reflection and dispersion) and subsequent reduction in the calculated distance. Figure 5.13 shows the electrical resistivity dependence of attenuation of EM wave propagation inside a carbon steel cylindrical drill pipe of radius 3cm, acting as a wave guide for different carbon content of the carbon steel. It is observed that the attenuation increases with increasing electrical resistivity.

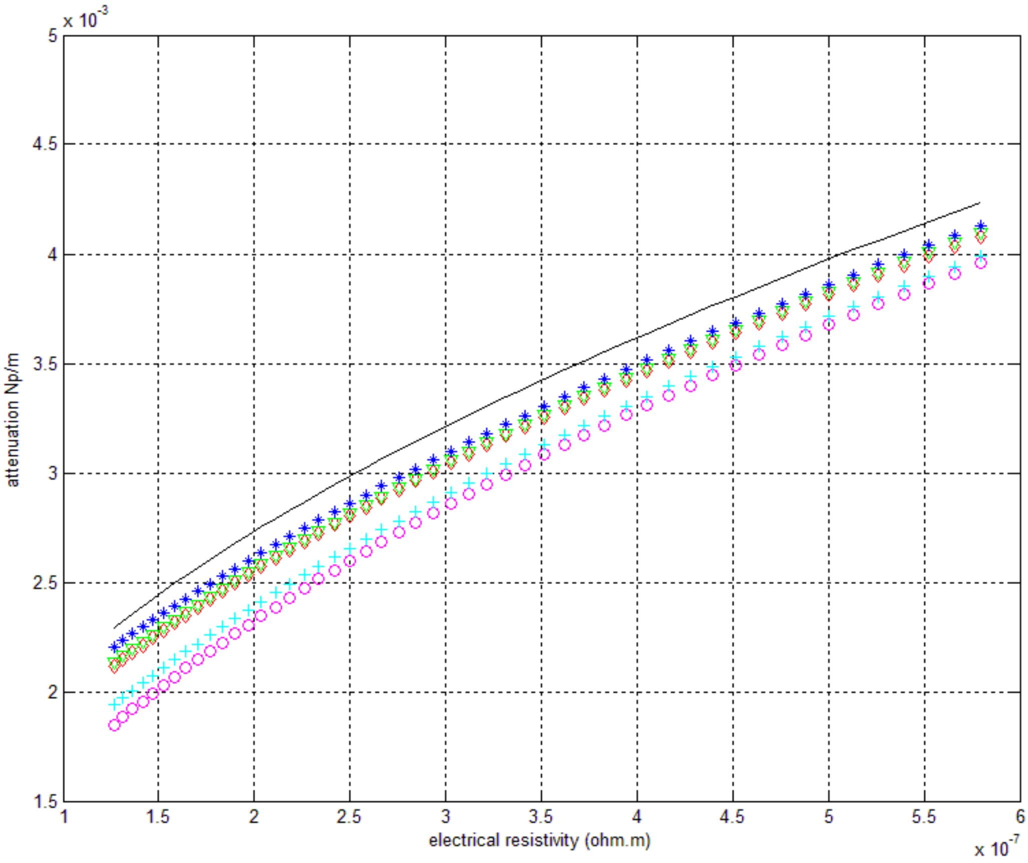

Figure 5.13: Electrical resistivity dependency of carbon steel on temperature

CHAPTER 6

6. Conclusion, Contribution of Thesis and Outlook

The first chapter basically gave an overview of the vertical drilling concept used in industry for in-situ soil mixing and highlighted the challenges in attaining accuracy in the determination of the wellbore path with regards to the measurement techniques currently used. It proceeded to give an overview of the wellbore path within the concept of the tracking of the BHA or drillhead in a designated reference frame and highlighted the parameters necessary for keeping accurate track of to impove the tracking of the wellbore trajectory.

The second chapter touched on the wellbore trajectory computation techniques as well as the error model derivation defined by the ISCWSA which forms a basis by which the determination of the error uncertainty in the computation of the wellbore path is based. This region of uncertainty is generally modelled as a 3-dimensional Gaussian probability density function whereby a linear regression solution approach is used to determine the estimation of the parameters that relate the independent true values of the survey station position to the observed or measured values.

Chapter 3 presented the mathematical model scheme developed for processing data from the inertia measurement unit output data with measurements from the external encoder for the overall tracking of the wellbore path. It also discussed a probabilistic approach to improving survey station measurements using data from multiple sensor clusters. These input data are available because of different sensor clusters taking measurements at the same survey station of interest sequentially in the time domain as the wellbore depth increases. The data fusion concept using the indirect Kalman filter in the feed forward configuration was adopted as a basis for fusing sensor input data with external measurements to improve the tracking of the sensor position within the drill string.

In chapter 4, an application of the concepts described in chapter 3 was used with actual field data as well as simulated data to investigate the overall effectiveness of the outlined methods therein. The ISCWSA error model was used as a framework by which to appreciate the use of the outlined concepts, for the analysis of the region of uncertainty in error using sensors with different performance specifications. This approach highlighted the main error sources of more significance to the region of uncertainty in error of the survey measurements, served as a prelude to aid comparison to the results of the implementation of the mathematical model and processing scheme and showed the improvement achieved in the survey position measurements thereof. It commenced by showing how the performance specification on the datasheet is converted to the required error source magnitude used in the error model to compute the region of uncertainty in error at each of the survey stations. It was observed that there is a strong correlation between the sensor performance specifications and the region of uncertainty in error and that the major contributing factor to the error uncertainty is from the gyroscope bias and gyroscope drift by way of the angle random walk and bias instability. External updates from a rotary encoder for tracking the physical position of the sensor unit within the drill tube was used as a high accurate measurement source in the filter to improve its yaw position estimate which improves its azimuth errors and consequently the survey position accuracy. The gyroscope bias was modeled as a Gauss-Markov process which was used to augment the state variables in the model equation used in the indirect Kalman filter. Two measurement update modes were used in this approach by which aiding data from the rotary encoder is used as measurement update within the sensor node unit to improve the yaw position estimate of the sensor device. A comparison of the improved tracking output data is made with that defined by the ISCWSA, which is a standardization committee for wellbore surveying accuracy in collaboration with the society of petroleum engineers (SPE).

It has been shown that, depending on the measurement update mode, using the low-cost MEMS gyroscope with an aiding system such as the rotary encoder, an improved azimuth error of uncertainty can be achieved as compared to that provided by the magnetic based surveying tool. Results show that the continous measurement update mode interspersed with periodic data time updates provides a better performance in terms of the reduction of azimuth errors as compared with single measurements update at varying frequencies. It is therefore inferred that with such processing scheme results, there is no need for the incorporation of the NMDC in an extra effort in reducing the effect of the magnetic influence of the metallic drill string which induces errors in the azimuth measurements thereby helping to cut down on production costs. Furthermore, in the case of the measurement approach used in vertical drilling processes for in situ soil mixing, surveying is done using the digital inclinometer probe and carried out only after completion of the drilling process, this situation results in the increase in production time and subsequently, an increase in production costs due to the need to “break” the drillstring before the digital inclinometer probe is inserted for measurement. This concept therefore in addition to the in-house developed borehole telemetry system will cut down on such costs without sacrificing performance and accuracy. Finally, the probabilistic scheme was applied to investigate how the effect of multiple measurements at a single survey station which are statistically combined are affected by a shift in the measurement at a survey station under investigation and how the weights can be distributed to the respective measurements to improve the overall accuracy of the survey station of interest. It was observed that an appropriate weighting scheme is best selected depending on the difference between the previous survey measurements and the current survey measurements. For small differences, a simple linear weighting scheme can be adopted, and for larger differences, a quadratic or cubic weighting scheme so as to give a more accurate reflection of the inclination or azimuth at the survey station of interest.

Chapter 5 investigated the concept of real-time acquisition of sensor data over a wireless ad hoc network by way of electromagnetic telemetry. This involves sensor nodes data acquisition and preprocessing, on the back of an in-house developed wireless data routing scheme for real-time acquisition of survey measurements. One aspect investigated the electromagnetic wave propagation through the soil during tube-to-tube wireless communication externally underground to enable for real time borehole telemetry. In this concept, the effect of the losses in the soil medium due to the main soil constituents such as clayey, sand and volumetric water content of the soil is investigated using well established model equations. It is observed that the wireless signals attenuate strongly with increasing clayey and volumetric water content for a given displacement between transceiver and receiver modules. From this observation, it was deduced that for a given practical displacement of 300mm between these modules at a given transmission power, the signal sensitivity threshold would not be exceeded for a given practical range of soil conditions. This therefore enables for reliable wireless communication for an implementation of the telemetry system based on the concept. Another aspect was the results of a feasibility study and the investigation and implementation of the “inside” drill tube wireless communication by determining a selection criterion for the transmission frequency based on the physical properties of the drill tube. It was deduced that the physical and material properties of the cylindrical drill string within which electromagnetic waves propagate makes it acts as a high pass filter only enabling wireless transmission after exceeding a frequency threshold. We learned that specification of carbon steel seamless pipes & tubes used in the drilling industry by the American Petroleum Institute (API) gives an indication of its constituent mechanical and chemical properties of the carbon steel grade. It is therefore deduced that there is a variation of the electrical resistivity for carbon steel with different carbon steel content with increasing temperature with results from the investigation showing a strong dependence of the electrical resistivity on the carbon content of carbon steel within the range of 0.06-1.22C wt. From this the carbon content of the respective specification for the drill tube was looked into; and investigated the effect of temperature rise on the electrical resistivity of the metal drill tube from which one could infer the effect on the attenuation of the electromagnetic signals used within it. We learned that there is a linear increase in the electrical resistivity of the tube with increase in temperature and therefore the distance threshold between transceiver nodes by which reliable wireless connectivity can be sustained given a tube with specified dimensions could be deduced. So, for instance, a drill tube with a radius of approximately ~3cm, one can effectively transmit data at 5Ghz without significant losses due to the material properties of the drill tube which affect its resistivity.

This thesis provides for a further extension of the current work as it provides a test bed for further research work. For instance, it provides a platform for possible further sensor integration, processing and communication to monitor the physical condition of the drill tube such as tube defects and cracks, over time among other purposes.

Appendix I

I. Mathematical Derivation of the Error Propagation Model

The survey measurements define the depth, inclination and azimuth at either end of an interval, the position over an interval depends on the survey measurements at the two stations (ISCWSA).

Let vector $\Delta\vec{r}_k$ be the displacement between survey station $k-1$ and k and $\Delta\vec{r}_{k+1}$ the displacement between stations k and $k+1$, then it follows that $\frac{\partial\vec{r}}{\partial p}$ can be split into the variation over the preceding and following intervals and this is given as [5]

$$\vec{e}_{i,l,k} = \sigma_{i,l}\left(\frac{\partial\Delta\vec{r}_k}{\partial p_k} + \frac{\partial\Delta\vec{r}_{k+1}}{\partial p_k}\right)\cdot\frac{\partial p_k}{\partial\varepsilon_i} \tag{I.1}$$

where $\vec{e}_{i,l,k}$ denotes the error vector due to the i^{th} error source at the k^{th} survey station in the l^{th} survey leg, $\frac{\partial\Delta\vec{r}_k}{\partial p_k}$ denotes the effect of the errors in the survey measurements at station k, on the position vector from survey station $k-1$ to survey station k, and $\frac{\partial\Delta\vec{r}_{k+1}}{\partial p_k}$ denotes the effect of the errors in the survey measurements of station k to survey station $k+1$.

Using the balanced tangential method as a wellbore survey method of preference $\frac{\partial\Delta\vec{r}_k}{\partial p_k}$ is determined with no significant loss of accuracy [30].

$$\Delta\vec{r}_j = \begin{pmatrix}\Delta N\\ \Delta E\\ \Delta V\end{pmatrix}_j = \frac{MD_i + MD_{i-1}}{2}\begin{pmatrix}\sin I_{i-1}\cos A_{i-1} + \sin I_i\cos A_i\\ \sin I_{i-1}\sin A_{i-1} + \sin I_i\sin A_i\\ \cos I_{i-1} + \cos I_i\end{pmatrix} \tag{I.2}$$

for the interval between stations $k-1$ and k, it can be written as

$$\frac{d\Delta\vec{r}_k}{dp_k} = \begin{pmatrix} \frac{\partial \Delta r_k}{\partial MD_k} & \frac{\partial \Delta r_k}{\partial I_k} & \frac{\partial \Delta r_k}{\partial A_k} \end{pmatrix} \tag{I.3}$$

Substituting k for i and differentiating Eqn. I.3 gives

$$\frac{\partial\Delta\vec{r}_k}{\partial MD_k} = \frac{1}{2}\begin{pmatrix} \sin I_{k-1}\cos A_{k-1} + \sin I_k \cos A_k \\ \sin I_{k-1}\sin A_{k-1} + \sin I_k \sin A_k \\ \cos I_{k-1} + \cos I_k \end{pmatrix} \tag{I.4}$$

$$\frac{\partial\Delta\vec{r}_k}{\partial I_k} = \frac{1}{2}\begin{pmatrix} (MD_k - MD_{k-1})\cos I_k \cos A_k \\ (MD_k - MD_{k-1})\cos I_k \sin A_k \\ -(MD_k - MD_{k-1})\sin I_k \end{pmatrix} \tag{I.5}$$

$$\frac{\partial\Delta\vec{r}_k}{\partial A_k} = \frac{1}{2}\begin{pmatrix} -(MD_k - MD_{k-1})\sin I_k \sin A_k \\ (MD_k - MD_{k-1})\sin I_k \cos A_k \\ 0 \end{pmatrix} \tag{I.6}$$

When put together it becomes

$$\frac{d\Delta\vec{r}_k}{dp_k} = \frac{1}{2}\begin{pmatrix} \sin I_{k-1}\cos A_{k-1} + \sin I_k \cos A_k & (MD_k - MD_{k-1})\cos I_k \cos A_k & -(MD_k - MD_{k-1})\sin I_k \sin A_k \\ \sin I_{k-1}\sin A_{k-1} + \sin I_k \sin A_k & (MD_k - MD_{k-1})\cos I_k \sin A_k & (MD_k - MD_{k-1})\sin I_k \cos A_k \\ \cos I_{k-1} + \cos I_k & -(MD_k - MD_{k-1})\sin I_k & 0 \end{pmatrix} \tag{I.7}$$

Similarly, the interval between stations k and $k+1$ can be given as

$$\frac{d\Delta\vec{r}_{k+1}}{dp_k} = \begin{pmatrix} \frac{\partial \Delta r_{k+1}}{\partial MD_k} & \frac{\partial \Delta r_{k+1}}{\partial I_k} & \frac{\partial \Delta r_{k+1}}{\partial A_k} \end{pmatrix} \tag{I.8}$$

Substituting $i = k+1$ and differentiating equation (I.2) gives

$$\frac{d\Delta\vec{r}_{k+1}}{dMD_k} = \frac{1}{2}\begin{pmatrix} -\sin I_k \cos A_k - \sin I_{k+1}\cos A_{k+1} \\ -\sin I_k \sin A_k - \sin I_{k+1}\sin A_{k+1} \\ -\cos I_k - \cos I_{k+1} \end{pmatrix} \tag{I.9}$$

$$\frac{\partial\Delta\vec{r}_{k+1}}{\partial I_k} = \frac{1}{2}\begin{pmatrix} (MD_{k+1} - MD_k)\cos I_{k+1} \cos A_{k+1} \\ (MD_{k+1} - MD_k)\cos I_{k+1} \sin A_{k+1} \\ -(MD_{k+1} - MD_k)\sin I_{k+1} \end{pmatrix} \tag{I.10}$$

$$\frac{\partial \Delta \vec{r}_{k+1}}{\partial A_k} = \frac{1}{2}\begin{pmatrix} -(MD_{k+1} - MD_k)\sin I_{k+1} \sin A_{k+1} \\ (MD_{k+1} - MD_k)\sin I_{k+1} \cos A_{k+1} \\ 0 \end{pmatrix} \tag{I.11}$$

And subsequently

$$\frac{d\Delta \vec{r}_{k+1}}{dp_k} = \frac{1}{2}\begin{pmatrix} -\sin I_k \cos A_k - \sin I_{k+1} \cos A_{k+1} & (MD_{k+1} - MD_k)\cos I_{k+1} \cos A_{k+1} & -(MD_{k+1} - MD_k)\sin I_{k+1} \sin A_{k+1} \\ -\sin I_k \sin A_k - \sin I_{k+1} \sin A_{k+1} & (MD_{k+1} - MD_k)\cos I_{k+1} \sin A_{k+1} & (MD_{k+1} - MD_k)\sin I_{k+1} \cos A_{k+1} \\ -\cos I_k - \cos I_{k+1} & -(MD_{k+1} - MD_k)\sin I_{k+1} & 0 \end{pmatrix} \tag{I.12}$$

This represents the 3x3 matrix equation which describes the change in the wellbore position, in the north, east, true vertical depth co-ordinate frame caused by changes to the survey measurement at any preceding given station, k. For the last survey station of interest, only the preceding interval is applicable and this is given as

$$\vec{e}^{\,*}_{i,l,K} = \sigma_{i,l} \cdot \frac{\partial \vec{r}_K}{\partial p_K} \cdot \frac{\partial p_K}{\partial \varepsilon_i} \tag{I.13}$$

All calculated contributions to the error ellipse from each error source, at each survey station in each leg of the well are summed up. There are two basic error cases, these include

- Correlated errors eg. The z-axis magnetometer bias which has the same value from survey station to survey station and the effects of the error builds all the way down the wellbore. For cases like this error are added in the usual arithmetic way ie

$$\vec{e}_{total} = \vec{e}_1 + \vec{e}_2 \tag{I.14}$$

- Uncorrelated or statistically independent errors. This used fused using the root sum squared method

$$\vec{e}_{total} = \sqrt{\vec{e}_1 + \vec{e}_2} \tag{I.15}$$

All the error sources are combined by make a sum over all survey legs, survey stations and error sources which apply to a particular well. The propagation mode is used to define at what step in the summation arithmetic addition is used and at what stage root sum squared addition is required. Generalizing the sums to include more than two error sources, and remembering that for the error model at a particular point, the $\vec{e}$ variables will actually be 3x1 vectors and the squaring would actually be $\vec{e}_i \cdot \vec{e}_i^{\,\mathrm{T}}$. The equations become

$$E_{total} = \left(\sum \vec{e}_1\right) \cdot \left(\sum \vec{e}_1\right)^{\mathrm{T}} \tag{I.16}$$

$$E_{total} = \left(\sum \vec{e}_1 \cdot \vec{e}_i^{\mathrm{T}}\right) \tag{I.17}$$

Therefore E_{total} is a 3x3 covariance matrix, whose lead diagonal terms are the $\vec{e}_{total}^{\;2}$ values along the principal axes. For the final error summations, three summations are considered – over the error sources, the surveys legs and the survey stations. The propagation modes are used to determine at which steps arithmetic summation is appropriate and at which root squared summation is required. The overall summation of random, systematic and global/well by well error sources is

$$[C]_k^{svy} = \sum_{i\in R}[C]_{i,k}^{rand} + \sum_{i\in S}[C]_{i,k}^{syst} + \sum_{i\in\{W,G\}}[C]_{i,k}^{well} \tag{I.18}$$

where $\vec{e}_{i,l,k}$ is the vector contribution of the i^{th} error source, in the l^{th} survey leg at the k^{th} survey station (3x1 vector)

$\vec{e}^{\,*}{}_{i,l,k}$ is the vector contribution of the i^{th} error source, in the l^{th} survey leg at the last survey point of interest. i.e. the K^{th} survey station (3x1 vector), i denotes the summation over error sources from $1\ldots l$, k denotes the summation of survey stations from $1\ldots K$: the current survey station and l denotes the summation over survey legs from $1\ldots L$: the current survey leg. The contribution of the random errors is given by

$$[C]_{i,K}^{rand} = \sum_{l=1}[C]_{i,l}^{rand} + \sum_{k=1}^{K-1}\left(\vec{e}_{i,l,k}\right)\cdot\left(\vec{e}_{i,l,k}\right)^{\mathrm{T}} + \left(\vec{e}^{\,*}_{i,L,K}\right)\cdot\left(\vec{e}^{\,*}_{i,L,K}\right)^{\mathrm{T}} \tag{I.19}$$

and

$$[C]_{i,l}^{rand} = \sum_{k=1}^{K_l}\left(\vec{e}_{i,l,k}\right)\cdot\left(\vec{e}_{i,l,k}\right)^{\mathrm{T}} \tag{I.20}$$

The systematic errors are given as

$$[C]_{i,K}^{syst} = \sum_{l=1}^{L-1}[C]_{i,l}^{syst} + \left(\sum_{k=1}^{K_l}\vec{e}_{i,L,K} + \vec{e}^{\,*}_{i,L,K}\right)\cdot\left(\sum_{k=1}^{K_l}\vec{e}_{i,L,K} + \vec{e}^{\,*}_{i,L,K}\right)^{\mathrm{T}} \tag{I.21}$$

$$[C]_{i,l}^{syst} = \left(\sum_{k=1}^{K_l}\vec{e}_{i,l,k}\right)\cdot\left(\sum_{k=1}^{K_l}\vec{e}_{i,lk}\right)^{\mathrm{T}} \tag{I.22}$$

The well by well and global errors:

$$[C]_{i,K}^{well} = E_{i,K}\cdot E_{i,K}^{\mathrm{T}} \tag{I.23}$$

$$E_{i,K}^{well} = \sum_{l=1}^{L-1}\left(\sum_{k=1}^{K_l}\vec{e}_{i,l,k}\right) + \sum_{k=1}^{K-1}\vec{e}_{i,L,k} + \vec{e}^{\,*}_{i,L,K} \qquad \text{(I.24)}$$

Appendix II

II. Development of the Attitude Dynamic Equation

The Euler angle method involves the transformation from one co-ordinate frame to another defined by three successive rotations about different axes taken in turn. The direction cosine matrix for vector transformation from body axes $\vec{r}^{\,b}$ to reference axes $\vec{r}^{\,n}$ is given as [20]

$$\vec{r}^{\,n} = C_b^n \cdot \vec{r}^{\,b} \tag{II.1}$$

The propagation of DCM with time or rate of change of C_b^n with time is derived as

$$\dot{C}_b^n = \lim_{\Delta t \to 0} \frac{\Delta C_b^n}{\Delta t} = \lim_{\Delta t \to 0} \frac{C_b^n(t+\Delta t) - C_b^n(t)}{\Delta t} \tag{II.2}$$

As a product of two matrices, $C_b^n\left(t+\Delta t\right)$ can be written as:

$$C_b^n\left(t+\Delta t\right) = C_b^n\left(t\right) \cdot A\left(t\right) \tag{II.3}$$

where $A(t)$ is a direction cosine matrix which relates the b-frame at time t to the b-frame at time $t+\Delta t$. For small angle rotations:

$$A\left(t\right) = \left[I + \Delta\psi\right] \tag{II.4}$$

where by

$$\Delta\psi = \begin{pmatrix} 0 & -\Delta\gamma & \Delta\beta \\ \Delta\gamma & 0 & -\Delta\alpha \\ -\Delta\beta & \Delta\alpha & 0 \end{pmatrix} \tag{II.5}$$

where $\Delta\alpha$,$\Delta\beta$ and $\Delta\gamma$ are the small rotation angles through which the b-frame has rotated over the time interval Δt about its yaw, pitch and roll axes, respectively. Substituting for $C_b^n\left(t+\Delta t\right)$ into Eqn. II.3 and using small angles, we get

$$\dot{C}_b^n = C_b^n \lim_{\Delta t \to 0} \frac{\Delta\psi}{\Delta t} \tag{II.6}$$

$$\lim_{\Delta t \to 0} \frac{\Delta\psi}{\Delta t} = \Omega_{nb}^b \tag{II.7}$$

which therefore results in

$$\dot{C}_b^n = C_b^n \cdot \Omega_{nb}^b \tag{II.8}$$

Transformation from one co-ordinate frame to another carried out as three successive rotations about different axes. These are γ, β and α which denote the rotation angle about the z, y, and x-axis respectively and are also referred to as the Euler rotation angles. The mathematical expression of the three rotations as three separate direct cosine matrices is given as

Rotation γ about z-axis,

$$C_1 = \begin{pmatrix} \cos\gamma & \sin\gamma & 0 \\ -\sin\gamma & \cos\gamma & 0 \\ 0 & 0 & 1 \end{pmatrix} \tag{II.9}$$

Rotation β about y-axis,

$$C_2 = \begin{pmatrix} \cos\beta & 0 & -\sin\beta \\ 0 & 1 & 0 \\ \sin\beta & 0 & \cos\beta \end{pmatrix} \tag{II.10}$$

Rotation α about x-axis,

$$C_3 = \begin{pmatrix} 1 & 0 & 0 \\ 0 & \cos\alpha & \sin\alpha \\ 0 & -\sin\alpha & \cos\alpha \end{pmatrix} \tag{II.11}$$

Transformation from reference to body axes is expressed as

$$C_b^n = C_3 \cdot C_2 \cdot C_1 \tag{II.12}$$

Transformation from body to reference axes given by

$$C_b^n = C_n^{b\mathrm{T}} = C_1^{\mathrm{T}} \cdot C_2^{\mathrm{T}} \cdot C_3^{\mathrm{T}} \tag{II.13}$$

$$C_b^n = \begin{pmatrix} \cos\beta\cdot\cos\gamma & -\cos\alpha\cdot\sin\gamma+\sin\alpha\cdot\sin\beta\cdot\cos\gamma & \sin\alpha\cdot\sin\gamma+\cos\alpha\cdot\sin\beta\cdot\cos\gamma \\ \cos\beta\cdot\sin\gamma & \cos\alpha\cdot\cos\gamma+\sin\alpha\cdot\sin\beta\cdot\sin\gamma & -\sin\alpha\cdot\cos\gamma+\cos\alpha\cdot\sin\beta\cdot\sin\gamma \\ -\sin\beta & \sin\alpha\cdot\cos\beta & \cos\alpha\cdot\cos\beta \end{pmatrix} \tag{II.14}$$

For small angle rotations:

$$C_b^n = \begin{pmatrix} 1 & -\gamma & \beta \\ \gamma & 1 & -\alpha \\ -\beta & \alpha & 1 \end{pmatrix} \tag{II.15}$$

Propagation of Euler angles with time is given as the Euler rotation rates as related to the body rates ω_x, ω_y, and ω_z and expressed as

$$\begin{pmatrix} \omega_x \\ \omega_y \\ \omega_z \end{pmatrix} = \begin{pmatrix} \dot{\varphi} \\ 0 \\ 0 \end{pmatrix} + C_3 \cdot \begin{pmatrix} 0 \\ \dot{\beta} \\ 0 \end{pmatrix} + C_3 \cdot C_2 \cdot \begin{pmatrix} 0 \\ 0 \\ \dot{\gamma} \end{pmatrix} \tag{II.16}$$

This is further re-arranged and expressed in the form:

$$\begin{pmatrix} \dot{\alpha} \\ \dot{\beta} \\ \dot{\gamma} \end{pmatrix} = \begin{pmatrix} 1 & \sin\alpha \cdot \tan\beta & \cos\alpha \cdot \tan\beta \\ 0 & \cos\alpha & -\sin\alpha \\ 0 & \sin\alpha \cdot \sec\beta & \cos\alpha \cdot \sec\beta \end{pmatrix} \cdot \begin{pmatrix} \omega_x \\ \omega_y \\ \omega_z \end{pmatrix} \tag{II.17}$$

Appendix III

III. Sensor Calibration

Mounting of the gyroscopic sensor presents the issue of misalignment which affects the accuracy of the computed angle of rotation. The sensor misalignment is described as the angular difference between each gyroscope's axis of rotation and the system defined inertial reference frame or global frame. The alignment accuracy is basically depended on the IMU's misalignment error and the precision of the mechanical system that holds it in place during operation. This section focuses on a detailed account on the development of a correction alignment matrix that corrects the gyroscope to respond as if they were aligned with the global frame when it is applied to the gyroscope array.

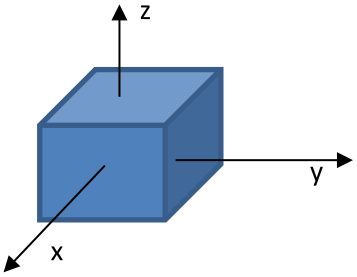

Figure III.1.1: Sensor Module showing its body-fixed reference frame

Rotation around each axis on the global frame (system input) = $\vec{\omega}$

System input bias = $\vec{b}$

Gyroscope output/responses (system output) = $\vec{G}$

Misalignment Matrix (Misalignment & Scale factor) between input and output = M

$$\vec{G} = M\vec{\omega} + \vec{b} \tag{III.1.1}$$

$$\begin{pmatrix} G_x \\ G_y \\ G_z \end{pmatrix} = \begin{pmatrix} M_{11} & M_{12} & M_{13} \\ M_{21} & M_{22} & M_{23} \\ M_{31} & M_{32} & M_{33} \end{pmatrix} \cdot \begin{pmatrix} \omega_x \\ \omega_y \\ \omega_z \end{pmatrix} + \begin{pmatrix} b_x \\ b_y \\ b_z \end{pmatrix} \tag{III.1.2}$$

Also implies that,

$$\vec{\omega} = M^{-1}\left(\vec{G} - \vec{b}\right) \tag{III.1.3}$$

$$\begin{pmatrix} \omega_x \\ \omega_y \\ \omega_z \end{pmatrix} = \begin{pmatrix} M_{11} & M_{12} & M_{13} \\ M_{21} & M_{22} & M_{23} \\ M_{31} & M_{32} & M_{33} \end{pmatrix}^{-1} \cdot \begin{pmatrix} G_x - b_x \\ G_y - b_y \\ G_z - b_z \end{pmatrix} \tag{III.1.4}$$

The accuracy of motion and the gyroscope measurement have a direct impact on the process. The reduction of the impact of the residual bias error is done by the application of rotation twice of equal magnitude and opposite in direction. Given the true rotation about an axis in a given reference frame or system input to be ω_{TR}, the positive rotation as ω_P and the negative rotation (opposite) as ω_N, the following can be expressed

$$\vec{G}_P = M\vec{\omega}_{TR} + \vec{b} \tag{III.1.5}$$

$$\vec{G}_N = -M\vec{\omega}_{TR} + \vec{b} \tag{III.1.6}$$

$$M = \frac{\vec{G}_P - \vec{G}_N}{\vec{\omega}_P - \vec{\omega}_N} = \frac{\vec{G}_P - \vec{G}_N}{2\vec{\omega}_{TR}} \tag{III.1.7}$$

The assumption is that the bias error is constant during both measurements and therefore can be obtained by expressing as

$$\vec{G}_P + \vec{G}_N = 2\vec{b} \tag{III.1.8}$$

$$\vec{b} = \frac{\vec{G}_P + \vec{G}_N}{2} \tag{III.1.9}$$

Generation of the misalignment matrix for compensation; by rotation of the entire system around one axis at a time to isolate each element

Rotation about the x-axis $\left(\omega_x = \omega_{TR}, \omega_y = 0, \omega_z = 0\right)$

$$M_{11} = \frac{G_{xP} - G_{xN}}{2\omega_{TR}} \tag{III.1.10}$$

$$M_{21} = \frac{G_{yP} - G_{yN}}{2\omega_{TR}} \tag{III.1.11}$$

$$M_{31} = \frac{G_{zP} - G_{zN}}{2\omega_{TR}} \tag{III.1.12}$$

Rotation about the y-axis ($\omega_x = 0, \omega_y = \omega_{TR}, \omega_z = 0$)

$$M_{12} = \frac{G_{xP} - G_{xN}}{2\omega_{TR}} \tag{III.1.13}$$

$$M_{22} = \frac{G_{yP} - G_{yN}}{2\omega_{TR}} \tag{III.1.14}$$

$$M_{32} = \frac{G_{zP} - G_{zN}}{2\omega_{TR}} \tag{III.1.15}$$

Rotation about the z-axis ($\omega_x = 0, \omega_y = 0, \omega_z = \omega_{TR}$)

$$M_{13} = \frac{G_{xP} - G_{xN}}{2\omega_{TR}} \tag{III.1.16}$$

$$M_{23} = \frac{G_{yP} - G_{yN}}{2\omega_{TR}} \tag{III.1.17}$$

$$M_{33} = \frac{G_{zP} - G_{zN}}{2\omega_{TR}} \tag{III.1.18}$$

III.1 Least-Squares Estimation Approach

This approach uses no stochastic information but instead treats the parameter-estimation task as a deterministic optimization problem. It assumes the form

$$Y = H\vec{X} + \vec{n} \tag{III.1.19}$$

where n denotes an unknown disturbance or noise. The problem is to select an estimate $\hat{\vec{X}}$ of $\vec{X}$ such that the mean-square error criterion

$$J(\vec{X}) = \frac{1}{2}(Y - H\vec{X})^T W (Y - H\vec{X}) \tag{III.1.20}$$

is minimized. The necessary condition for the LS estimator is

$$\left.\frac{\partial J(\vec{X})}{\partial \vec{X}}\right|_{\vec{X} = \hat{\vec{X}}_{LS}} = 0 \tag{III.1.21}$$

The Least Square Estimator is therefore given as

$$\hat{\vec{X}}_{LS} = (H^T W H)^{-1} H^T W \vec{Y} \tag{III.1.22}$$

This is further written as

$$\hat{\vec{X}}_{LS} = (H^T R_n^{-1} H)^{-1} H^T R_n^{-1} \vec{Y} \tag{III.1.22}$$

Where

$$W = R_n^{-1} \tag{III.1.23}$$

$$R_n = \operatorname{cov}\{\vec{n}\} \tag{III.1.24}$$

where H is the observation matrix, W is the weighing matrix, $\vec{Y}$ is a vector of measurement made and $\vec{n}$ is the zero-mean white Gaussian noise process with a covariance matrix R and $\vec{X}$ is the unknown vector to be estimated. Given that the IMU sensor output is given as:

$$\vec{a}_m = M\vec{a}_t + \vec{b} + \vec{w} \tag{III.1.25}$$

where $\vec{a}_m$ is the observed measurement vector, $\vec{a}_t$ is the true value vector, M is the misalignment Matrix, $\vec{b}$ is the static bias and $\vec{w}$ is the zero-mean white Gaussian noise. The equation represents that for which a linear regression analysis by which an attempt to find the best, in the least-square sense, straight line to fit a given set of data can be made. Given a set of parameter values H_i and observations $\vec{Y}_i$, the estimate $\vec{X}$ can be calculated. The general equation is written in the form

$$\vec{Y}_i = H_i\vec{X} + \vec{n}_i \tag{III.1.26}$$

This is further expressed as

$$\vec{Y}_i = \begin{bmatrix} a_{imx} \\ a_{imy} \\ a_{imz} \end{bmatrix} \tag{III.1.27}$$

$$H_i = \begin{bmatrix} 1 & 0 & 0 & a_{itx} & a_{ity} & a_{itz} & 0 & 0 & 0 & 0 & 0 & 0 \\ 0 & 1 & 0 & 0 & 0 & 0 & a_{itx} & a_{itx} & a_{itx} & 0 & 0 & 0 \\ 0 & 0 & 1 & 0 & 0 & 0 & 0 & 0 & 0 & a_{itx} & a_{itx} & a_{itx} \end{bmatrix} \tag{III.1.28}$$

$$\vec{X} = \begin{bmatrix} b_x & b_y & b_z & M_{xx} & M_{xy} & M_{xz} & M_{yx} & M_{yy} & M_{yz} & M_{zx} & M_{zy} & M_{zz} \end{bmatrix}^T \tag{III.1.29}$$

$$\vec{n}_i = \begin{bmatrix} w_x & w_y & w_z \end{bmatrix}^T \tag{III.1.30}$$

where i denotes the i^{th} measurement for a series of measurements of the same parameters. The noise parameter values are obtained from the datasheet or the result of the Allan variance curve.

The MPU6500A IMU sensor module was placed on the turn table and rotated twice at a specified speed; each in the opposite directions to the other and of equal magnitude. This is repeated for each of the three axes in turn and the gyroscope sensor output data is recorded. The sensor module is then placed at a position aligned with known gravity; first in the upward direction and then in the downward (opposite) direction. This is repeated for each of the three axes in turn and the accelerometer sensor output data is recorded. The room temperature is at 25°. The speed is at 2Hz or 720°s^{-1}.

Table III.1. Main sensor node A1 measurement data:

Gyro A1 Rot.	**x A (°s^{-1})**	**x B (°s^{-1})**	**y A (°s^{-1})**	**y B (°s^{-1})**	**z A (°s^{-1})**	**z B (°s^{-1})**
1	716.2084308	-715.9929612	14.49795449	-6.80763253	0.364140862	1.999178115
2	-12.03490368	12.55532309	720.9942175	-713.3807697	-4.558543653	6.297926614
3	-2.385929991	2.653575454	0.876423744	6.638105506	718.6773275	-716.7366958
Accel A1 Pos.	**(g)**	**(g)**	**(g)**	**(g)**	**(g)**	**(g)**
1	1.000935045	-1.005289688	-0.00404969	-0.023163268	0.059909618	0.054202705
2	0.005217674	0.012908493	0.996808028	-1.007808505	0.063251776	0.062394318
3	-0.010567275	0.014795754	-0.007718669	-0.016554088	1.060747885	-0.955146155

Table III.2. Results using the basic alignment approach:

Gyro Static Bias		**Misalignment Error**					
Bgx	0.167255742	M11	0.9945843	M12	-0.017076546	M13	-0.003499657
Bgy	3.803049838	M21	0.014795547	M22	0.996093741	M23	-0.004001168
Bgz	1.007222273	M31	-0.001135443	M32	-0.007539215	M33	0.996815294
Accel. Static Bias							
Bax	0.003	M11	1.003112367	M12	-0.003845409	M13	-0.012681514
Bay	-0.010414365	M21	0.009556789	M22	1.002308266	M23	0.00441771
Baz	0.057560025	M31	0.002853456	M32	0.000428729	M33	1.00794702

Table III.3. Results using the least-squares estimation approach:

Gyro A1	**Static Bias**	**Misalignment Error**					
Bgx	0.167256	M11	0.994584	M12	-0.0170765	M13	-0.00349966
Bgy	3.80305	M21	0.0147955	M22	0.996094	M23	-0.00400117
Bgz	1.00722	M31	-0.00113544	M32	-0.00753922	M33	0.996815
Accel A1							
Bax	0.003	M11	1.00311	M12	-0.00384541	M13	-0.0126815
Bay	-0.0104144	M21	0.00955679	M22	1.00231	M23	0.00441771
Baz	0.05756	M31	0.00285346	M32	0.000428729	M33	1.00795

Appendix IV

IV. Wellpath Calculation Methods

Wellpath is calculated by finding the approximation of the trajectory between adjacent survey stations which are added up to determine the final wellpath. There are several methods of determining or computing this trajectory of which includes the average angle method, the tangential method, the balanced tangential method, radius of curvature method and minimum curvature method [10,56]. The next section explains how some of the above listed survey methods are derived.

IV.1 Balanced Tangential Method

The balanced tangential method calculates the survey position measurements in the north, east and true vertical direction of both the upper and lower survey station and then finds the average of the two survey position measurements to represent the survey measurement over the incremental measured path. From figure IV.1 the change in displacement in the north, east and true vertical depth is obtained as shown below using simple geometry.

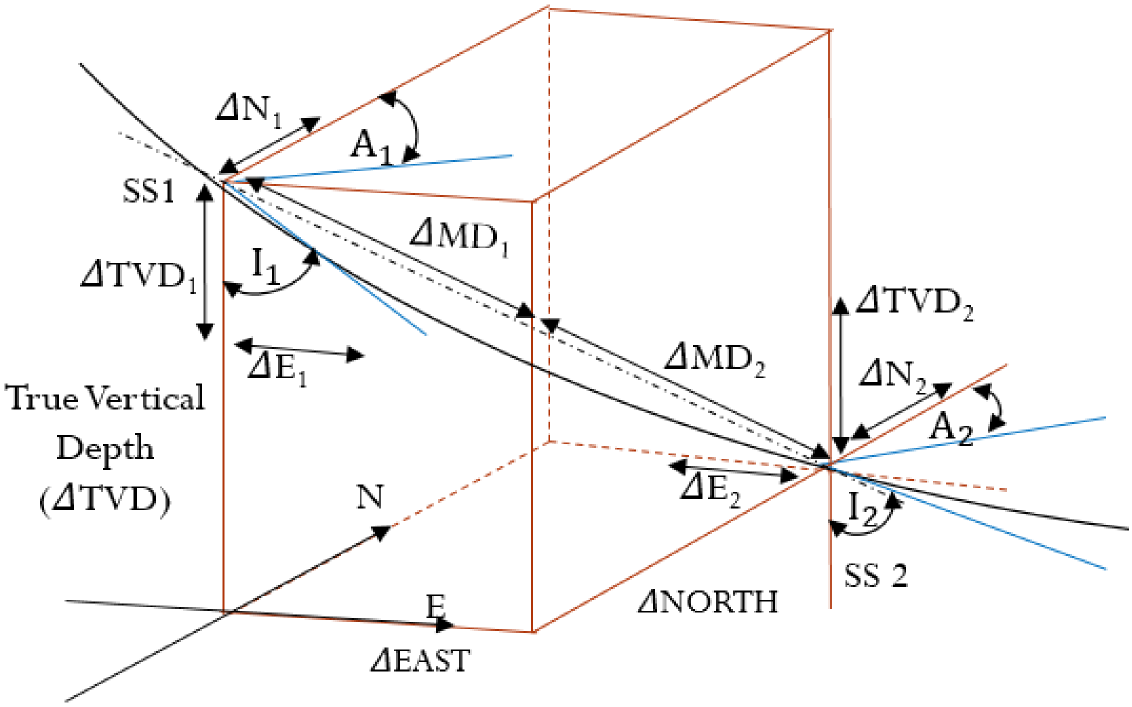

Figure IV.1 Balanced tangential method of wellpath computation

The first part is considered tantential to A_k and I_k and the second part is considered as being tangential to A_{k+1} and I_{k+1}. The average survey position of these two parts is used as the survey position from survey station k to survey station $k+1$.

For the upper part

$$\Delta \mathrm{N}_k = \frac{1}{2}\left(MD_{k+1} - MD_k\right) \cdot \sin \mathrm{I}_k \cdot \cos \mathrm{A}_k \tag{IV.1}$$

$$\Delta \mathrm{E}_k = \frac{1}{2}\left(MD_{k+1} - MD_k\right) \cdot \sin \mathrm{I}_k \cdot \sin \mathrm{A}_k \tag{IV.2}$$

$$\Delta TVD_k = \frac{1}{2}\left(MD_{k+1} - MD_k\right) \cdot \cos \mathrm{I}_k \tag{IV.3}$$

The lower part is also given as

$$\Delta \mathrm{N}_{k+1} = \frac{1}{2}\left(MD_{k+1} - MD_k\right) \cdot \sin \mathrm{I}_{k+1} \cdot \cos \mathrm{A}_{k+1} \tag{IV.4}$$

$$\Delta \mathrm{E}_{k+1} = \frac{1}{2}\left(MD_{k+1} - MD_k\right) \cdot \sin \mathrm{I}_{k+1} \cdot \sin \mathrm{A}_{k+1} \tag{IV.5}$$

$$\Delta TVD_{k+1} = \frac{1}{2}\left(MD_{k+1} - MD_k\right) \cdot \cos \mathrm{I}_{k+1} \tag{IV.6}$$

The computation for the wellpath between the two stations is therefore deduced as

$$\Delta \mathrm{N}_{k,k+1} = \Delta \mathrm{N}_k + \Delta \mathrm{N}_{k+1} = \frac{MD_{k+1} - MD_k}{2} \cdot \left(\sin \mathrm{I}_k \cdot \cos \mathrm{A}_k + \sin \mathrm{I}_{k+1} \cdot \cos \mathrm{A}_{k+1}\right) \tag{IV.7}$$

$$\Delta \mathrm{E}_{k,k+1} = \Delta \mathrm{E}_k + \Delta \mathrm{E}_{k+1} = \frac{MD_{k+1} - MD_k}{2} \cdot \left(\sin \mathrm{I}_k \cdot \sin \mathrm{A}_k + \sin \mathrm{I}_{k+1} \cdot \sin \mathrm{A}_{k+1}\right) \tag{IV.8}$$

$$\Delta TVD_{k,k+1} = \Delta TVD_k + \Delta TVD_{k+1} = \frac{MD_{k+1} - MD_k}{2} \cdot \left(\cos \mathrm{I}_k + \cos \mathrm{I}_{k+1}\right) \tag{IV.9}$$

Appendix V

V. Allan Variance Method for Stochastic Parameter Determination

Allan variance is a method of analysis which is used to obtain the intrinsic noise characteristics (random noise) of the IMU sensor in the time domain. It describes the variance of a signal as a function of integration time. It was originally developed to study frequency stability of oscillators. It basically quantifies the various stochastically-driven errors present on an inertial sensor output which includes angle random walk, rate random walk, bias instability, quantization noise and rate ramp [53-54]. The results of the Allan variance curve provide the parameter values for the bias model used in the dyanamic model for the indirect Kalman filter in Chapter 3.

V.1 Mathematical Description

The IMU sensor instantaneous output can be denoted as a signal with noise which creates an uncertainty in the output signal. This noise is expressed as a frequency deviation error or a phase noise normally expressed as a time error.

Background:

Given the instantaneous signal, based on the oscillator model, as a function of time and denoted as

$$V(t) = V_o \cdot \sin\left(\Theta(t)\right) \tag{V.1}$$

where V_o denotes the signal amplitude and $\Theta(t)$ denotes the instantaneous angle measurement. Assuming the signal has a nominal frequency v_n and a corresponding nominal angular frequency denoted as ω_n where by it is expressed as

$$\omega_n = 2 \cdot \pi \cdot v_n \tag{V.2}$$

The noise associated with this signal is denoted either as a phase noise or a frequency noise which is expressed as a time error $x(t)$ or frequency deviation error $y(t)$ respectively.

The expression in V.2 can be rewritten as

$$V(t) = V_o \cdot \sin\left(2 \cdot \pi \cdot v_n \cdot t + \phi(t)\right) \tag{V.3}$$

and the time error and frequency deviation can subsequently be derived as follows:

For the time error $x(t)$:

$$V(t)=V_o\cdot\sin\left(2\cdot\pi\cdot v_n\left(t+x(t)\right)\right) \tag{V.4}$$

where $x(t)$ is expressed as:

$$x(t)=\frac{\phi(t)}{2\cdot\pi\cdot v_n} \tag{V.5}$$

For the frequency deviation error $y(t)$:

Rewriting equation V.1 as an instantaneous frequency expression

$$V(t)=V_o\cdot\sin\left(2\cdot\pi\cdot v(t)\right) \tag{V.6}$$

whereby

$$v(t)=\frac{1}{2\cdot\pi}\cdot\frac{d\left(2\cdot\pi\cdot v_n\cdot t+\phi(t)\right)}{dt}=v_n+\frac{1}{2\cdot\pi}\cdot\frac{d\phi(t)}{dt} \tag{V.7}$$

The 2nd part of the right-hand side of Eqs V.7 represents the frequency noise which is given as

$$\Delta v(t)=\frac{1}{2\cdot\pi}\cdot\frac{d\phi(t)}{dt} \tag{V.8}$$

The frequency deviation which is expressed as the change in frequency (frequency noise) nomalized with the norminal frequency is given as

$$y(t)=\frac{\Delta v(t)}{v_n}=\frac{1}{2\cdot\pi\cdot v_n}\cdot\frac{d\phi(t)}{dt} \tag{V.9}$$

From the above equation, it becomes obvious that the frequency deviation error is a derivative of the time error and can be expressed as

$$y(t)=\frac{dx(t)}{dt} \tag{V.10}$$

A further expression for the average frequency deviation error which is basically the average taken over the observation time τ (also known as the integration time) is given as

$$\bar{y}(t,\tau)=\frac{1}{\tau}\int_{0}^{\tau} y(t+t_v)dt_v \tag{V.11}$$

And since $y(t)$ is a derivative of the time error $y(t)$, it follows that the above equation can be rewritten as

$$\bar{y}(t,\tau)=\frac{x(t+\tau)-x(\tau)}{\tau} \tag{V.12}$$

Assuming the number of frequency samples in a frequency deviation series is M and assuming the number of time error samples in a time error series is denoted with N. The time error series is written as $x_i = x(i\mathrm{T})$ which denotes the ith sample of the continuous time function $x(t)$ whereby the time error sample series N denotes the number of samples $(x_o \ldots x_{n-1})$. For the average frequency deviation series, $\bar{y}_i$ denotes the ith sample of the average continuous frequency deviation function $y(t)$ which can be written as $\bar{y}_i = \bar{y}(i\mathrm{T},\tau)$. This is further written as

$$\bar{y}_i=\frac{1}{\tau}\int_{0}^{\tau} y(i\mathrm{T}+t_v)dt_v=\frac{x(i\mathrm{T}+\tau)-x(i\mathrm{T})}{\tau} \tag{V.13}$$

where by in the case of the Allan variance, T which is the time between each frequency sample is equal to τ the integration time, and the resulting expression can be rewritten as

$$\bar{y}_i=\frac{x_{i+1}-x_i}{\tau} \tag{V.14}$$

M as defined earlier is represented by the number of samples $(\bar{y}_1 \cdots \bar{y}_M)$ from which the M-sample variance is defined as

$$\sigma_y^2(M,\tau,\tau)=\frac{1}{M-1}\cdot\left\{\sum_{i=0}^{M-1}\left[\frac{x_{i+1}-x_i}{\tau}\right]^2-\frac{1}{M}\cdot\left[\sum_{i=0}^{M-1}\frac{x_{i+1}-x_i}{\tau}\right]^2\right\} \tag{V.15}$$

or with the averaged frequency deviation time series expressed as

$$\sigma_y^2(M,\tau,\tau)=\frac{1}{M-1}\cdot\left\{\sum_{i=0}^{M-1}\bar{y}_i^2-\frac{1}{M}\cdot\left[\sum_{i=0}^{M-1}\bar{y}_i\right]^2\right\} \tag{V.16}$$

The Allan variance is a two-sample variance and is defined with M=2 and denoted as

$$\sigma_y^2(\tau) = \left\langle \sigma_y^2(2,\tau,\tau) \right\rangle \qquad \text{(V.17)}$$

where $\langle \ \rangle$ represents the ensemble average and Eqn V.17 can be expressed as

$$\sigma_y^2(\tau) = \frac{1}{2}\left\langle \left(\bar{y}_k - \bar{y}_{k-1}\right)^2 \right\rangle = \frac{1}{2\cdot\tau^2}\left\langle \left(x_{n+2} - 2x_{n+1} + x_n\right)^2 \right\rangle \qquad \text{(V.18)}$$

with the estimate of the variance expressed as

$$\sigma_y^2(\tau) = \frac{1}{2(N-1)}\sum_{i=1}^{N}\left(\bar{y}_k - \bar{y}_{k-1}\right)^2 \qquad \text{(V.19)}$$

Considering it as a spectral analysis tool and in relation to the power spectral density, the Allan variance can be written as

$$\sigma_y^2(\tau) = \left\langle \left[\int_{-\infty}^{\infty} y(t)\cdot h_y(t_k - t)\,dt\right]^2 \right\rangle \qquad \text{(V.20)}$$

Filtering in the frequency domain, the Allan variance is given as

$$\sigma_y^2(\tau) = \int_0^{\infty} S_y(f)\cdot\left|H_y(f)\right|^2 df \qquad \text{(V.21)}$$

with the fourier transform $\left|H_y(f)^2\right|$ expressed as

$$\left|H_y(f)\right|^2 = \left|FT\left(h_y(t)\right)\right|^2 = 2\cdot\frac{\sin^4(\pi\cdot\tau\cdot f)}{(\pi\cdot\tau\cdot f)^2} \qquad \text{(V.22)}$$

Therefore, the spectral form of the Allan variance is given as

$$\sigma_y^2(\tau) = 4\int_0^{\infty} S_y(f)\cdot\frac{\sin^4(\pi\cdot\tau\cdot f)}{(\pi\cdot\tau\cdot f)^2}\,df \qquad \text{(V.23)}$$

V.2 Procedure

Each sensor was placed in a stationary position and connected to the PC via a serial interface. The Vectornav-100T was read at 40Hz while the MPU6500 IMU sensor was also read at 65Hz. For both sensors, two hours of data was collected and logged.

The procedure is such that a consecutive number of data points N from the logged data, at a data rate with period t_n is obtained. N is then subdivided into n conservative clusters such that the length for each cluster τ is related to the period of the sampling rate given as $\tau = t_n \cdot n$. For instantaneous output form the IMU sensor given as $\lambda(t)$, the cluster average is given as

$$\bar{\lambda}(t) = \frac{1}{\tau} \int_{t_k}^{t_k+\tau} \lambda(t)\,dt \tag{V.24}$$

where $\bar{\lambda}(t)$ denotes the cluster average of the instantaneous output data which starts from the k^{th} data point and contains n data points. The average for the subsequent cluster is given as

$$\bar{\lambda}_{next}(t) = \frac{1}{\tau} \int_{t_{k+1}}^{t_{k+1}+\tau} \lambda_{next}(t)\,dt \tag{V.25}$$

where

$$t_{k+1} = t_k + \tau \tag{V.26}$$

The differences for each two adjoining clusters; $\bar{\lambda}_{next}(\tau) - \bar{\lambda}_k(\tau)$ for each cluster of time τ forms a set of random variables. The variance over all such random variables for clusters of similar size is represented as the Allan variance. The Allan variance therefore of a cluster of length can τ therefore be denoted as

$$\sigma^2(\tau) = \frac{1}{2}\left\langle \left[\bar{\lambda}_{next}(\tau) - \bar{\lambda}_k(\tau)\right]^2 \right\rangle \tag{V.27}$$

where $\langle\ \rangle$ denotes the averaging operation over the ensemble of clusters. This is further be expressed as

$$\sigma^2(\tau) = \frac{1}{2(N-2n)} \sum_{k=1}^{N-2n} \left[\bar{\lambda}_{next}(\tau) - \bar{\lambda}_k(\tau)\right]^2 \tag{V.28}$$

where $n \leq N/2$.

This basically shows that for a finite number of data points N, a finite number of clusters of a fixed length τ can be formed. The estimated variance depends on the number of independent clusters of a fixed length. The characteristics of the underlining noise processes expressed as the Allan deviation is given as

$$\sigma(\tau) = \sqrt{\sigma^2(\tau)} \tag{V.29}$$

The given data-rate and duration of data collection was enough to show its random walk and bias instability as indicated on the accompanying graphs in figures V.1 and V.2. Errors occurring at higher averaging times such as rate random walk and drift ramp were not included since this is influenced much by temperature variations (Laboratory environment with no temperature control). Furthermore, the estimation of the Allan variance is based on a finite number of independent clusters that are formed from any finite length of data, where the confidence of estimation improves as the number of independent clusters is increased [55]. The error for the Allan variance is given as

$$\sigma(\varepsilon)=\frac{1}{\sqrt{2\left(\frac{\mathrm{N}}{n}-1\right)}} \tag{V.30}$$

where N is the total number of data points in the entire run, and n is the number of data points contained in the cluster. From Eq. V.29, it is obvious that the estimation error increases with increase in the averaging time or cluster size.

Errors:

Angle Random Walk (ARW): known as the wideband noise is the high frequency noise and it is observed as the short-term variation in the output [55]. The distribution is proportional to the square root of the elapsed time. It has a correlation time much shorter than the sampling time and is characterized by a white noise spectrum on the gyro rate output. The associated rate noise PSD is represented by

$$S_y(f)=N^2 \tag{V.31}$$

where N is the angles random walk co-efficient. Substitution of Eq. V.31 into Eq. V.23 and performing the integration results in

$$\sigma^2(\tau)=\frac{N^2}{\tau} \tag{V.32}$$

A log-log plot of $\sigma(\tau)$ versus τ has a slope of -0.5 and the numerical value of N is read directly from the slope line at $\tau=1$ (see figures V.1 and V.2).

Bias Instability: it has an impact on the long-term stability of the sensor output. It represents the slow fluctuations or low frequency noise in the sensor output [55]. Bias instability determines the best stability that could be achieved with fully modelled sensor and active bias estimation. The rate power spectral density associated with this noise is given as [53]

$$S_y(f) = \begin{cases} \left(\dfrac{B^2}{2\pi}\right)\dfrac{1}{f}, f \le f_0 \\ \\ 0, f > f_0 \end{cases} \tag{V.33}$$

where B and f_o denotes the bias instability coefficient respectively. Substituting Eq. V.33 into Eq. V.23 and performing the integration results in

$$\sigma^2(\tau) = \frac{2B^2}{\pi}\left[\ln 2 - \frac{\sin^3 x}{2x^2}(\sin x + 4x\cos x) + Ci(2x) - Xi(4x)\right] \tag{V.34}$$

where x denotes $\pi \cdot f_o \cdot \tau$ and C_i denotes cosine-integral function. The log-log plot of Eq. V.34 reaches a horizontal or flat form for τ much longer than the inverse cut off frequency [53]. This region is thus examined to estimate the limit of the bias instability as well as the cutoff frequency of the underlying low-frequency noise.

Table V.1: Summary of the stochastic parameters of the MPU6500 and the Vectornav-100T gyroscopic sensors as read from figures V.1 and V.2

	MPU6500 IMU Gyroscope		**Vectornav-100T Gyroscope**	
Axis	Random Walk °/$\sqrt{s}$	Bias Stability °/s +/- 4.2% err	Random Walk °/$\sqrt{s}$ +/- 0.83% err	Bias Stability °/s +/- 4.6% err
x-axis	$8.9 * 10^{-3}$	$7.9 * 10^{-3}$	$1.87 * 10^{-3}$	$1.92*10^{-4}$
y-axis	$6.9 * 10^{-3}$	$3.83 * 10^{-3}$	$2.01 * 10^{-3}$	$3. 4*10^{-4}$
z-axis	$7.38 * 10^{-3}$	$3.33 * 10^{-3}$	$3.11 * 10^{-3}$	$4.66 * 10^{-4}$

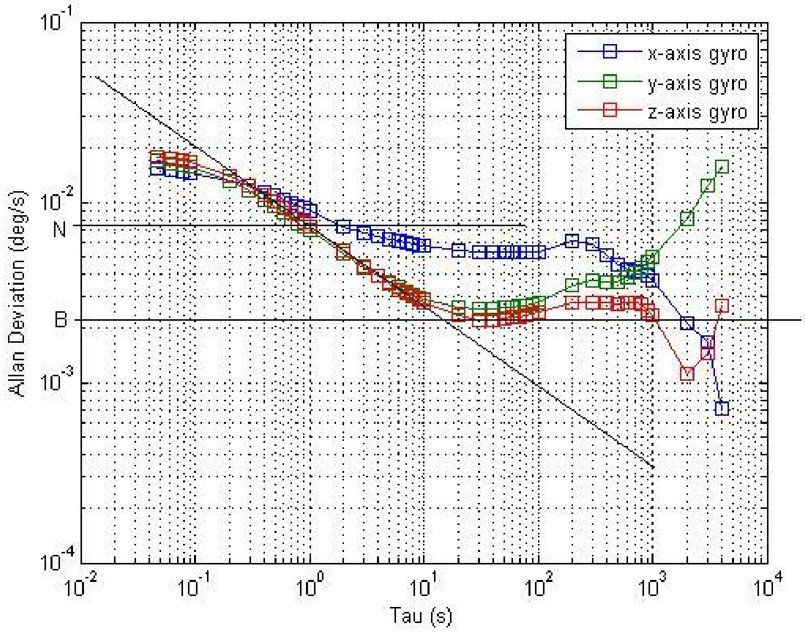

Figure V.1 Allan deviation curve for the MPU6500 Gyroscopic MEMS Sensor

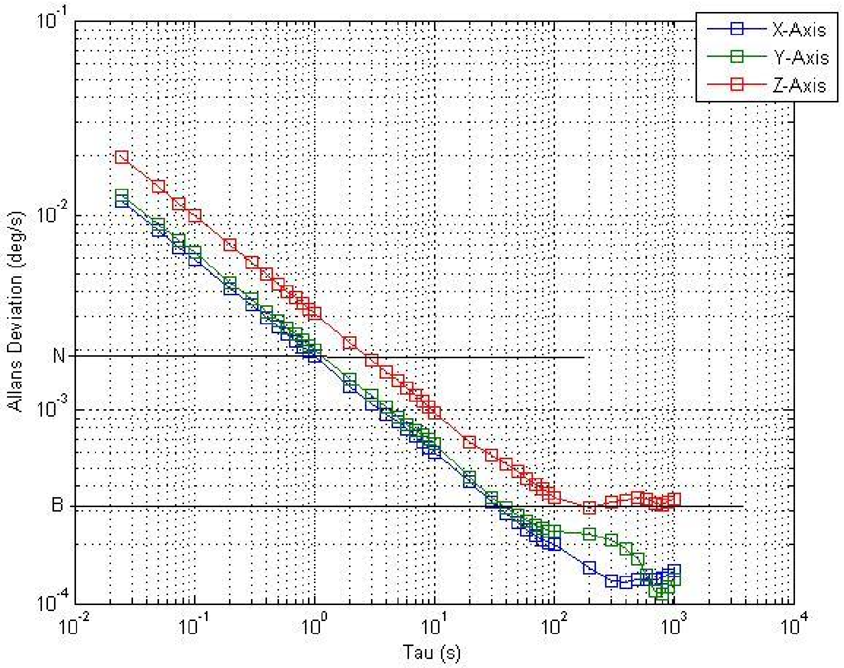

Figure V.2 Allan deviation curve for the Vectornav-100T Gyroscopic MEMS Sensor

The results of the Allan variance are compared to the given specification of the sensors. It is observed that the Vectornav-100T sensor clearly has a better parameter specification with an angle random walk of averaging at 2 * 10^{-3} deg/$\sqrt{s}$ as compared to the MPU6500 gyroscope averages at about 7.5 * 10^{-3} deg/$\sqrt{s}$. The bias stability of the Vectornav-100T also shows a superior performance to that of the MPU6500 as observed from table V.1 and Figures V.1-2. The values of both sensors come close to their datasheet specification. In the datasheet, the MPU6500 has an angle random noise (rate noise spectral density) specified as 0.01°/s/$\sqrt{Hz}$. This is very close to the values of obtained using the Allan variance method. The bias instability and the rate random walk are however not specified. The bias drift or angle random walk given by the Vectornav-100 in its datasheet is 0.005°/s/$\sqrt{Hz}$

BIBLIOGRAPHY

[1] "Deep Soil Mixing (DSM), Improvement of weak soils by the DSM method," Brochure 32-0IE, Keller Group plc, 2016, http://www.kellerholding.com/download-keller-publications.html, Downloaded: 09/08/2016

[2] H. Leung, C. Ghani, W Okada, S. Terzaghi, "Comparison of the effectiveness of Deep Soil Mix columns using 2-D and 3-D plaxis," Plaxis Practice, SKM Sydney

[3] M. Siepi, "Borehole Deviation, Measurement and Control," 4th International Conference on Grouting and Deep Mixing, Deep Foundations Institute, February 2012

[4] G. Downton, "Challenges of Modeling Drilling Systems For the Purposes of Automation and Control", proceedings of the 2012 IFAC Workshop on Automatic Control in Offshore Oil and Gas Production, Trondheim, Norway, May 31 – June 1, 2012

[5] B. Dukas, H. Morkel, "Surface and underground drilling techniques used in exploration drilling," Journal of the South African Institute of Mining and Metallurgy, July 1983

[6] D. Bruce, "The Basics of Drilling for Specialty Geotechnical Construction Processes," Geosystems L.P., Venetia

[7] A. Jamieson, "Introduction to Wellbore Positioning," ISCWSA initiative, UHI, 2012

[8] A. Noureldin, "New Measurement-While-Drilling Surveying Technique Utilizing Sets of Fiber Optic Rotation Sensors, "Degree of Doctor of Philosophy, University of Calgary, March, 2002

[9] A. S. Jurkov, J. Cloutier, E. Pecht, M. P. Mintchev, "Experimental Feasibility of the In-Drilling Alignment Method for Inertial Navigation in Measurement-While-Drilling," IEEE Transactions on Instrumentation and Measurements, Vol. 60, No. 3, March 2011

[10] Z. Wang, M. Poscente, D. Filip, M. Dimanchev, M. P. Mintchev, "Rotary In-Drilling Alignment using an Autonomous MEMS-Based Inertial Measurement Unit for Measurement-While-Drilling Processes," IEEE Instrumentation & Measurement Magazine, 2013

[11] E. Pecht, M. P. Mintchev, "Modeling of Observability During In-Drilling Alignment for Horizontal Directional Drilling, " IEEE Transactions on Instrumentationa and Measurement, Vol. 56, No. 5, October 2007

[12] R. Amorin, E. Broni-Bediako, "Application of Minimum Curvature Method to Wellpath Calculations," Research Journal of Applied Sciences, Engineering and Technology 2(7): 679-686, 2010, ISSN: 2040-7467

[13] Q. M. Lam, J.L. Crassidis, “Precision Attitude Determination Using a Multiple Model Adaptive Estimation Scheme,” IEEE IEEEAC paper #1439, Version 8, 2006

[14] J. Zhou, E. Edwan, S. Knedlik, O. Loffeld, “Low-cost INS/GPS with Nonlinear Filtering Methods, “ IEEE, 2010

[15] M.E.M. Zhang, “Data Fusion for Ground Target Tracking in GSM Networks,” Doctor Thesis

[16] Lefferts, E. J., Markley, F. L., and Shuster, M. D., “Kalman filtering for Spacecraft Attitude Estimation,” Journal of Guidance, Control, and Dynamics, Vol. 5, No. 5, 1982, pp. 417-429

[17] I. Reid, “Estimation II, Discrete-time Kalman filter,” Hilary Term, 2001

[18] A.G. Quinchia, G. Falco, E. Falletti, F. Dovis, C. Ferrer “A Comparison between Different Error Modeling of MEMS Applied to GPS/INS Integrated Systems,” Open Access, Senosrs, ISSN 1424-8220, 2013

[19] Q.M. Lam, J.L. Crassidis, “Precision Attitude Determination Using a Multiple Model Adaptive Estimation Scheme,” IEEEAC paper, IEEE, 1-4244-0525-4/07 2007

[20] J.L. Crassidis, “Sigma-Point Kalman filtering for Integrated GPS and Inertial Navigation,” IEEE Transactions on Aerospace and Electronic Systems, Aerospace & Electronics Systems Society, pp750-756, April 2006

[21] D. Gebre-Egziabher, R.C. Hayward, J. D. Powell, “Design of Multi-Sensor Attitude Determination System,“ IEEE Transactions on Aerospace and electronic system, Vol. 40, No.2 April 2004

[22] D.H. Titterton, J.L. Weston, “Strapdown Inertial Navigation Technology – 2nd Edition,” The Institute of Electrical Engineers, 2004

[23] L Rong, Z Jianhui, L Fan, “Accuracy Improvements of Gyro-Based Measurement-While-Drilling Surveying Instruments by a Laser-Testing Method,” International Symposium on Photoelectronic Detection and Imaging 2009: Laser Sensing and Imaging, Proceedings of SPIE Vol. 7382 73822J-1

[24] D. Gebre-Egziabher, R.C. Hayward, J.D. Powel, “Design of Multi-Sensor Attitude Determination System,” IEEE Transactions on aerospace and electronic systems, Vol. 40, No. 2, April 2004

[25] E. Odei-Lartey, K. Hartmann, “Wireless Ad hoc and Sensor Network Underground with Sensor Data in Real-Time,” IARIA, 2011. ISBN: 978-1-61208-166-3

[26] D. Simon, “Optimal State Estimation, Kalman, H∞ and Nonlinear Approaches,” Cleveland State University, John Wiley & sons, Inc, 2006

[27] N. El-Sheimy, H. Hou, X. Niu, “Analysis and Modelling of Inertial Sensors Using Allan variance,” IEEE Transactions on Instrumentation and measurement, Vol. 57, No. 1, January 2008

[28] O. Loffeld, “Estimations-theorie I,“ Grundlagen und stochastische Konzepte, ISBN 3-486-21616-3, 1990

[29] Peter S. Maybeck, “Stochastic Models, Estimation and Control,“ Mathematics in Science and Engineering, Volume 141, Academic Press, Harcourt Brace Jovanovich, Publishers, 1979

[30] E. Odei-Lartey, K. Hartmann, “In-drilling alignment scheme for borehole assembly trajectory tracking over a wireless ad hoc network,” Proc. SPIE 9872, Multisensor, Multisource Information Fusion: Architectures, Algorithms, and Applications 2016, 98720B

[31] A. A. E Ibrahim, T. A. Musa, T. FengLin, Y. AiGou, „New Trajectory Control Directional MWD Accuracy Prediction and Wellbore Positioning Method,” American Journal of Applied Sciences 2 (3): 711-718, 2005, ISSN 1546-9239, Science Publications

[32] A. Jamieson, “Introduction to Wellbore Positioning,” ISCWSA, University of the Highlands and Islands, 2012

[33] L. Li, M. C. Vuran, and I. F. Akyildiz, “Characteristics of Underground Channel for Wireless Underground Sensor Networks,” Med-Hoc-Net ’07, Corfu, Greece, pp. 92-99, June 13-15

[34] N. R. Peplinski, F. T. Ulaby, and M. C. Dobson, “Dielectric Properties of Soils in the 0.3-1.3-GHz Range”, IEEE Transactions on Geoscience and Remote Sensing, Vol. 33, No. 3, pp. 803-807, May 1995

[35] I. F. Akyildiz, Z. Sun, and M. C. Vuran, “Signal propagation techniques for wireless underground communication networks,” Elsevier Journal, Physical Communication, pp. 167-183, 2009

[36] R. J. Edwards, “RF Skin Depth in the Ground vs. Frequency for Given Soil Characteristics,” Ground Systems, Tigertek Inc, 2010, http://www.smeter.net/grounds/rf-skin-depth-in-soil.php [Last Accessed: 18 July 2011]

[37] “AMB8420 Compact Low-Cost Radio Module 868MHz ISM Band,” datasheet, Amber Wireless, 2009

[38] A. R. Silva and Mehmet C. Vuran, “Communication with Aboveground Devices in Wireless Underground Sensor Networks: An Empirical Study,” IEEE Communications Society, IEEE ICC, pp. 1-6, 2010

[39] S. Kazemian and B. K. Haut, “Assessment of Stabilization Methods for Soft Soils by Admixtures,” International Conference on Science and Social Research, Kuala Lumpur, Malaysia, pp. 118-121, 2010

[40] R. D. Andrus and R M. Chung, “Ground Improvement Techniques for Liquefaction Remediation Near Existing Lifelines,” U.S. Department of Commerce, National Institute of Standards and Technology, pp. 1-85, Ocotober 2005

[41] Daniel S. Weile , “Cylindrical Waves, Guided Waves,” Department of Electrical and Computer Engineering, University of Delaware, ELEG 648 – Waves in Cylindrical Coordinates

[42] Fawwaz T. Ulaby, “Fundamentals of Applied Electromagnetics,” 6th Ed., Prentice-Hall, 2010, ISBN-13: 978-0-13-213931-1

[43] “Specifications for steel pipe,” The industrial group, 2015, LLC. (downloaded: 22/02/2018)http://www.industrialgroupco.com/assets/files/common-pipe-specifications.pdf

[44] S. Yafei, N. Dongjie, S. Jing, “Temperature and Carbon Content Dependence of Electrical Resistivity of Carbon Steel,” 978-1-4244-2800-7/09, IEEE 2009

[45] R. M. Ahmed, M. Sharma, V. Soriano, H. L. Stalford, “Assessment of Borehole telemetry components (Task VI),” RPSEA, Document Number:10121.4504.01.02, ICIFT, March 2014

[46] “Deep hole drilling,” Product catalogue and application guide, Metalworking products, SANDVIK Coromant 2009

[47] Fawwaz T. Ulaby, “Fundamentals of Applied Electromagnetics,” 6th Ed., Prentice-Hall, 2010, ISBN-13: 978-0-13-213931-1

[48] E. Odei-Lartey, K. Hartmann, “Wireless Ad hoc and Sensor Network Underground with Sensor Data in Real-Time,” ICSNC, IARIA, September 2012

[49] http://www.fedsteel.com/products/carbon-pipe-and-tube/api-5l-seamless-line-pipe.htm

[50] G. Cicco, “The Underwater Cut-off at the Walter F. George Dam,” TREVIICOS Corporation, Boston, MA, USA

[51] R.I. Leine, D.H. van Campen, W.J.G. Keultjes, “Stick-slip Whirl Interaction in Drillstring Dynamics,” Journal of Vibration and Acoustics, SME, Vol. 124, Pg.209, April 2002

[52] T. Vromen, “Control of stick-slip vibrations in drilling systems,” ISBN:978-90-386-3966-6, CPI – Koninklijke Wöhrmann, Zutphen, the Netherlands, T.G.M. 2015

[53] IEEE Standard Specification Format Guide and Test Procedure for Single Axis Interferometric Fiber Optic Gyros, IEEE Std 952-1997 (R2008)

[54] A.G. Quinchia, G. Falco, E. Falletti, F. Dovis, C. Ferrer, “A Comparism between Different Error Modeling of MEMs Applied to GPS/INS Integrated Systems,” Open Access, Sensors ISSN 1424-8220, 2013

[55] N. El-Sheimy, H. Hou, X. Niu, “Analysis and Modeling of Inertial Sensors Using Allan variance,” IEEE Transactions on Instrumentation and Measurement, Vol. 57. No. 1, January 2008.

[56] F. O. Farah, “Directional Well Design, Trajectory and Survey Calculations, with a Case Study in Fiale, Asal Rift, Djibouti,” Geothermal Training Programme, United Nations University, Reports 2013

[57] H. Durrant-Whyte, “Multi Sensor Data Fusion,” Australian Centre for Field Robotics, University of Sydney NSW 2006, Version 1.2

[58] O. J. Woodman, “An introduction to inertial navigation,” Technical Report, Number 696, ISSN 1476-2986, University of Cambridge Computer Laboratory, August 2007